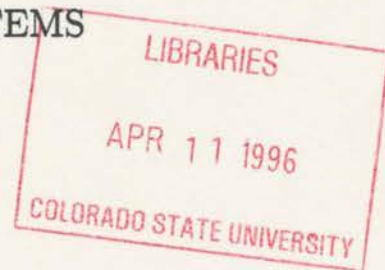


NSF grant ATM-9420045
DOE grant DE-FG03-94ER61749

EVOLUTION OF POTENTIAL VORTICITY ASSOCIATED
WITH MESOSCALE CONVECTIVE SYSTEMS

by Rolf F.A. Hertenstein



William R. Cotton, P.I.

**Colorado
State
University**

**DEPARTMENT OF
ATMOSPHERIC SCIENCE**

PAPER NO. 599

EVOLUTION OF POTENTIAL VORTICITY ASSOCIATED
WITH MESOSCALE CONVECTIVE SYSTEMS

by

Rolf F.A. Hertenstein

Department of Atmospheric Science

Colorado State University

Fort Collins, CO 80523

Research Supported by

National Science Foundation

under Grant ATM-9420045

Department of Energy

under Grant DE-FG03-94ER61749

March 21, 1996

Atmospheric Science Paper No. 599



U18401 3998301

QC
852
CL
no. 599
ATMOS

ABSTRACT OF DISSERTATION

EVOLUTION OF POTENTIAL VORTICITY ASSOCIATED WITH MESOSCALE CONVECTIVE SYSTEMS

In recent years, there has been much interest in cyclonic and anticyclonic circulations which form in association with Mesoscale Convective Systems (MCSs). Using data from the simulations of two MCSs, we investigate the evolution of potential vorticity (PV) associated with these systems. It is found that a positive and negative PV couplet forms at mid levels early during the MCS lifecycle. As the system matures, the couplet is replaced by a dominant positive PV anomaly. At upper levels, a negative PV anomaly dominates and its size depends on the mode of convection. It is found that the MCS with tilted and organized internal flow branches has less of an effect at upper levels than does the MCS with more randomly-organized upright convection.

The analysis performed considers Ertel's PV equation including diabatic and frictional effects. The flux form of this equation is also considered. A budget study of the various terms in the PV equation has been completed over the lifetime of the simulated MCSs. We find that caution must be exercised when applying traditional large-scale approximations of PV to mesoscale systems. For instance, horizontal vorticity contributions to both PV and to the diabatic heating may not be negligible and may even locally dominate. A main result is that the vertical part of the diabatic heating term is a major contribution to the mid-level positive anomaly as anticipated. The negative anomaly forms due to both horizontal and vertical parts of the diabatic heating term. We also investigate the possible role of turbulent eddies in the dissipation of the negative mid-level PV anomaly.

We compare our results to those obtained by nonlinear balance simulations as well as primitive equation simulations of idealized MCSs. In our analysis and comparisons with

previous studies, we focus on blending *PV* and vorticity concepts where possible. Based on the results, a new conceptual model of *PV* evolution in MCSs is presented.

Rolf F.A. Hertenstein
Department of Atmospheric Science
Colorado State University
Fort Collins, Colorado 80523
Spring 1996

ACKNOWLEDGEMENTS

At the risk of appearing politically incorrect, I first wish to thank Emily Walker for putting up with me during this process. Exams, classes, conferences, and a variety of deadlines caused me to be less than pleasant to deal with. These tasks were necessary and Emily ignored my grumpy times and always encouraged me to reach this goal. I believe that graduate student spouses deserve a medal as much or more than the candidates deserve their degrees.

I would like to express thanks to my advisor, William R. Cotton, who provided the opportunity for me to undertake and ultimately complete this task. I am especially grateful for Bill's generously offering me use of his sailplane(s), allowing me to return to flying after many years on the ground. My committee members, Wayne Schubert and Mike Montgomery are also to be thanked. Mike and I sometimes have differences of opinion on how atmospheric science fits into the bigger picture, but in the end, his criticism and critiques were extremely helpful. It is from Wayne Schubert that I really learned the importance of careful, thoughtful research. Discussions with Wayne were always thought provoking, bringing out the creative side of science which is, in my opinion, sadly often lacking in today's scientific community.

A variety of colleagues also deserve acknowledgement. Peter Olsson generously offered data from one of the simulations that I analyzed; a great deal of effort on his part went into the simulation. Peter is also thanked for many discussions about *PV* and convective systems. Bob Walko is thanked for plenty of advice (read the documentation) concerning RAMS. Discussions with Hongli Jiang provided insights into the relation between my work and earlier studies. Rob Cifelli is also thanked for many thought-provoking discussions on our seemingly endless commutes.

Two people from my undergraduate days are acknowledged as well. Peter F. Lester of San Jose State is responsible for my return to atmospheric science and encouraged me

to pursue graduate work. Bob Haberle of NASA-Ames Research Center gave me a great introduction to research during my senior year at San Jose State.

Brenda Thompson and Abby Hodges are thanked for their help in preparing this manuscript. This research was funded by the National Science Foundation under grant ATM-9420045 and the Department of Energy under grant DE-FG03-94ER61749.

TABLE OF CONTENTS

1	Introduction	1
2	Potential Vorticity and Mesoscale Convective Systems	4
2.1	Potential Vorticity	4
2.1.1	<i>Ertel's potential vorticity</i>	5
2.1.2	<i>Applications of potential vorticity</i>	7
2.1.3	<i>Impermeability theorem</i>	11
2.1.4	<i>Potential vorticity and balance</i>	12
2.1.5	<i>Moist potential vorticity</i>	13
2.2	Mesoscale Convective Systems	14
2.2.1	<i>What is an MCS?</i>	14
2.2.2	<i>MCS climatologies</i>	17
2.2.3	<i>MCS forcing and organization</i>	19
2.2.4	<i>The Mid-Level Vortex Associated with MCSs</i>	21
2.3	Potential Vorticity Concepts Applied to MCSs	22
2.4	Summary	28
3	Simulation of the Mesoscale Convective Systems	30
3.1	The Regional Atmospheric Modeling System – RAMS	30
3.1.1	<i>The Level 2.5w Convective Adjustment Scheme</i>	31
3.2	The 10–11 June 1985 MCS	32
3.2.1	<i>Observational and modeling studies of the 10–11 June 1985 MCS</i>	32
3.2.2	<i>System overview</i>	33
3.2.3	<i>Model setup for the 10–11 June 1985 MCS simulation</i>	40
3.2.4	<i>General verification of the RAMS simulation</i>	41
3.2.5	<i>Heating rates</i>	43
3.2.6	<i>Comparison with a simulation using the Kuo cumulus parameterization</i>	46
3.3	The 23–24 June 1985 MCS	46
3.3.1	<i>Observational and model studies of the 23–24 June 1985 MCS</i>	46
3.3.2	<i>System overview</i>	47
3.3.3	<i>Model setup for the 23–24 June 1985 MCS</i>	48
3.3.4	<i>General verification</i>	52
3.3.5	<i>Heating rates</i>	53
4	PV Evolution Associated with the Mesoscale Convective Systems	55
4.1	Post-model Processing	55
4.2	PV evolution during 10-11 June	56
4.2.1	<i>Structure prior to MCS initiation</i>	56
4.2.2	<i>Evolution at mid levels</i>	58

4.2.3	<i>Evolution at upper levels</i>	61
4.2.4	<i>Vertical structure</i>	63
4.2.5	<i>Summary</i>	69
4.3	PV evolution during 23–24 June	71
4.3.1	<i>Structure prior to MCS initiation</i>	71
4.3.2	<i>Evolution at mid levels</i>	73
4.3.3	<i>Evolution at upper levels</i>	75
4.3.4	<i>Vertical structure</i>	75
4.3.5	<i>Summary</i>	83
5	PV Budget Analysis	86
5.1	Contributions to \mathcal{P}	86
5.2	Diagnostic analysis of the \mathcal{P} equation	93
5.2.1	<i>Evolution at mid levels</i>	94
5.2.2	<i>Evolution at upper levels</i>	120
5.2.3	<i>Comparison with Raymond (1992)</i>	123
5.2.4	<i>Comparison with Davis and Weisman (1994)</i>	127
5.2.5	<i>Summary</i>	134
5.3	Material change of \mathcal{P} due to the residual	135
5.3.1	<i>Residual (RES) in the predictive \mathcal{P} equation</i>	135
5.3.2	<i>Possible mechanisms for RES</i>	136
6	Summary and Conclusions	149
6.1	Summary	149
6.2	Conclusions	151
6.3	Conceptual model	155
6.4	Future work	156

LIST OF FIGURES

2.1	(a) Positive PV anomaly (stippled). Potential temperature (quasi-horizontal lines), with the thick line representing the tropopause. Also shown are isotachs, with the + indicating flow into the page and —, flow out of the page. The horizontal axis spans 5000 km. (b) As in (a), except for a negative PV anomaly (from Hoskins et al. 1985).	9
2.2	(a) Heating function ($K\ hr^{-1}$), for an MCS dominated by deep convection only. (b) Resulting PV with a negative anomaly overlying a positive anomaly (from Hertenstein and Schubert 1991).	24
2.3	(a) Heating function ($K\ hr^{-1}$), for an MCS with a convective line and stratiform precipitating region. (b) Resulting PV showing a mid-level positive anomaly and negative anomalies above and below (from Hertenstein and Schubert 1991).	25
3.1	(a) Radar summary at 10/2035 UTC, (b) Surface features at 10/2100 UTC. Iso-bars (solid contours) in inches, station temperature and dew point in degrees C [from JH88], (c) 500 mb analysis showing trough axis at 11/0000 UTC and 12 hours before and after that time [from JH88].	34
3.2	(a) Radar Summary at 10/2335 UTC, (b) Vertical velocity (10/2330 UTC) at 5 km on Grid #2. Contour interval is $0.5\ ms^{-1}$	36
3.3	As in Fig.(3.2) except (a) at 11/0135 UTC, and (b) at 11/0130 UTC.	36
3.4	As in Fig.(3.2) except (a) at 11/0335 UTC, and (b) at 11/0330 UTC.	37
3.5	As in Fig.(3.2) except (a) at 11/0535 UTC, and (b) at 11/0530 UTC.	37
3.6	All figures at 11/0600 UTC. (a) Reduced mean-sea-level pressure from the RAMS simulation, (b) Surface pressure from observations. Solid contour in inches as in Fig.(3.1b) [from Zhang et al. 1989], (c) Surface pressure (solid contours) and temperature in C (dashed contours) from the simulation of Zhang et al. (1989).	38
3.7	All figures at 11/0600 UTC. (a) Total precipitation (mm) from the simulation, (b) Total precipitation (mm) from observations [from Zhang et al. (1989)], (c) Total precipitation from the simulation of Zhang et al. (1989).	39
3.8	Location of the 80 and 20 km grids for the 10–11 June 1985 MCS simulation.	42
3.9	(a) Diagnosis of Q_1/c_p at 11/0300 UTC from observations [from Gallus and Johnson (1991)], (b) Q_1/c_p from the simulation at 11/0300 UTC.	44
3.10	As in Fig.(3.9) except at 11/0600 UTC.	45
3.11	(a) 500 mb analysis at 24/0000 UTC, (b) Surface analysis at 23/2100 UTC.	49
3.12	(a) Radar Summary at 23/2235 UTC, (b) Vertical velocity (23/2235 UTC) at 5 km on Grid #2. Contour interval is $0.5\ ms^{-1}$	49
3.13	As in Fig.(3.12) except at (a) 24/0235 UTC, and (b) at 24/0230 UTC.	50
3.14	As in Fig.(3.12) except at (a) 24/0635 UTC, and (b) at 24/0630 UTC.	50
3.15	Location of the model grids for the 23–24 June 1985 MCS simulation.	52
3.16	Q_1/c_p from the simulation at 24/0600 UTC.	54

4.1	(a) \mathcal{P} and winds at 10/2000 UTC and 5 km over a portion of the Grid #1 domain. Contour interval is 0.3 PVU and maximum wind vector is 27 ms^{-1} , (b) \mathcal{P} and winds at 10/2000 UTC and 10 km, maximum wind vector is 45 ms^{-1} , (c) potential vorticity and potential temperature at 10/2000 UTC along the section shown in (b).	57
4.2	\mathcal{P} and winds over the Grid #2 domain at 5 km. Contour interval is 0.7 PVU and maximum wind vector $\approx 30 \text{ ms}^{-1}$. (a) 10/2330 UTC, (b) 11/0130 UTC, (c) 11/0330 UTC, (d) 11/0530 UTC.	60
4.3	\mathcal{P} and winds over a portion of the Grid #1 domain at 10 km. Contour interval is 0.3 PVU and maximum wind vector $\approx 50 \text{ ms}^{-1}$. (a) 10/2330 UTC, (b) 11/0130 UTC, (c) 11/0330 UTC, (d) 11/0530 UTC.	62
4.4	North-south section of \mathcal{P} at 10/2330 UTC, shown in Fig.(4.2a).	64
4.5	Northwest-southeast sections at 11/0130 UTC, shown in Fig.(4.2b), (a) \mathcal{P} , (b) \mathcal{P} average along the MCS, (c) Standard deviation of \mathcal{P}	65
4.6	Northwest-southeast sections at 11/0330 UTC, shown in Fig.(4.2c), (a) \mathcal{P} , (b) \mathcal{P} average along the MCS, (c) Standard deviation of \mathcal{P}	67
4.7	Northwest-southeast sections at 11/0530 UTC, shown in Fig.(4.2d), (a) \mathcal{P} , (b) \mathcal{P} average along the MCS, (c) Standard deviation of \mathcal{P}	68
4.8	East-west section of \mathcal{P} (bold contours) and potential temperature (light quasi-horizontal contours) at 11/0530 UTC along the same section as shown in Fig.(4.1c).	70
4.9	(a) \mathcal{P} and winds at 23/1900 UTC and 5 km over a portion of the Grid #1 domain. Contour interval is 0.3 PVU and maximum wind vector is 36 ms^{-1} , (b) \mathcal{P} and winds at 23/1900 UTC and 10 km, maximum wind vector is 41 ms^{-1} , (c) \mathcal{P} and potential temperature along the section shown in (b).	72
4.10	\mathcal{P} and winds over a portion of the Grid #2 domain at 5 km. Contour interval is 0.7 PVU and maximum wind vector $\approx 30 \text{ ms}^{-1}$. (a) 23/2230 UTC, (b) 24/0030 UTC, (c) 24/0230 UTC, (d) 24/0430 UTC, (e) 24/0630 UTC.	74
4.11	\mathcal{P} and winds over a portion of the Grid #1 domain at 10 km. Contour interval is 0.3 PVU and maximum wind vector $\approx 45 \text{ ms}^{-1}$. (a) 23/2230 UTC, (b) 24/0230 UTC, (c) 24/0630 UTC.	76
4.12	North-south section of \mathcal{P} at 23/2230 UTC shown in Fig.(4.10a).	77
4.13	North-south section of \mathcal{P} at 24/0030 UTC shown in Fig.(4.10b).	78
4.14	North-south sections at 24/0230 UTC, shown in Fig.(4.10c), (a) \mathcal{P} through the western portion of the MCS, (b) \mathcal{P} through the eastern portion of the MCS, (c) \mathcal{P} average along the MCS, (d) Standard deviation of \mathcal{P}	79
4.15	North-south sections at 24/0430 UTC, shown in Fig.(4.10d), (a) \mathcal{P} , (b) \mathcal{P} average along the MCS, (c) Standard deviation of \mathcal{P}	81
4.16	North-south sections at 24/0630 UTC, shown in Fig.(4.10e), (a) \mathcal{P} , (b) \mathcal{P} average along the MCS, (c) Standard deviation of \mathcal{P}	82
4.17	East-west section of \mathcal{P} (bold contours) and potential temperature (light quasi-horizontal contours) at 24/0630 UTC along the same section as shown in Fig.(4.9c).	83

5.1	Vertical profiles of \mathcal{P} terms at 10/2330 UTC, (a) Through the positive \mathcal{P} anomaly at 5 km, (b) Through the negative \mathcal{P} anomaly at 5 km, (c) Storm-scale average. Vertical profiles of \mathcal{P} terms at 11/0330 UTC, (d) Through the positive \mathcal{P} anomaly at 5 km, (e) Through the negative \mathcal{P} anomaly at 5 km, (f) Storm-scale average.	88
5.2	Vertical sections of the contributions to \mathcal{P} through the positive anomaly at 11/0330 UTC, (a) \mathcal{P}_x (PVU), (b) \mathcal{P}_y (PVU), (c) \mathcal{P}_z (PVU). Contour interval in (a) and (b) is 0.3 PVU, while in (c) it is 0.6 PVU	90
5.3	Vertical sections of vertical velocity (shaded - see color bar), in ms^{-1} and parts of \mathcal{P}_x (contours), (a) zonal vorticity and, (b) zonal potential temperature gradient. Vertical velocity and parts of \mathcal{P}_z , (c) zonal vorticity, (d) zonal potential temperature gradient	92
5.4	(a) Time series of conditionally-sampled \mathcal{P} equation terms, averaged between 3 and 7 km, for the 10-11 June MCS, (b) time series of the number of conditionally-sampled points. (c) Time series of conditionally-sampled \mathcal{P} equation terms, averaged between 3 and 7 km, for the 23-24 June MCS, (d) time series of the number of conditionally-sampled points.	96
5.5	Vertical profile of the \mathcal{P} equation terms for conditional sampling criteria $\mathcal{P} > 0.5$ at (a) 10/2330 UTC, (b) 11/0130 UTC, (c) 11/0330 UTC, (d) 11/0530 UTC. Note the change in magnitude range of the abscissas.	99
5.6	Vertical profiles of contributions to \mathcal{H} at (a) 10/2330 UTC, (b) 11/0330 UTC.	100
5.7	Vertical velocity (contoured) and \mathcal{P} (shaded - see color bar) (a) 10/2330 UTC, (b) 23/2230 UTC.	101
5.8	Vertical profile of the \mathcal{P} terms at (a) 23/2330 UTC, (b) 24/0230 UTC, (c) 24/0430 UTC, (d) 24/0600 UTC. Note change in the range of magnitude on the abscissas.	103
5.9	Vertical profiles of contributions to \mathcal{H} at (a) 23/2330 UTC, (b) 24/0230 UTC.	104
5.10	Horizontal sections of \mathcal{P} (shaded - see color bar) and vertical velocities (contours) at 5 km and (a) 11/0130 UTC, (b) 24/0230 UTC.	105
5.11	(a) Time series of terms ($\mathcal{P} < -0.5$ PVU) for the 10-11 June case, (b) time series of the number of points sampled. (c) Time series of terms ($\mathcal{P} < -0.5$ PVU) for the 23-24 June case, (d) time series of the number of points sampled.	109
5.12	Vertical N-S sections at 11/0130 UTC through the "kink" in the convective line for (a) \mathcal{P} (shaded - see color bar) and vertical velocities (contours), and (b) vertical velocities (shaded) and material change to potential temperature Q	112
5.13	Vertical profiles through the negative \mathcal{P} anomaly north of the "kink" in the convective line, (a) \mathcal{P} equation terms, and (b) contributions to \mathcal{H}	113
5.14	Vertical profile of the \mathcal{P} terms at (a) 10/2330 UTC, (c) 11/0330 UTC, and vertical profiles of contributions to \mathcal{H} at (b) 10/2330 UTC, (d) 11/0330 UTC.	115
5.15	Vertical profile of the \mathcal{P} terms at (a) 23/2330 UTC, (b) 24/0230 UTC.	116
5.16	Vertical profiles of contributions to \mathcal{H} at 23/2330 UTC. Blank areas are those in which no points were sampled.	117
5.17	Vertical velocity (shaded - see color bar), the residual (RES) (contour), and v -component of the flow (vectors).	118
5.18	Storm-scale average of \mathcal{P} terms between 3 and 7 km for (a) 10-11 June, (b) 23-24 June.	138
5.19	Time series of \mathcal{P} equation terms ($\mathcal{P} > 1.2$ PVU), between 9 and 11 km for the 10-11 June MCS.	139

5.20	Time series of \mathcal{P} equation terms ($\mathcal{P} < 0$. PVU), (a) 10–11 June, (b) 23–24 June.	140
5.21	Time series of storm-scale average of \mathcal{P} equation terms between 9 and 11 km, (a) 10–11 June, (b) 23–24 June.	141
5.22	(a) Schematic of a convective storm looking west showing vertical and horizontal dimensions, h and d . Positive westerly shear is assumed, so that the shear vector is out of the page, and the absolute vorticity vector is shown (from Raymond 1992, his Fig. 10). (b) Horizontal section at 5km showing imposed heating (stippling), wind vectors, and PV (positive – vertical hatching, negative – horizontal hatching). Maximum PV is about 0.5 PVU (from Raymond 1992, his Fig. 11).	142
5.23	Non-advective flux divergences due to diabatic effects, (a) $\partial\mathcal{H}_y/\partial y$ at 10/2330 UTC, (b) $\partial\mathcal{H}_z/\partial z$ at 10/2330 UTC, (c) $\partial\mathcal{H}_y/\partial y$ at 11/0330 UTC, (d) $\partial\mathcal{H}_z/\partial z$ at 11/0330 UTC.	143
5.24	(a) Total flux, (b) advective flux, (c) nonadvective flux, (d) q tendency (from Davis and Weisman 1994, their Fig. 11). Contour interval for (a)–(c) is $6 \times 10^{-7} \text{ K s}^{-2}$	144
5.25	Schematic showing tilting of (a) westerly shear, and (b) easterly shear. View is towards the west (from Davis and Weisman 1994), their Fig. 13.	144
5.26	North–south section through the horizontal \mathcal{P} dipole at 10/2330 UTC, (a) meridional advective and non-advective flux divergence, (b) vertical advective and non-advective flux divergence.	145
5.27	Vertical profiles of vorticity tilting and stretching (s^{-2}) averaged over the positive anomaly for, (a) 10/2300 UTC, and (b) 23/2200 UTC. Values along the abscissa have been multiplied by 10^8	146
5.28	Vertical profiles of vorticity tilting and stretching (s^{-2}) averaged over the negative anomaly for, (a) 10/2300 UTC, and (b) 23/2200 UTC. Values along the abscissa have been multiplied by 10^8	147
5.29	Horizontal section of flow vectors, vertical velocity (thick contours), and θ' (shading) at 6 hours, (a) near the surface, (b) 3 km, (c) 8 km. Plotting domain is 300 by 400 km (from Skamarock et al. 1994, their Fig. 13).	148
5.30	(a) horizontal vorticity tilting, (b) vorticity stretching, at 3 km and 6 hr of simulation. Darker shading indicates higher values (from Skamarock et al. 1994, their Fig. 9).	148

LIST OF TABLES

3.1	Model configuration for the 10–11 June 1985 MCS simulation.	41
3.2	Model configuration for the 23–24 June 1985 MCS simulation	51
5.1	Horizontal dimension of heating d , vertical shear $S = \partial u / \partial z$, and for aspect ratio calculations. Vertical dimension of heating $h = 10$ km, and $f = 10^{-4} \text{s}^{-1}$. . .	125

Chapter 1

INTRODUCTION

Mesoscale Convective Systems (MCSs) are important precipitating weather phenomena during spring and summer months in the central United States and in many regions worldwide. These systems not only contribute strongly to the precipitation budgets of the affected region, but are also often associated with severe weather, including tornados, hail, strong straight-line winds, and flash flooding. Distinguishing features of MCSs compared to ordinary thunderstorms include their much larger size and longer lifetime, both of which are approximately an order of magnitude greater for MCSs. In addition, MCSs often feature organized mesoscale circulations, which can last for hours or sometimes days.

An interesting and largely unanswered question regarding MCSs is that of scale interactions. For instance, it is not yet completely understood how or to what extent the synoptic environment influences the initiation, upscale growth, organization, or longevity of an MCS. And although MCSs have often been documented to leave in their wake mesoscale circulations, it is not fully understood how these may affect mesoscale or synoptic-scale weather after the MCS has dissipated. A more complete understanding of the scale interactions would be useful not only in improving forecasts of MCSs, but also for its potential to improve synoptic-scale forecasts in the wake of these systems. In addition, there is also some evidence that MCSs may sometimes act as "seeds" for tropical cyclones, making an understanding of these systems important for both the midlatitude and tropical meteorologist.

Several recent studies (e.g., Raymond and Jiang 1990; Hertenstein and Schubert 1991; Davis and Weisman 1994) have indicated that a mid-level potential vorticity PV anomaly is a common signature left behind by the MCS, and may be a useful quantity to

investigate this problem. Thus, it is important to better understand how *PV* evolves in association with MCSs. Past studies have investigated *PV* in association with MCSs using either idealized numerical models (Raymond and Jiang 1990; Hertenstein and Schubert 1991; Raymond 1992; Jiang and Raymond 1995), primitive equation models using idealized initial conditions (e.g., Davis and Weisman 1994), or via large-scale data sets (e.g., Fritsch et al. 1994). These studies have focused on the influence of diabatic heating in the final *PV* distribution associated with MCSs. Most, if not all, past studies have neglected the effects of friction. While the studies are valuable to further our understanding, the data sets used in these studies necessarily leave out details which potentially may be important to *PV* evolution in MCSs.

An understanding of *PV* evolution in MCSs has possible practical value for the problem of parameterizing MCSs in General Circulation Models (GCMs), which usually have grid spacings too large to fully resolve MCSs. It has been suggested that *PV* (or specifically *PV* variance) may make a useful framework for an MCS parameterization for GCMs (Bill Cotton, personal communication).

This dissertation is mainly concerned with the documentation and analysis of the evolution of *PV* associated with two MCSs which occurred during the PRE-STORM field experiment in 1985. The Regional Atmospheric Modeling System (RAMS) was used to simulate both systems; output from these simulations provides us with a high-resolution data set for analysis. The main processes responsible for the *PV* evolution are identified. In addition, our results are compared with earlier studies. To gain further insight into the main processes, we use an analogy between vorticity and *PV* viewpoints, which helps us build a conceptual model. One interesting aspect of this research will focus on the frictional "source/sink" term in the *PV* equation, which has been largely neglected in previous studies.

The dissertation is organized as follows. In Chapter 2, we review some previous work on *PV*, MCSs, and studies which apply *PV* concepts to MCSs. The numerical model used (i.e., RAMS) is discussed in Chapter 3 as well as a general verification of the simulations. We next examine *how PV* evolved over the entire lifecycle of the MCSs in Chapter 4,

while in Chapter 5 we examine *why PV* evolved as it did. A summary, conclusions, and future work are presented in Chapter 6.

Chapter 2

POTENTIAL VORTICITY AND MESOSCALE CONVECTIVE SYSTEMS

The concept of potential vorticity has been known and used for decades. Applications of potential vorticity diagnostics have traditionally been restricted to large-scale problems. More recently, however, potential vorticity has been utilized in mesoscale problems, e.g., in the examination of fronts and also organized convective systems.

In this chapter we first review potential vorticity concepts and their applications. We then aspects of our current knowledge of MCSs, from both observational and modeling studies is reviewed. Finally, we explore how potential vorticity concepts have been and could be used in the study of MCSs before addressing some unanswered questions.

2.1 Potential Vorticity

The earliest mention of potential vorticity is found in a paper by Rossby (1940), in which he was exploring the character of flow patterns in the atmosphere and how they change. Rossby defines potential vorticity in the shallow-water framework as

$$PV = \frac{\zeta + f}{h}, \quad (2.1)$$

where ζ is the relative vorticity, f the Coriolis parameter, and h the depth of the fluid. For adiabatic, frictionless flow this quantity is conserved. Thus if we stretch the fluid (i.e., increase h) we must increase the absolute vorticity. For zonal flows this means we must increase ζ , resulting in increased cyclonic flow. This compact quantity combines information about mass and flow fields in one variable and has been used to explain, among other things, lee cyclogenesis, as a column of air is stretched after crossing a mountain barrier.

It was Rossby's intention that potential vorticity be used as a measure of the potential for a mass of air to obtain relative vorticity. Indeed, quoting from Rossby (1940):

....the potential vorticity, represents the vorticity the air column would have if it were brought, isopycnally or isentropically, to a standard latitude and stretched or shrunk vertically to a standard depth or weight.

This is analogous to the notion of potential temperature, whereby a parcel has the potential to obtain a certain temperature through adiabatic expansion or compression.

2.1.1 Ertel's potential vorticity

A more general definition of potential vorticity is found in Ertel (1942). Starting with a three-dimensional vector form of the equations of motion for frictionless flow, along with the thermodynamic equation for adiabatic motion and the mass continuity equation, Ertel derived the conservation principle,

$$\frac{d}{dt}(\alpha \zeta_{\mathbf{a}} \cdot \nabla \psi) = 0 \quad (2.2)$$

where α is the specific volume (i.e., $1/\rho$), $\zeta_{\mathbf{a}}$ is the absolute vorticity vector, and ψ is any conservative thermodynamic variable. In meteorology we generally use potential temperature, θ , for the conserved thermodynamic quantity. An example of an alternate conserved scalar is found in Lait (1994).

Using θ , our equation becomes

$$\frac{d\mathcal{P}}{dt} = \frac{d}{dt}(\alpha \zeta_{\mathbf{a}} \cdot \nabla \theta) = 0. \quad (2.3)$$

The conserved quantity $\mathcal{P} = \alpha \zeta_{\mathbf{a}} \cdot \nabla \theta$ is referred to as Ertel's potential vorticity.¹ It is important to note that the only assumptions are for frictionless, adiabatic flow; an extension of Ertel's theory to include diabatic and frictional effects is straightforward.

¹We will use PV for general use in describing potential vorticity-like quantities, i.e., a vorticity divided by some measure of fluid depth or mass. The symbol \mathcal{P} will be used only for Ertel's PV as defined above. EPV is sometimes used in the literature for \mathcal{P} .

Starting with the vector equation of motion which includes friction, and a thermodynamic equation with a term representing diabatic processes, we obtain

$$\frac{d\mathcal{P}}{dt} = \mathcal{H} + \mathcal{F} \quad (2.4)$$

where $\mathcal{H} = (1/\rho)\zeta_a \cdot \nabla Q$, and $Q = d\theta/dt$ is a diabatic potential temperature source (material change in potential temperature) and $\mathcal{F} = (1/\rho)\nabla\theta \cdot \nabla \times \mathbf{F}$ is the material change in \mathcal{P} due to frictional effects. We will discuss \mathcal{H} and \mathcal{F} , especially in regards to PV and MCSs, in Section 2.3.

Expanding the dot product in Eq. (2.3), we find that \mathcal{P} is a scalar quantity made up of three parts, i.e.,

$$\mathcal{P} = \frac{1}{\rho} \left[\left(\frac{\partial w}{\partial y} - \frac{\partial v}{\partial z} \right) \frac{\partial \theta}{\partial x} + \left(\frac{\partial u}{\partial z} - \frac{\partial w}{\partial x} \right) \frac{\partial \theta}{\partial y} + \left(\frac{\partial v}{\partial x} - \frac{\partial u}{\partial y} + f \right) \frac{\partial \theta}{\partial z} \right]. \quad (2.5)$$

The first two terms represent the product of horizontal vorticity and horizontal gradients of θ , (baroclinic terms), while the final term is the product of the vertical component of absolute vorticity and static stability (vertical θ gradients).

The units associated with \mathcal{P} merit comment; from (2.5) these are a rather unintuitive $\text{m}^2 \text{s}^{-1} \text{K kg}^{-1}$. Pedlosky (1979, pg. 41) states: “the name seems poorly chosen, for PV does not even have the dimensions of vorticity”. Bleck (1973) says of Ertel’s PV : “we are as comfortable as Rossby about the physical meaning of this dimensionally awkward quantity”. The most common units used for \mathcal{P} today are those suggested by Hoskins et al. (1985). They define $1 \text{ PVU} = 10^{-6} \text{ m}^2 \text{ s}^{-1} \text{K kg}^{-1}$. Using this definition, ambient tropospheric \mathcal{P} values are typically less than 0.5 PVU, with a typical tropopause value of 2 PVU. It can be argued that redefining \mathcal{P} , such that only units of s^{-1} (i.e., the units of vorticity) remain, is more consistent with the appellation “potential” vorticity. In this work, we will abide by recent tradition and use PVU.

While (2.4) is expressed in material form, it can also be written in flux form. Decomposing the total time derivative on the left-hand side of (2.4), multiplying through by ρ and using mass continuity yields

$$\frac{\partial(\rho\mathcal{P})}{\partial t} = -\nabla \cdot [\rho\mathbf{u}\mathcal{P} - \zeta_a Q - \mathbf{K}\theta] \quad (2.6)$$

where \mathbf{u} is the three-dimensional velocity vector and $\mathbf{K} = \nabla \times \mathbf{F}$ is the frictional force-curl. The predicted quantity $\rho\mathcal{P}$ has been referred to as “potential vorticity substance”, which will be further discussed in Section 2.1.3. The first term in brackets on the right-hand side of (2.6) is the advective flux of $\rho\mathcal{P}$, while the second and third terms in brackets are the non-advective flux.

2.1.2 Applications of potential vorticity

Traditional applications of potential vorticity were limited to large-scale studies in which the first two terms of (2.5) are neglected from scaling arguments. We often see a pressure-coordinate definition (e.g., Hoskins et al. 1985)

$$PV = -g(\zeta + f) \frac{\partial \theta}{\partial p} \quad (2.7)$$

Dunkerton and Delisi (1986) refer to (2.7) as the “hydrostatic, high-Richardson number form” of Ertel’s PV . Large Richardson number (R_i) implies that vertical shear is small (thus also horizontal derivatives of θ are small). From the hydrostatic approximation, horizontal derivatives of the vertical velocity are neglected, thus two terms

$$\left(\frac{\partial w}{\partial y} - \frac{\partial v}{\partial z} \right) \frac{\partial \theta}{\partial x}$$

and

$$\left(\frac{\partial u}{\partial z} - \frac{\partial w}{\partial x} \right) \frac{\partial \theta}{\partial y}$$

are neglected in (2.5).

In the four decades following Ertel’s original derivation, the usefulness of PV was not widely explored, however several references can be found in the literature. In a series of papers, Kleinschmidt (1950a,b, 1951) and later Eliassen and Kleinschmidt (1957) applied Ertel’s theorem to cyclone theory, showing that surface cyclones were accompanied by a positive PV anomaly (i.e., high- PV air relative to the environment) aloft. Kleinschmidt was also apparently the first to recognize that PV has an important further use. Under certain constraints, information about the mass and wind fields can be diagnosed from PV ; we will return to this notion of an “invertibility principle” later. Bleck (1973) expanded

on Kleinschmidt's work with a PV -predicting model using isentropic vertical coordinates. The model successfully predicts surface cyclogenesis with the approach of high- PV air aloft, in agreement with the analysis of Kleinschmidt.

Other early work involves the use of PV as a tracer of stratospheric air. Since PV is a function of static stability, regions with strong static stability should also be regions of high potential vorticity (assuming the absolute vorticity doesn't vary greatly from f). The stratosphere has been recognized as a possible source region or reservoir of high- PV air; above the tropopause $\partial\theta/\partial z$ rapidly increases and hence so does PV . An early example of such work can be found in Staley (1960) who explored the possibility that PV could be used as a tracer to forecast the transfer of radioactive debris. Other studies investigating PV and other stratospheric tracers near tropopause folds using aircraft data have been carried out by Shapiro (1976) and Danielson et al. (1987).

Much of the early work on PV and the invertibility principle mentioned above is summarized in the review by Hoskins et al. (1985). The authors demonstrate the usefulness of PV when viewed on isentropic maps for both cutoff cyclones and blocking highs, and point to conceptual links between the two phenomena. An important concept they discuss is the "action at a distance" idea associated with the invertibility principle, which we will return to in Section 2.1.4.

Circulations and mass perturbations associated with a given PV anomaly extend both horizontally and vertically well beyond the anomaly itself. Note that the positive PV anomaly is made up of both anomalously high absolute vorticity and static stability (Fig. 2.1).

In another important section of their review, Hoskins et al. discuss the vertical motions below and ahead of an upper-level PV anomaly which are required to maintain balance. The authors then go on to further discuss the invertibility concept, applying these ideas to propagating Rossby waves as well as baroclinic and barotropic shear instabilities. Here, the conceptual model they present relies on "action at a distance" as well as the idea of the Rossby height, fL/N . The basic idea is that given two positive PV anomalies, one at upper levels and one at a lower level, separated by less than a Rossby height, the

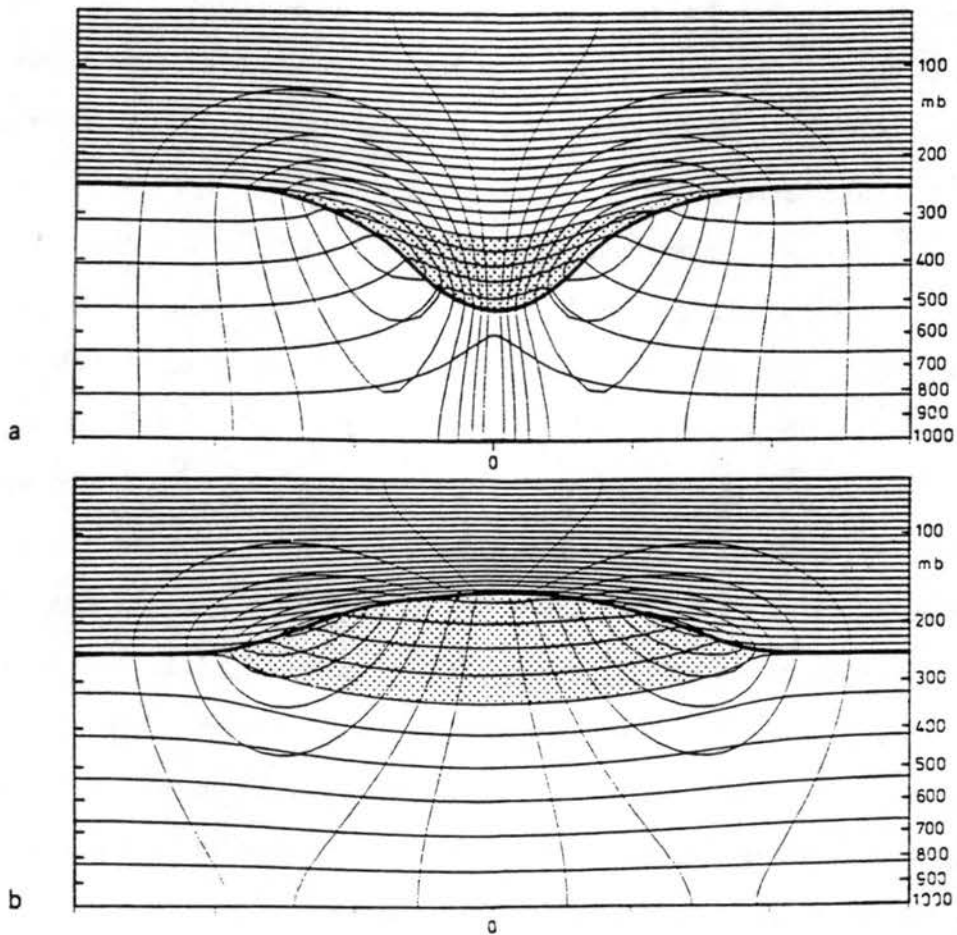


Figure 2.1: (a) Positive PV anomaly (stippled). Potential temperature (quasi-horizontal lines), with the thick line representing the tropopause. Also shown are isotachs, with the $+$ indicating flow into the page and $-$, flow out of the page. The horizontal axis spans 5000 km. (b) As in (a), except for a negative PV anomaly (from Hoskins et al. 1985).

induced circulation of each anomaly helps the other track with it and helps the other anomaly strengthen. (see Fig. 18 of Hoskins et al.). The same idea holds for barotropic disturbances separated horizontally by less than the Rossby radius of deformation. This offers us a conceptually simple model for the baroclinic and barotropic instability problem.

Hoskins et al. next discuss frictional and diabatic effects with the important conclusion that non-conservative effects can only change the PV distribution at a material boundary. In the interior, friction or diabatic effects only act to rearrange the PV distribution. It is important to note that here we have only highlighted some of the more important aspects of this review. The details are enlightening and the reader is referred to the full manuscript.

Two case studies involving severe surface winds associated with extratropical cyclones are presented by Hoskins and Berrisford (1988) and Browning and Reynolds (1994). In each case, the investigators were able to identify a strong upper-level PV anomaly associated with a sharp lowering of the tropopause. Strong surface winds were noted to migrate in conjunction with the movement of this upper-level feature and were especially strong when the upper-level PV anomaly "locked onto" a region of low-level baroclinicity, as discussed above. A review of the theory of extratropical cyclones, with emphasis on the PV perspective is found in Hoskins (1990). Hoskins also links theory and many of the features seen in the first case study (i.e., Hoskins and Berrisford 1988).

Another use of PV is in the diagnosis of Symmetric Instability (SI). Generally, this type of instability can be thought of as a combination of inertial and static stability concepts, where instead of strictly horizontal or vertical displacements resulting from these instabilities, SI leads to slantwise parcel displacements.

Hoskins (1974) demonstrates that a condition for SI is that $PV < 0$. Recall that if the atmosphere is adiabatic and inviscid, PV is materially conserved. Thus frictional and/or diabatic effects are required for SI to be generated from an initial state with $PV > 0$ everywhere. Bennetts and Hoskins (1979) added the complexity of latent heat effects to the analysis of SI. When SI can occur due to latent heat release, we have Conditional Symmetric Instability (CSI). It turns out that the condition for CSI is that the *moist*

PV be negative, i.e., either the conditional static stability or the absolute vorticity be less than zero. We will define moist PV and further discuss its use in section 2.1.5. Applications of the CSI ideas to rainbands can be found in Bennetts and Sharp (1982) and Emanuel (1983a). Emanuel (1983b) discusses analysis of CSI using upper-air soundings while Snook (1992) looks at real-time forecasting of CSI using a higher-resolution observational network combined with mesoscale models for more “local” problems.

Since in this dissertation we are mainly concerned with the evolution of PV associated with MCSs, a discussion of PV concepts applied to MCSs will appear separately in Section 2.3.

2.1.3 *Impermeability theorem*

Haynes and McIntyre (1987) derived an important theorem for potential vorticity which can be summarized in two statements taken directly from Haynes and McIntyre:

1. *There can be no net transport of Rossby–Ertel potential vorticity (PV) across any isentropic surface.*
2. *PV can neither be created nor destroyed, within a layer bounded by two isentropic surfaces.*

The authors point out, however, that PV can be transported along isentropically bounded layers and can be created/destroyed where an isentropic layer contacts the surface. This theorem is very general, being independent of the coordinate system used or whether or not the hydrostatic approximation is made. Further, the theorem holds in differential or integral form. These properties constitute what is known as the “impermeability theorem”.

This theorem caused some debate. Based on arguments largely from the analysis of observational data, Danielson (1990) contradicted the theorems. Haynes and McIntyre (1990) responded with further clarification of their ideas and replaced PV in their earlier paper with the notion of “ PV substance” ($\rho\mathcal{P}$). As we have already seen, this PV substance lends itself nicely to the flux form of the PV Eqn. (2.6). Although there is no physical PV substance analogous to say, water substance, it is a useful quantity for

conceptual purposes. One way to consider the fact that PV cannot be transported across isentropic surfaces is to split velocity and vorticity into components perpendicular and parallel to the isentropes. From this decomposition, it turns out that as PV is apparently transported across isentropes, potential temperature changes locally, compensating for the apparent cross-isentrope transport. Thus, the isentropes act as a semi-permeable membrane, allowing mass but not PV to be transported across.

As pointed out by Keyser and Rotunno (1990), the controversy stems from a difference in the definition of “mixing ratio” as well as differences in the averaging procedure used by Haynes and McIntyre (1987) and Danielson (1990), leading to fundamental differences in the definition of PV . This latter point is important; a domain-averaged potential vorticity (\overline{PV}) derived from the domain-averaged momentum equations is not the same as deriving PV from the exact momentum equations and then averaging. In the latter case, several terms involving Reynold’s stresses of unresolved quantities appear.

In a recent paper, Bretherton and Schär (1993) remind us of the fact that the Haynes and McIntyre (1990) non-conservative flux is only unique up to a non-divergent vector field. They then present a “new and extremely simple” proof of the PV conservation theorem based on a somewhat different choice of the nonadvective flux vector.

2.1.4 *Potential vorticity and balance*

It has been said that “ PV is only as useful as the attendant balance approximation” (M. Montgomery, loosely quoted from personal communication). This is especially true for an atmospheric model in which PV is the main predicted quantity. However, a balance approximation may not be necessary for studies in which PV is simply used as a tracer. Since our main concern in this dissertation is the evolution of PV itself, we will only briefly discuss some balance concepts. A complete review of balance approximations and the evolution of balanced flows in MCSs can be found in Olsson (1994).

A model which uses PV as the main predicted variable requires an invertibility relationship to close the model by supplying needed wind and thermodynamic fields for the next time step. The invertibility relation is based on two balance assumptions, the hydrostatic assumption in the vertical, and a horizontal balance condition, e.g., geostrophic or

nonlinear balance. An example of one such model is that of Schubert et al. (1989) which uses semigeostrophic theory on an isentropic vertical coordinate. In this model, the inverse of PV is predicted, a stream function \mathcal{M} is diagnosed via an invertibility relation, and then the balanced wind and mass fields needed to further predict PV are diagnosed from \mathcal{M} . This type of model has advantages in its simplicity (only one predictive equation), however is limited in its physics by the balance assumptions employed.

Another important issue concerning PV and balance is the “action at a distance” idea mentioned previously. This is illustrated by noting that in Fig. 2.1 the effects of the PV anomaly on the balanced wind and mass fields extend well beyond the anomaly itself. This has ramifications for the effects of upper-level PV anomalies inducing low-level flow fields, for instance in the formation of extratropical or tropical cyclones (Montgomery and Farrell 1992,1993). The potential role of upper-level PV anomalies in MCS formation has been speculated (M. Montgomery, personal communication) but has not been tested. Another view of the “action at a distance” idea is presented by Bishop and Thorpe (1994) who make the analogy between wind and mass fields associated with a PV anomaly and the electrostatic field induced by an electric charge.

It should not be inferred from this brief treatment that these concepts are relatively unimportant. Rather, these ideas are extremely important in a complete “ PV view” of atmospheric dynamics, and are thus worthy of further study (e.g., Olsson 1994).

2.1.5 *Moist potential vorticity*

Moist potential vorticity (MPV) is usually defined by replacing θ with θ_e in the expression for Ertel’s PV , i.e.,

$$MPV = \alpha \zeta_a \cdot \nabla \theta_e. \quad (2.8)$$

At first glance, this simple change looks appealing in that we now have included the effects of moisture and hence the PV concepts should be more general. However, there are complications which arise using (2.8). First, it is not at all apparent how one could use MPV as the main predicted quantity for a closed model as described in Section 2.1.4. We encounter this difficulty because there exists no hydrostatic balance associated

with θ_e as we have with θ . Thus we lose the associated invertibility relation to close the model. Second, use of θ_e leads to a more complex form of a predictive equation for MPV as compared to PV (Guinn and Schubert 1994). Specifically, we gain a solenoidal term of the form $\alpha \nabla \theta_e \cdot (\nabla p \times \nabla \alpha)$. To alleviate this second problem, one could choose saturated equivalent potential temperature (θ_{es}) instead of θ_e but this leads to interpretation difficulties in unsaturated regions. Thus the extension of PV concepts to include moist thermodynamics is not a straightforward problem.

This does not, however, imply that MPV is a useless quantity. As discussed in Section 2.1.2, MPV is useful for diagnosing conditional symmetric instability, e.g., in the formation of frontal rainbands (Bennetts and Hoskins 1979). Recently, CSI has found application in a simulated MCS. Zhang and Cho (1992) show how low-level air with negative MPV (the condition for CSI) is transported upwards and leads to the slantwise ascent (the so called front-to-rear flow branch) seen in many mature MCSs. This is an interesting idea which should be further pursued.

2.2 Mesoscale Convective Systems

In this section, we will temporarily leave our discussion of PV and consider a special weather phenomenon, the Mesoscale Convective System (MCS). In the final section of this chapter, we will bring together ideas about PV and MCSs.

In the summertime, the MCS is the main precipitation producer for the central U.S., and hence has been the subject of dozens (perhaps hundreds) of observational and modeling studies. Here we will highlight only a sampling of these studies; further information (e.g., regarding the internal structure of an MCS, cloud microphysics, etc.) can be found in a recent review by Rutledge (1991) or in Cotton and Anthes (1989, Chapter 10).

2.2.1 What is an MCS?

As compared to the rigidly-defined Mesoscale Convective Complex (MCC), which will be discussed shortly, the MCS is more loosely defined. Here we will follow and summarize definitions (or really descriptions) given by Zipser (1982) and Rutledge (1991). The MCS distinguishes itself from ordinary thunderstorms or supercell thunderstorms in

several ways. They contain merged and/or organized groups of thunderstorms during at least some portion of their lifecycle; this lifecycle must be longer than several lifetimes of the component thunderstorms. During its lifecycle, an MCS usually goes from convective precipitation, to a combination of convective and stratiform precipitation, finally to a system with mainly stratiform precipitation. Some ordinary thunderstorms also exhibit a similar, although much shorter, precipitation lifecycle (personal observation). Thus an MCS is comparatively large, with a precipitating area up to a few hundreds of kilometers in size, with an upper-level cirrus shield extending even further. In addition, they are long lived, with a lifetime typically 6–12 hours; stratiform precipitation can sometimes last for days (Cotton and Anthes 1989). Other features of an MCS include organized circulation systems, organized downdraft and surface cold pool. Some of these features may in part be found in some ordinary or supercell thunderstorms, but in an MCS these features are again larger in scale, longer lived, and more organized. Another criteria discussed by Zipser (1982) is a common upper-tropospheric cloud shield produced by the ensemble of thunderstorms within the MCS. It is also important to note that, aside from their contribution to the summertime precipitation budget, it is not uncommon for MCSs to have associated severe weather, such as tornadoes, hail, and flooding. This is especially true during their developing stages.

Cotton and Anthes (1989) summarize some of these ideas with their definition of an MCS: “a cloud system that occurs in connection with an ensemble of thunderstorms and produces a contiguous precipitation area approximately 100 km or more in horizontal scale in at least one direction”.

Using infrared (IR) satellite imagery, Maddox (1980) defined the Mesoscale Convective Complex (MCC) based on sizes of observed convective cirrus cloud shields meeting a specified temperature criteria, the duration of the cold cloud shield, and an eccentricity of the cloud shield. The definition was based on 43 MCC systems occurring over the U.S. in 1978. Using his criteria, the MCC has a cirrus cloud shield about two orders of magnitude larger than an individual thunderstorm, thus the MCC is a relatively large (spatially speaking) subset of MCSs.

While such a definition is useful it does have problems. The definition based on IR temperatures assumes something (at least qualitatively) about the characteristics of the precipitation and circulations under the cirrus shield. Radar results from a recent tropical field program, TOGA-CORE, indicate that the coldest cloud tops do not always correspond to the heaviest precipitation (Robert Cifelli, personal communication). This is not necessarily the case for midlatitude MCSs. A further criticism is that limiting climatologies to MCSs that only meet MCC criteria (e.g., Velasco and Fritsch 1987) can eliminate smaller, yet dynamically interesting MCSs (e.g., Knupp and Cotton 1987). The aim here is not to downplay the pioneering work of Maddox, however, in subsequent discussions we will consider MCSs in their broader sense as described above.

Another view of the MCS can be given the appellation “dynamically-based definition”. Cotton et al. (1989) investigated the evolution of 134 MCSs using a blend of National Meteorological Center (NMC) gridded data and rawinsondes. The authors considered wind, divergence, vertical motion and relative vorticity during eight stages of the MCS lifecycle, as well as heat and water budgets. Based on their results, Cotton et al. estimated the various terms for the Rossby radius of deformation

$$\lambda_R = \frac{C_N}{(\zeta + f)^{1/2}(2VR^{-1} + f)^{1/2}}. \quad (2.9)$$

They concluded that a dynamically-based definition of an MCS (actually their work is based on MCCs using a definition similar to Maddox 1980) is as follows: “A mature MCC represents an inertially stable mesoscale convective system which is nearly geostrophically balanced and whose horizontal scale is comparable to or greater than λ_R ”. For the systems studied by Cotton et al., λ_R was found to be on the order of 300 km.

Although this study was one of the first to view MCSs as balanced systems, there remain questions as to the estimation of terms in (2.9) and indeed, there is no easy or straightforward way to determine these. First, there is the question of R , which the authors obtained somewhat arbitrarily from satellite data. Second, the inertia-gravity wave phase speed is difficult to determine, as the authors admit. Third, as discussed by Olsson (1994), since the balanced flow associated with an MCS is usually highly curved, there remain

questions as to the best balance condition to represent an MCS. As an example of the complications, Chen and Frank (1993) estimated λ_R to be 47 km in the stratiform region of their simulated MCS, where N for this saturated region is much smaller. Thus, it is likely that MCSs exhibit balanced flow over a wide range of scales and the dynamically-based definition may apply over spatial scales differing by an order of magnitude. This by no means makes this definition any less useful to the dynamicist, here we only add a note of caution when attaching a specific size to a “balanced” MCS.

2.2.2 *MCS climatologies*

Several studies have focused on the common characteristics and background meteorological conditions associated with MCSs using satellite data (e.g., Maddox 1980), upper-air and surface data (e.g., Cotton et al. 1989; Augustine and Caracena 1994), and precipitation data (e.g., McAnelly and Cotton 1989,1992; Fritsch et al. 1986). These studies are mostly based on MCCs, defined in a fashion similar to Maddox (1980). However, the features described below apply generally to MCSs as well. From these and many other studies, we can summarize the common features of the environment and character of MCSs in the United States:

- MCSs occur largely over land, although they sometimes drift over oceans (see below)
- In the U.S., they tend to form in the lee of the Rocky Mountains. Worldwide, they also form in the lee of major mountain ranges.
- Form under or more often along the west side of a mid-tropospheric ridge, sometimes associated with embedded shortwave troughs.
- MCSs form in regions with high Convective Available Potential Energy (CAPE), usually on the order of 1000 J kg^{-1} or more. In addition, their genesis occurs in a region of low-level forcing, e.g., convergence from colliding outflow boundaries from previous convection. A low-level jet (LLJ) is often present which leads to convergence of high- θ_e air.

- Often synoptic-scale forcing is present, e.g., mid-level lifting ahead of a shortwave trough or along a low-level front.
- MCSs tend to form in the late afternoon or early evening; since their lifetime extends over many hours, these systems are largely nocturnal.
- Propagation of midlatitude MCSs is with the mid-tropospheric flow, modified by the presence of low-level moisture gradients and low-level moisture convergence.
- Seasonally, midlatitude MCSs migrate poleward from spring to late summer, following the seasonal migration of the jet stream.

Regeneration sometimes occurs associated with the remnant circulation of decaying or dissipated MCSs (e.g., Fritsch et al. 1994). This may occur several times over several days. Tropical cyclogenesis has been observed in association with decaying or dissipated MCSs drifting over adjacent warm oceans (Emanuel et al. 1993).

Using a variety of data sources, summaries of MCC activity have been published for several convective seasons (Rodgers et al. 1983,1985; Augustine and Howard 1988,1991), which display most of the above features of MCSs. Although the number of MCCs varies from year to year, it is interesting to note that somewhere between 30 and 50 have occurred in the U.S. during the years surveyed. An attempt to predict a relatively active or inactive MCC *season*, i.e., several months in advance, has not been attempted.

The formation of MCCs is not limited to the U.S. Several recent papers, based mostly on satellite climatologies, have demonstrated that these systems occur over many regions of the globe, and display many similar characteristics to those found in the U.S. The study areas include South America (Velasco and Fritsch 1987), the western Pacific (Miller and Fritsch 1991), Africa (Laing and Fritsch 1993a), and the Indian monsoon region (Laing and Fritsch 1993b). These studies provide common locations and tracks of MCCs, as well as some useful comparative statistics. For instance, Velasco and Fritsch find that although MCCs are similar across the Americas, some differences in size, latitudinal distribution and seasonality do occur. While these studies were restricted to systems meeting the MCC criteria, they are likely applicable to the more ubiquitous MCS as well.

2.2.3 *MCS forcing and organization*

Favorable environments and forcing mechanisms for thunderstorms are fairly well understood. Less well understood, and hence an active area of research (e.g., Nachamkin et al. 1992), is why individual thunderstorms sometimes organize into coherent, long-lasting precipitating systems. The “forcing” mechanisms for an MCS are sometimes seemingly obvious, e.g., organized uplift along a frontal or other convergent boundary. Even so, systems sometimes fail to develop under conditions of strong low-level forcing (e.g., Stensrud and Maddox 1988; Johnson et al. 1995). In other situations, large, heavily-precipitating systems develop for which the forcing mechanism is less apparent, such as the series of MCSs occurring over the central U.S. during 3–4 June 1985 (Fortune et al. 1992; Smull and Augustine 1993; Trier and Parsons 1993). These more subtle systems are a challenge to forecasters and numerical modelers alike. The term “forcing” is, in some circumstances, likely too strong; it may be that a particular mechanism sets up a more favorable background environment for strong convection or MCS development. In any case, the obvious criteria for any enhancing mechanism is that it lead to upward motion. Some of the mechanisms described below apply to ordinary thunderstorms as well as MCSs.

Low-level forcing simply refers to some lifting mechanism rooted in the boundary layer or otherwise in the lowest atmospheric layers. Examples are convergence along a front, along an outflow boundary from earlier convection, or moisture convergence at the terminus of a LLJ. Maddox and Doswell (1982) study three cases of intense convection forming in environments without a coupling of low- and upper-level forcing. They identify low-level warm advection as the dominant process in the genesis region of the convection, and go as far as to suggest that forecasters concentrate on low-level processes to anticipate potential strong convection. Augustine and Caracena (1994) also emphasize low-level processes, especially focusing on regions in which the terminus of the LLJ encounters a frontal (or frontogenetic) boundary. Colman (1990) examines thunderstorms that are triggered at low levels but are not surface based. These “elevated” storms occur in regions with no surface-based CAPE above frontal surfaces making their forecast difficult. They

account for many thunderstorms in the United States, especially during the winter season. The 3–4 June 1985 series of MCSs discussed above may also be of this type.

The problem of upper-level forcing is less well understood, largely because upper-air data is more sparse than surface and low-level data. The most widely accepted upper-level forcing of convection occurs due to secondary circulations associated with jet streaks (Uccellini and Johnson 1979). Viewed from above, the most favored regions for upward motion through a fairly deep layer in the troposphere are the left-exit region (left-front quadrant) and the right-entrance region (right-rear quadrant) of the jet streak. Uccellini and Johnson found that severe weather outbreaks were especially favored in regions where upward motion associated with a jet streak propagated over a region of low-level forcing, e.g., at the terminus of a LLJ.

Blanchard and Cotton (1994), using observations and idealized simulations, hypothesized that inertial instability at upper levels may aid the upscale growth of convection. This instability (or at least weak inertial stability) may exist in the ambient flow and/or may be enhanced by divergent outflow from deep convection. They note that this mechanism may not be widely seen due to the coarse resolution of the standard observation network.

Other mechanisms are more speculative. We have previously discussed the role of upper-level *PV* anomalies in extratropical and tropical cyclogenesis (Montgomery and Farrell 1992,1993) and the possible applications of these ideas to MCS formation or growth. Along these lines, Browning and Reynolds (1994) document severe straight-line winds along a convective cold front associated with an upper-level positive *PV* filament, extending from a more widespread region of lowered stratospheric air. Although different in detail, this scenario fits well with the more idealized situation postulated by Montgomery and Farrell. Ciesielski et al. (1989) identified instabilities from satellite photos of an anticyclonically-curved cirrus shield. From rawinsonde data they determined that the most likely cause of the observed instabilities was asymmetric inertial instability. It is possible that such instabilities exist but are not observed (due to lack of cloud and/or

their small scale), and in a manner described by Blanchard and Cotton (1994) lead to enhanced MCS growth. This seems feasible, especially recalling the climatological-favored MCS location on the west side of midtropospheric ridges.

How and why MCSs organize are still largely open questions, especially the latter (i.e., why). To help answer the former (i.e., how) Houze et al. (1990) undertook a study of six years of rainfall and radar data from Oklahoma springtime convective systems which produced significant rainfall (at least 25 mm in 24 h). They showed that about two-thirds of the cases exhibited some type of organization, while the remaining one-third were classified as "chaotic" in terms of their organization. The organized cases were further subdivided depending on the symmetry of the overall system. They also present mean soundings for various subcategories of cases. One interesting finding was that 75% of major rain events occurred from systems which did not meet the strict MCC criteria. Houze et al. only considered systems occurring from April through June however. Also interesting was the finding that organized systems were associated with a LLJ and a curved hodograph, while these were lacking in more chaotically-organized systems. The fact that Houze et al. found no major discrepancies between their climatologies and many earlier observational and modeling studies is encouraging for our general understanding of MCSs. Recently, Loehrer and Johnson (1995) studied surface features and precipitation patterns for 16 PRE-STORM MCSs. In general, their findings agree with those of Houze et al. in that three-quarters of the storms showed distinct patterns. They note, however, that the symmetric/asymmetric classification for organized systems of Houze et al. may be more indicative of *stages* of the MCS lifecycle, rather than being indicative of a *type* of MCS.

2.2.4 *The Mid-Level Vortex Associated with MCSs*

One feature frequently seen in modeling and observational studies of MCSs is a mid-level cyclonic circulation (e.g., Zhang and Fritsch 1988; Menard and Fritsch 1989; Cotton et al. 1989; Brandes 1990; Johnson and Bartels 1992). These are most often seen between 2 to 8 km above ground level, and sometimes form a closed vortex, which are on the order of 100 to 200 km in size. Characteristic tangential winds associated with the MCVs are on the order of 5–10 ms^{-1} (Bartels and Maddox 1991). Menard and Fritsch (1989)

suggest that this mid-level cyclonic circulation is one of the three main features of a mature MCS, the other two being an upper-level anticyclonic circulation and a low-level divergent outflow. They also show that longer-lived cyclonic circulations tend to form in environments with weak mid-tropospheric vertical shear.

Bartels and Maddox (1991) present a climatology of "mesoscale convectively generated vortex" or MCV, based on eight years of satellite photography. They note that the large-scale environmental features favorable for MCV formation include weak flow, weak vertical shear, and weak background relative vorticity, along with strong vertical and horizontal moisture gradients. Bartels and Maddox also note that few MCVs are seen in satellite imagery, but that is possibly due to the fact that these mid-level features are hidden by overlying cirrus or they may exist in cloud-free skies.

Smaller-scale MCVs also exist but are usually not seen with a synoptic observing network. Verlinde and Cotton (1990) document a vortex pair observed with dual-Doppler radar during the PRE-STORM field program. The size of each vortex in the cyclone/anticyclone pair was on the order of 40 km. Calculations by Verlinde and Cotton show that these vortices were relatively short lived, unbalanced circulations. Similar small vortices in the stratiform region of MCSs have been observed by other investigators, e.g., Stirling and Wakimoto (1989).

The question of whether or not MCVs are balanced circulations has important ramifications for interactions of the decaying MCS with larger scales, as well as for possible convective regeneration (e.g., Raymond and Jiang 1990). The question of MCSs and balance is the topic of a recent study by Olsson (1994).

2.3 Potential Vorticity Concepts Applied to MCSs

Traditionally, MCSs have been thought of as a fast manifold process, in which the unbalanced processes (e.g., associated with individual convective cells) dominate the more balanced dynamics. More recently it has become recognized that, at least during some stages of the MCS lifecycle, the system often obtains some measure of balance. Determining to what degree an MCS is a balanced system is important because of implications for

the system's longevity as well as its potential interaction with larger-scale disturbances. Since the concepts of PV and balance are closely linked, it is important to understand how \mathcal{P} evolves with an evolving MCS.

We begin our discussion by considering again Eq. (2.4). If the atmosphere is adiabatic ($Q = d\theta/dt = 0$) and frictionless ($\mathcal{F} = 0$), \mathcal{P} is exactly conserved. In terms of (2.6), an adiabatic and frictionless atmosphere leads to exact conservation of $\rho\mathcal{P}$. However, MCSs by their nature are diabatic phenomena, hence \mathcal{H} is an important term. Although the role of friction in MCSs (especially above the planetary boundary layer) has not been considered, as we will see in a later chapter, this term may be significant in the PV budgets of MCSs.

Expanding the diabatic term, we have

$$\mathcal{H} = \frac{1}{\rho} (\zeta_a \cdot \nabla) Q = \frac{1}{\rho} \left[\left(\frac{\partial w}{\partial y} - \frac{\partial v}{\partial z} \right) \frac{\partial Q}{\partial x} + \left(\frac{\partial u}{\partial z} - \frac{\partial w}{\partial x} \right) \frac{\partial Q}{\partial y} + \left(\frac{\partial v}{\partial x} - \frac{\partial u}{\partial y} + f \right) \frac{\partial Q}{\partial z} \right]. \quad (2.10)$$

Note that material change in PV is due to the variation of Q along the absolute vorticity vector. From scaling arguments it can be shown that the vertical part of \mathcal{H} , i.e.,

$$\mathcal{H}_z = \frac{1}{\rho} \left(\frac{\partial v}{\partial x} - \frac{\partial u}{\partial y} + f \right) \frac{\partial Q}{\partial z} \quad (2.11)$$

dominates on large scales. For MCSs this approximation is not always true, since large horizontal vorticities (relative to the absolute vorticity) can exist in conjunction with relatively large horizontal potential temperature gradients. As Raymond (1992) points out, for environments with moderate vertical shear, the assumptions leading to this scaling are marginal. For small-sized storms (e.g., ordinary thunderstorms) in moderate or large shear, the other two terms become important. Nonetheless, a qualitative understanding of how ambient PV is modified by diabatic processes can be gained by considering only \mathcal{H}_z . Figure 2.2 shows the results from the two-dimensional semigeostrophic model (Schubert et al. 1989) using a heating function representative of growing MCS with deep convection and little or no stratiform precipitation. From the definition of \mathcal{H}_z we can see that the vertical derivative of Q is important; where $\partial Q/\partial z > 0$, PV should increase, whereas where $\partial Q/\partial z < 0$, PV should decrease. In the wake of such a system we would expect

a positive PV anomaly at low levels with a negative anomaly at upper levels. This anticipated result is predicted by the model (Fig. 2.2b).

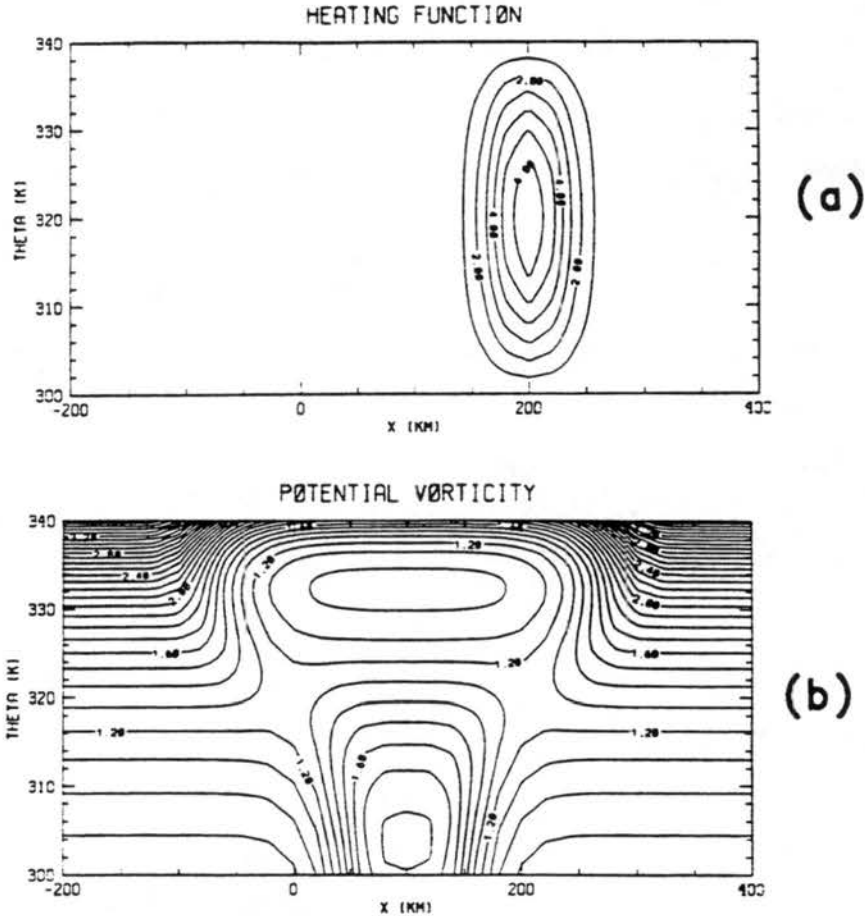


Figure 2.2: (a) Heating function ($K\ hr^{-1}$), for an MCS dominated by deep convection only. (b) Resulting PV with a negative anomaly overlying a positive anomaly (from Hertenstein and Schubert 1991).

Figure (2.3a) shows a somewhat modified heating function designed to represent the effects of an MCS with a deep convective line as well as a trailing stratiform precipitation area. In this profile, we now have a low-level and an upper-level region where $\partial Q/\partial z < 0$ and a deep mid-tropospheric layer in which $\partial Q/\partial z > 0$. Thus, for a mature MCS, we would expect to see a low-level negative PV anomaly, a mid-level positive anomaly, and an upper-level negative PV anomaly. Hertenstein and Schubert (1991) found this structure using the model of Schubert et al. (1989) as well as from observations of the 10–11 June 1985 squall line (Fig. 2.3b).

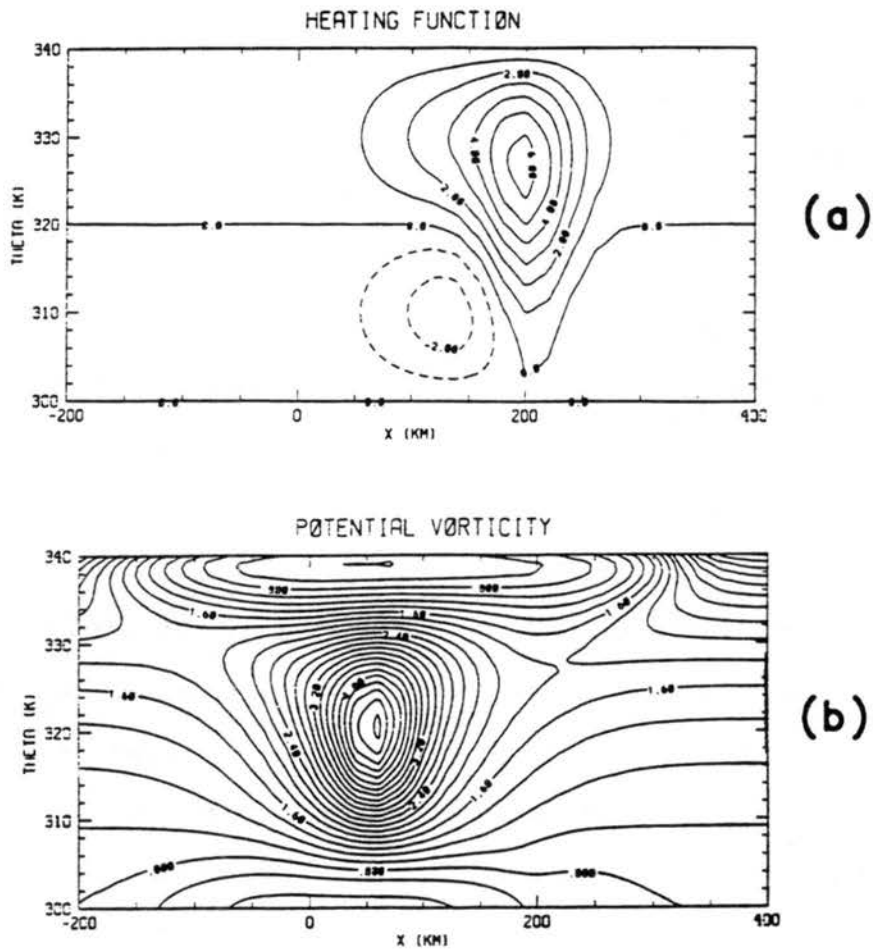


Figure 2.3: (a) Heating function (K hr^{-1}), for an MCS with a convective line and stratiform precipitating region. (b) Resulting PV showing a mid-level positive anomaly and negative anomalies above and below (from Hertenstein and Schubert 1991).

This type of vertical PV tripole structure has been observed in other cases as well. Fritsch et al. (1994) were especially interested in the mid-level cyclonic vortex associated with the positive PV anomaly. The mid- and upper-level circulations (associated with the PV anomalies) are most commonly observed. This is likely due to the disruption of organized circulations at low levels due to frictional effects. We note that the model of Schubert et al. does not include friction. The upper-level anticyclonic circulation (associated with the negative PV anomaly aloft) has also been noted in several observational studies (e.g., Maddox et al. 1981; Fritsch and Maddox 1981; Fritsch and Brown 1982; Read and Maddox 1983). Apparently at that time, meso-scale (i.e., between about 200 and 2000 km) effects of MCSs were not well known. These studies were motivated by

forecast errors observed in numerical models in the wake of MCSs. At upper levels, they generally found a cold anomaly on the order of 5 C and anomalous anticyclonic low (on the order of 10–20 ms^{-1}). These are simply components of the upper-level negative *PV* anomaly.

In the decaying stages of the MCS, we are left with little or no convective region and mostly stratiform precipitation. This would tend to further strengthen or maintain the mid- and upper-level *PV* anomalies. The anomalies could then be advected with the ambient flow, or become distorted in the presence of strongly-sheared flow.

We thus have a conceptual model of the perturbation *PV* field associated with the lifecycle of an MCS. Early in the MCS lifecycle, a *PV* dipole forms, with a negative *PV* anomaly overlying a positive one. As the system matures, a tripole structure develops, with a positive *PV* anomaly at mid levels and a negative anomaly above and below, the upper-level negative anomaly dominating the low-level negative anomaly in strength and size. The upper-level negative anomaly is typically twice as large as the mid-level positive anomaly as well. Two processes lacking in this conceptual model are as follows. First, radiation at the cloud top will likely lead to cooling there, which would steepen the top of the gradient in Fig. 2.3 leading to a stronger anomaly there. Second, vertical shear of the ambient flow may distort the *PV* tripole, or if strong enough, may disrupt it completely.

Raymond and Jiang (1990) used this conceptual model to investigate the balanced flow associated with an MCS-produced *PV* anomaly using three-dimensional nonlinear balance (NLB) to invert *PV*. They identify two regions of adiabatic upglide associated with tilted isentropic surfaces, which are one component of the *PV* anomaly. At mid levels, the cyclonic circulation is forced up tilted adiabats in one part of the MCS and downwards on the opposite side. Thus the balanced mid-level circulation can help maintain the MCS. At the same time (or possibly at a later time) low-level air flowing into the remnant MCS can again be adiabatically lifted. If this air is lifted to the Level of Free Convection (LFC), deep convection can occur and an MCS may regenerate. Fritsch et al. (1994) document a case study where an MCS underwent five (re)generations over a period of three days. In support of the ideas of Raymond and Jiang, they found that new convection formed

near the center of each remnant MCS circulation. This contrasts with the idea that new convection would trigger along surface outflow boundaries which would occur away from central regions of a decaying MCS. Fritsch et al. also suggest that inflow and upglide could occur in different regions of the MCS, depending on the ambient flow near the decaying MCS. Intuitively one might expect new growth due to inflow on the “front” side of the decaying MCS, “front” being the side in the direction of storm movement.

The model of Raymond and Jiang (1990) has been further extended by Raymond (1992) who derives two models which consider somewhat different balance approximations, each generally stemming from nonlinear balance. Each of the models also includes advection by the unbalanced part of the wind, which was lacking in the model of Raymond and Jiang, and is thought to be important in the evolution of MCSs. In a recent study, Jiang and Raymond (1995) added a level of complexity to their original model by including a simple parameterization of convection. Their results agree with earlier balanced model results and again point to the importance of diabatic heating. They also suggest that the mid-level isentropic upglide described earlier is responsible for the mesoscale updraft seen in the mature stage of many MCSs.

Davis and Weisman (1994) explore MCVs using a three-dimensional cloud model simulation with an idealized initialization, i.e., one representative sounding and a series of warm bubbles to start convection. They found that NLB dynamics were useful for describing the long-lived vortex that ensues, but less useful for the details of the MCV evolution, since horizontal vorticity is not accurately enough treated. Some of their results appear to contradict Raymond (1992), but this is unclear since the two studies consider the MCV at different vertical levels. Davis and Weisman also note that if vertical shear is confined to relatively low levels, it does not substantially alter the MCV structure and may enhance the system longevity, in a fashion described by Raymond and Jiang (1990). In a similar study, Olsson (1994) used a PE model simulation of the 23–24 June 1985 PRE-STORM MCS to address the question: Is the MCS a dynamically-balanced system? He found that to a large degree over the life of the MCS the system is balanced. He also notes that balanced dynamics performed less well at upper levels, where divergent outflow was

inertially unstable or at least weakly inertially stable. We will return to a detailed look at PV evolution with this system in Chapter 4.

The material change in PV due to frictional effects (\mathcal{F} in (2.4)) has been largely neglected in PV studies, especially those on the mesoscale. Most considerations of \mathcal{F} have been applied to surface friction problems, e.g., Cooper et al. (1992). Raymond (1992) suggests that \mathcal{F} may be important at upper levels, where viscosity associated with gravity wave dissipation should lead to PV anomalies. Hertenstein et al. (1994) calculated a PV budget using simulations of two PRE-STORM MCSs and found that neglecting \mathcal{F} in (2.4) lead to an imbalance in the remaining terms. Further, the calculated residual was larger than expected at mid levels during the mature stage of both systems, suggesting some physical process (e.g., turbulent mixing) was perhaps at work.

In this section we have reviewed the use of PV concepts applied to MCSs. A conceptual model arises in regards to PV anomalies due to diabatic heating from a balanced-dynamics standpoint. Some details of the PV evolution may involve unbalanced dynamics (Davis and Weisman 1994). An open question is a detailed look at PV evolution in real systems, which is the main topic of this dissertation. An additional topic of interest involves the role of \mathcal{F} in the evolution of PV . These topics are the subjects of Chapters 4 and 5.

2.4 Summary

In this chapter, we have considered PV concepts, mesoscale convective systems, and some applications of PV concepts to MCSs. This is by far not a complete treatment of any of these subjects, rather we have reviewed some of the many highlights. A complete treatment of these topics alone would fill a volume. The reader seeking more detail is encouraged to seek out the references listed herein as well as other studies mentioned in those references.

Many questions remain unanswered. Previous simulations have used balanced models or primitive equation models with idealized (i.e., horizontally homogeneous) initial conditions. How does PV evolve in more realistic MCSs? Raymond (1992) as well as Davis and

Weisman (1994) point to this area for further research. What additional physical insight can be gained by investigation of realistic systems? How do results from these simulations compare with previous studies? Past studies have neglected frictional effects in Eq. (2.4). Is this a reasonable assumption for convective systems?

This dissertation revolves around the use of *PV* concepts applied to MCSs. Specifically, we examine the detailed evolution of *PV* in the simulations of two observed MCSs which occurred during PRE-STORM. The *PV* evolution is documented at mid and upper levels, then a budget analysis of the terms in Eq. (2.4) is performed to identify the most important processes. Further, we will investigate the friction term in the *PV* equation, which, as we saw in section 2.3, has been largely neglected. These topics have not been completely explored in past studies and are the subjects of the following chapters.

Chapter 3

SIMULATION OF THE MESOSCALE CONVECTIVE SYSTEMS

In this chapter we will first discuss the nonhydrostatic primitive equation (PE) model and convective parameterization used for the simulations. We then overview the MCSs and discuss the model setup for each simulation, followed by a verification of the simulations.

3.1 The Regional Atmospheric Modeling System – RAMS

The Regional Atmospheric Modeling System (RAMS) has its origins in the CSU cloud/mesoscale model described by Tripoli and Cotton (1982). This modeling system is, like many atmospheric models, in a state of rather constant evolution and features of the version used in this study will be described below. Pielke et al. (1992) describe many recent applications of this versatile system, including Large Eddy Simulations (LES), simulations of thunderstorms and convective systems, mid-latitude cirrus clouds, winter storms, terrain-forced phenomena, and dispersion modeling. A complete list of RAMS options can be found in Pielke et al. (their Table 1). Since RAMS is a rapidly evolving model, some of the options may have been updated in newer versions. A similar model description, with settings for a specific case, can be found in Cram et al. (1992).

RAMS is comprised of three main parts, all of which were used in this study. At the core of the system is a nonhydrostatic PE model, using a σ_z terrain-following vertical coordinate as described in Appendix A of Tripoli (1986). Details on the basic model equations, vertical coordinate, grid structure, time differencing, as well as parameterizations available (e.g., radiation) can be found in Tripoli (1986) and Pielke et al. (1992). For brevity, these details will not be repeated here, however a summary of model options used and the basic experimental setup are discussed and summarized in later sections.

Another essential part of RAMS is the ISentropic ANalysis (ISAN) package. This package makes possible the simulation of real systems by combining NMC pressure-level data with rawinsonde and surface data for a specific case, and then interpolating these fields onto the model grid at the initial time (Tremback 1990). The observational data is first blended into a data set using an isentropic vertical coordinate; these data are then interpolated onto the model grid. Advantages of the isentropic vertical coordinate are well known (e.g., Kasahara, 1974); however problems may occur when a deep neutral layer is present, for instance if the model is initialized in the late afternoon for a summertime simulation. Other recently used alternate data sets for initializing the model can be found in Cotton et al. (1994).

An alternate method for initializing the model uses the assumption that one atmospheric sounding is representative of the conditions over the model domain. This method is called “horizontally homogeneous” initialization and is used for more idealized simulations. This type of initialization was not used in any of the simulations analyzed here.

A Visualization and ANalysis (VAN) package is available for examination of model output (Tremback 1990). This package was used for initial inspection of model output, but a somewhat more flexible diagnostic package was needed and developed for this study.

3.1.1 *The Level 2.5w Convective Adjustment Scheme*

One component of the simulations of the two PRE-STORM MCSs is the convective parameterization. For both simulations, a newly developed scheme was used, the Level 2.5w Convective Adjustment Scheme (Weissbluth and Cotton 1993).

This parameterization scheme was designed to be used for grid spacings between about 5 km (just above a threshold for “explicitly” resolving convection) and 50 km, i.e., for mesoscale applications. Tests with grid spacings up to 80 km indicate that the scheme may be effective for a more general range of scales. The scheme follows the Mellor and Yamada (1974) hierarchy of equations, but is based on vertical velocity variance $\overline{w'w'}$, instead of turbulent kinetic energy. In this scheme, $\overline{w'w'}$ is the predicted variable. A main advantage of this scheme over other cumulus parameterization schemes is that it allows for a “memory” of convection, by allowing $\overline{w'w'}$ to be advected from one grid box

to another during the time integration. Another feature of this scheme is that it has a source function for hydrometeors, thus the host model is not expected to deal just with a moistening profile as is common among cumulus parameterization schemes.

It should be noted that these simulations were completed at a time when this convective parameterization was relatively untested. The 10–11 June simulation was the first performed of an actual system using this parameterization. As we will see later in this chapter, despite its experimental nature, this scheme performed very well in a test with another well-known parameterization, as well as against observations of this system.

3.2 The 10–11 June 1985 MCS

3.2.1 *Observational and modeling studies of the 10–11 June 1985 MCS*

The 10–11 June 1985 squall line is very likely the most widely studied MCS on record. Johnson and Hamilton (1988, hereafter JH88) used special surface and upper-air data to study surface pressure features and flow features within the squall line. They especially concentrate on the wake low, which they attribute to subsidence warming, and suggest that it is the manifestation of the descending rear-inflow jet. In addition, they present an overview of the MCS, including synoptic setting, satellite and radar images of the system's evolution, making this a good study for the reader wishing to familiarize themselves with this case. In a later paper, Johnson et al. (1990) examine downward vertical velocities near the top of the stratiform region and a lowering of the tropopause in the wake of this system. The upward bowing of isentropes directly over the MCS is possibly associated with a negative potential vorticity anomaly there.

A single-Doppler analysis of the system by Rutledge et al. (1988) reveals many of the flow features internal to the MCS which are also seen in studies of other systems. However, these observations are more extensive in space and time than studies of other systems, thus revealing more details of the flow features (e.g., the front-to-rear jet) in relation to vertical velocities. For instance, they find that mesoscale updrafts in the stratiform region approach 0.5 ms^{-1} , greater than previously thought.

These features, along with vorticity budgets, are examined in greater detail by Biggerstaff and Houze (1991a,b, 1993). The authors blend (in space and time) rawinsonde, wind

profiler, surface, and dual-Doppler data to obtain a more highly-resolved data set than previous studies. This data set also gives us a new look at the transition zone between the convective line and stratiform region. It should be noted that the time compositing used in this and other studies assume the MCS is in "steady state"; this may or may not be completely accurate.

Heat, moisture, and momentum budgets are calculated for the 10-11 June 1985 MCS in two papers by Gallus and Johnson (1991,1992). Many system-average figures are presented, along with a clear explanation of the data limitations, making these results valuable for verification of model simulations of this system, as well as providing a data set for those interested in the parameterization of these quantities.

The most widely published simulation of this system was reported by Zhang et al. (1989). The Pennsylvania State University/National Center for Atmospheric Research (MM4) mesoscale model is used; the authors document a simulation of this MCS which verifies very well against observations. In a companion study, Zhang and Gao (1989) present details of the rear-inflow jet, surface pressure features and precipitation structure predicted by the simulation. These were found to generally agree well with results from the enhanced observation network. Based on their success with this simulation, the authors envision prediction of MCSs using mesoscale models in the not-too-distant future.

The data set supplied by the simulation of Zhang et al. has lead to several additional studies for this MCS, including a momentum budget (Gao et al. 1990), development of moist *PV* (Zhang and Cho 1992), and the formation of a mesovortex in the stratiform region (Zhang 1992).

3.2.2 *System overview*

The 10-11 June MCS initiated as a broken line of thunderstorms in SE¹ Colorado, SW Kansas, and the Oklahoma Panhandle around 10/2000 UTC. Figure 3.1 shows surface and 500 mb feature, as well as a radar summary for 10/2100 UTC.

¹We will use compass points, e.g., SE = southeast, NW = northwest, etc., for notational brevity throughout. Additionally, a commonly used date/time abbreviation is employed, thus 10/2000 UTC is short for June 10 at 2000 UTC. To obtain local time, subtract 6 hours from UTC.

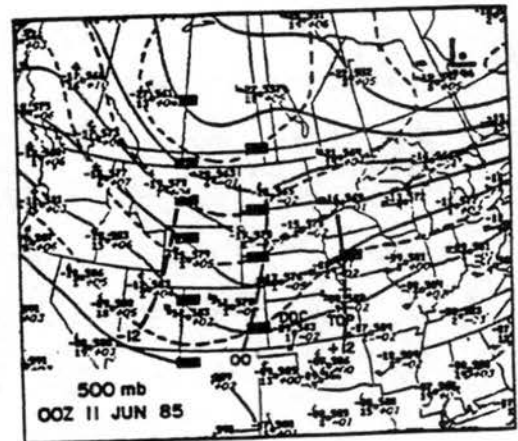
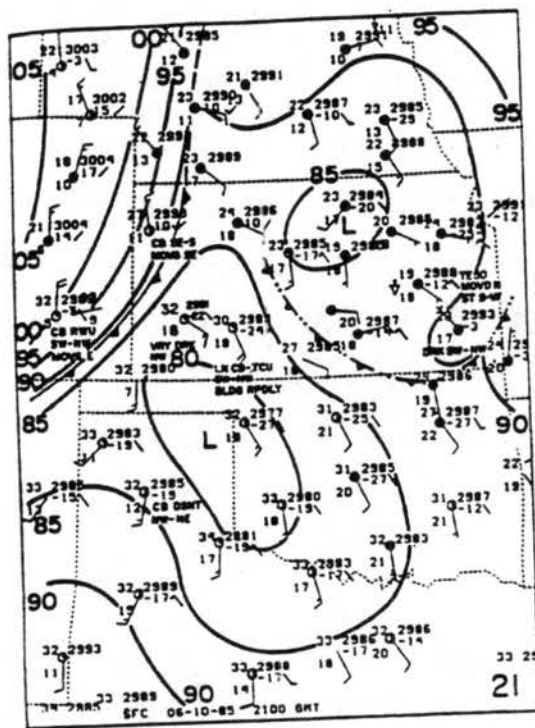
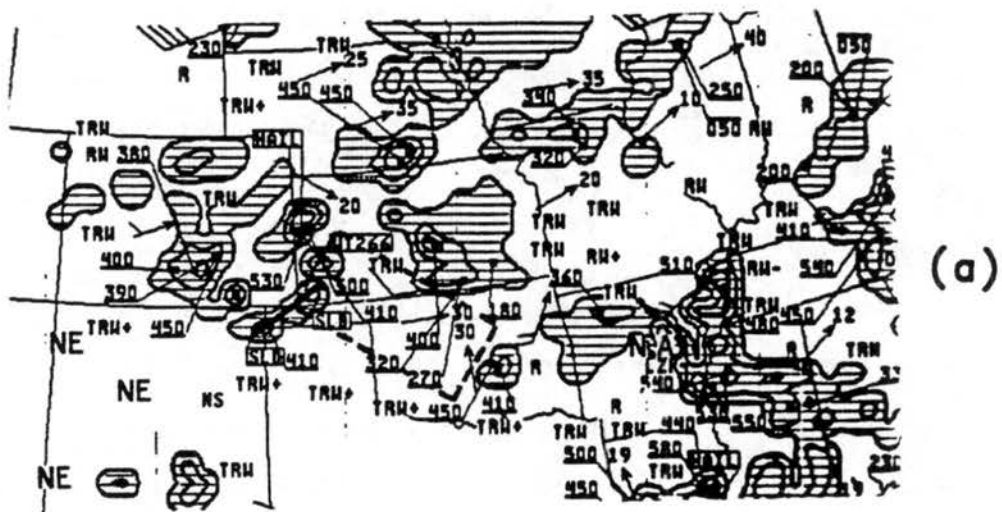


Figure 3.1: (a) Radar summary at 10/2035 UTC, (b) Surface features at 10/2100 UTC. Isobars (solid contours) in inches, station temperature and dew point in degrees C [from JH88], (c) 500 mb analysis showing trough axis at 11/0000 UTC and 12 hours before and after that time [from JH88].

The developing MCS at 10/2100 UTC was located in the vicinity of a surface confluence zone which was generally oriented in a SW to NE line. A 500 mb trough is located just to the NW of the system at this time and propagates eastward over the lifetime of the MCS. The squall line forms ahead of this upper-level feature, then rapidly expands along the confluence zone and propagates towards the SE. By 10/2330 UTC the MCS continues to intensify and move in a southeasterly direction at approximately 15 ms^{-1} (Fig. 3.2a). During the developing stages of this system (i.e., 10/2000 to 11/0000 UTC) the northern end of the system produces some severe weather, including high winds, hail, and a tornado (JH88, their Fig. 7) as it intersects a weak outflow boundary moving from the NE.

Two hours later, during the growing stage at 11/0130 UTC, the MCS is oriented NE-SW, has expanded in size, and has moved further into Oklahoma and the Texas Panhandle at about 16 ms^{-1} . During this stage, the MCS is still comprised mostly of a convective line, although a stratiform cloud area is beginning to form (Fig. 3.3a). By 11/0330 UTC the observed MCS has achieved its mature stage, with a convective line stretching from the Texas Panhandle into Kansas and now exhibits an expanding stratiform region (Fig. 3.4a).

By 11/0530 UTC, the system has greatly weakened and is in its dissipating stage (Fig. 3.5a). The convective line is still active, while the stratiform precipitating area continues to expand and now dominates the system. The MCS continues to move in a SE direction as before, but now propagates more slowly, consistent with the weakening convective line. A surface analysis at this time shows a characteristic tripole in the pressure perturbation, with the pre-squall mesolow, the squall mesohigh, and the wake low (Fig. 3.6b).

It is also interesting to note that after 11/0600 UTC the system moves out of the PRE-STORM mesonetwork, and most studies in the literature (both observational and modeling) do not consider the remnant MCS after this time. By 11/0800 UTC a new convective line forms at the leading edge of the decaying system, and goes through an entire new, shorter-lived nocturnal lifecycle in NE Texas. Unfortunately, our simulation did not capture this interesting regeneration.

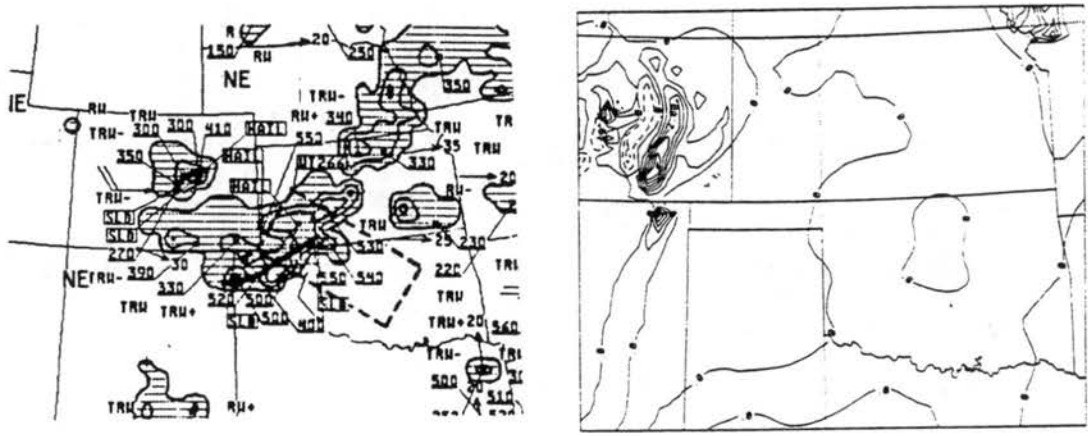


Figure 3.2: (a) Radar Summary at 10/2335 UTC, (b) Vertical velocity (10/2330 UTC) at 5 km on Grid #2. Contour interval is 0.5 ms^{-1} .

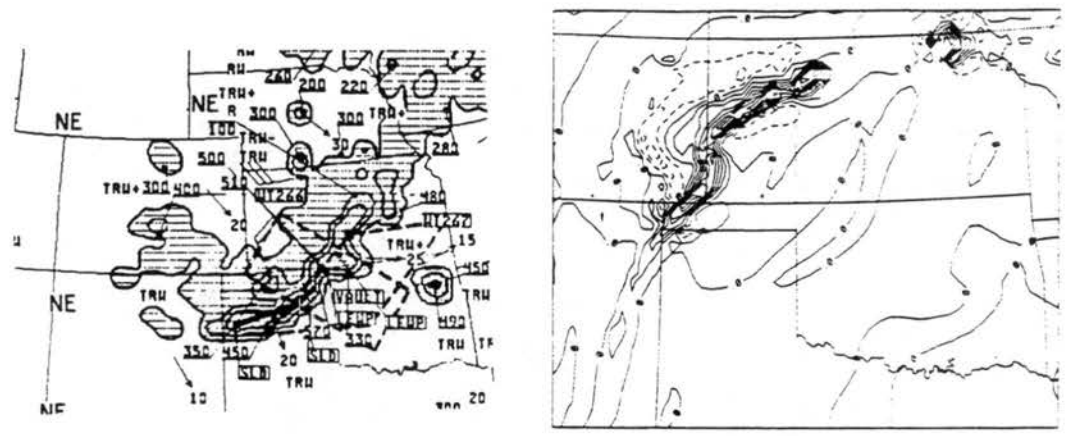


Figure 3.3: As in Fig.(3.2) except (a) at 11/0135 UTC, and (b) at 11/0130 UTC.

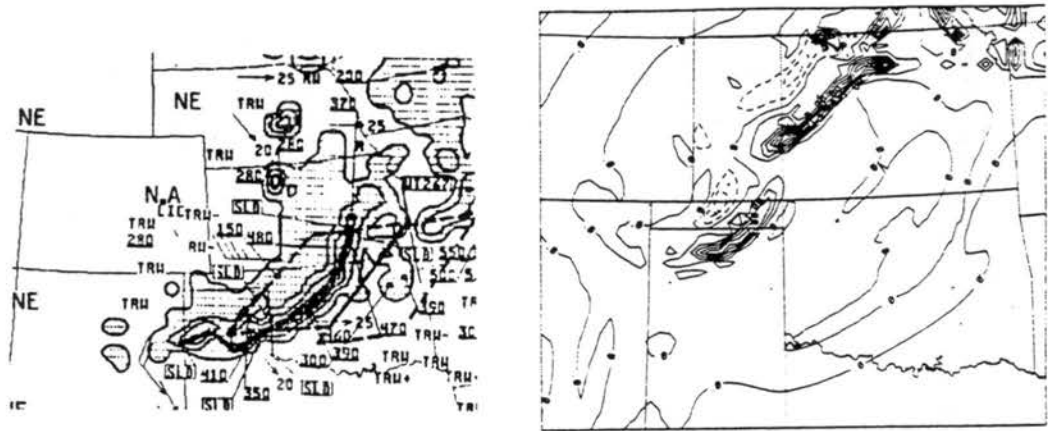


Figure 3.4: As in Fig.(3.2) except (a) at 11/0335 UTC, and (b) at 11/0330 UTC.

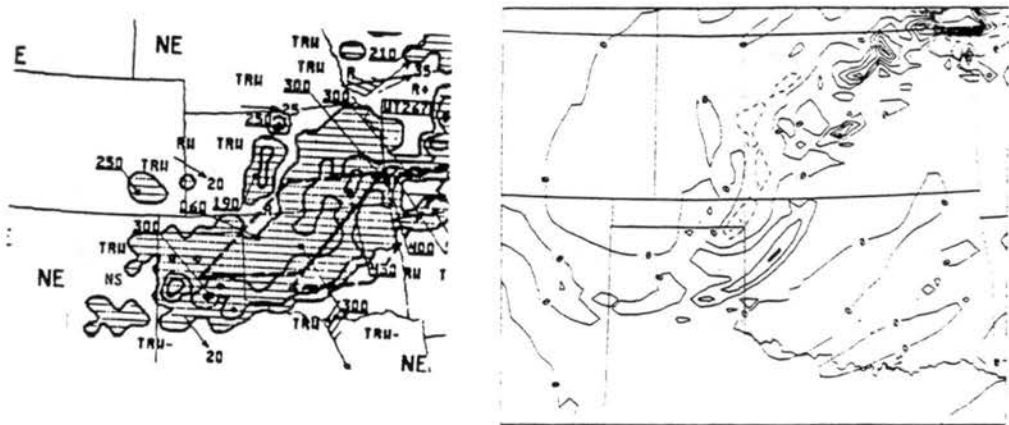


Figure 3.5: As in Fig.(3.2) except (a) at 11/0535 UTC, and (b) at 11/0530 UTC.

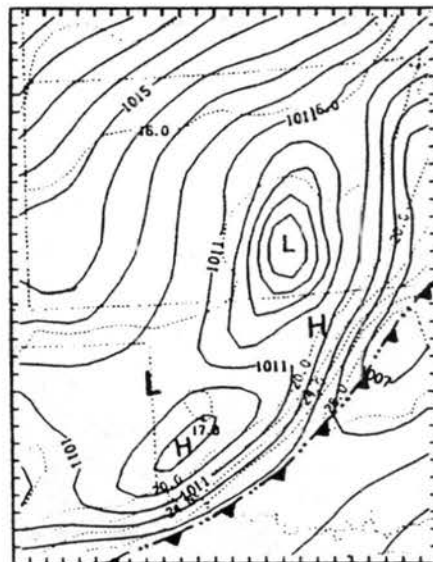
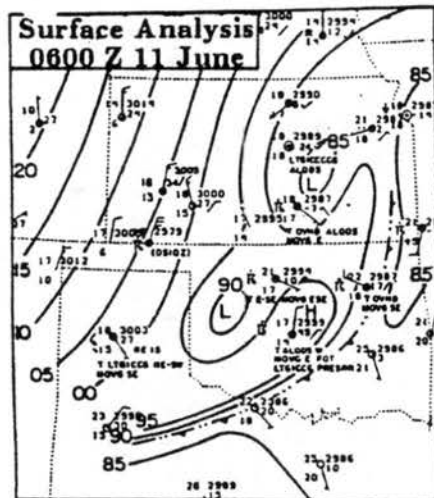
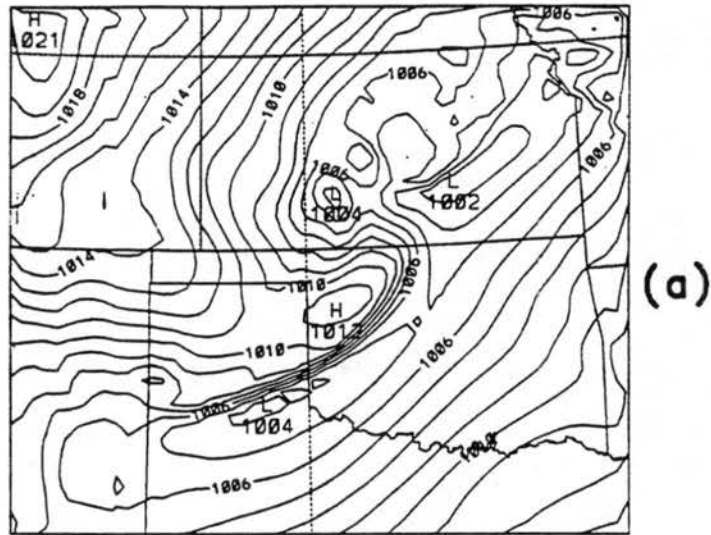
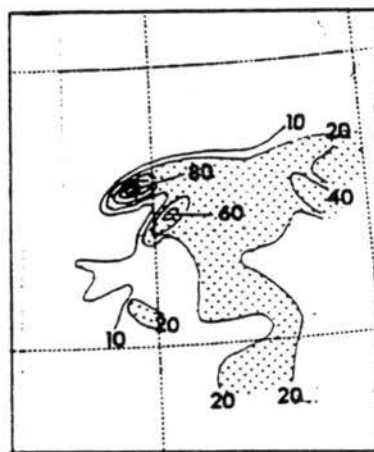
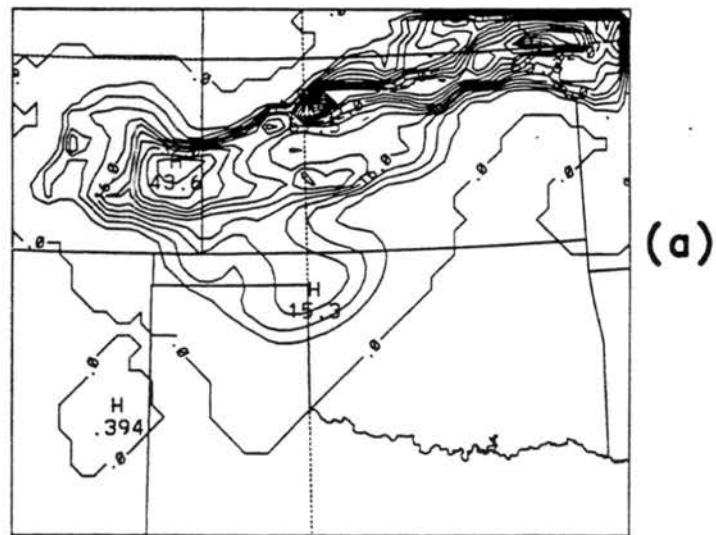
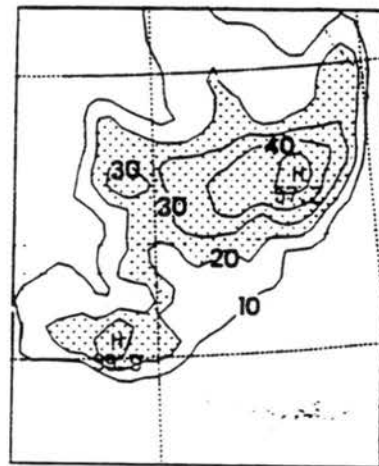


Figure 3.6: All figures at 11/0600 UTC. (a) Reduced mean-sea-level pressure from the RAMS simulation, (b) Surface pressure from observations. Solid contour in inches as in Fig.(3.1b) [from Zhang et al. 1989], (c) Surface pressure (solid contours) and temperature in C (dashed contours) from the simulation of Zhang et al. (1989).



Total Rainfall (mm)
Observed

(b)



Total Rainfall (mm)
Predicted

(c)

Figure 3.7: All figures at 11/0600 UTC. (a) Total precipitation (mm) from the simulation, (b) Total precipitation (mm) from observations [from Zhang et al. (1989)], (c) Total precipitation from the simulation of Zhang et al. (1989).

3.2.3 Model setup for the 10–11 June 1985 MCS simulation

Generally, this simulation used the same model physics, etc., as a simulation of the 23–24 June 1985 MCS completed by Olsson (1994). The simulation was nonhydrostatic with grid-scale microphysics which specify the mean diameter for rain, ice, snow, and graupel. Time differencing uses a leapfrog scheme, while second-order leapfrog is used for horizontal advection and second-order forward for vertical advection. Radiation follows Chen and Cotton (1983,1987) and is updated every 900 seconds; turbulence uses a deformation-K closure parameterization (Tremback 1990). Lateral boundary conditions are time varying, and are nudged to time-interpolated boundary values from initial files. The top boundary uses a Rayleigh friction absorbing scheme (Olsson 1994).

The simulation of the 10–11 June 1985 MCS contained two grids, using a two-way interactive nesting (Clark and Farley 1984) and is shown in in Fig. 3.8. The coarser Grid #1, with 80 km spacing, was set up large enough to capture the synoptic-scale dynamics influencing the MCS, while the finer Grid #2, with 20 km spacing, was placed to capture details of the MCS. The vertical grid spacing is 200 m at the first level and is then stretched at a ratio of 1.1 to a maximum of 800 m. Below the 30 atmospheric layers are 11 soil layers. The soil model uses the soil moisture and vegetation scheme developed by Tremback and Kessler (1985). Some other details concerning the simulation appear in Table 3.1.

This simulation was initialized using European Centre for Medium-Range Forecasting (ECMWF) data, which is on seven constant-pressure levels from 1000 to 100 mb and every 2.5 degrees latitude/longitude. These data are enhanced with rawinsonde data, which are first vertically and then horizontally interpolated onto a common grid. Surface data are blended into this intermediate data set, before finally being interpolated onto the RAMS $x-y-\sigma_z$ model grid.

Using this initial data, the simulation was begun at 1200 UTC on June 10 (10/1200 UTC) with only Grid #1 active. This configuration was run for 10 hours, until 10/2200 UTC, at which time Grid #2 was spawned. Both grids remained active for the remainder of the simulation, i.e., eight more hours ending at 11/0600 UTC. The convective parameterization is active on both grids for the duration of the simulation.

Table 3.1: Model configuration for the 10–11 June 1985 MCS simulation.

	Grid #1	Grid #2
number of grid points	48 × 41	54 × 46
domain size (km)	3840 × 3280	1080 × 920
grid spacing (km)	80	20
vertical levels	30	30
time step (s)	90	45
cumulus parameterization used ?	yes	yes

3.2.4 General verification of the RAMS simulation

By comparison to observations, the simulated system initiates between 10/2100 UTC and 10/2200 UTC in SE Colorado. Within two hours (10/2330 UTC), the simulated system consists mainly of a line of convective cells 325 km long and has begun to propagate towards the ESE (Fig. 3.2b). Compared to observations, the simulated MCS initiates too far towards the west, i.e., nearer the foothills of the Rocky Mountains instead of in the extreme SE corner of Colorado (Fig. 3.2b). At this time, the observed MCS is oriented more NE–SW, while the simulated system is oriented more N–S, parallel to the topography. This, as it turns out, is our only serious criticism of the simulation. The model develops strong diurnal upslope flow, thus a convergence zone (both in the model and observations) at 10/1200 UTC in SE Colorado which acts as a focus for the observed MCS, migrates westward in the simulation during the late morning and early afternoon. The observed convergence zone did not migrate westward. The simulated system subsequently correctly orients itself and propagates in agreement with the observed system. This positioning error in the initial stages of the simulated MCS leads to a position error during its entire lifetime. As we will see in the next section, the heating rates, which are more important to this study than exact positioning, agree very well. We should also note that the simulation of Zhang et al. (1989) did not encounter the difficulty in MCS positioning.

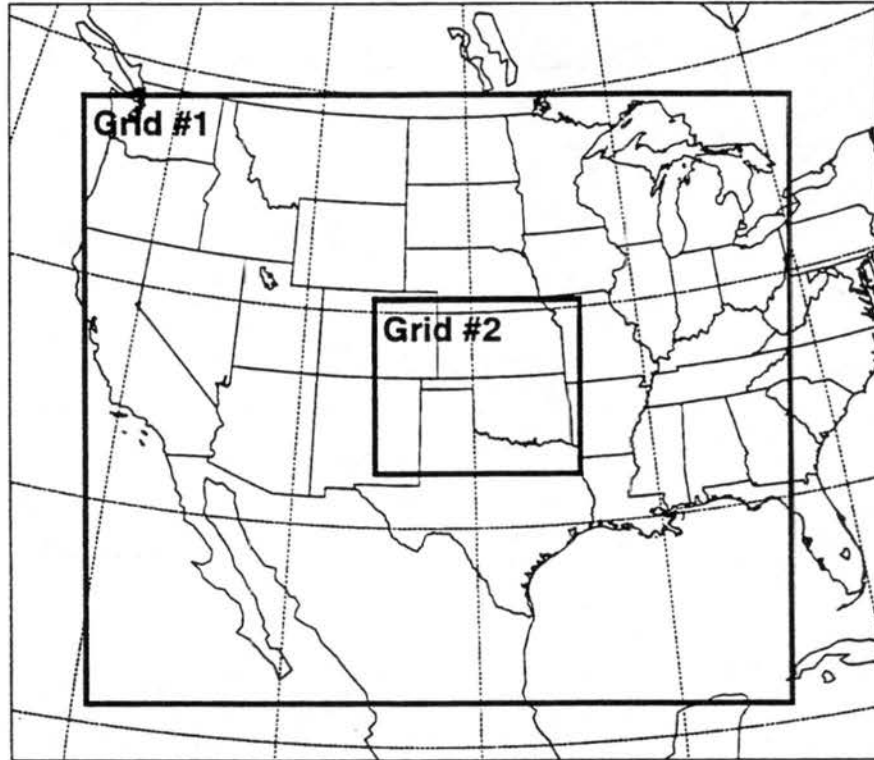


Figure 3.8: Location of the 80 and 20 km grids for the 10–11 June 1985 MCS simulation.

Two hours later during the growing stage at 11/0130 UTC, the simulated MCS is oriented NE-SW, has expanded in size, and has moved into the Oklahoma Panhandle. At this stage, the MCS is still comprised mostly of a convective line, although a stratiform cloud area is beginning to form (Fig. 3.3). The simulated MCS also continues to propagate towards the SE at approximately 18 ms^{-1} . This compares well with an observed propagation speed of 16 ms^{-1} .

The simulated system continues to grow (especially the stratiform region) and propagate towards the SE during the mature stage (Fig. 3.4b). The propagation speed of the simulated MCS still closely matches the observed system, so the simulated position still lags the observed, due to the initial position error.

The simulated system has begun to dissipate by 11/0530 UTC (Fig 3.5b), in agreement with the observations. Vertical velocities in the leading convective line have decreased and the propagation speed has slowed. The stratiform precipitation region continues to ex-

pand. After this time, the simulated system continues to gradually weaken and continues drifting towards the SE.

Surface pressure features in the wake of the simulated system are found in Fig. 3.6a. For comparison, surface pressure is also shown for observations from JH88 (Fig. 3.6b), and from the Zhang et al. (1989) model simulation (Fig. 3.6c). We note that the main observed surface pressure features are very well reproduced by the RAMS simulation, including the pre-squall low, the squall high, and the wake low. Details of these features appear to be much better captured by the RAMS simulation than that of Zhang et al. (1989). Total precipitation is similarly compared among the three data sources in Fig. 3.7. Both models generally, but certainly not precisely, represent the observed precipitation. Neither model picks up a small area of intense precipitation (associated with observed severe weather mentioned above) in western Kansas. It is also interesting to note that both models err similarly in producing the maximum simulated precipitation in central Kansas.

3.2.5 Heating rates

As previously mentioned, although the simulation did not verify perfectly in terms of the MCS location, the size, shape, and speed of the system did verify reasonably well. And, more importantly for this study, the simulated heating rates compare very well with those diagnosed from observations, as we will now see.

Gallus and Johnson (1991) studied heat and moisture budgets from the 10–11 June MCS using special rawinsonde data taken during PRE-STORM. Data from three times (at 90 min intervals) were composited to give a total of 33 soundings for analysis. These were interpolated onto a rectangular grid with a spacing of approximately 50 km and then data were averaged along the squall line at various times. These observational data form the basis of our comparison.

Gallus and Johnson consider the form of the thermodynamic equation,

$$Q_1 = \frac{\partial \bar{s}}{\partial t} + \nabla \cdot \bar{s}\mathbf{V} + \frac{\partial \bar{s}\omega}{\partial p}$$

where $s = c_p T + gz$ is the dry static energy, p is pressure, $\omega = dp/dt$, and the overbar denotes a horizontal average. Some confusion arises because Q_1 has the units $\text{J kg}^{-1} \text{hr}^{-1}$,

but most figures in literature present units of K hr^{-1} . To convert to these more intuitive units, we simply divide by c_p , thus plots presented here are actually Q_1/c_p .

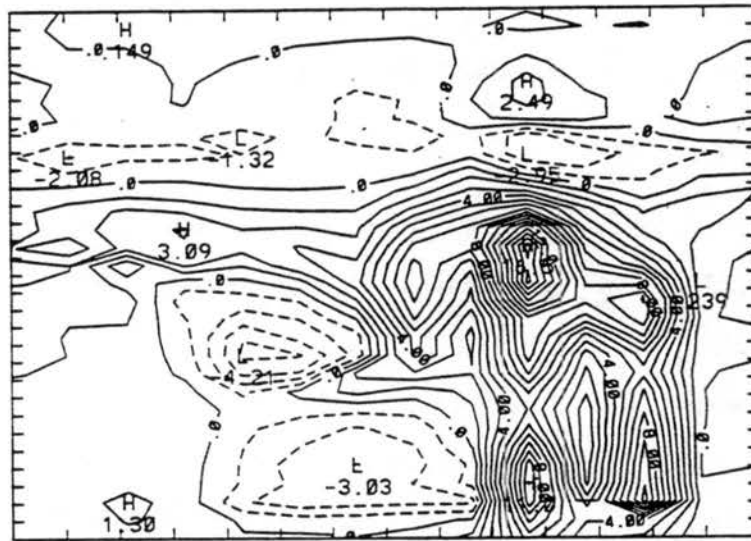
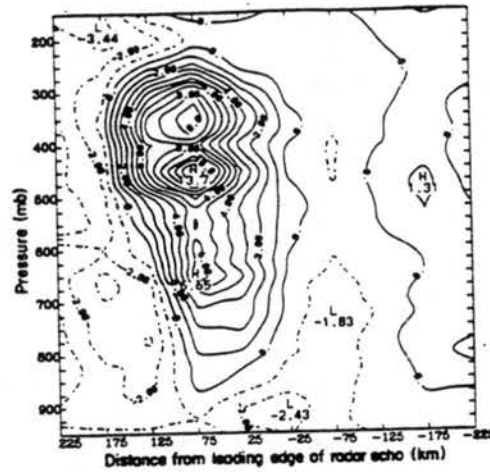


Figure 3.9: (a) Diagnosis of Q_1/c_p at 11/0300 UTC from observations [from Gallus and Johnson (1991)], (b) Q_1/c_p from the simulation at 11/0300 UTC.

Figure 3.9a shows Q_1/c_p from Gallus and Johnson at 11/0300 UTC while Fig. 3.9b is the corresponding analysis from the simulation. Immediately apparent is the good qualitative and quantitative agreement. For instance, maximum heating rates are almost 14 K hr^{-1} from the observational study, and 16.5 K hr^{-1} for the simulated system. Minimum cooling rates in the stratiform region show similar agreement. The main difference between heating rates diagnosed from observations and those from the model occurs in the lowest

levels along the convective line. One possibility is that the convective parameterization is not correctly representing heating there. Another, perhaps more likely, possibility is that the relatively narrow, leading convective line is not resolved by the observations of Gallus and Johnson. Although the observed gridded data has a spacing of approximately 50 km, the composited station spacing is about 80 km, making smaller-scale features difficult to resolve. Gallus and Johnson point to this limitation, stating that lack of resolution leads to a 40% underestimate in the convective rainfall rates. Despite the differences at low levels, the general agreement between observations and the model was very encouraging.

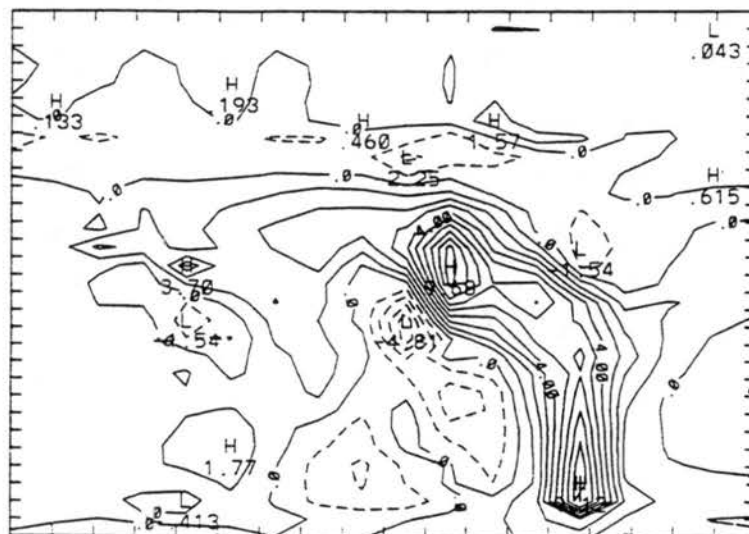
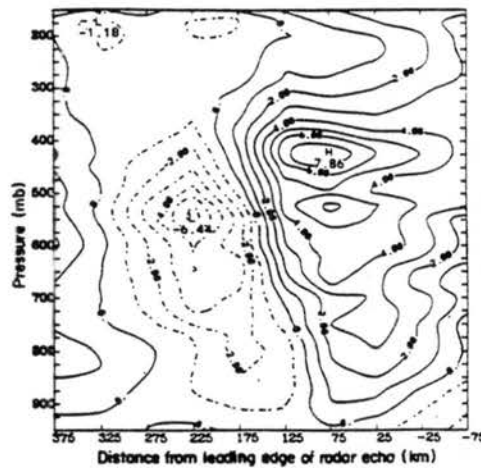


Figure 3.10: As in Fig.(3.9) except at 11/0600 UTC.

Shown in Fig. 3.10 are observed and model heating rates at 11/0600 UTC. At this time the system is beginning to dissipate; heating rates are lower while cooling associated with stratiform precipitation has increased. The agreement is again very good; the main difference is again at lower levels.

It is interesting to note the conspicuous lack of presentation of any heating rates in the "remarkable" simulation of this system by Zhang et al. (1989). Inaccurate representation of heating would bring into question the usefulness of that simulation in any *PV* study (e.g., Zhang and Cho 1992).

3.2.6 *Comparison with a simulation using the Kuo cumulus parameterization*

One sensitivity experiment worth noting was a comparison between the Level 2.5w Convective Adjustment Scheme and a modified Kuo-type convective parameterization (Tremback 1990). This comparison is not completely fair, since the 20 km grid spacing used on the second grid for these runs is smaller than that for which the Kuo scheme was originally designed.

The main result can be briefly summarized: the Level 2.5w scheme much more realistically reproduced the observed position, movement, and structure of the observed system. Specifically, major surface features (e.g., the wake low), and main flow features (e.g., the rear-to-front descending flow branch) were not well captured by the modified Kuo scheme. Tremback (1990) modified the original Kuo scheme to include downdrafts. These modifications should, if anything, have enhanced these features; thus the original Kuo scheme would be expected to perform worse than the modified scheme.

3.3 **The 23–24 June 1985 MCS**

3.3.1 *Observational and model studies of the 23–24 June 1985 MCS*

Although not nearly as widely studied as the 10–11 June MCS, the 23–24 June MCS has been the subject of several studies. The system is first mentioned by Augustine and Howard (1988) in their climatology of MCCs occurring in 1985. They note that this was a particularly active MCS year, due to a "mean quasi-geostrophic forcing pattern",

especially in June. The 23–24 June case distinguished itself for a relatively large amount of death and destruction (see their Table 3) among 1985 MCSs.

The 23–24 June MCS was also noteworthy for what did *not* occur. Stensrud and Maddox (1988) document the MCS from a forecaster’s standpoint. Two distinct systems sent out outflow boundaries which were forecast to form new deep convection upon collision. None occurred. Further analysis (completed after the fact) revealed upper-level mesoscale circulations induced by the two MCSs which lead to mid-level divergence, effectively capping any deep convection.

Johnson and collaborators performed the most complete observational studies regarding this system. Johnson et al. (1989) document surface features associated with this system, especially heat bursts (sudden, dramatic rises in temperature with a drop in dewpoint) and surface mesowave formation. They also note that this system is “an outstanding example of upscale development of convection”. In a later study, Bernstein and Johnson (1994) focus on the heat bursts, which they attribute to dry, adiabatically sinking air as part of the rear-to-front flow branch. Johnson and Bartels (1992) examine upper-level features, especially a warm-core mesovortex, which forms between 3 and 8 km above the surface. They note the complex structure of the mesovortex as well as its complicated formation, which is due to the interaction of multiple scales ranging from the synoptic down to the microscales.

Olsson (1994) completed the only known simulation of one of the MCSs occurring on 23–24 June 1985. His emphasis was on the analysis of balanced circulations associated with the observed mesovortex. This simulation is described in greater detail in the next section.

3.3.2 *System overview*

Upper-air and surface analyses near the time of convective initiation are shown in Fig. 3.11. At 500 mb, a large ridge is located over the southeastern USA, with a weak shortwave evident over Nebraska, near the developing MCS (see Fig. 3.12a). Weak cold-air advection at 500 mb is also taking place at this time. At the surface (Fig. 3.11b), a quasi-stationary front runs approximately east-west across the central USA, with relatively dry

air north and much more moist air south of the front. This moist air rapidly advected northward. Initial convection fires along this front in Iowa about 23/1900 UTC.

The 23–24 June 1985 PRE-STORM MCS might actually be better termed an “MCS event”, since two main MCSs formed in the region. The larger of these two systems (which was the focus of the simulation) has expanded along the front in western Iowa and southeastern Nebraska by 23/2235 UTC (Fig. 3.12a). A second smaller MCS is located in western Kansas. This smaller MCS is not captured by the simulation at this time (Fig. 3.12b) since that area is not included in Grid #3 (Fig. 3.15). Hereafter, we simply refer to the larger of the two MCSs as the 23–24 June MCS, and will neglect the other, smaller system.

The propagation speed of this system is less steady than the 10–11 June MCS and points to a difference between the two MCSs. The 10–11 June MCS had a classic squall line structure, with a long, well-defined leading edge that could be easily tracked over time. By contrast, the 23–24 June MCS featured deep convection embedded more randomly along the leading edge, making a propagation speed more difficult to define.

After 24/0000 UTC, the system continues to expand and move southward. At 24/0230 UTC the MCS is located along the Iowa–Missouri border, extending into NE Kansas (Fig. 3.13a). Four hours later, the MCS has continued to move southward and has begun the transition from a mature to dissipating MCS (Fig. 3.14). After this time the MCS slows its southward progress and dissipates.

A much more detailed analysis of the evolution and movement of the simulated MCS is presented in Olsson (1994), as previously discussed.

3.3.3 *Model setup for the 23–24 June 1985 MCS*

The major difference between this simulation and that for 10–11 June was in the grid structure, which is summarized for the 23–24 June MCS in Table 3.2 (cf. Table 3.1). The 23–24 June simulation used three grids (Fig. 3.15) instead of only two used for the 10–11 June case. Three grids were needed for two reasons (Olsson 1994). First, forcing for this MCS was apparently not strong enough to allow the parameterization to trigger with the 25 km spacing used on Grid #2. Second, convection near the boundaries of Grid #2 would

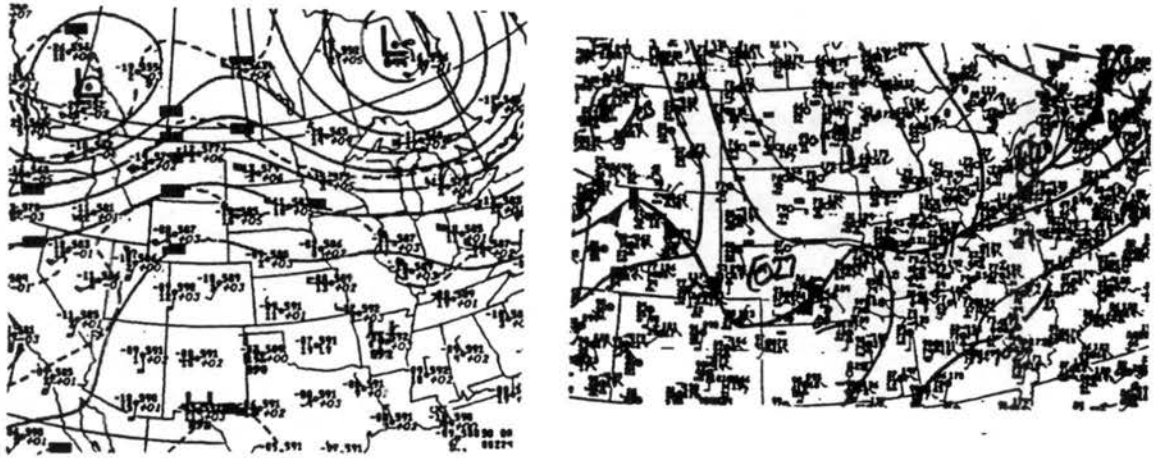


Figure 3.11: (a) 500 mb analysis at 24/0000 UTC, (b) Surface analysis at 23/2100 UTC.

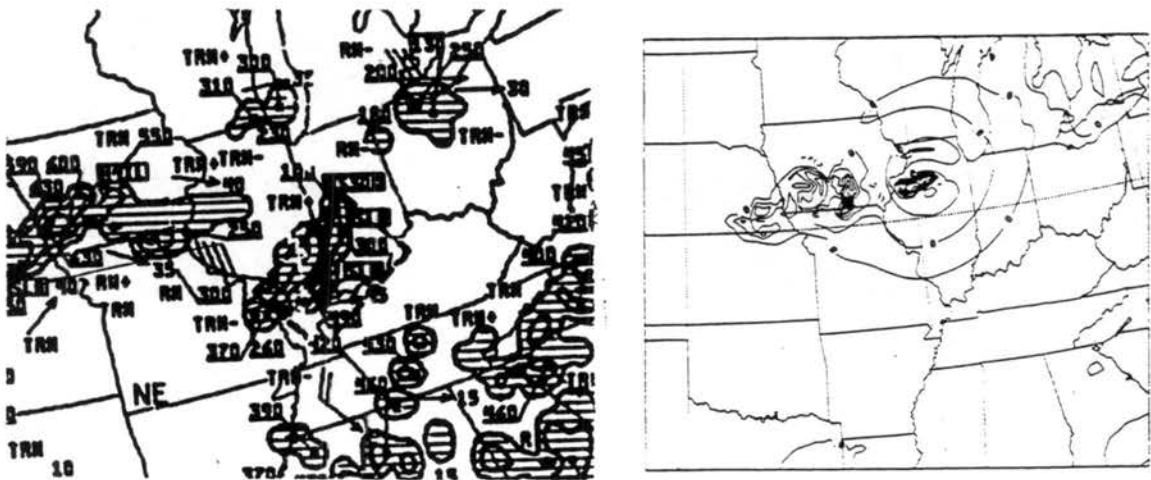


Figure 3.12: (a) Radar Summary at 23/2235 UTC, (b) Vertical velocity (23/2235 UTC) at 5 km on Grid #2. Contour interval is 0.5 ms^{-1} .

possibly cause problems with the analysis of balanced dynamics, which was the main goal of that work. Thus to reduce spurious convection away from the area of interest, the Level 2.5w Convective Adjustment Scheme was only used on the finest grid (i.e., Grid #3) for the 23–24 June case. This potentially leads to problems in the representation of heating in the two simulations, since in the case of 10–11 June the convective parameterization was employed on the 20 km grid, while in the 23–24 June case, it was used on the 8.33 km grid. The vertical grid structure differs somewhat from the 10–11 June simulation as well. The 23–24 June simulation uses 175 m at the lowest level, stretching at a ratio of 1.1 to a maximum vertical spacing of 1000 m.

Table 3.2: Model configuration for the 23–24 June 1985 MCS simulation

	Grid #1	Grid #2	Grid #3
number of grid points	55 × 44	80 × 65	101 × 77
domain size (km)	4050 × 3225	1975 × 1600	833 × 633
grid spacing (km)	75	25	8.33
vertical levels	32	32	32
time step (s)	90	45	22.5
cumulus parameterization used ?	no	no	yes

Grids #1 and #2 (Fig. 3.15) were active from the beginning of the simulation, i.e., 23/1200 UTC. This configuration was run until 23/1800 UTC, when Grid #3 was added. All three grids were then active until the end of the simulation, 24/1200 UTC. The Level 2.5w Convective Adjustment Scheme was activated (on Grid #3 only) at 23/1900 UTC, near the time of convective onset, and remained active until the system was well into its dissipating stage, at 24/0800 UTC.

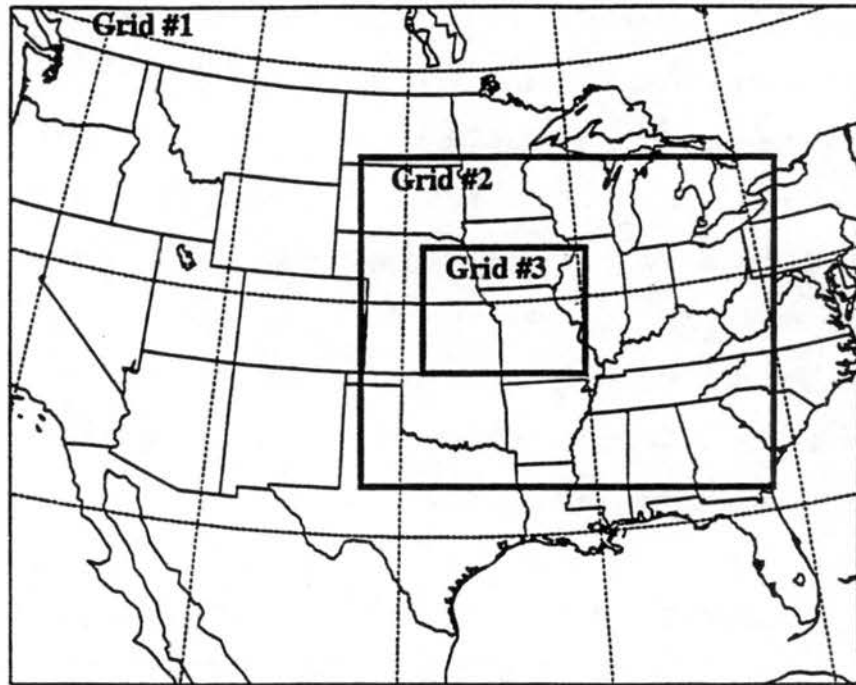


Figure 3.15: Location of the model grids for the 23–24 June 1985 MCS simulation.

3.3.4 General verification

Deep convection with the simulated system also starts in southern Iowa and at 23/2230 UTC agrees well with the observed system (Fig. 3.12b). At this time deep convection which is not observed is also occurring over Illinois.

The simulated system grows and moves south in agreement with the observed MCS. At 24/0230 UTC (Fig. 3.13b) the both the simulated and observed systems are on the Iowa–Missouri border. The simulated system is aligned E–W, whereas the observed system is oriented somewhat more WSW–ENE. Recall that the Grid #3 domain does not extend into western Kansas, hence the convection observed there at this time is not captured by the simulation.

Four hours later, at 24/0630 UTC (Fig. 3.14b), the simulated MCS has continued to move south and has begun to dissipate. In agreement with the observations, the speed of the simulated MCS slows as it weakens. After this time, the simulated MCS continues to dissipate.

3.3.5 Heating rates

The magnitude of the heating rate (Q_1/c_p) is potentially higher in the 23–24 June case than the 10–11 June case, due to the finer resolution of the grid on which the convective parameterization was active. We will now determine whether the averaging done to place Grid #3 data onto Grid #2 (which will be used for our analysis) gave consistent heating rates for our analysis.

Heating rates were calculated from the 23–24 June simulation as they were for the 10–11 June case. Unfortunately, no observations of heating rates exist for this system as they do for the 10–11 June MCS. Thus, we are restricted to a somewhat qualitative evaluation of heating rates for the 23–24 June case.

Figure. 3.16 shows heating rates averaged along the MCS (in an east–west direction) during the dissipating stages of this system. Maximum heating rates at this time are about 12 K hr^{-1} and are associated with the weakening convective line. Cooling in the precipitating stratiform region is about 3 K hr^{-1} . The shape and magnitude of the heating for this system are consistent with both the simulation and observations of the 10–11 June MCS (cf. Fig. 3.10). One noticeable difference is the lack of low-level heating along the convective line of the 23–24 June case, which occurs for two reasons. First, at this time the convective line is weaker than for the 10–11 June MCS. Second, the convective line in the 23–24 June MCS was much more broken, with many gaps in deep convective cells, as opposed to the solid, unbroken convective line associated with the 10–11 June MCS.

Thus it appears that heating rates on Grid #2 are consistent, at least qualitatively, with both observations and the results from the 10–11 June simulation.

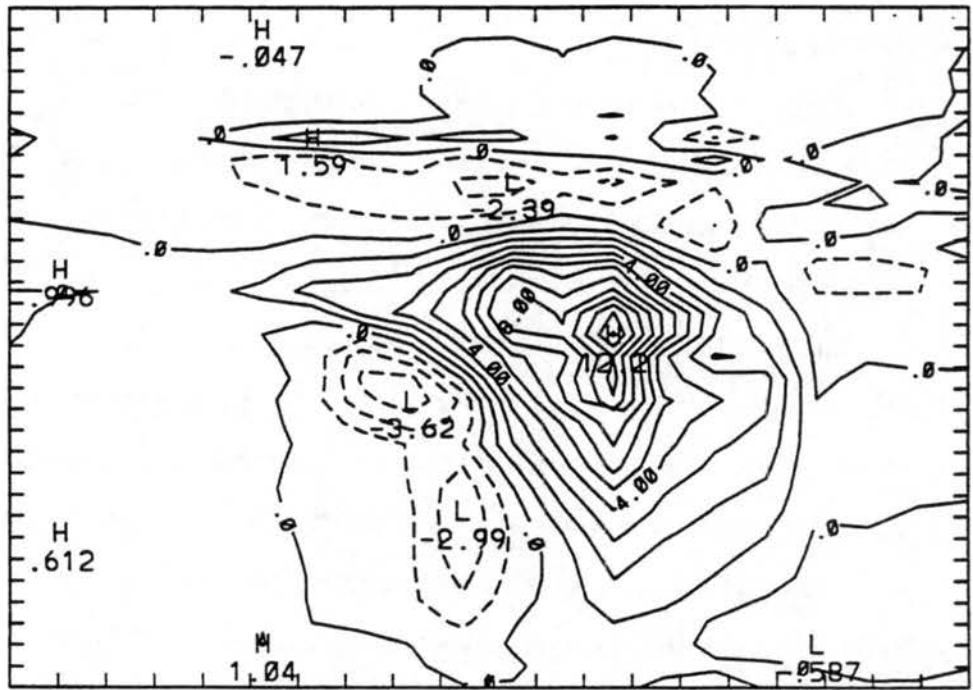


Figure 3.16: Q_1/c_p from the simulation at 24/0600 UTC.

Chapter 4

PV EVOLUTION ASSOCIATED WITH THE MESOSCALE CONVECTIVE SYSTEMS

We begin this chapter with a short discussion of the data processing carried out from model output data. The remainder of this chapter is devoted to a description of the evolution of \mathcal{P} associated with two simulated MCSs, from the pre-MCS environment to the dissipating stages. We will focus our attention on two levels, a middle level where a positive \mathcal{P} anomaly is often observed and an upper level, below the tropopause, where a negative anomaly is observed. Our description here is meant to show *how* \mathcal{P} evolved; *why* it evolved as it did is the subject of the quantitative budget analysis in the next chapter.

4.1 Post-model Processing

Model output was written out every 30 min during the simulation in files which contain data on the model σ_z coordinate. These coordinates can, however, be inconvenient for analysis, especially at low levels. Even on the relatively small Grid #2 domain for the 10–11 June simulation, the lowest model level extends from about 900 to 700 mb, or from about 500 m to 3000 m, making interpretation difficult. For this reason, another vertical coordinate was chosen for analysis.

Two likely choices for a vertical coordinate were pressure or Cartesian. Pressure coordinates have an advantage of being quasi-horizontal and compatible with standard weather charts for comparison. This latter point was less important since most of the products considered in this analysis were not on standard charts. A disadvantage of pressure coordinates compared to Cartesian coordinates was an extra level of calculation, e.g., calculating $\omega = dp/dt$ in the total derivative. Thus it was concluded that Cartesian was the most straightforward choice for a vertical coordinate.

From the model output files, u, v, w, θ, ρ , and \mathcal{P} were linearly interpolated to Cartesian space at 500 m intervals. These files were saved and form the “raw” data used for the analysis. The analysis further required calculations of temporal and spatial derivatives, e.g., in the code to calculate (2.4). Time derivatives were calculated using centered time differencing. Spatial derivatives were also calculated using centered differencing. In addition, for consistency, spatial derivatives were averaged over the three times spanning the temporal derivatives. Further averaging will be addressed as results are presented in Chapter 5.

4.2 PV evolution during 10-11 June

In this section we examine the mid- and upper-level \mathcal{P} evolution associated with the 10–11 June 1985 MCS, from ambient fields prior to MCS initiation to those as the MCS is dissipating.

4.2.1 *Structure prior to MCS initiation*

The ambient \mathcal{P} field before MCS initiation is fairly quiet at mid levels. Fig. 4.1 shows \mathcal{P} and winds at 5 km over most of the Grid #1 domain. One feature that is apparent is some slightly higher- \mathcal{P} air extending downwards from upper levels through Wyoming and into South Dakota. In general, ambient values at this level are on the order of 0.5 PVU or less.

At upper levels (Fig. 4.1b) we see a strong “inverted ridge” of high- \mathcal{P} air in the north-central U.S.A. associated with an upper-level trough there. A large region is under the influence of stratospheric air (defined as $\mathcal{P} > 2$ PVU) at this level, with maximum values of 6 PVU over Wyoming. It is interesting to note that the MCS initiates ahead of the upper-level \mathcal{P} gradient and the squall line grows parallel to it, suggesting a possible influence of this upper-level feature.

A cross section through the upper-level high- \mathcal{P} air in the vicinity of the MCS genesis region shows that the stratospheric air dips down to about 10 km at its lowest point (Fig. 4.1c). What effect this feature had on the development of this MCS is difficult to ascertain due to possible influences of the mountains. Potential temperature contours are

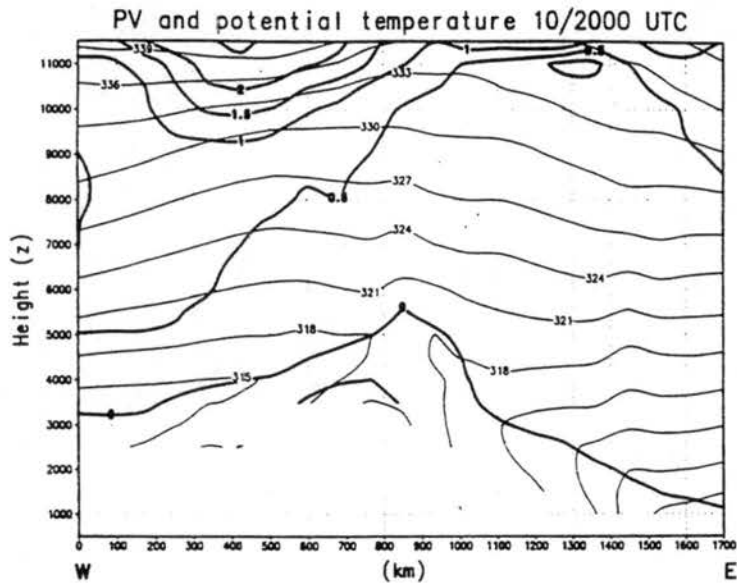
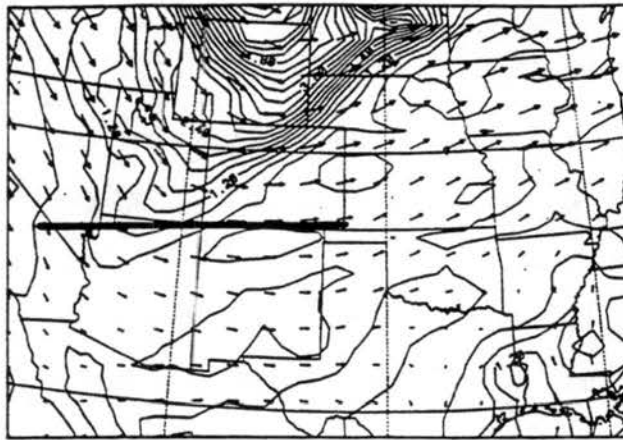
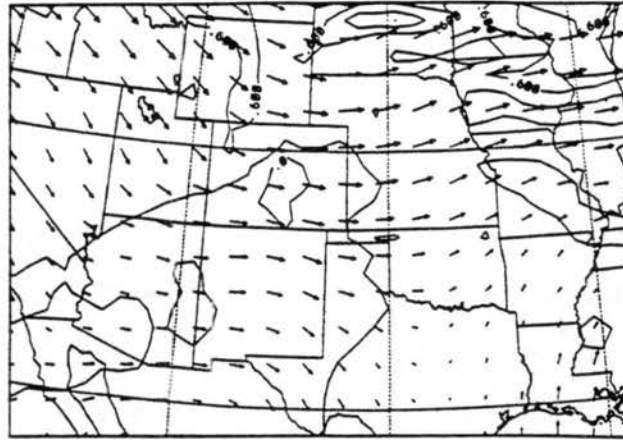


Figure 4.1: (a) \mathcal{P} and winds at 10/2000 UTC and 5 km over a portion of the Grid #1 domain. Contour interval is 0.3 PVU and maximum wind vector is 27 ms^{-1} , (b) \mathcal{P} and winds at 10/2000 UTC and 10 km, maximum wind vector is 45 ms^{-1} , (c) potential vorticity and potential temperature at 10/2000 UTC along the section shown in (b).

also plotted; in upper levels some packing of isentropes associated with high- \mathcal{P} air is seen. At 11.5 km the maximum θ is 341 K.

In order to better determine the effect of the convection, an additional experiment was run using only Grid #1 in which the convective parameterization was never activated, thus simulating a situation in which an MCS did not occur. In this experiment, the upper-level inverted \mathcal{P} ridge simply advects eastward without a significant change in structure. At mid levels, no significant changes occur. Thus, changes in \mathcal{P} investigated in the next subsections can be attributed to the influence of the MCS.

4.2.2 *Evolution at mid levels*

The size of the mid-level \mathcal{P} anomaly that forms as the MCS develops is largely contained within Grid #2. Thus we will take advantage of this more highly-resolved domain for an examination of \mathcal{P} evolution at this level.

By 10/2300 UTC the MCS has begun to develop as a short N-S oriented convective line in SE Colorado. The ambient \mathcal{P} pattern has now been replaced by strong anomalies¹ (Fig. 4.2a). A region of high \mathcal{P} air, with a maximum of 6 PVU, is located towards the southern end of the MCS, while negative \mathcal{P} air to almost -3 PVU is located in the southern region of the MCS. At this time the \mathcal{P} anomalies are collocated with the MCS (cf. Fig. 3.2a).

Negative \mathcal{P} air consists of either strong anticyclonic shear (i.e., negative absolute vorticity) or a superadiabatic layer (i.e., $\partial\theta/\partial z < 0$). Since the latter is unlikely except in a shallow layer near the surface, we anticipate the former. This is also seen in Fig. 4.2a, which shows the flow deflected anticyclonically around the north end of the MCS, and cyclonically around the south end. From the figure the impression is that the MCS is acting as a barrier to the ambient flow, with deflection around it.

This vorticity pattern also resembles that obtained in a thunderstorm simulation by Rotunno (1981). This vortex couplet forms due to tilting of ambient horizontal vorticity

¹Here we use the term "anomaly" somewhat loosely. Any \mathcal{P} that deviates from the time-varying ambient value that would have occurred in the absence of the MCS is considered an anomaly.

(associated with strong low-level shear) by the main thunderstorm updraft. Verlinde and Cotton (1990) observed such vortex pairs using dual-Doppler radar. It is important to note that the horizontal scale of vortex pairs in the above two studies is between 10 and 40 km. In the 10–11 June MCS, the \mathcal{P} (and vorticity) couplet spans about 300 km.

Two hours later, at 11/0130 UTC, the MCS and associated \mathcal{P} anomalies have taken on a more NE–SW orientation as the simulated system begins to move into Kansas and Oklahoma (Fig. 4.2b). Peak values of the positive and negative \mathcal{P} anomalies have increased to +8.4 and -3.5 PVU respectively. More important, the character of the \mathcal{P} anomalies and flow vectors have dramatically changed.

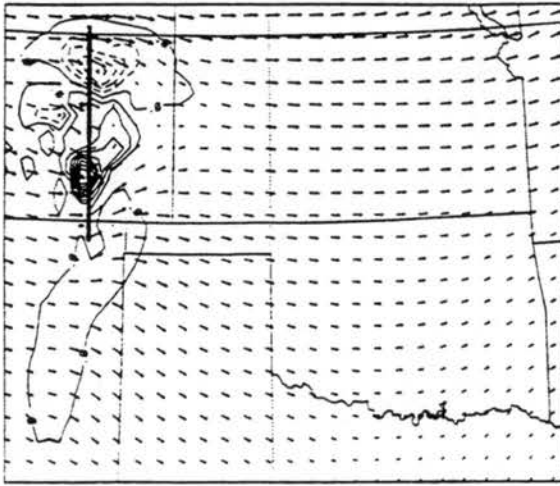
The positive and negative \mathcal{P} dipole seen two hours earlier at this level is no longer apparent. Both anomalies have expanded with a shape oriented along the MCS. The positive \mathcal{P} anomaly is still collocated with the MCS at this time (cf. Fig. 3.3a). However, the negative anomaly is now located to the rear of the system, is spatially less expansive than the positive anomaly, and is also less organized than two hours previous.

The flow field is necessarily altered as well. Specifically, with the loss of the \mathcal{P} dipole pattern, the flow no longer has the “bookend” appearance of the earlier time. The MCS still qualitatively appears to present a barrier to the ambient flow, with very weak winds directly downwind of the MCS.

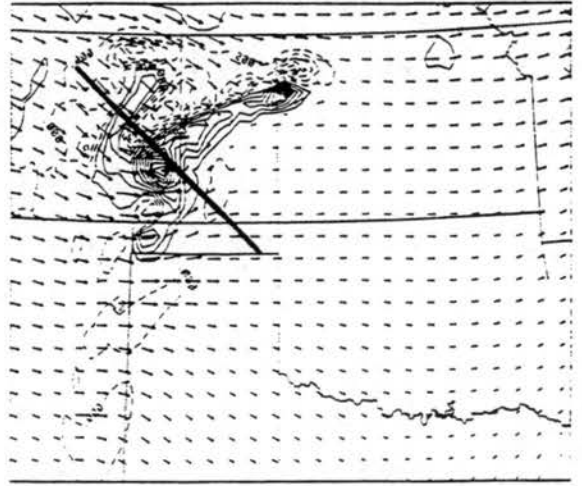
The area encompassed by the negative \mathcal{P} anomaly at this level continues to decrease at 11/0330 UTC, although it maintains about the same magnitude (Fig. 4.2c). The negative anomaly is still located to the rear of the positive anomaly (which has weakened to 6.3 PVU). Another important change has taken place. Both anomalies are now towards the rear of the storm, and are hence associated with the stratiform precipitating region. In addition, the strongest part of the positive anomaly is now located towards the NE end of the storm.

The flow field shows a trough along the rear portion of the MCS, although no closed vortical circulation has formed either in the absolute wind field or in the system–relative winds.

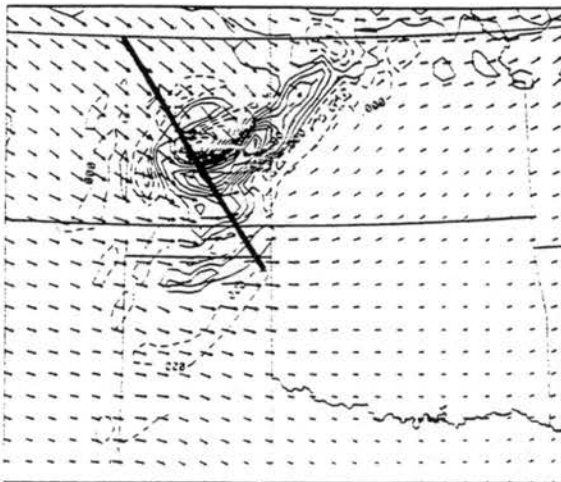
During the dissipating stages at 11/0530 UTC, the system is dominated by positive \mathcal{P} anomalies (Fig. 4.2d). Both positive and negative anomalies have weakened (5 and -1.4



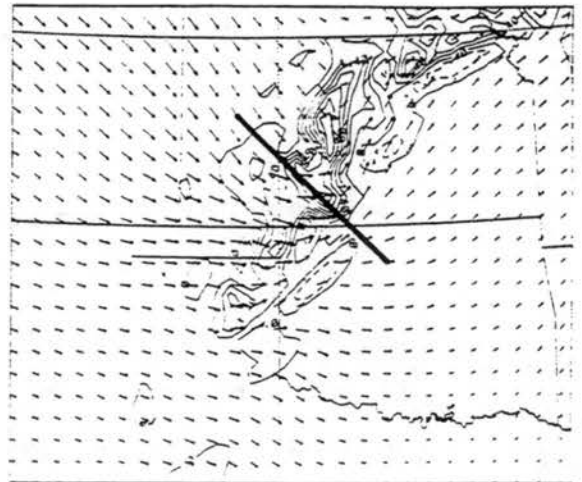
(a)



(b)



(c)



(d)

Figure 4.2: \mathcal{P} and winds over the Grid #2 domain at 5 km. Contour interval is 0.7 PVU and maximum wind vector $\approx 30 \text{ ms}^{-1}$. (a) 10/2330 UTC, (b) 11/0130 UTC, (c) 11/0330 UTC, (d) 11/0530 UTC.

PVU respectively). Small negative anomalies are now located at the front of the MCS. The main positive anomaly is still located towards the rear and NE end of the storm. The flow field at this time is similar to 11/0330 UTC, with cyclonic flow dominating the system.

Summarizing, the perturbation \mathcal{P} field at 5 km starts as a dipole, with positive (negative) anomalies at the south (north) collocated with the convective line. A gradual evolution takes place, with the anomalies migrating towards the rear of the MCS and a widespread positive anomaly greatly dominating smaller and weaker negative anomalies. The processes responsible for the demise of the negative anomaly as well as the growth of the positive anomaly are subjects of the budget analysis in the Chapter 5.

4.2.3 *Evolution at upper levels*

The upper-level \mathcal{P} anomaly that forms as the MCS grows is more strongly influenced by ambient flow at this level, and is not contained within the Grid #2 domain. We will thus not be able to use the more highly-resolved model data from this grid and will examine the \mathcal{P} evolution at this level using Grid #1 data.

As we have seen, the MCS at 10/2330 UTC has begun to organize in SE Colorado. The upper-level high- \mathcal{P} air has translated eastward (Fig. 4.3a) as can be seen by examination of the 2.1 PVU contour (cf. Fig. 4.1b). In addition, we see from Fig. 4.3a the beginnings of an "erosion" of the high- \mathcal{P} air collocated with the MCS, with a decrease of about 1 PVU from ambient values. Winds also show this perturbation, with more diffluent flow appearing over the MCS.

Two hours later, at 11/0130 UTC, an area with $\mathcal{P} = -1.8$ PVU now has developed north of the MCS (Fig. 4.3b). It appears that this area has become separated from the MCS. Over the north end of the MCS itself, a positive \mathcal{P} anomaly is seen, while a weaker negative anomaly is located over the south end of the MCS. The diffluent outflow has increased as well.

This trend continues as the main negative \mathcal{P} anomaly weakens slightly (by 0.3 PVU) but continues to advect towards the NE as the storm itself propagates towards the SE. By 11/0330 UTC, the main negative anomaly and associated anticyclonic flow (Fig. 4.3c)

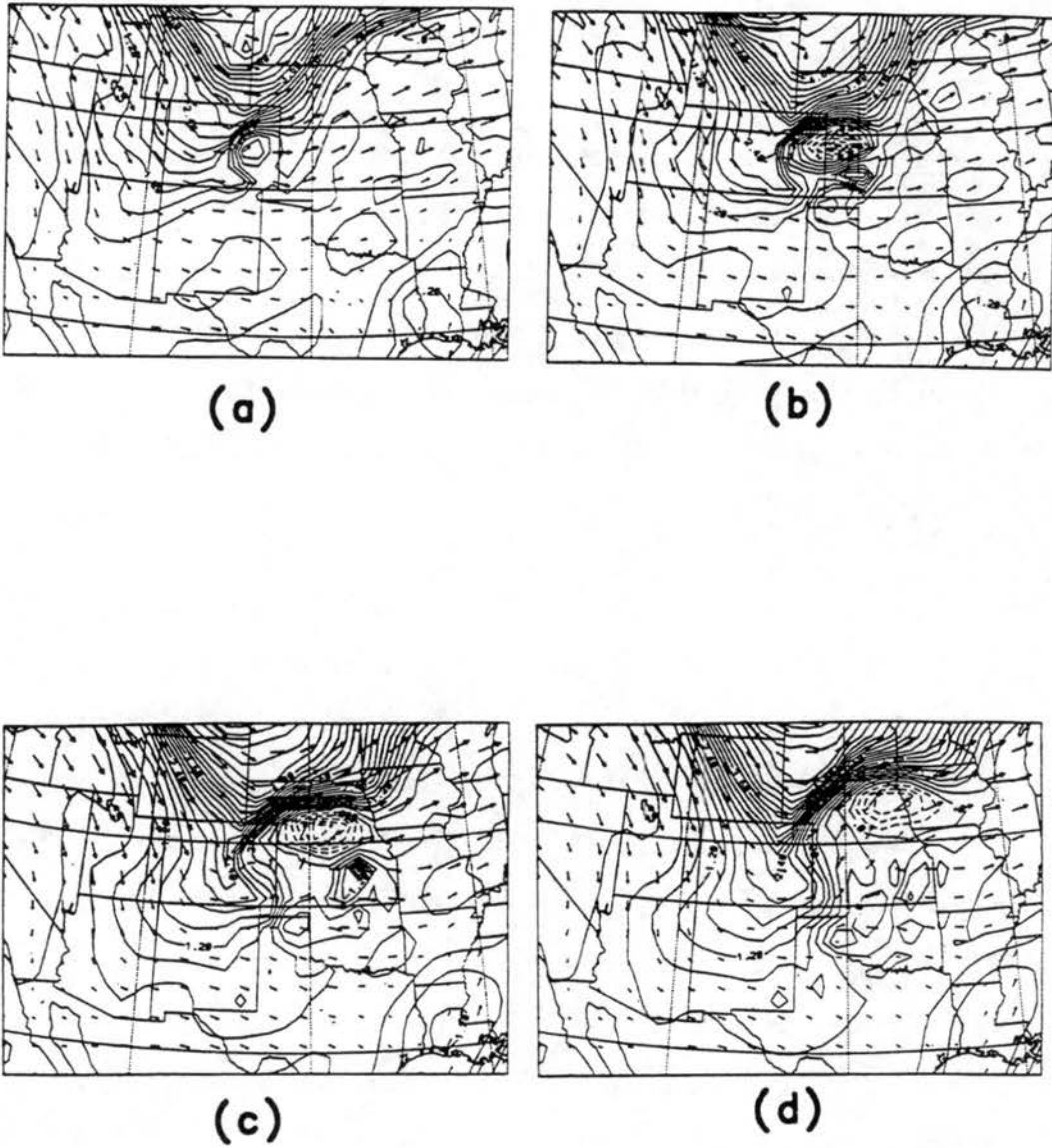


Figure 4.3: \mathcal{P} and winds over a portion of the Grid #1 domain at 10 km. Contour interval is 0.3 PVU and maximum wind vector $\approx 50 \text{ ms}^{-1}$. (a) 10/2330 UTC, (b) 11/0130 UTC, (c) 11/0330 UTC, (d) 11/0530 UTC.

have become completely detached from the MCS. A positive \mathcal{P} anomaly is still associated with the NE end of the MCS and has strengthened. From this overview, it is not obvious whether the positive anomaly forms *in situ* or is advected in from the reservoir upstream.

During the early dissipating stages (11/0530 UTC), the features previously seen are all still evident, although all anomalies have weakened (Fig. 4.3d). The strong deformation of the inverted \mathcal{P} ridge due to the formation of the MCS is also evident by this time.

4.2.4 Vertical structure

We will first investigate the vertical structure of the mid-level \mathcal{P} anomalies that form on Grid #2 during the life of the simulated MCS. Then we will again utilize Grid #1 data to investigate the change in vertical structure of the inverted \mathcal{P} ridge over the larger-scale domain.

Shown in Fig. 4.4 is a north-south section through the MCS at 10/2330 UTC. Both the positive and negative \mathcal{P} anomalies that were apparent in Fig. 4.2 extend through most of the troposphere. The sign does reverse in the lowest 2 km under each anomaly, but these are an order of magnitude weaker than the main, mid-level anomalies. The positive anomaly has a maximum of almost 8 PVU near 5 km, while the negative anomaly is weaker. An east-west section through each anomaly (not shown), does not show much additional structure, i.e., these anomalies are (in a smoothed sense) quite symmetrical.

As we saw earlier, the structure of \mathcal{P} at 5 km changes dramatically in the next two hours; the north-south dipole is gone and features are becoming more linear along the squall line. For the remaining times we examine sections through some of the more prominent features. We will also look at the average \mathcal{P} along the MCS, as well as a standard deviation to ascertain the amount of variability from the average along the line.

A NW-SE section through the MCS at 11/0130 UTC is shown in Fig. 4.5a. A deep positive \mathcal{P} anomaly, with a maximum of almost 6 PVU, exists at mid levels. The positive anomaly corresponds to the main convective updraft and tilts rearward² with

²We use front to mean towards the direction of MCS propagation, i.e., southeast, and thus rear refers to a direction toward the northwest.

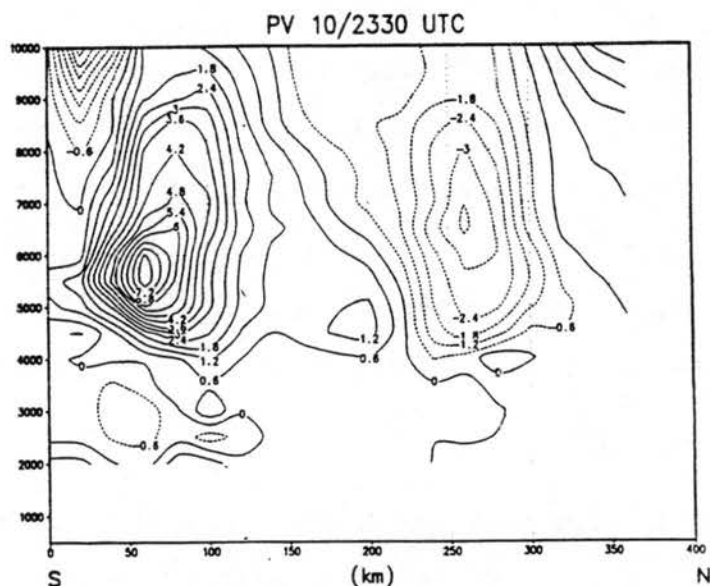


Figure 4.4: North-south section of \mathcal{P} at 10/2330 UTC, shown in Fig.(4.2a).

height towards the forming stratiform region. A deep region with negative \mathcal{P} is seen to the rear of the positive anomaly, associated with a developing rear-inflow jet. The boundary between positive and negative \mathcal{P} corresponds well to the boundary between rising and sinking air. Rearward of the negative anomaly is another, weaker mid-level positive anomaly. Strong anomalies are seen near the surface, located near the leading convective line and cold pool due to baroclinic effects.

Average \mathcal{P} along the squall line is shown in Fig. 4.5b. Generally, we have positive values towards the front of the system, with a maximum of 2.4 PVU, and a minimum (about -1 PVU) towards the rear. The tilt of the anomalies seen in the sample section is not seen in the average and the maximum positive anomaly is somewhat elevated. The standard deviation (Fig. 4.5c) shows values on the same order as the average, indicating a large variance along the MCS. This can also be interpreted as the MCS being highly three-dimensional, and thus a two-dimensional slice would not necessarily be representative of the system as a whole. Most of the deviation occurs along the boundary between positive and negative \mathcal{P} and an even stronger contribution in the region of surface baroclinicity.

At 11/0330 UTC, the pattern is similar to the previous time, as seen in Fig. 4.6a. However, the \mathcal{P} anomalies now show more tilt towards the northwest, corresponding to more tilt in the vertical velocity field. The anomalies are stronger, with the negative

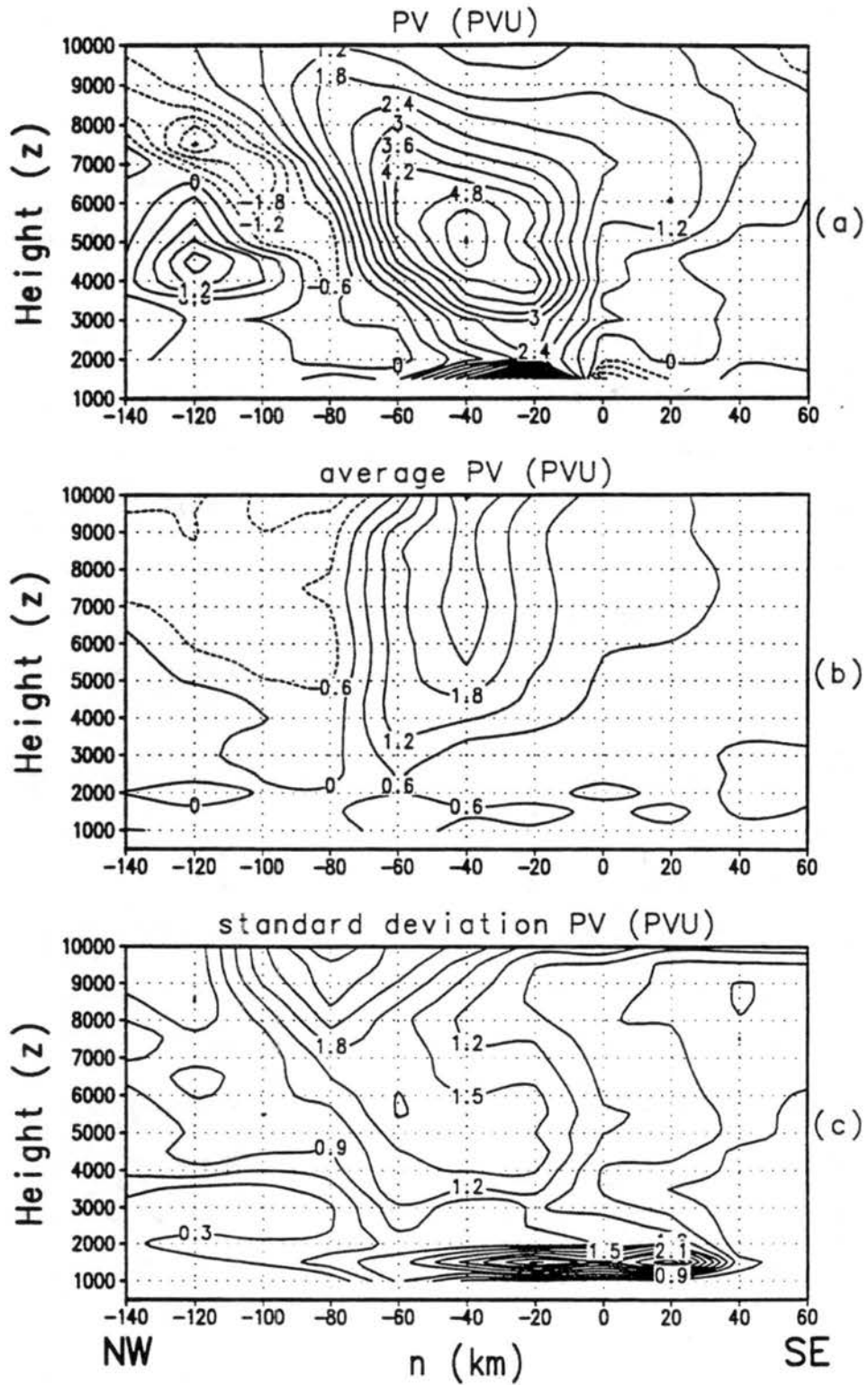


Figure 4.5: Northwest-southeast sections at 11/0130 UTC, shown in Fig.(4.2b), (a) \mathcal{P} , (b) \mathcal{P} average along the MCS, (c) Standard deviation of \mathcal{P} .

anomaly now -3.6 PVU. The maximum value of the positive anomaly along this section has also decreased slightly. It should be kept in mind that these are “snapshots” across one portion of the MCS at one time, so care must be exercised when comparing magnitudes of the anomalies at different times.

At this time, the average along the squall line much better matches the individual section (Fig. 4.6b), with a mid-level maximum at around 4 km, and tilting region of negative \mathcal{P} towards the rear of the system. The average negative anomaly is not as well defined as the positive anomaly because it does not extend along the full length of the system, as does the the positive anomaly (cf. Fig. 4.2c). The pattern of standard deviation along the MCS (Fig. 4.6c) qualitatively matches the average. Thus the structure seen in the average is more representative of the system as a whole, and thus at this time the MCS might be considered more two dimensional.

During this stage of the MCS lifecycle, the negative \mathcal{P} anomaly appears to be associated with the rear-inflow jet. Since negative \mathcal{P} indicates symmetric instability (SI), it appears that the rear-inflow jet is associated with SI, while the front-to-rear flow is associated with symmetric stability. As we saw in Chapter 2, negative *moist* \mathcal{P} (*MPV*) indicates conditional symmetric instability (CSI). It is interesting to note that Zhang and Cho (1992) analyze negative *MPV* (and hence CSI) associated with the front-to-rear flow, and conditional symmetric stability associated with the rear-inflow jet.

As the system enters its dissipating stages, the \mathcal{P} pattern takes on a more asymmetric shape (Fig. 4.2d), with the stronger positive anomaly towards the NE end of the MCS. A section through the approximate center of the system (Fig. 4.7a) shows a rather complicated structure, but generally there is tilted positive \mathcal{P} along the front-to-rear ascending flow. Vertical velocities along the rear-inflow jet have decreased and we have lost most of the negative \mathcal{P} anomaly here. The main features are a mid-level maximum of almost 4.2 PVU at 4 km, with secondary maxima near the surface, and aloft towards the rear of the system. A weak region of negative \mathcal{P} is seen at upper levels towards the front of the MCS.

Figure 4.7b shows the average along the MCS at 11/0530 UTC. Generally, the average shows the titled positive \mathcal{P} anomaly seen in the individual section, with weaker magnitudes.

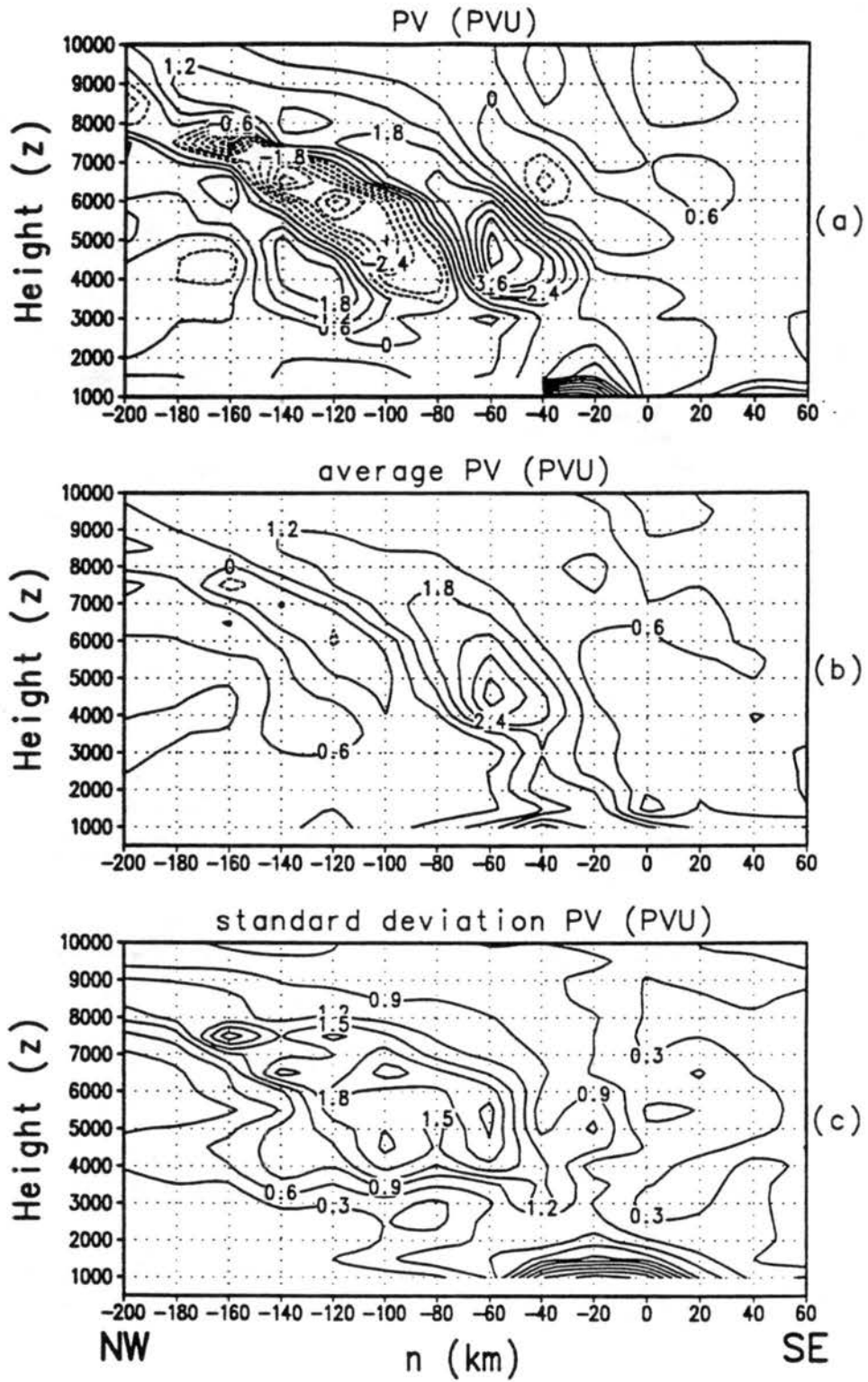


Figure 4.6: Northwest-southeast sections at 11/0330 UTC, shown in Fig.(4.2c), (a) \mathcal{P} , (b) \mathcal{P} average along the MCS, (c) Standard deviation of \mathcal{P} .

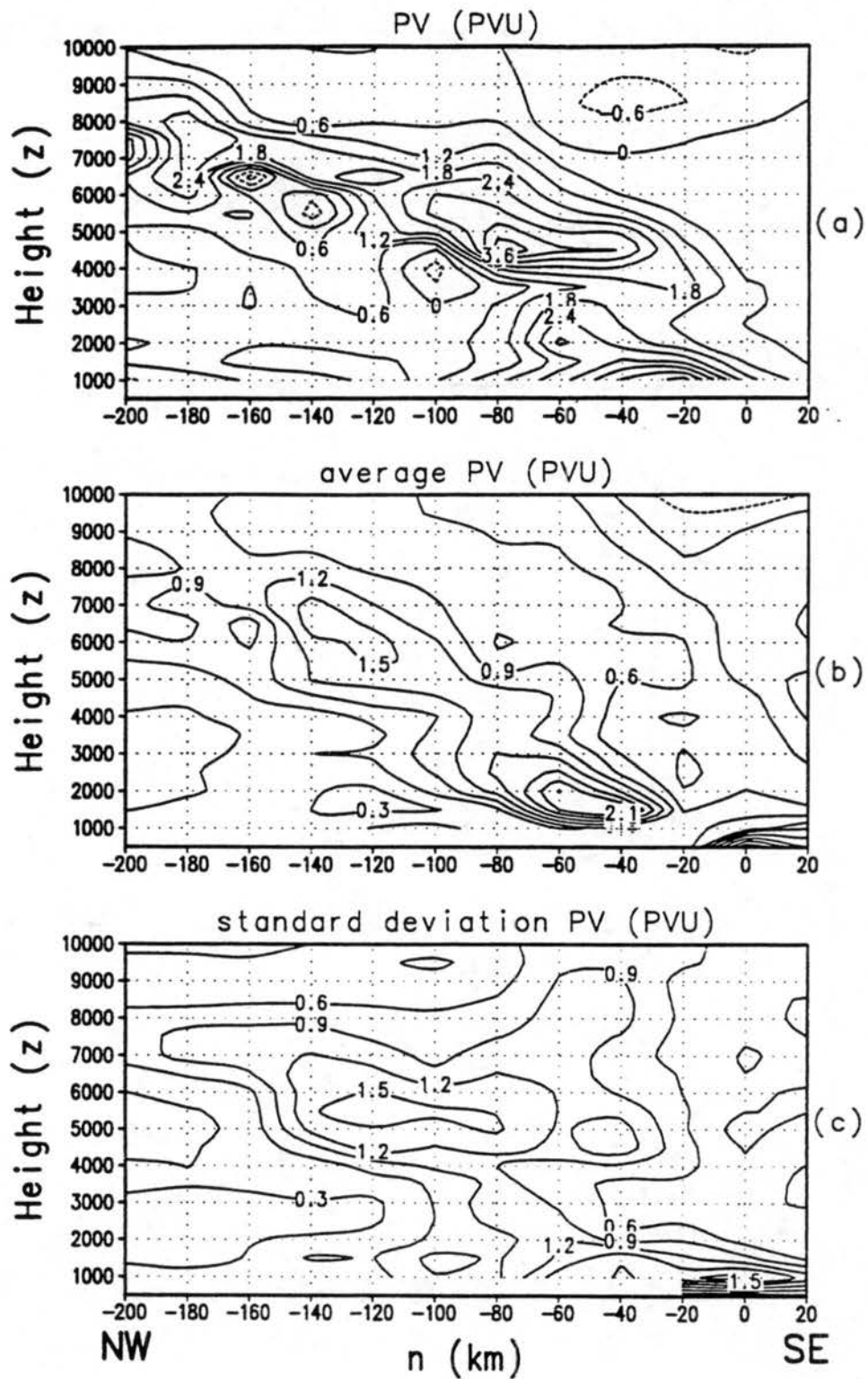


Figure 4.7: Northwest-southeast sections at 11/0530 UTC, shown in Fig.(4.2d), (a) \mathcal{P} , (b) \mathcal{P} average along the MCS, (c) Standard deviation of \mathcal{P} .

The average extends to include the much weaker SE portion of the storm, thus much detail is lost. It is interesting to note that the maximum in the average is now located near the surface. A secondary, weaker maximum is seen near 6 km. The standard deviation at this time (Fig. 4.7c) shows little resemblance to either the individual section or the average. We now see a broad region in mid levels, indicating that at this time, the MCS has once again evolved into a highly three-dimensional system. This can be inferred from Fig. 4.2d as the MCS has become more asymmetrical than during its mature stage.

To examine the larger-scale modification of \mathcal{P} , we take an east-west section through Grid #1 (Fig. 4.8). This section is similar to the previous one (cf. Fig. 4.1c) and is not perpendicular to the MCS but across the original inverted \mathcal{P} ridge at upper levels. At once apparent is the distortion of the ambient structure by the MCS. On this scale and at this location, we see weak positive \mathcal{P} at upper levels with a smaller-sized positive anomaly at around 5 km and another above 9 km. A lobe of \mathcal{P} , as seen by the $\mathcal{P} = 1$ PVU contour, extending down from near the tropopause is interesting as well. A region of weak negative \mathcal{P} is seen centered at approximately 3 km. Potential temperature shows lowered stratospheric air in the wake of the MCS, with a maximum value at 11.5 km of 351 K, or 10 K greater than the initial time. This pattern of a raised tropopause and lowered isentropes (i.e., warming) directly over the MCS, followed by a lowered tropopause to the rear of the system closely resembles observations of this MCS by Johnson et al. (1990). From (Fig. 4.8) we also see a lobe of high- \mathcal{P} air extending down to mid levels. There is some suggestion that an exchange of air between the stratosphere and troposphere may be taking place.

4.2.5 *Summary*

We now briefly summarize the evolution of \mathcal{P} with this MCS. At mid levels, we initially see a horizontal positive-negative dipole structure. Over its lifetime, the \mathcal{P} anomalies grow along the developing MCS. However, the negative anomaly eventually disappears, while a broader positive anomaly dominates.

A comparison with Raymond (1992) shows general agreement in the early stages of this MCS (cf. his Fig. 11). Raymond shows a positive-negative PV dipole at mid levels

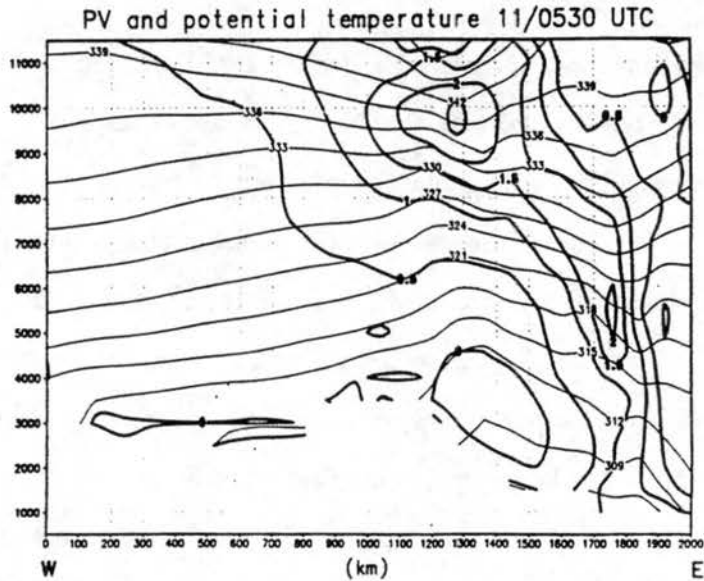


Figure 4.8: East-west section of \mathcal{P} (bold contours) and potential temperature (light quasi-horizontal contours) at 11/0530 UTC along the same section as shown in Fig.(4.1c).

similar to our results at 10/2330 UTC. As the 10–11 June MCS continues to grow, the \mathcal{P} anomalies go from a mostly horizontal structure and attain a more vertical structure. This is in qualitative agreement with Raymond’s paradigm for small vs. large MCSs.

Our results show less agreement with those of Davis and Weisman (1994). Reference to their Fig. 2 does show a \mathcal{P} dipole at 2.1 km, but in an opposite sense to our results at 5 km. A section through their simulated MCS shows that forcing reverses itself at about 5 km (see their Fig. 11), hence at mid levels, the two simulations may indeed be similar. During the mature stage of both simulations, there appears to be more agreement.

One aspect that we should keep in mind when comparing various studies is the nature and structure of the convection. Raymond (1992) considers “sphere”-shaped heating functions, approximately like the 10–11 or 23–24 June systems in their early stages. Davis and Weisman (1994) consider a line of convection initiated by spherical warm bubbles. We will compare similarities and differences between our results and the study of Davis and Weisman, as well as the results of Raymond, in greater detail in the next Chapter 5.

At upper levels, a strong negative \mathcal{P} anomaly initially forms, associated with deep convective cells. Over time, this anomaly appears to advect away and become detached from the MCS. A positive-negative dipole subsequently forms, but in the opposite sense

of the dipole at mid levels. Thus, the large-scale ambient \mathcal{P} structure is dramatically altered at upper levels.

Sections across the system at various times generally show deep positive \mathcal{P} anomalies associated with the front-to-rear flow and deep negative \mathcal{P} anomalies in the rear-inflow jet. Although there is usually a maximum of the positive anomaly at mid levels, there is no distinct vertical dipole during the forming stages or vertical tripole structure during the mature stage as simulated by Hertenstein and Schubert (1991) with their two-dimensional semigeostrophic model. Averages taken along the MCS, as well as standard deviations, suggest that during most stages in the MCS lifecycle, the \mathcal{P} distribution is very three-dimensional. An exception is during the mature stage.

4.3 PV evolution during 23–24 June

We now examine the evolution of \mathcal{P} over the lifetime of the second simulated MCS. As we saw in Chapter 3, the structure of convection with this MCS differs from the 10–11 June case. Instead of a long squall line with tilted updraft and downdraft branches, this system is dominated by more randomly organized deep convective cells.

4.3.1 *Structure prior to MCS initiation*

The ambient \mathcal{P} field at 5 km before convection begins is, as in the previous case, relatively quiet (Fig. 4.9a). Some higher \mathcal{P} is seen over Wisconsin and Michigan which is associated with lowered stratospheric air in this region. At 10 km (Fig. 4.9b) we see high- \mathcal{P} air in the northern USA which is at the southern end of an upper-level trough centered over Hudson Bay. The north-south gradient across this feature somewhat resembles that of the 10–11 June case, but is not as strong. The MCS starts just to the south of this gradient, although in this case the MCS propagates towards the south, while the high- \mathcal{P} air moves eastward. An experiment without convection shows that this feature remains unaltered, except for moving eastward, much as the previous case.

A north-south section taken through the \mathcal{P} gradient at 23/1900 UTC before the MCS initiates (Fig. 4.9c) shows a tropopause (in terms of \mathcal{P}) with some waviness before distinctly dipping downward near the north end of the domain. Potential temperature

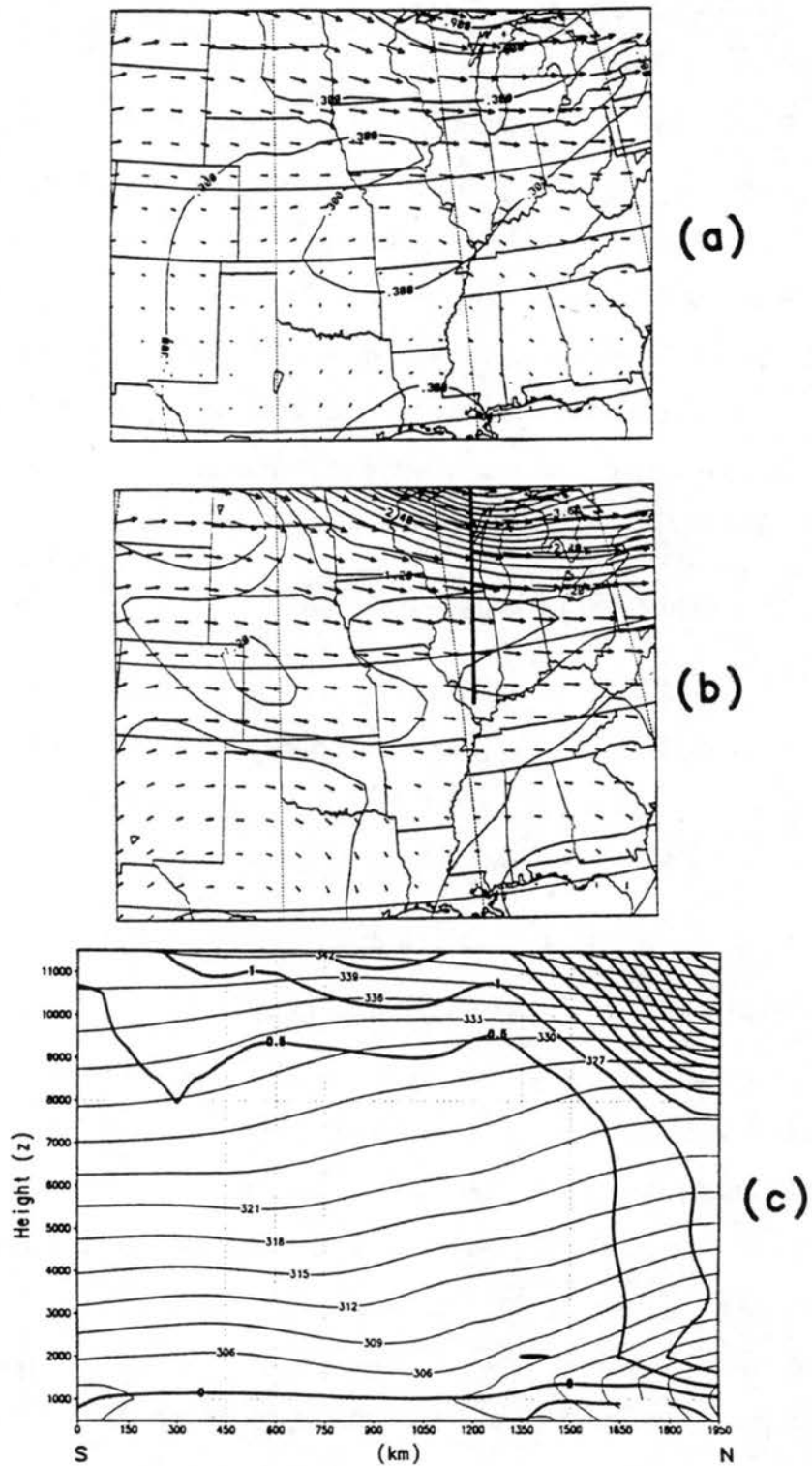


Figure 4.9: (a) \mathcal{P} and winds at 23/1900 UTC and 5 km over a portion of the Grid #1 domain. Contour interval is 0.3 PVU and maximum wind vector is 36 ms⁻¹, (b) \mathcal{P} and winds at 23/1900 UTC and 10 km, maximum wind vector is 41 ms⁻¹, (c) \mathcal{P} and potential temperature along the section shown in (b).

is much more closely packed near the high- \mathcal{P} air. As previously mentioned, the MCS subsequently initiates to the south of this feature. Vertical velocities do not show signs of deep or organized updrafts through the troposphere. Some organization in vertical velocity and divergence fields is seen near the surface front (see Fig. 4.9c). A small region of 0.5 PVU air also marks the location of the surface front.

4.3.2 *Evolution at mid levels*

We now examine the evolution of \mathcal{P} at mid levels; as in the previous case, we will examine results on Grid #2 (25 km grid spacing) for this level. By 23/2230 UTC, deep convective cells have been firing for about two hours. At this time, two main convective cells are active with no real organization and each cell has a positive-negative \mathcal{P} dipole (Fig. 4.10a). These resemble the dipole seen in the 10–11 June MCS, although the anomalies here are weaker, with $-1.4 \text{ PVU} < \mathcal{P} < 3.5 \text{ PVU}$. Winds show cyclonic (anticyclonic) shear with each positive (negative) anomaly.

In general, this MCS takes longer to organize than the 10–11 June case. However, two hours later, the cells begin to merge, as do the \mathcal{P} anomalies (Fig. 4.10b). Positive-negative \mathcal{P} dipoles are still apparent, but these have also begun to blend together. The anomalies have strengthened, now ranging from $-2.1 \text{ PVU} < \mathcal{P} < 6.3 \text{ PVU}$. Winds now appear to be deflected more around the entire system rather than around each dipole.

The system continues to organize and grow as it moves towards the south. The main part of the MCS is now located over northern Missouri. As in the 10–11 June case, as the system matures, the positive \mathcal{P} anomaly begins to dominate and the area of negative anomaly shrinks (Fig. 4.10c). Both anomalies have weakened somewhat, and the positive anomaly now begins to display an asymmetric shape. Wind vectors now show what appears to be a rear-inflow jet developing, with some anticyclonic shear, while cyclonic shear dominates the southern portion of the system.

Two hours later, the MCS appears to have weakened. The rear-inflow jet is still obvious (Fig. 4.10d), but it has lost most of its anticyclonic shear and no longer appears to penetrate to the front of the system. Dissipation of the anticyclonic shear can be seen in the disappearance of the negative \mathcal{P} anomaly at this level. South of the system, the

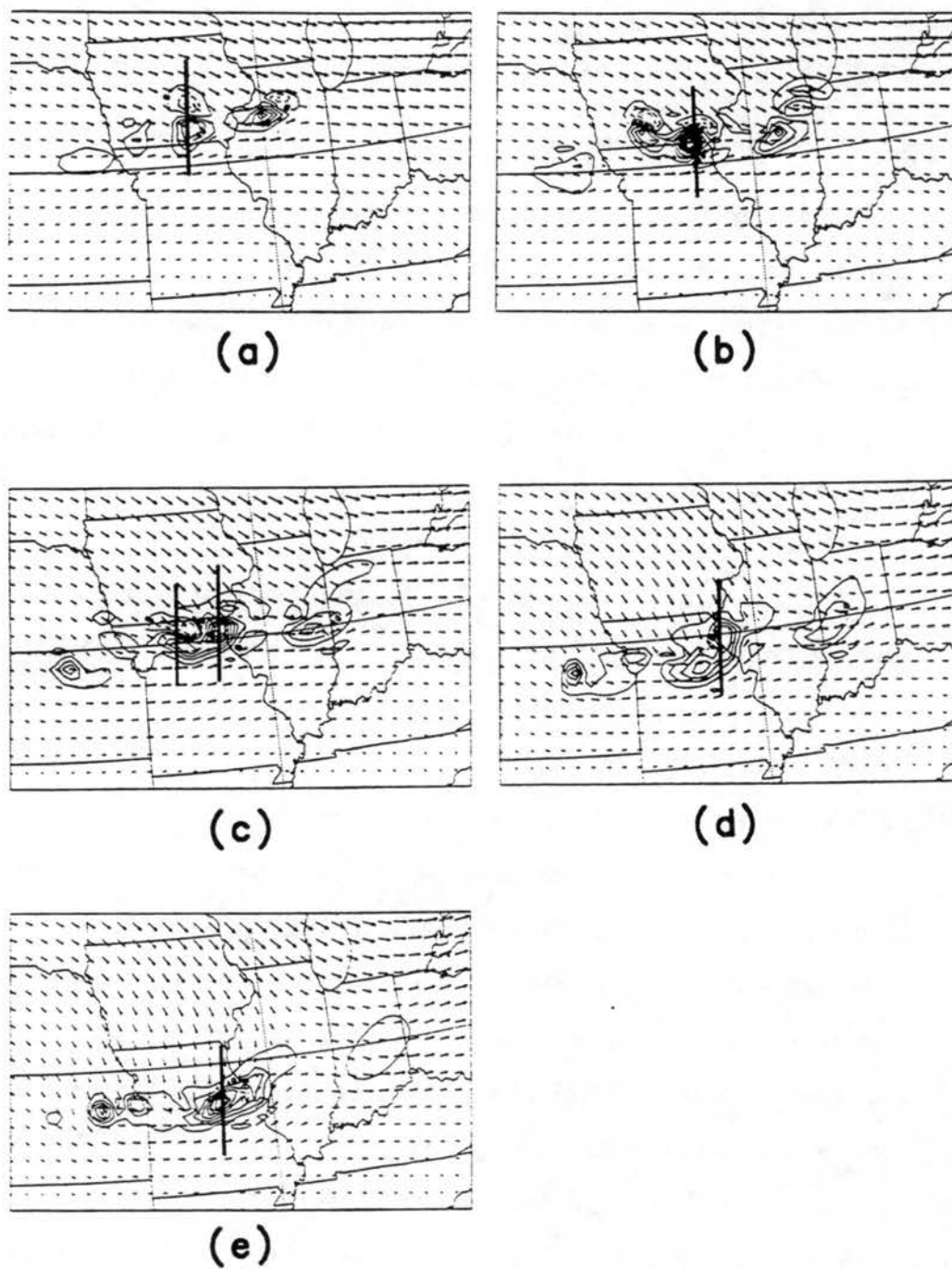


Figure 4.10: \mathcal{P} and winds over a portion of the Grid #2 domain at 5 km. Contour interval is 0.7 PVU and maximum wind vector $\approx 30 \text{ ms}^{-1}$. (a) 23/2230 UTC, (b) 24/0030 UTC, (c) 24/0230 UTC, (d) 24/0430 UTC, (e) 24/0630 UTC.

cyclonic shear has likewise weakened considerably, with the maximum positive \mathcal{P} now half its value (i.e., 2.8 PVU) compared to two hours earlier. The area encompassed by the $\mathcal{P} = 1.4$ PVU contour is about the same as two hours previous however.

By 24/0630 UTC as the system is well into its dissipating stages, the straight-line rear-inflow jet is still seen, but now the cyclonic shear south of the MCS has again strengthened (Fig. 4.10e). Thus, although no new negative \mathcal{P} has developed, the maximum positive anomaly has once again increased to 5.6 PVU, or double the maximum two hours earlier.

4.3.3 *Evolution at upper levels*

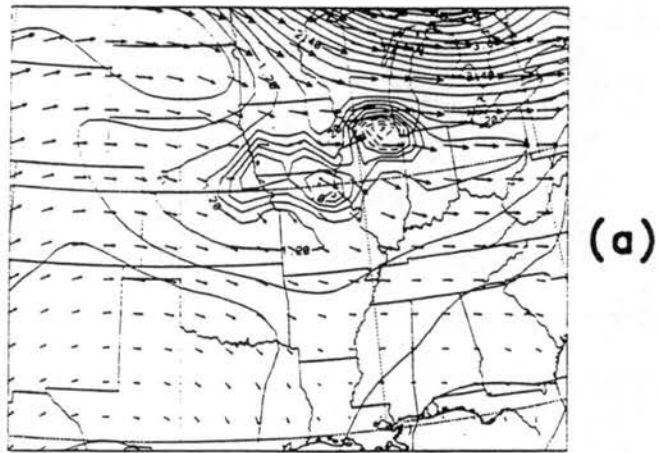
At 23/2230 UTC, the MCS has been active for about two hours. As seen with the 10–11 June case during the early stages, a large negative anomaly with $\mathcal{P} = -1.2$ PVU develops (Fig. 4.11a). The strongest negative anomaly has advected away from its “source”, i.e., earlier deep convection SW of the anomaly. Winds in the vicinity of the MCS are diffluent and anticyclonic.

Four hours later, at 24/0230 UTC, the largest area of negative \mathcal{P} has continued to advect away (Fig. 4.11b) Two other smaller regions of negative \mathcal{P} have formed over new deep convective cells and the area of low \mathcal{P} has greatly expanded due to the divergent outflow. Unlike the 10–11 June MCS, there is only weak flow south of the MCS, thus we see no cyclonic shear and associated positive \mathcal{P} anomaly as in the previous case.

The negative \mathcal{P} anomaly continues to expand and by 24/0630 UTC the divergent outflow has even advected some low- \mathcal{P} upstream (Fig. 4.11c). Very little negative \mathcal{P} remains, although a large region of negative perturbation \mathcal{P} remains. The system now displays a large area of anticyclonic flow to the north of the MCS. Thus, the ambient flow has been altered due to the presence of the MCS over much of the central USA.

4.3.4 *Vertical structure*

As we saw in Section 3.3.4, at 23/2230 UTC the MCS has not become organized as yet, and displays mainly two deep convective cells, each with a north-south oriented negative-positive \mathcal{P} dipole (Fig. 4.10). A section through the western dipole shows similarities to the 10–11 June MCS (Fig. 4.12). Both the positive and negative \mathcal{P} anomaly extend



through most of the troposphere. Some weakly negative \mathcal{P} is seen aloft near the positive anomaly. Unlike the 10–11 June MCS, both anomalies in this case show signs of two maxima in the vertical. In addition, no hint of a reversal at low levels is seen as in the 10–11 June case (cf. Fig. 4.4).

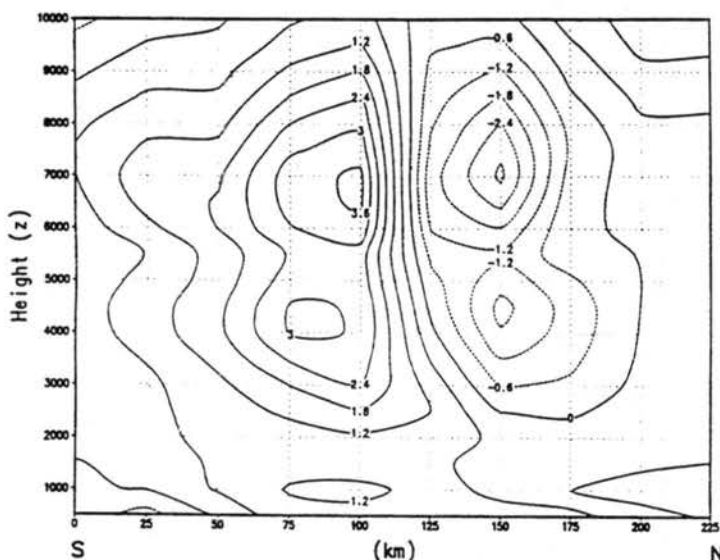


Figure 4.12: North-south section of \mathcal{P} at 23/2230 UTC shown in Fig.(4.10a).

Two hours later, the system has begun to merge somewhat, but is still comprised of essentially two main convection areas, and the \mathcal{P} still shows two main dipoles, one associated with each dipole. A section through the eastern (and stronger) dipole (Fig. 4.13) shows that some differences have occurred from the previous time. Only a single maximum is now seen with either the positive or negative \mathcal{P} anomaly. The negative anomaly has become broader and the maximum elevated from the previous time by about 3 km. The positive anomaly has almost doubled in strength, with a maximum now of 6.6 PVU. At this time, neither anomaly displays any tilt from the vertical.

After this time, the system does begin to organize, with the main part of the MCS advecting southward through Missouri. As before, we will now consider individual sections across the system, as well as averages and standard deviations along the MCS.

By 24/0230 UTC, the system has become more organized. Two N-S sections are taken through the main \mathcal{P} anomaly in northern Missouri (see Fig. 4.10c). As before, we refer to the “front” of the storm as towards the direction of movement, in this case,

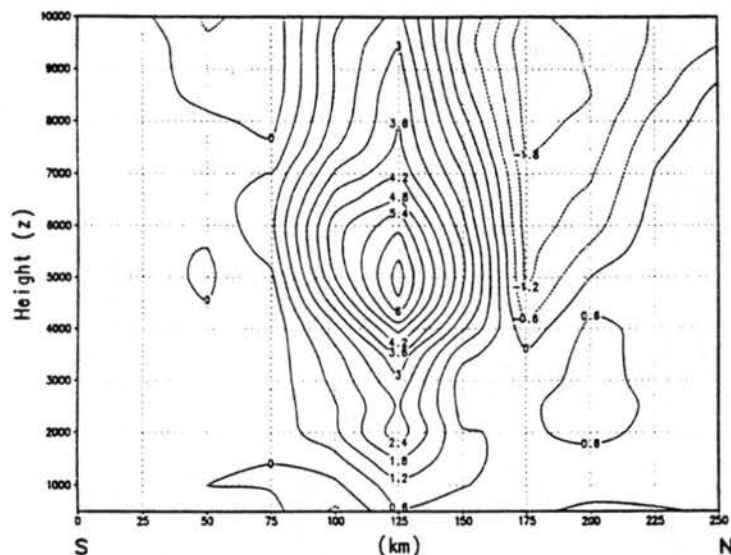


Figure 4.13: North-south section of \mathcal{P} at 24/0030 UTC shown in Fig.(4.10b).

south. The western N-S section (Fig. 4.14a) shows a similar pattern to that seen during the mature stage of the 10-11 June MCS, with a deep positive anomaly centered at 5.5 km along the leading edge and a tilting negative anomaly associated with the rear inflow. A main difference is that the positive anomaly does not tilt rearward. Both anomalies are also weaker than the previous case. By contrast, the eastern N-S section shows little negative \mathcal{P} and is dominated by a large, mid-level positive anomaly, centered somewhat lower at 4.5 km (Fig. 4.14b). Although different in shape, the magnitude of the anomaly is similar to the 10-11 June case at this stage.

An average along the MCS at this time (Fig. 4.14c) shows a large positive \mathcal{P} anomaly centered at about 6.5 km, somewhat higher than the positive anomaly from either individual section. Some weak negative \mathcal{P} is seen sloping downwards from the north. In general, the average fields do not show the degree of tilt seen in the 10-11 June MCS. The standard deviation (Fig. 4.14d) shows a maximum towards the rear of the MCS. This is likely due to the fact that the negative \mathcal{P} anomaly only occurs in part of the system as well as the difference in position of the positive anomaly along the MCS. Once again, the standard deviation is on the same order as the average, indicating three-dimensional structure along the MCS.

A striking difference is seen two hours later at 24/0430 UTC in the vertical structure of the positive \mathcal{P} anomaly along the eastern end of the MCS (Fig. 4.15a). An area of

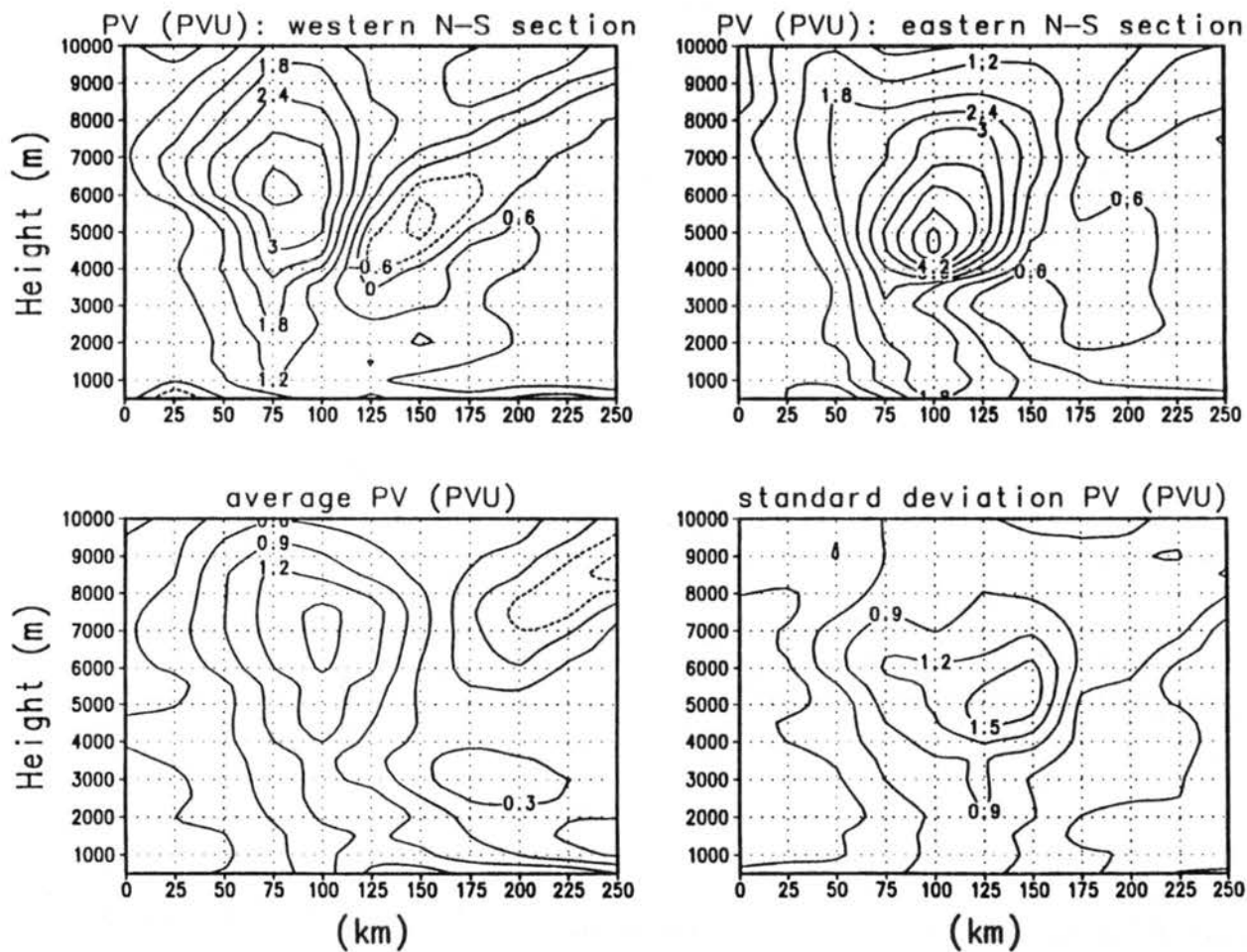


Figure 4.14: North-south sections at 24/0230 UTC, shown in Fig.(4.10c), (a) \mathcal{P} through the western portion of the MCS, (b) \mathcal{P} through the eastern portion of the MCS, (c) \mathcal{P} average along the MCS, (d) Standard deviation of \mathcal{P} .

weakly negative \mathcal{P} now exists above about 7 km in the center of the section, giving the appearance that the broad positive anomaly has been eroded from the top down. The positive anomaly centered at 4 km extends upwards on either side of the negative anomaly.

The average along the MCS at 24/0430 UTC (Fig. 4.15b) does not show this complicated structure, and is very similar to the average two hours earlier. However, at this time, the average positive \mathcal{P} is centered about 500 m lower and is about 20 % weaker. In addition, the tilted negative region is no longer seen on the south side of the system. The maximum standard deviation has shifted, so that it is now collocated with the maximum average positive \mathcal{P} (Fig. 4.15c).

During the dissipating stages, the positive \mathcal{P} anomaly actually strengthens somewhat. A section through the eastern portion of the MCS (Fig. 4.16a) very closely resembles that 4 hours earlier (cf. Fig. 4.14b). The maximum anomaly is again 5.4 PVU located at 4 km. The positive anomaly does show some extension upward and towards the north. The average along the MCS (Fig. 4.16b) is also again very similar to 4 hours earlier except the maximum extends a few hundred meters lower. The tilted negative anomaly has not reappeared on the north end of the averaged field. The standard deviation (Fig. 4.16c) has increased in size and magnitude somewhat from two hours previous. It also shows the upward and northward extension of the maximum, indicating that this feature (not seen in the average) is quite variable along the MCS.

We now examine the larger scale changes in vertical structure. A N-S section across Grid #1 taken in the same location as the 23/1900 UTC, is shown in (Fig. 4.17). We still see evidence of lowered stratospheric air to the north, but the \mathcal{P} field in the vicinity of the MCS has been greatly altered. The high- \mathcal{P} air directly above the MCS has been eroded significantly, with some negative \mathcal{P} evident. At mid levels, a positive \mathcal{P} anomaly of 1.5 PVU is seen centered at around 5.5 km. Unlike the 10-11 June MCS, there does not appear to be a link between the mid-level positive anomaly and the upper-level stratospheric reservoir (cf. Fig. 4.8). The potential temperature distribution resembles that associated with the ideal PV anomaly (cf. Fig. 2.1a). This resemblance is not seen in the 10-11 June MCS because of both the influence of the ambient high- \mathcal{P} inverted ridge and the nearness of mountains, both of which cause distortions.

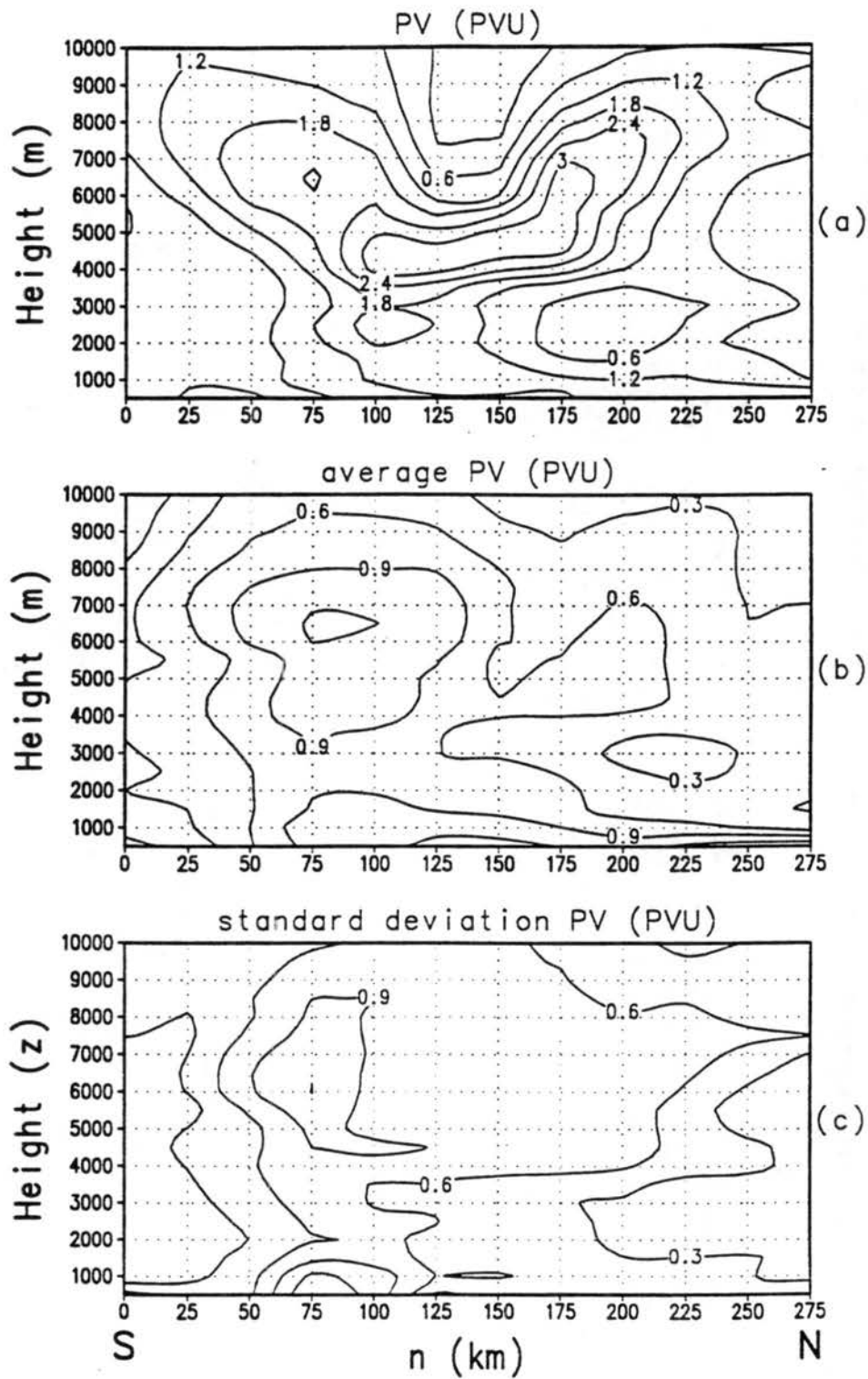


Figure 4.15: North-south sections at 24/0430 UTC, shown in Fig.(4.10d), (a) \mathcal{P} , (b) \mathcal{P} average along the MCS, (c) Standard deviation of \mathcal{P} .

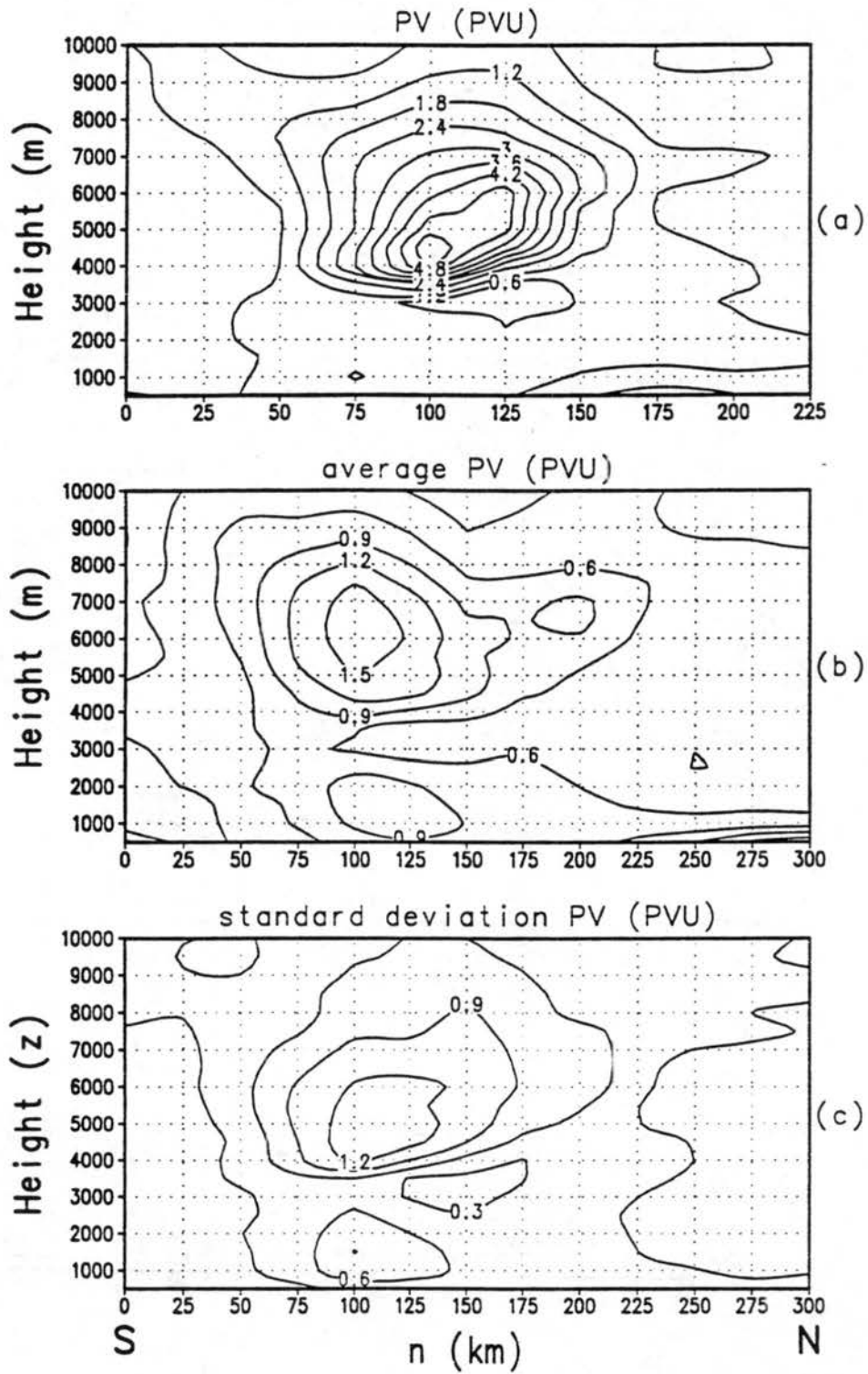


Figure 4.16: North-south sections at 24/0630 UTC, shown in Fig.(4.10e), (a) \mathcal{P} , (b) \mathcal{P} average along the MCS, (c) Standard deviation of \mathcal{P} .

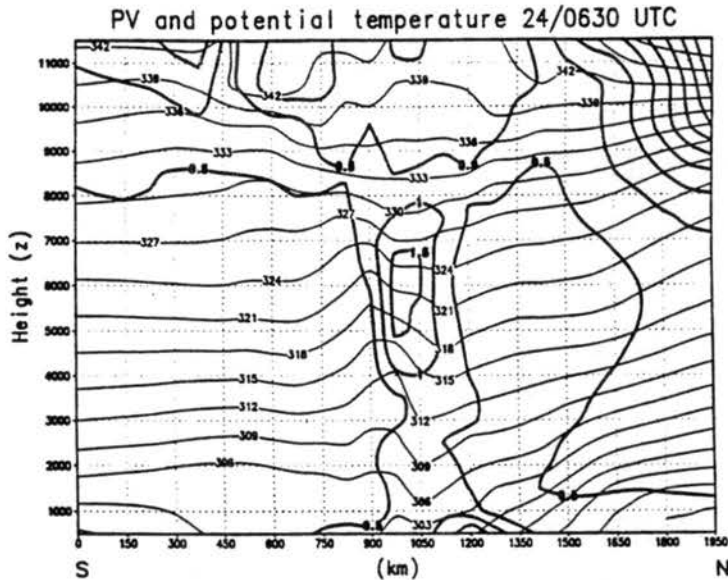


Figure 4.17: East-west section of \mathcal{P} (bold contours) and potential temperature (light quasi-horizontal contours) at 24/0630 UTC along the same section as shown in Fig.(4.9c).

4.3.5 Summary

We now summarize the evolution of \mathcal{P} during the 23–24 June MCS and compare these results to those for the 10–11 June MCS. We have noted the generally different nature of convection between these two systems. Both systems start with deep, upright convection. The 10–11 June MCS then quickly develops into a system with tilted front-to-rear updraft and rear-inflow downdraft branches. The 23–24 June system also develops a tilted rear-inflow downdraft along portions of the MCS, but updrafts remain upright and are more randomly organized. This leads to differences in the evolution of \mathcal{P} between the two MCSs. Some differences also occur due to differences in the interactions with the ambient environment between the two MCSs.

At mid levels, both systems initially display \mathcal{P} dipoles, with positive (negative) anomalies on the south (north) sides of deep convective cells. In both systems, the negative \mathcal{P} anomaly slowly disappears with time, and the MCSs become dominated by positive \mathcal{P} anomalies. As the systems go from mature to dissipating stages, the positive anomalies tend to concentrate on the downwind (relative to the ambient flow at 5 km) side of the MCS. In this sense, they resemble the results of Davis and Weisman (1994) in that the area of strongest positive \mathcal{P} is concentrated on one end of the MCS. The positive anomaly is generally weaker in the 23–24 June case.

The greatest differences between the two MCSs are found at upper levels. It appears that the mode of convection has a dramatic effect on the negative \mathcal{P} anomalies at upper levels. The 10–11 June MCS produces a strong negative anomaly when it is dominated by deep, upright convection. As the system matures, the tilted updrafts no longer produce much negative \mathcal{P} aloft, and the original negative anomaly quickly is advected away. By contrast, the 23–24 June MCS continually produces negative \mathcal{P} , due to its continuing deep, upright convection. Even though the early negative anomalies also advect away, they are continually replenished, and this results in a negative anomaly aloft over a much larger area. Thus it appears that an MCS with more randomly organized upright convection has a much greater effect on the ambient upper-level environment than an MCS with organized tilted updrafts, such as a squall line.

Blanchard (1994) studied the effects of ambient inertial instability at upper levels in the upscale growth of MCSs. Assuming that we have a stably-stratified atmosphere, regions with negative \mathcal{P} also means we have regions with inertial instability. Although no inertial instability exists aloft initially with either system studied here, it quickly develops with the onset of deep convection. In the 23–24 June MCS, regions with weak inertial stability or inertial stability exist for many hours. It is thus possible that inertial instability plays a role not only in the upscale growth of this system, as suggested by Blanchard, but in its longevity as well. The role of convectively-induced inertial instability has been discussed by Emanuel (1979) and more recently by Seman (1990).

The two MCSs develop in differing synoptic settings. The 10–11 June MCS is embedded in stronger ambient upper-level winds, thus some of the flow aloft displays cyclonic curvature as it is deflected south of the MCS. This results in a positive and negative \mathcal{P} anomalies as well at upper levels with this case. In the 23–24 June case, the stronger upper-level flow is north of the MCS, hence only weak flow occurs in the vicinity of the MCS, and we see no similar positive \mathcal{P} anomaly aloft. Another difference occurs because the ambient upper-level inverted \mathcal{P} ridge moves across the region associated with MCS in the case of 10–11 June, but remains north in the case of 23–24 June. Thus, the 10–11 June MCS appears to interact with the ambient stratospheric air, while the 23–24 June MCS has little influence on it.

The vertical \mathcal{P} structure associated with both systems starts out similar and on average remains somewhat similar on the storm scale, especially early in their lifecycle when the convective mode is similar. During the mature stages, both systems display a tilted region located toward the rear of the storm, with negative \mathcal{P} . Only the 10–11 June case has a tilted positive \mathcal{P} anomaly, associated with the tilted updraft. On average, the 10–11 June MCS has a positive anomaly which is about twice as strong as the 23–24 June case. In addition, the positive anomaly in the 23–24 June case is generally one to two kilometers higher. Standard deviations associated with both systems do not appear to show one or the other system as being more three-dimensional. Higher standard deviations associated with the 10–11 June MCS can generally be attributed to the stronger anomalies with that system. In the dissipating stages, both MCSs display a positive anomaly of similar strength, with the 10–11 June system showing a tilted structure, while the 23–24 June system remains upright.

A quantitative analysis of the above features seen in the data is given in the next chapter.

Chapter 5

PV BUDGET ANALYSIS

We begin this chapter with a closer look at the definition of \mathcal{P} . The objective of this chapter is to complete a budget study of the important terms in the evolution of \mathcal{P} associated with the two simulated MCSs. We then compare our results with those of Raymond (1992) and Davis and Weisman (1994). In the final section we examine possible processes responsible for the friction term in Eqn. (2.4).

5.1 Contributions to \mathcal{P}

Equation (2.5) can be rewritten

$$\mathcal{P} = \mathcal{P}_x + \mathcal{P}_y + \mathcal{P}_z \quad (5.1)$$

where

$$\mathcal{P}_x = \frac{1}{\rho} \left(\frac{\partial w}{\partial y} - \frac{\partial v}{\partial z} \right) \frac{\partial \theta}{\partial x}, \quad (5.2)$$

$$\mathcal{P}_y = \frac{1}{\rho} \left(\frac{\partial u}{\partial z} - \frac{\partial w}{\partial x} \right) \frac{\partial \theta}{\partial y}, \quad (5.3)$$

$$\mathcal{P}_z = \frac{1}{\rho} \left(\frac{\partial v}{\partial x} - \frac{\partial u}{\partial y} + f \right) \frac{\partial \theta}{\partial z}, \quad (5.4)$$

It is tempting to refer to $(\mathcal{P}_x, \mathcal{P}_y, \mathcal{P}_z)$ as components of \mathcal{P} . However, since \mathcal{P} is a scalar, and not a vector, this terminology would not be quite correct. Thus, we will refer to \mathcal{P}_x as the zonal contributor, \mathcal{P}_y as the meridional contribution, and \mathcal{P}_z as the vertical contribution to \mathcal{P} . The two terms, \mathcal{P}_x and \mathcal{P}_y , are also referred to as the baroclinic terms.

As discussed in Chapter 2, for large-scale, stably-stratified flows, \mathcal{P} is often approximated by \mathcal{P}_z . While this approximation can usually be justified for large-scale motions (except near very strong fronts or strong vertical shear) it is not clear whether these terms

are negligible for all mesoscale applications. This is especially true in situations with deep convection, where phenomena such as surface cold pools or strong upper-level divergent outflow may display strong horizontal gradients of θ and/or strong vertical shear. To shed some light on this question, we will examine \mathcal{P}_x , \mathcal{P}_y , and \mathcal{P}_z using Grid #2 data from the MCS simulations.

During the early stages of the 10–11 June MCS, \mathcal{P}_z is the dominant contribution to \mathcal{P} . Figure 5.1a shows a vertical profile of \mathcal{P} and the contributions at 10/2330 UTC through the center of the maximum 5 km positive anomaly. The maximum of 8 PVU at 5 km is apparent, and is due entirely to \mathcal{P}_z . Above this level, \mathcal{P}_x and \mathcal{P}_y contribute somewhat to \mathcal{P} , but these terms also tend to cancel each other. Below 3.5 km, \mathcal{P} is much smaller; a negative region at 2.5 km is due to an almost equal contribution by all terms. At the lowest level, all terms are relatively large, but combine for a very small \mathcal{P} .

A vertical profile taken through the strongest negative anomaly (Fig. 5.1b) shows a more significant difference between \mathcal{P} and \mathcal{P}_z through a deep layer, by almost as much as 0.5 PVU. This difference is due mainly to contributions by \mathcal{P}_y and accounts for approximately 20% of \mathcal{P} .

A vertical profile over the storm-scale average (Fig. 5.1c) shows that \mathcal{P} is dominated by \mathcal{P}_z at levels above 3.5 km; \mathcal{P}_x and \mathcal{P}_y are not completely negligible however. Approximation of \mathcal{P} by \mathcal{P}_z at these levels would lead to an overestimate of 20–25%. In the lowest 2 km, the approximation would fail in magnitude and sign. Here, negative \mathcal{P} is due to negative values of \mathcal{P}_x and \mathcal{P}_y .

Four hours later, the MCS attained maturity and the contributions to \mathcal{P} evolve in a fashion consistent with the evolution of the MCS. The profile through the strongest part of the positive anomaly (Fig. 5.1d) still shows the dominant contribution of \mathcal{P}_z , but now \mathcal{P}_x contributes about 25% in the mid levels. This is due, as we will see shortly, to strong horizontal vorticity associated with the front-to-rear and rear-to-front flow branches and this feature remains through the dissipating stages. Below 2.5 km, there is little contribution to \mathcal{P} .

A vertical profile through the negative \mathcal{P} anomaly at 11/0330 UTC suggests a more complicated structure than during the early stages (Fig. 5.1e). The mid-level minimum is

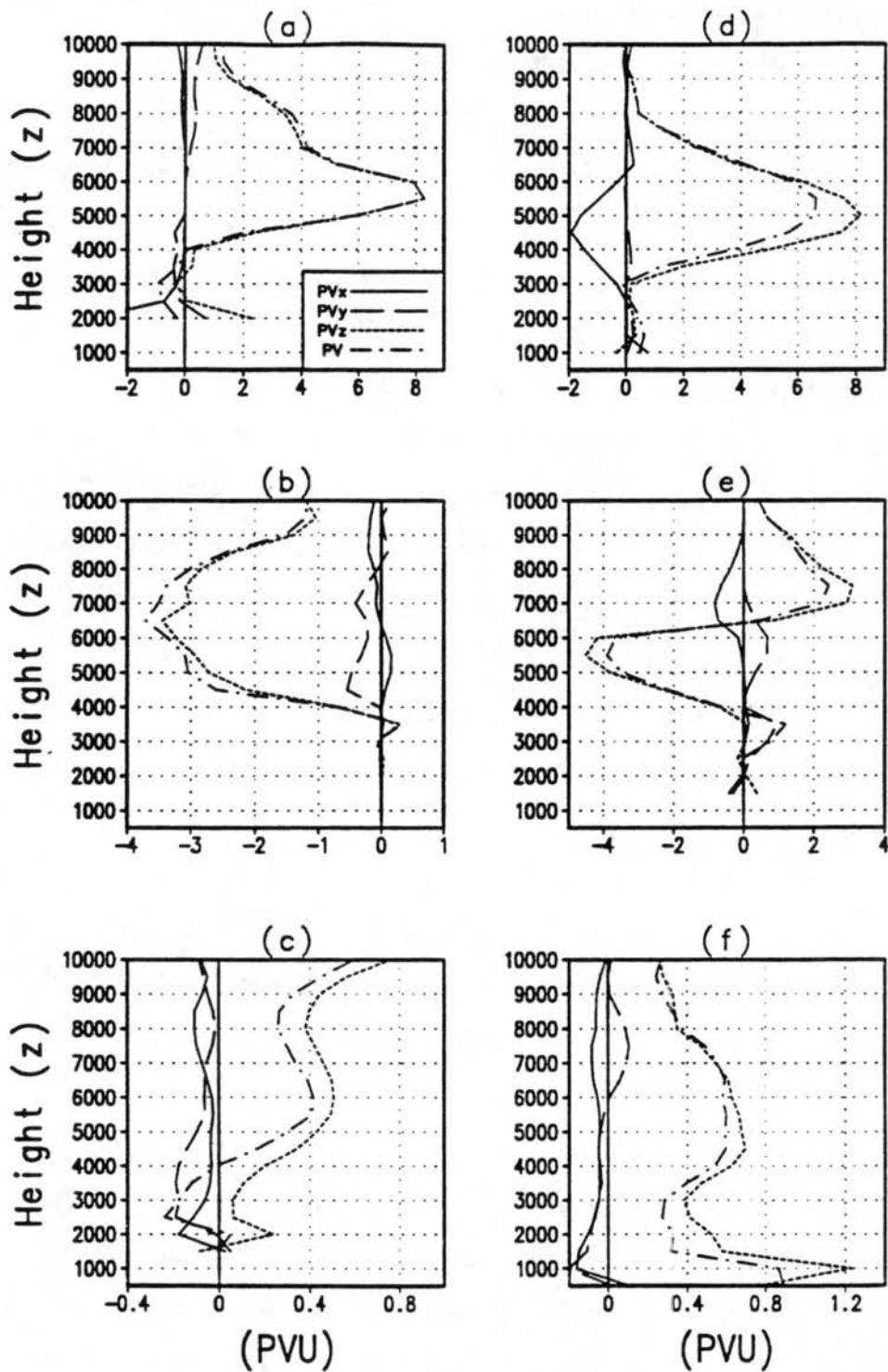


Figure 5.1: Vertical profiles of \mathcal{P} terms at 10/2330 UTC, (a) Through the positive \mathcal{P} anomaly at 5 km, (b) Through the negative \mathcal{P} anomaly at 5 km, (c) Storm-scale average. Vertical profiles of \mathcal{P} terms at 11/0330 UTC, (d) Through the positive \mathcal{P} anomaly at 5 km, (e) Through the negative \mathcal{P} anomaly at 5 km, (f) Storm-scale average.

now overlaid with a positive anomaly. This agrees with the general trend for the negative anomaly to diminish at mid levels as was seen in the previous chapter. The negative contribution by \mathcal{P}_x is elevated relative to its position in the positive anomaly. Since this vertical profile is taken rearward of that in Fig. 5.1d, this is consistent with the notion that this contribution (and also possibly that by \mathcal{P}_y) is due to horizontal vorticity developed between flow branches. The contribution by \mathcal{P}_y is again relatively large at 3.5 km, but the reason for this is not obvious however.

The storm-scale average at this time (Fig. 5.1f) is similar to the early stage of the MCS. Below 6 km, both \mathcal{P}_x and \mathcal{P}_y contribute negatively to \mathcal{P} , thus calculation using only \mathcal{P}_z would again overestimate \mathcal{P} by 10–20%. In portions of the upper levels, \mathcal{P}_x and \mathcal{P}_y tend to cancel one another.

To further investigate the structure of the various contributions to \mathcal{P} , we now consider sections across the MCS during its mature stage. The section is taken through the maximum positive anomaly and the structure of \mathcal{P} closely resembles that seen in Fig. 4.6a. The contributions by \mathcal{P}_x and \mathcal{P}_y both have maxima at the surface near the leading edge of the MCS, near $n = -70$ km (Fig. 5.2).¹ This is due to strong baroclinicity at the leading edge, seen in both horizontal potential temperature gradients and vertical shear. All three contributions (i.e., \mathcal{P}_x , \mathcal{P}_y , and \mathcal{P}_z) show a structure following the tilted flow branches. In addition, the sections of \mathcal{P}_x and \mathcal{P}_y confirm that the largest contributions (except near the surface) are associated with the tilted flow branches. There also appears to be a signature in all three contributions near the top of the leading line convection, again near $n = -70$ km. Generally, these sections confirm the conclusions from the vertical profiles. The main contribution to \mathcal{P} is from \mathcal{P}_z , although neglecting the other two contributions tends to overestimate \mathcal{P} at mid levels. Average sections of the \mathcal{P} contributions along the squall line at this time show similar features to the individual sections, although the detailed structure in \mathcal{P}_x and \mathcal{P}_y is lost.

¹We define the direction n as across the squall line while s is along the squall line.

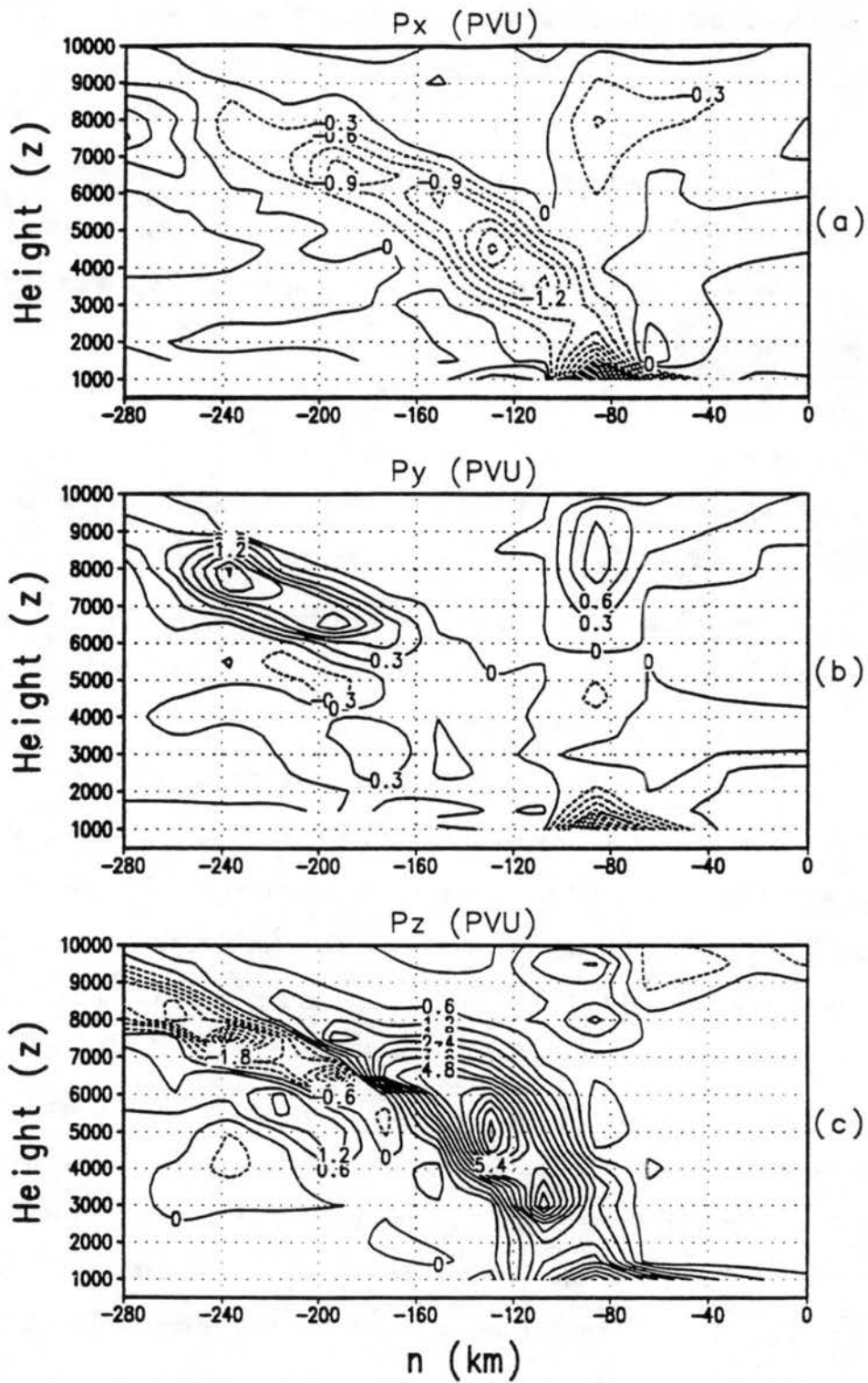


Figure 5.2: Vertical sections of the contributions to \mathcal{P} through the positive anomaly at 11/0330 UTC, (a) \mathcal{P}_x (PVU), (b) \mathcal{P}_y (PVU), (c) \mathcal{P}_z (PVU). Contour interval in (a) and (b) is 0.3 PVU, while in (c) it is 0.6 PVU

Referring again to Eqn. (5.2), we see that \mathcal{P}_z is the product of a horizontal vorticity and a horizontal potential temperature gradient. Likewise, Eqn. (5.4) is the product of vertical vorticity and the vertical potential temperature gradient. Figure (5.3a,b) shows cross sections of zonal vorticity and $\partial\theta/\partial z$ taken at the same location as Fig.(5.2a). Note that we are considering zonal (east–west) vorticity and not the projection of the horizontal vorticity parallel to the squall line. Projections of vorticity along squall line show qualitatively similar structure and will comprise the analysis in the next section. Zonal vorticity shows negative values along the boundary between the FTR and RTF flow branches, while positive values are associated with shear below the RTF branch. Values are on the order of 10^{-2} s^{-1} , which corresponds to vertical wind shear of 10 ms^{-1} over 1 km. Zonal potential temperature gradients are strongest near the surface with a magnitude of 0.2 K km^{-1} . This is a strong cold pool, but it is on the order of what was observed during this MCS. Similar magnitudes and structure are found for the components of \mathcal{P}_y (not shown).

In general, vertical vorticity (Fig. 5.3c,d) exhibits a similar structure to \mathcal{P}_z with magnitudes between 2 and $12 \times 10^{-4} \text{ s}^{-1}$. Vertical potential temperature gradients correspond roughly to an standard ambient stratification of about 4 K km^{-1} ; substantial variability exists, as well as a small area of static instability. This unstable region appears to be under the RTF branch and is possibly associated with dry, turbulent decent in a region where precipitation has evaporated.

Although the vertical vorticity is strong, i.e., several times f , the zonal vorticity is much stronger, by almost two orders of magnitude. However, $\partial\theta/\partial z$ is somewhat more than two orders of magnitude greater than $\partial\theta/\partial x$. Thus, as we have seen, total \mathcal{P} is dominated by \mathcal{P}_z , but not because vertical vorticity is greater than horizontal vorticity. These results sound a note of caution when interpreting anticipated horizontal flows associated with \mathcal{P} anomalies on the mesoscale. In regions of strong vertical shear or strong horizontal temperature gradients, anticipated vertical vorticity may be much weaker than actually associated with a given \mathcal{P} anomaly. It is also interesting to speculate on the usefulness of \mathcal{P} on smaller scales, e.g., an individual thunderstorm, in the interpretation of underlying dynamics.

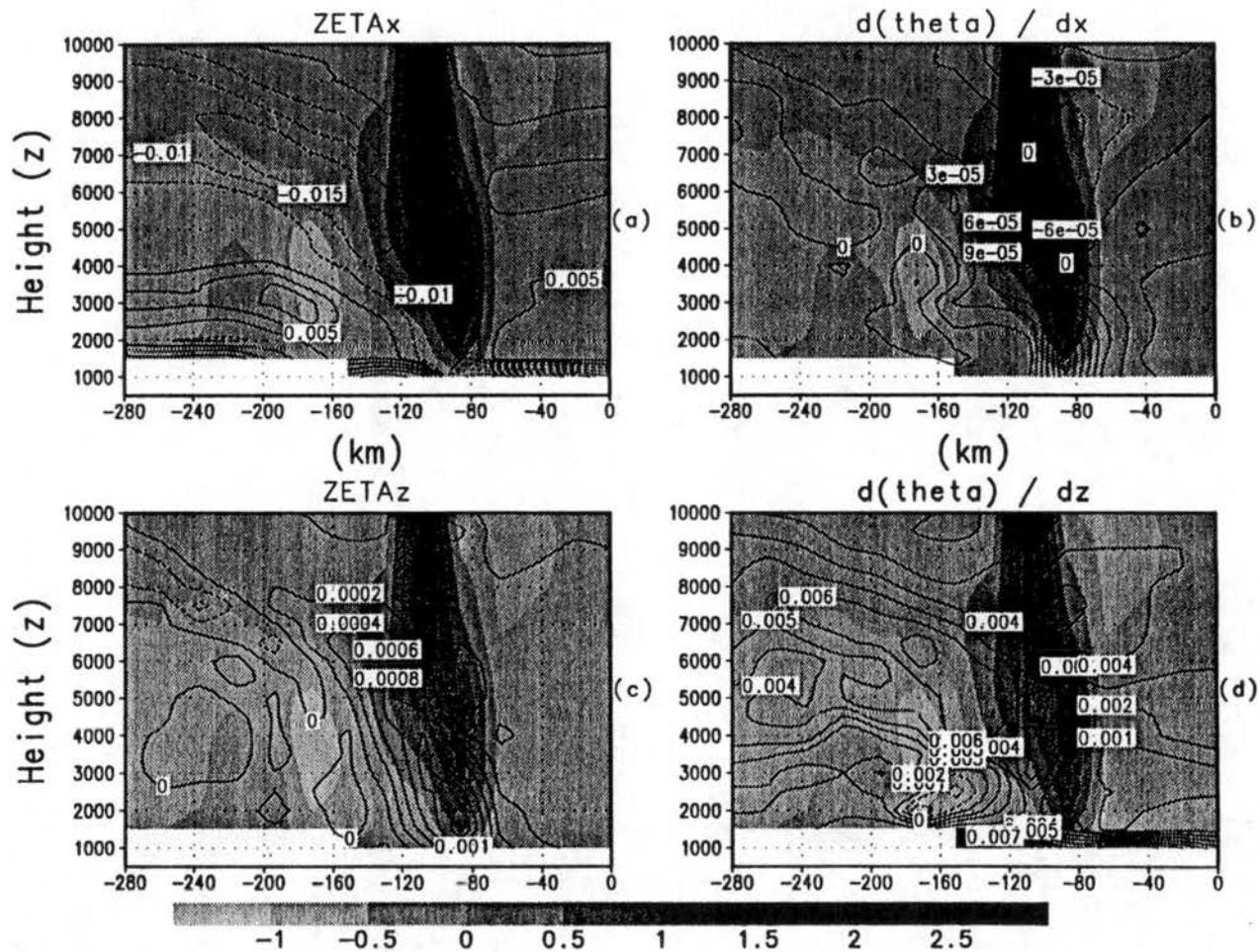


Figure 5.3: Vertical sections of vertical velocity (shaded – see color bar), in ms^{-1} and parts of \mathcal{P}_x (contours), (a) zonal vorticity and, (b) zonal potential temperature gradient. Vertical velocity and parts of \mathcal{P}_x , (c) zonal vorticity, (d) zonal potential temperature gradient.

The entire analysis described above was repeated for the 23–24 June MCS. Results were generally similar to the 10–11 June MCS. One notable difference occurred during the mature to dissipating stages of the 23–24 June case. At upper levels, \mathcal{P}_z did not show much contribution to \mathcal{P} . This is believed due to the fact that this MCS did not feature the tilted flow branches (at least not the FTR tilted branch) and thus the zonal vorticity, which in this case is actually approximately parallel to the MCS, was not as important at mid to upper levels.

Summarizing this section, we have demonstrated that for some mesoscale applications, neglecting horizontal vorticity contributions in the calculation of \mathcal{P} is marginal. By marginal, we refer to the normal meteorological scaling, where processes at least an order of magnitude smaller than the dominant ones can be neglected. Although horizontal vorticity contributions are usually smaller than the vertical vorticity contribution, they are often not very much smaller and are locally even as large. Conceptually, this can lead to problems when using the analogy between small-scale fields of vertical vorticity and \mathcal{P} , since horizontal vorticity can actually be stronger than vertical vorticity.

5.2 Diagnostic analysis of the \mathcal{P} equation

We now examine the processes responsible for the evolution of \mathcal{P} seen in Chapter 4. We will concentrate our efforts away from the lowest levels because surface friction, topography, and adiabatic layers make interpretation of \mathcal{P} difficult. Recall that at mid levels each MCS first shows a horizontal \mathcal{P} dipole (positive anomaly south, negative anomaly north) and then evolves to a system with a spatially large, dominant positive anomaly. At upper levels, a negative anomaly develops early in each MCS lifecycle. In the 10–11 June case, this area advects away, but in the 23–24 June case, negative anomalies continue to develop over the system, eventually causing a more widespread perturbation. To examine the \mathcal{P} evolution, we rewrite Eqn.(2.4) in Eulerian form

$$\frac{\delta \mathcal{P}}{\delta t} = -u \frac{\partial \mathcal{P}}{\partial x} - v \frac{\partial \mathcal{P}}{\partial y} - w \frac{\partial \mathcal{P}}{\partial z} + \mathcal{H} + RES \quad (5.5)$$

and investigate contributions by advective, diabatic, and frictional processes. We consider frictional processes² as a residual, defined simply by

$$RES = \frac{\partial \mathcal{P}}{\partial t} + u \frac{\partial \mathcal{P}}{\partial x} + v \frac{\partial \mathcal{P}}{\partial y} + w \frac{\partial \mathcal{P}}{\partial z} - \mathcal{H}. \quad (5.6)$$

Material changes to \mathcal{P} due to \mathcal{H} will be referred to simply as as diabatic effects while material changes to \mathcal{P} due to RES will be referred to simply as the residual.

The development of \mathcal{P} over the entire MCS is very complicated. To simplify the presentation, we first consider the evolution of the positive and negative anomalies at mid levels separately, then we consider the negative anomaly at upper levels. Since the structure of the anomalies vary greatly over the MCS lifetime, it is difficult to examine averages over only the positive or negative anomalies. To limit analyses to desired areas, we employ a conditional sampling technique described as follows. For the mid-level positive anomaly, we consider only those points with $\mathcal{P} > 0.5$. This sampling is performed at each level, the number of points sampled are counted and an average is then taken over the points sampled. Time series and vertical profiles of the various conditionally-sampled terms will be presented. Different sampling criteria were tested and while the magnitude varies (e.g., using a criteria of 2 PVU rather than 0.5 PVU) the overall structure of the time series or vertical profiles did not. The terms are presented with the sign that indicates their effect on the local time tendency of \mathcal{P} as in Eqn.(5.5). Thus advections are negative and by “vertical advective effects are negative”, we simply mean that $w\partial\mathcal{P}/\partial z$ is negative.

Finally, in the remaining two subsections, we compare our results with the nonlinear balance experiments of Raymond (1992) as well as the primitive equation solutions of an idealized squall line by Davis and Weisman (1994). We then summarize our findings.

5.2.1 *Evolution at mid levels*

²These processes may include molecular dissipation near the surface or Reynold’s stresses away from the surface. We will discuss this term further in Section 5.3.

Positive \mathcal{P} anomaly at mid levels – time series

As mentioned above, the conditional sampling criteria for the mid-level positive anomaly is $\mathcal{P} > 0.5$ PVU. Figure (5.4a) shows a time series of the conditionally-sampled terms averaged between 3 and 7 km over the life of the 10–11 June MCS. In a Lagrangian sense, \mathcal{H} closely follows $d\mathcal{P}/dt$; the difference is determined by RES . The diabatic effects are largest during the early and growing stages of the MCS, and decreases rapidly during the mature to dissipating stages.³ The residual becomes negative and is a minimum as the MCS grows and by the early dissipating stages, it is almost as large as the other terms. From an Eulerian perspective, the horizontal advective effect is negative throughout the MCS lifetime thus contributing negatively to the local time tendency. This indicates stronger flow upstream of the maximum \mathcal{P} anomaly than downstream. Vertical advective effects contribute to \mathcal{H} , but until the mature stage, these effects are two to four times weaker, thus these terms do not balance. In general, all terms weaken as the MCS matures and begins to dissipate.

Consideration of time series at individual levels sheds some light on the 3 to 7 km layer average. At 3 km, \mathcal{H} peaks during the growing stage, and is partially offset by vertical advection. At this level, horizontal advective effects vary in sign, while RES weakens towards the end of the system lifetime. At 5 km, the peak in \mathcal{H} occurs during the early stages. Thus the broad peak in \mathcal{H} average between 3 and 7 km occurs due to both contributions at both 3 and 5 km. Horizontal advective effects at 5 km display a fairly consistent negative contribution (-0.2 to -0.8 PVU hr^{-1}) to $\partial\mathcal{P}/\partial t$ as seen in the layer average. The residual at this level is weak until the dissipating stages. By 7 km, all terms are weaker than at lower levels but peak in the initial to growing stage. As at 3 km, vertical advective effects are somewhat larger than \mathcal{H} at this level and RES weakens with time. Thus, the general trend in the 3 to 7 km layer average is well represented by each individual level.

³Recall from Chapter 3 that the initial stage for 10–11 June occurs between 10/2200 and 11/0000 UTC, the growing stage between 11/0000 and 11/0200 UTC, the mature stage between 11/0230 and 11/0430 UTC and the dissipating stage after 11/0500 UTC. For 23–24 June, times at which the stages of development occur are similar, but are more difficult to identify.

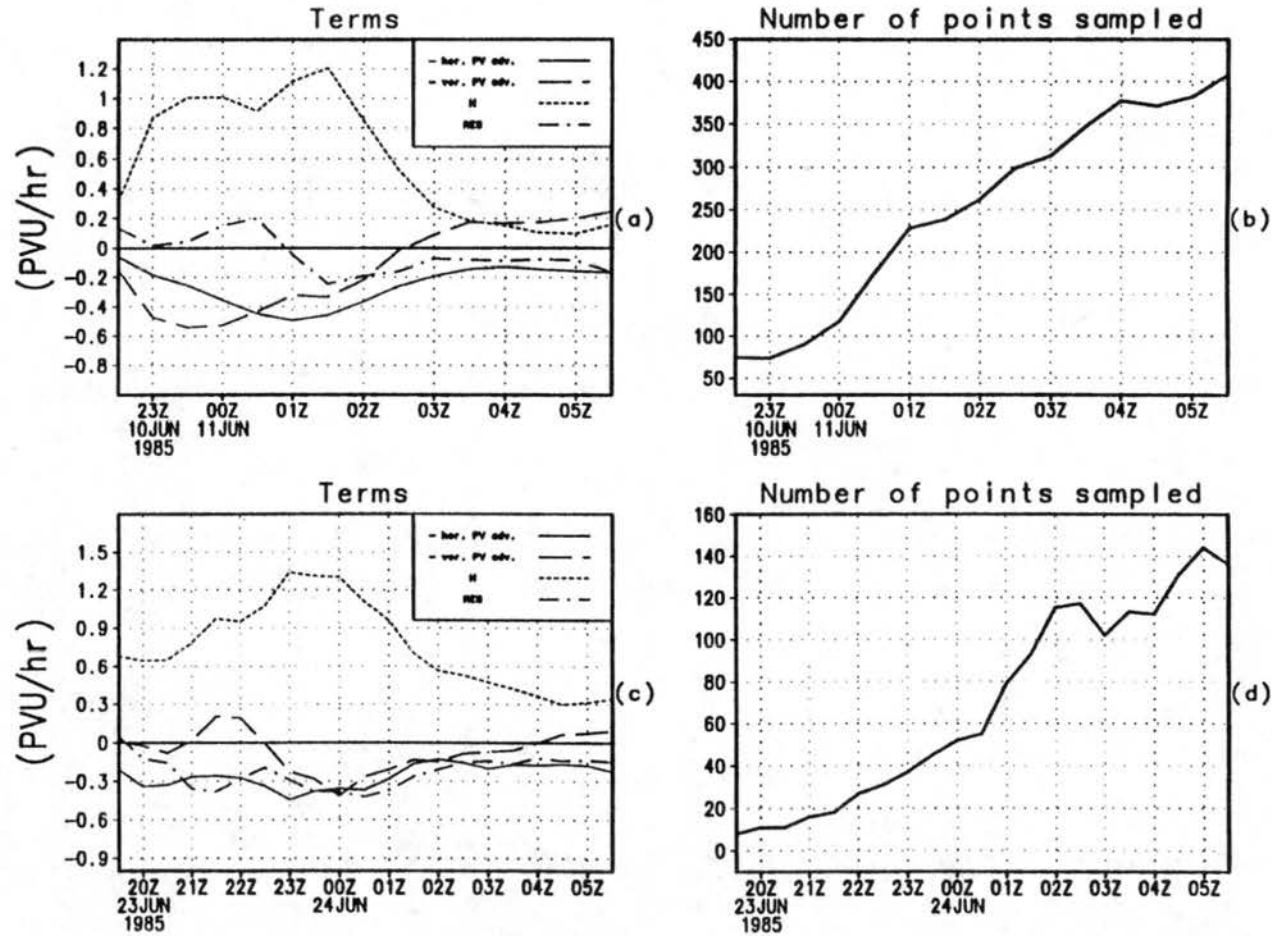


Figure 5.4: (a) Time series of conditionally-sampled \mathcal{P} equation terms, averaged between 3 and 7 km, for the 10-11 June MCS, (b) time series of the number of conditionally-sampled points. (c) Time series of conditionally-sampled \mathcal{P} equation terms, averaged between 3 and 7 km, for the 23-24 June MCS, (d) time series of the number of conditionally-sampled points.

Figure (5.4b) shows a time series of the number of points sampled at 5 km. The area covered by the positive \mathcal{P} anomaly increases from 30,000 km² to 164,000 km² or more an increase of than five times. For comparison, the state of Colorado covers approximately 274,000 km².

Convection during 23–24 June starts around 23/1930 UTC but the main MCS does not become easily discernible until 23/2230 UTC. Sampling for this case will be limited to only the main MCS which forms over southern Iowa and moves southward into Missouri (see Figs. 3.13a and 3.14a). The convection further east and west is not included in the sampling. A time series of conditionally-sampled terms (again using $\mathcal{P} > 0.5$ PVU) between 3 and 7 km again shows that \mathcal{H} again dominates vertical advective effects (Fig. 5.4c). In general the shape and magnitude of the time series are similar to the 10–11 June case, with a few differences. Unlike the previous case, RES is always negative. The vertical advective effects change sign during the MCS evolution (from negative to positive) but this occurs about 2 hours later than during the 10–11 June MCS. Since the average positive \mathcal{P} anomaly has not changed position vertically, this sign change indicates a slight weakening of the anomaly. Horizontal advective effects remain negative as in the 10–11 June case but are somewhat weaker.

Individual levels for the 23–24 June case show that at 3 km we see no strong peak in the time series as was present in the previous case. By 5 km however, more structure is evident. Before the main MCS becomes well defined (i.e., before 23/2230 UTC), \mathcal{H} is negative and vertical advective effects are positive. Since $w > 0$ here, $\partial\mathcal{P}/\partial z < 0$ and the positive anomaly is centered in the lower levels below 5 km. This would agree with the \mathcal{P} distribution predicted by Hertenstein and Schubert (1991) during the early convective stages of an MCS and as we will see in the next section, agrees with the positive \mathcal{H} seen at 3 km. By 7 km, \mathcal{H} is large and negative during the growing and mature stages reflecting the mid-level \mathcal{P} maximum which remains much better defined in this system. Unlike the 10–11 June case, RES remains positive until the end of the mature stage. Horizontal advective effects at this level remain small throughout, as in the previous case. Thus, in general, for the 23–24 June MCS stronger material changes to \mathcal{P} occur between 5 to 7 km, while for the 10–11 June MCS more occurs between 3 to 5 km.

The number of points sampled (Fig. 5.4d) increases rapidly during the growing stage (i.e., 11/0130 UTC) but shows more oscillation after the mature stage than in the 10–11 June case. This is most likely a reflection of the more randomly organized, deep upright convection that continues in this case, as noted in the previous chapter. The total area occupied by the positive \mathcal{P} anomaly is about half that of the 10–11 June case, or about 87,500 km². Keep in mind that we are only considering the MCS that moves from Iowa southward into Missouri.

Positive \mathcal{P} anomaly at mid levels – vertical structure

Vertical profiles through the conditionally-sampled \mathcal{P} (> 0.5 PVU as before) reveal some interesting structures. At 10/2330 UTC, \mathcal{H} shows a sharp maximum at 5 km, while vertical advective effects show a strong minimum (Fig. 5.5a). Vertical advective effects do not entirely balance \mathcal{H} , the latter being stronger by about 0.7 PVU hr⁻¹. Above 6 km, profiles of both terms change sign, although both are much weaker. We should note here that if these were actual *vertical* profiles through one point, the terms would be larger at upper levels since a negative anomaly exists aloft. However, since this is a vertical profile of *conditionally-sampled* terms, the terms sampled likely do not lie directly above the maximum \mathcal{P} anomaly. Figure(5.6a) shows profiles of \mathcal{H} at 10/2330 UTC, as well as the three contributions (refer to Eq. 2.10). At this time \mathcal{H}_z dominates both \mathcal{H}_x and \mathcal{H}_y .⁴

Vertical profiles also reveal differences between the 23–24 June and 10–11 June MCS during the first half of the MCS lifecycle. The initial stage, at 23/2330 UTC, shows \mathcal{H} with a deeper, although weaker, contribution (Fig. 5.8a). A double maximum is seen, with peaks at 4 and 6 km, reflecting the double maximum seen in \mathcal{P} in Fig. 4.12. This is likely an indication of a transition from the low-level positive anomaly very early in the development to a mid-level positive anomaly. Both \mathcal{H} and vertical advective effects change sign and weaken above 6.5 km. As in the previous case, \mathcal{H}_z is the main contribution to \mathcal{H} ; \mathcal{H}_x is weaker whereas \mathcal{H}_y shows some structure at this time in mid levels (Fig. 5.9a).

⁴ \mathcal{H}_z is the first term in brackets in Eqn. (2.10), while \mathcal{H}_y is the second term.

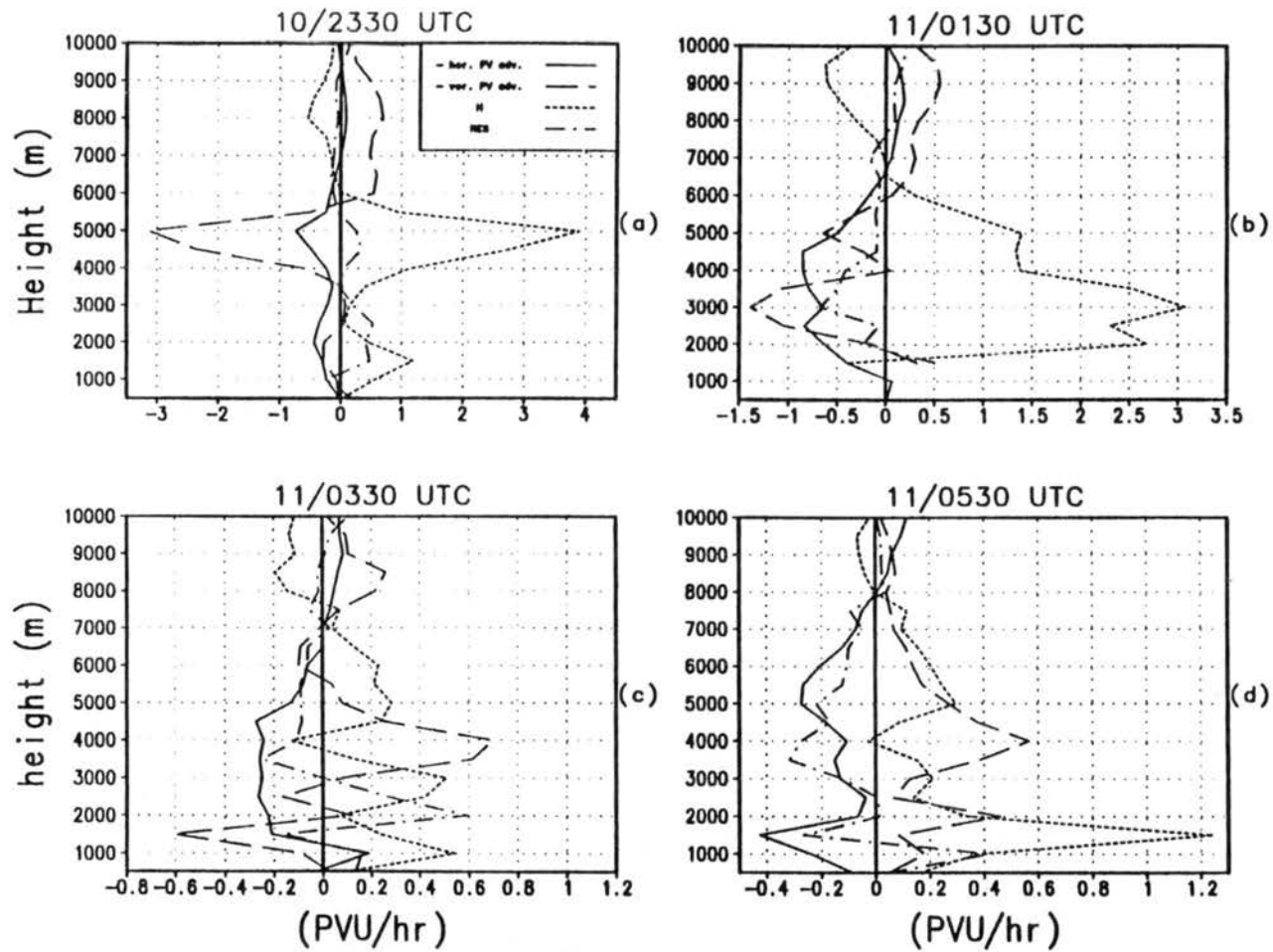


Figure 5.5: Vertical profile of the \mathcal{P} equation terms for conditional sampling criteria $\mathcal{P} > 0.5$ at (a) 10/2330 UTC, (b) 11/0130 UTC, (c) 11/0330 UTC, (d) 11/0530 UTC. Note the change in magnitude range of the abscissas.

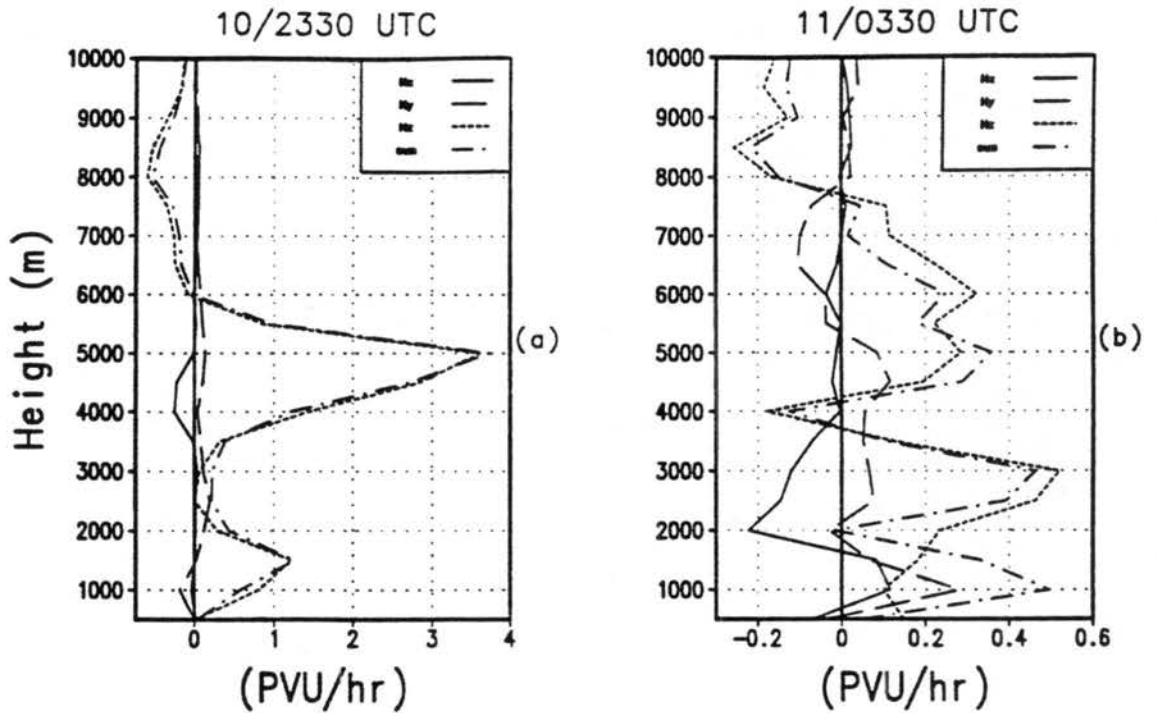


Figure 5.6: Vertical profiles of contributions to \mathcal{H} at (a) 10/2330 UTC, (b) 11/0330 UTC.

As we saw in Chapter 4, one of the distinctive features at mid levels is the north (south) negative (positive) \mathcal{P} dipole during the initial and growing stages of both MCSs. This pattern resembles that predicted by Raymond (1992). Davis and Weisman (1994) also predict a \mathcal{P} dipole but of the opposite sense and at lower levels. We return to a comparison with these two studies in Section 5.2.3 and 5.2.4. Here we look further into the formation of the positive anomaly which forms during the initial stages.

The positive \mathcal{P} anomaly at mid levels forms in conjunction with the strongest vertical velocities found along the south end of the 10–11 June convective line. At 10/2230 UTC this N–S oriented line is about 220 km in length and expands to 300 km by 10/2330 UTC (Fig. 5.7a). Between these times, a peak in \mathcal{H} occurs at 5 km and increases from 2 to 4 PVU hr^{-1} . In addition, the magnitude of \mathcal{H} is greater than that of advective effects, by 0.3 PVU hr^{-1} at 10/2230 UTC, increasing to 0.8 PVU hr^{-1} by 10/2330 UTC (Fig 5.6a). During this period, \mathcal{H}_z dominates \mathcal{H} at all levels. Since $(\zeta + f) > 0$ in the positive \mathcal{P} anomaly, $\partial Q/\partial z > 0$ as well, consistent with the heating profile during this stage.

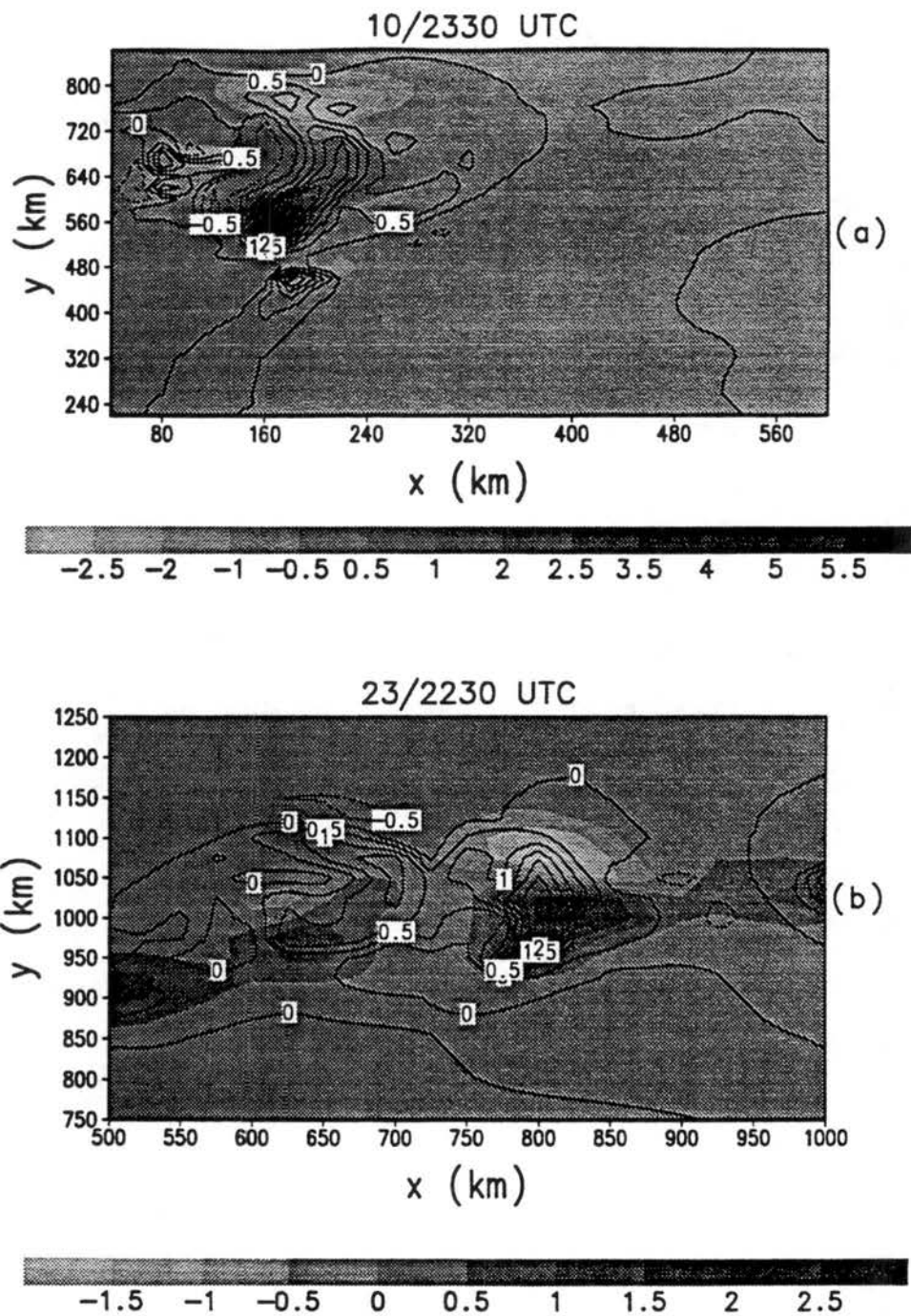


Figure 5.7: Vertical velocity (contoured) and \mathcal{P} (shaded – see color bar) (a) 10/2330 UTC, (b) 23/2230 UTC.

A similar situation occurs for the 23–24 June case, with the positive \mathcal{P} anomaly associated with the strongest vertical velocities along the south end of a 175 km long N–S oriented convective line (Fig. 5.7b). Unlike the previous case, at 23/2230 UTC, \mathcal{H} shows two positive peaks at 4 and 6 km (1.5 and 3.5 PVU hr⁻¹). A minimum of - 1.7 PVU hr⁻¹ is noted at 5 km. An hour later, \mathcal{H} at 23/2330 UTC (Fig. 5.8a) is positive through a deep layer from 0.5 to 6.5 km with a maximum of about 2 PVU hr⁻¹. The magnitude of \mathcal{H} again exceeds vertical advective effects by about 1 PVU hr⁻¹. Also as before, \mathcal{H}_z dominates \mathcal{H} at 23/2330 UTC, but unlike the 10–11 June case, \mathcal{H}_y accounts for about 20% of the total between 5 and 6 km. An hour later, at 24/0030 UTC (not shown) \mathcal{H}_z absolutely dominates the profile of \mathcal{H} .

Thus, it appears that the positive, mid-level \mathcal{P} anomaly is due mainly to $\mathcal{H}_z > 0$, with some early contribution by \mathcal{H}_y . In terms of the flux form of the \mathcal{P} equation, this is the non-advective flux divergence due to diabatic effects. The profiles of \mathcal{H} are consistent with cross sections of \mathcal{P} from Chapter 4. For the 10–11 June MCS, the sharp \mathcal{H} maximum at 5 km leads to a strong mid-level \mathcal{P} anomaly with strong vertical gradients (cf. Fig. 4.4). By comparison, for the 23–24 June MCS, the weaker, broader double \mathcal{H} maximum leads to a \mathcal{P} maximum with similar vertical structure (cf. Fig. 4.12). This scenario is also consistent with a vorticity viewpoint, discussed further in Section 5.2.4.

By 11/0130 UTC, the maximum in \mathcal{H} is lower and somewhat weaker (Fig. 5.5b). In addition, \mathcal{H} is now substantially stronger than vertical advective effects, by as much as 1.5 PVU hr⁻¹. The main contribution to the budget by RES is negative (-0.6 PVU hr⁻¹) at 3 km. Profiles of the contributions to \mathcal{H} is similar to the previous time, with \mathcal{H}_z dominating (not shown).

In the growing stage at 24/0230 UTC (Fig. 5.8b), the vertical profile is similar to that of three hours previous, with a weaker but still vertically deep layer of $\mathcal{H} > 0$. Diabatic effects are dominated by \mathcal{H}_z and remain almost twice as large as vertical advection (Fig. 5.9b). The residual provides a negative contribution on the order of vertical advective effects from the surface to 6.5 km.

A closer look at events leading up to the growing stage shows that after 10/2330 UTC, the 300 km N–S convective line moves at about 17 ms⁻¹ for an hour. The horizontal \mathcal{P}

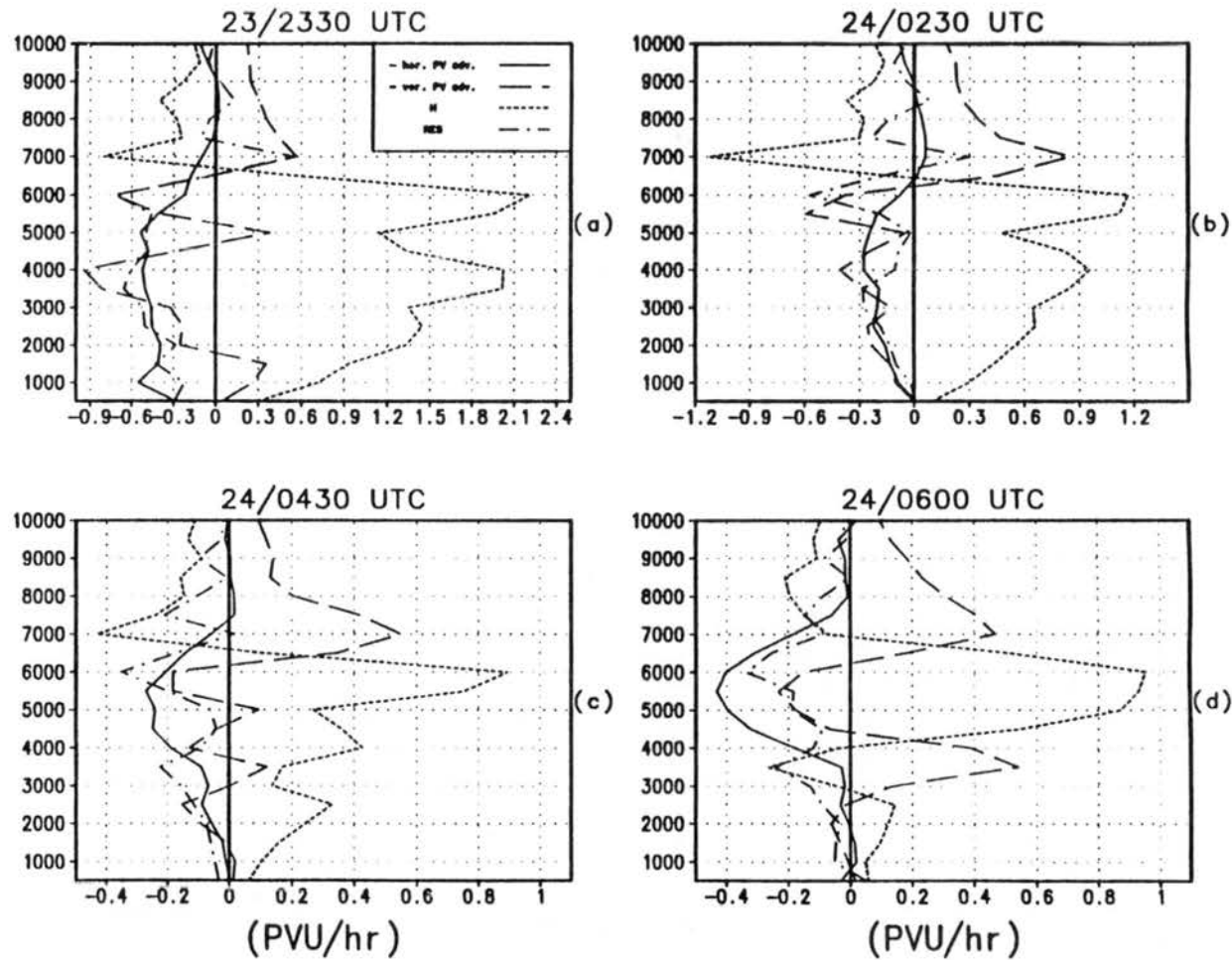


Figure 5.8: Vertical profile of the \mathcal{P} terms at (a) 23/2330 UTC, (b) 24/0230 UTC, (c) 24/0430 UTC, (d) 24/0600 UTC. Note change in the range of magnitude on the abscissas.

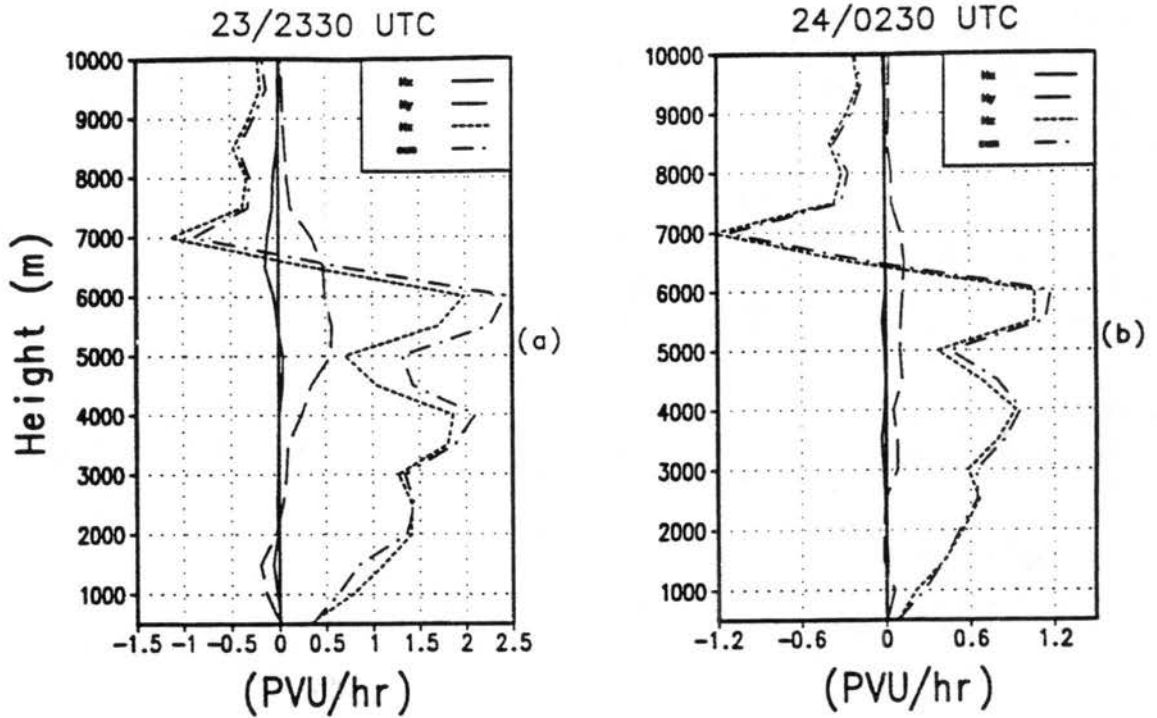


Figure 5.9: Vertical profiles of contributions to \mathcal{H} at (a) 23/2330 UTC, (b) 24/0230 UTC.

dipole persists during this time. In the next half hour, a new line forms at an angle from the N end of the original line. By 11/0130 UTC, this new line has explosively developed, while the original line has merely changed orientation giving just one 560 km long convective line oriented SW-NE. The observed “kink” in \mathcal{P} at this time (Fig. 4.2b) is located at the north end of the initial line.

Figure (5.10a) shows \mathcal{P} and vertical velocity at 5 km and 11/0130 UTC over a portion of the Grid #2 domain centered over the MCS at this time. Generally we have higher- \mathcal{P} air aligned along positive vertical velocities, but not directly coincident as before. This can be seen in a N-S section of vertical velocities and \mathcal{P} taken through the “kink” in the convective line (Fig. 5.12a). Two \mathcal{P} maximums exist, one located at the “kink” in the line, while the other is located with strong updrafts at the NE end of the line. What processes lead to the formation of these anomalies? Vertical profiles were taken through both positive \mathcal{P} anomalies and were found to be very much like those through the conditionally-sampled profiles (Fig. 5.5b). Contributions to \mathcal{H} along the new profile shows that \mathcal{H}_z dominates; the horizontal contributions are somewhat stronger at the NE

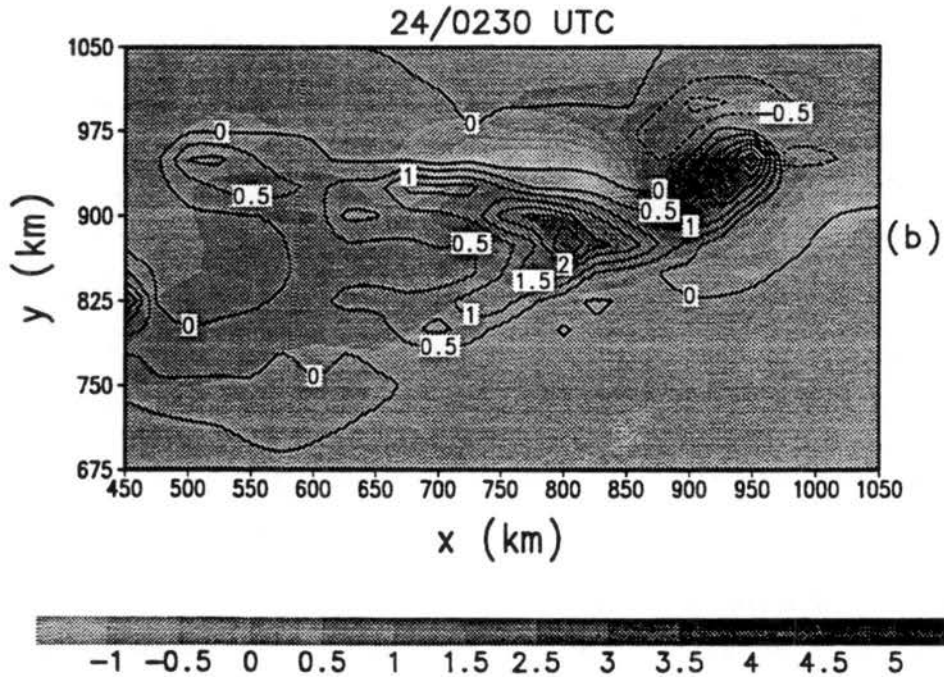
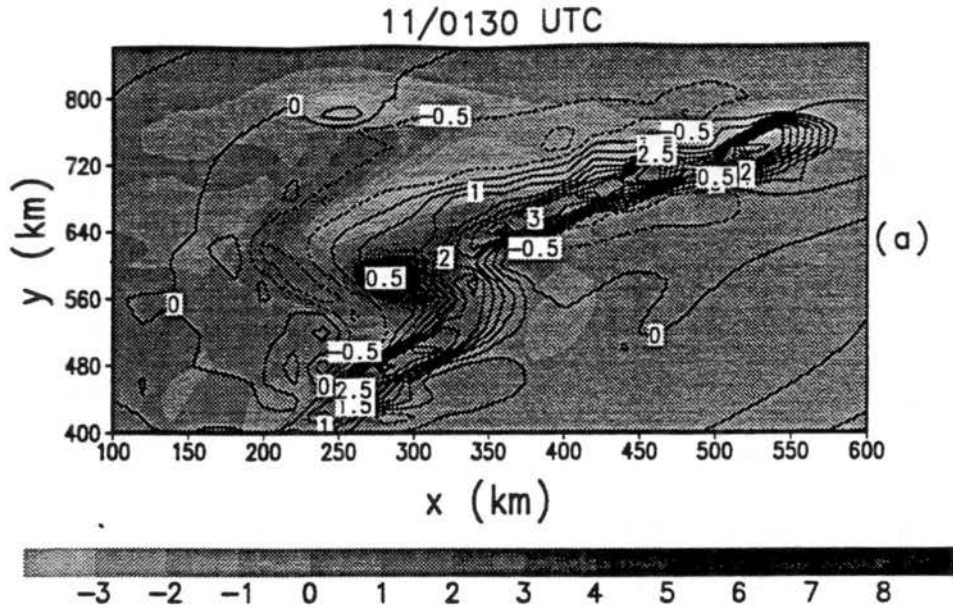


Figure 5.10: Horizontal sections of P (shaded – see color bar) and vertical velocities (contours) at 5 km and (a) 11/0130 UTC, (b) 24/0230 UTC.

\mathcal{P} maximum. Thus it appears that the positive \mathcal{P} forms for the same reasons as during the initial stage, but now the anomaly has expanded. The displacement between the vertical velocity and \mathcal{P} maxima indicate that perhaps after the anomaly forms the storm propagates SE, while the anomaly loses its collocation with the convective line.

After the initial stage of the 23–24 June MCS, the N–S oriented line rapidly changes to an E–W oriented line by 24/0030 UTC. The vertical velocities and \mathcal{P} remain collocated, and this trend continues through 24/0130 UTC. An hour later, at 24/0230 UTC, the E–W area of convection has expanded to about 450 km in length and still shows that \mathcal{P} maxima remain close to regions of maximum vertical velocities (Fig. 5.10b). The time taken for this entire transition is about twice as long as for the 10–11 June case.

Vertical profiles of the terms in the \mathcal{P} equation and contributions to \mathcal{H} were taken through the eastern positive anomaly. These profiles are again very similar to Figs. (5.8b) and (5.9b) and are therefore not shown. Profiles show that positive \mathcal{H} dominates the positive \mathcal{P} anomaly at this time and as during the initial stage, diabatic effects are dominated by \mathcal{H}_z . This also indicates that the conditionally-sampled profiles are representative of individual areas. So although the systems have expanded by the growing stage, the mechanisms behind the formation (or maintenance) of the positive \mathcal{P} anomaly has not changed.

During the mature stage of the 10–11 June MCS, i.e., at 11/0330 UTC, all terms are weaker (Fig. 5.5c), with no well-defined peaks in any of the terms as seen earlier. Contributions to \mathcal{H} (Fig. 5.6b) show that \mathcal{H}_z has weakened, while \mathcal{H}_x and \mathcal{H}_y are relatively stronger, especially in low to mid levels. This may be due to strong tilted flow branches. As we will see in Section 5.2.4, the terms \mathcal{H}_x and \mathcal{H}_y contain vorticity tilting thought to be important in vertical vorticity production in MCSs.

The mature stage of the 23–24 June MCS shows that all the terms have weakened considerably as well and begin to lose structure as in the 10–11 June case (Fig. 5.8c). However, more structure remains in \mathcal{H} compared to the 10–11 June MCS and a positive \mathcal{H} maximum still exists at 6 km. Unlike the mature stage of the 10–11 June MCS, \mathcal{H}_x and \mathcal{H}_y do not show much structure at this time (or, for that matter at any time during this MCS) and are much smaller than \mathcal{H}_z .

The relative positions of maxima in vertical velocity and \mathcal{P} have changed by the mature stage of the 10–11 June MCS. The \mathcal{P} maximum is now behind the convective line (i.e., towards the NW). However, for the 23–24 June case, vertical velocity and \mathcal{P} maxima are still fairly close together. This difference between the systems occurs, as was seen in Chapter 4, because a more tilted FTR updraft forms in the 10–11 June case while updrafts in the 23–24 June case remain more upright (Figs. 4.6b and 4.15b). Comparing Figs. (5.5c) and (5.8c) we see that \mathcal{H} remains stronger and better defined for the 23–24 June case. In addition, the horizontal vorticity contributions, i.e., \mathcal{H}_x and \mathcal{H}_y remain small for the 23–24 June MCS, while they become more important for the 10–11 June case. It appears that the positive \mathcal{P} anomaly is transported towards the back of the system by the FTR branch for the 10–11 June case, as qualitatively seen in Chapter 4. Little evidence for this is seen for the 23–24 June case. This difference is not noticeable in the profiles of the horizontal advective effects. As recently noted by Alexander and Cotton (1994) and also Cifelli (1995), isolating processes internal to MCSs is a difficult task; isolating effects along one of the flow branches would be even more difficult.

By 11/0530 UTC (Fig. 5.5d), the system has started to dissipate stage. The residual is negative and as large or larger than \mathcal{H} . It is possible that turbulence associated with shear between flow branches may be responsible for the magnitude of RES at this time and acts to weaken positive \mathcal{P} . Also at this time horizontal advective effects are relatively strong and negative while vertical advective effects are also strong but positive. Contributions to \mathcal{H} are again dominated by \mathcal{H}_z , as in the early and growing stages.

During the early dissipating stages of the 23–24 June MCS, at 24/0600 UTC, \mathcal{H} still shows a peak around 5–6 km, reflecting some deep convection which is still active (Fig. 5.8d). Thus, unlike the 10–11 June case, while the system as a whole begins to dissipate, locally it remains active, making “stages” of development more difficult to define with the 23–24 June case, as we saw in Chapter 3. Vertical advective effects are generally much weaker than \mathcal{H} , except where the former is positive. In addition, both horizontal advective effects and RES are somewhat stronger than the 10–11 June MCS at this stage.

Thus it appears that the mid-level \mathcal{P} anomaly during the 10–11 June is due mostly to \mathcal{H} and specifically \mathcal{H}_z during the initial and growing stages of the MCS. Other terms, while important at some times and levels, tend to be secondary.

The evolution of \mathcal{P} during the 23–24 June MCS is much like 10–11 June system in that the main contribution to the positive \mathcal{P} anomaly at mid levels is \mathcal{H} and specifically \mathcal{H}_z , especially in the initial and growing stages. Details between the two systems vary, reflecting the difference in convective organization and mode of convection (i.e., slanted vs. deep upright updrafts during the mature and dissipating stages). In the 23–24 June case, the contribution to the budget by RES is fairly steady, thus this term may not be due to processes, such as the shear between the flow branches, during one particular stage of the MCS, at least for the evolution of the positive anomaly. On the other hand, since the FTR flow branch with this system does not tilt much, shear between the flow branches would likely be weaker.

Negative \mathcal{P} anomaly at mid levels – time series

At mid levels during both simulations, a negative \mathcal{P} anomaly also forms. This anomaly expands with the system during the growing stage and then appears to dissipate. We now examine the evolution of the negative anomaly by considering conditionally-sampled regions with $\mathcal{P} < -0.5$ PVU.

Figure (5.11a) shows the 3-to-7 km layer average time series for 10–11 June using the conditional sampling criteria $\mathcal{P} < -0.5$ PVU. Throughout the MCS lifecycle, \mathcal{H} is negative, with a minimum during the growing stage, but decreasing in magnitude as the MCS matures and then dissipates. Horizontal advective effects are positive until the mature stage (11/0330 UTC) when they become weakly negative. Vertical advective effects supply a positive tendency as well for most of the MCS lifecycle and are never strong enough to offset \mathcal{H} . The unexpected term in this time series is RES , which provides the largest positive tendency from the growing through the mature stages before sharply decreasing as the system begins to dissipate. The number of points sampled at 5 km increases until the growing stage and then sharply drops off (Fig. 5.11b). The number of negative points sampled only reaches a maximum of 20% of the positive points sampled

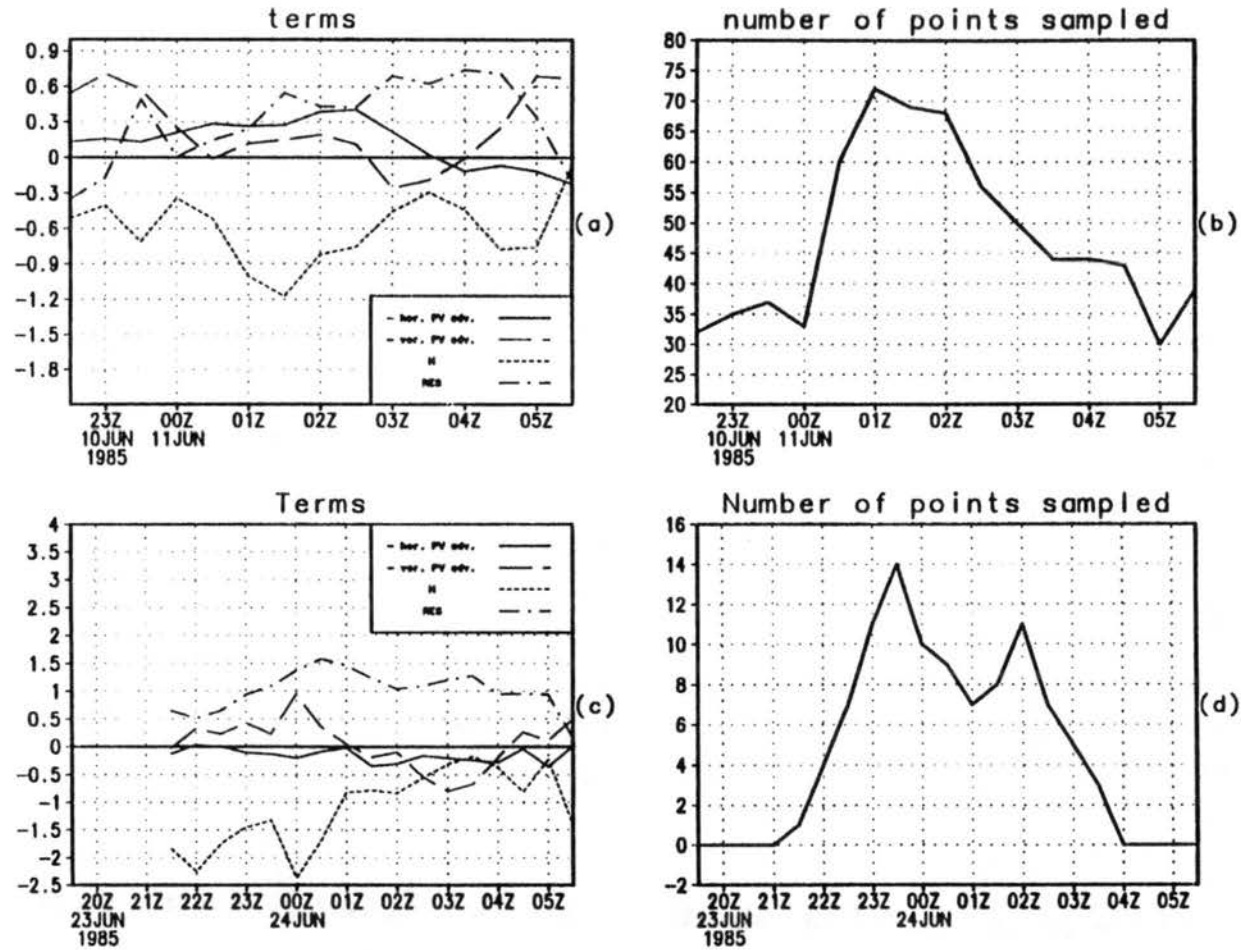


Figure 5.11: (a) Time series of terms ($\mathcal{P} < -0.5$ PVU) for the 10–11 June case, (b) time series of the number of points sampled. (c) Time series of terms ($\mathcal{P} < -0.5$ PVU) for the 23–24 June case, (d) time series of the number of points sampled.

and is the case even when relaxing the sampling criteria and considering points with $\mathcal{P} < 0$ PVU. This would indicate that the poorly understood residual is largely responsible for the deterioration of the negative anomaly.

The conditionally-sampled negative anomaly (same criteria) for the 23–24 June MCS shows a similar trend (Fig. 5.11c). Note that the time series of the 3–to–7 km layer average begins at 23/2130 UTC; no points met the sampling criteria before this time. In general, far fewer points met the sampling criteria than for the 10–11 June case (Fig. 5.11d). As before, \mathcal{H} is negative early in the MCS lifecycle, with a minimum near the growing stage, and a decrease in magnitude thereafter. Unlike the 10–11 June case, at about the time that \mathcal{H} is decreasing, advective effects also become negative, thus adding to the tendency due to \mathcal{H} . However, RES is once again positive and remains stronger than the 10–11 June case. Hence, it appears that processes associated with the residual may be even more important for the deterioration of the negative anomaly than in the 10–11 June case.

Negative \mathcal{P} anomaly at mid levels – vertical structure

A vertical profile of the \mathcal{P} equation terms at 10/2330 UTC shows that \mathcal{H} is negative above 4 km (Fig. 5.14a). The advective terms are weaker and mostly positive above this level. Note that by this time that RES changes sign and yields only a small positive contribution. Contributions to \mathcal{H} at 10/2330 UTC (Fig. 5.14b) show much more complex structure than for the positive \mathcal{P} anomaly at this time. Small contributions by \mathcal{H}_x are found but \mathcal{H}_y and \mathcal{H}_z have similar magnitudes and are both negative through a deep tropospheric layer. This indicates that different processes are at work in the formation of the positive vs. negative \mathcal{P} anomalies.

Vertical profiles at 23/2230 UTC show that \mathcal{H} is negative with a double minimum at 4 and 6.5 km, while other terms are weak and mostly positive as in the 10–11 June case (Fig. 5.15a). Also as in the previous case, contributions to \mathcal{H} dominated by \mathcal{H}_y (Fig. 5.16).

We previously examined the formation of the mid-level positive \mathcal{P} anomaly; we now examine the formation of the negative part of the horizontal \mathcal{P} dipole in this layer. For both systems, the negative anomaly is associated with weaker but still positive vertical

velocities along the northern end of the N–S oriented convective lines (Figs. 5.7a and 5.7b). Unlike the positive \mathcal{P} anomaly, which continues to strengthen throughout the initial to growing stages, the negative anomaly first strengthens, then weakens during this period.

At 10/2230 UTC, an hour earlier than Fig. (5.14b), \mathcal{H} is negative above 4 km, with a minimum of -1.6 PVU hr^{-1} at 6 km. The minimum increases in magnitude 30 minutes later to -1.8 PVU hr^{-1} and then decreases in magnitude to -1.1 PVU hr^{-1} by 10/2330 UTC. At all times, the magnitude of \mathcal{H} is weaker than for the positive anomaly. Examination of contributions to \mathcal{H} shows differences from the profiles seen for the positive \mathcal{P} anomaly. At all three times, \mathcal{H}_x is weak. However, \mathcal{H}_y and \mathcal{H}_z are of similar magnitude and both are negative above about 4 km.

A similar situation is seen during the initial stages of the 23–24 June MCS, with the exception that \mathcal{H}_y is actually somewhat stronger than \mathcal{H}_z . Thus it appears that as was the case for the positive \mathcal{P} anomaly, the negative mid-level anomaly forms similarly for both MCSs. However, the mechanisms for the formation of the positive anomaly differ from those for the negative anomaly. The latter anomaly forms due to negative \mathcal{H} from almost equal contributions by \mathcal{H}_y and \mathcal{H}_z . Since vertical velocities are positive in the vicinity of the negative \mathcal{P} anomaly, negative \mathcal{H}_z indicates negative vorticity, as seen in Figs.(4.2) and (4.10). The dominant term in \mathcal{H}_y is

$$\frac{\partial u}{\partial z} \frac{\partial Q}{\partial y}.$$

Since the vertical shear of the zonal wind is positive, $\partial Q/\partial y$ is negative, consistent with the heating gradient at the north end of the convective line. Another way of saying this is that the negative \mathcal{P} anomaly forms because of negative horizontal and vertical non-advective flux divergence due to diabatic heating. As we will see in section 5.2.4, \mathcal{H}_y contains vorticity tilting, thus the formation of the negative anomaly can also be explained using vorticity concepts.

For the growing stage of the 10–11 June MCS, we will consider only one negative \mathcal{P} anomaly, that just north of the “kink” seen in Fig. (5.10a). The processes associated with this anomaly are much more complex than the processes involved in the positive anomaly. From Fig. (5.12a) we see that the negative \mathcal{P} anomaly is located at the vertical

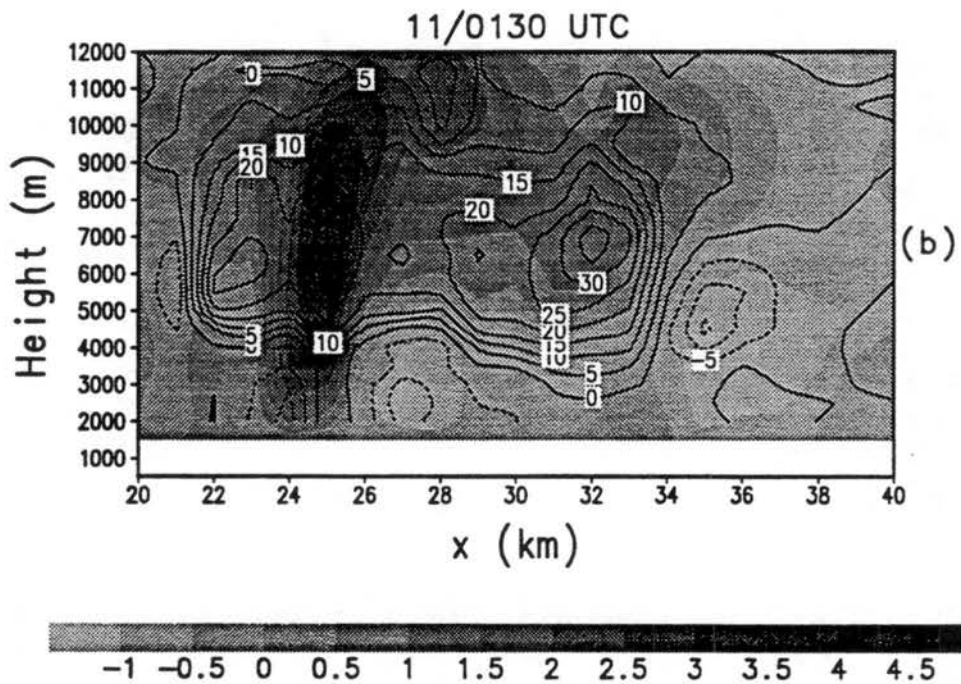
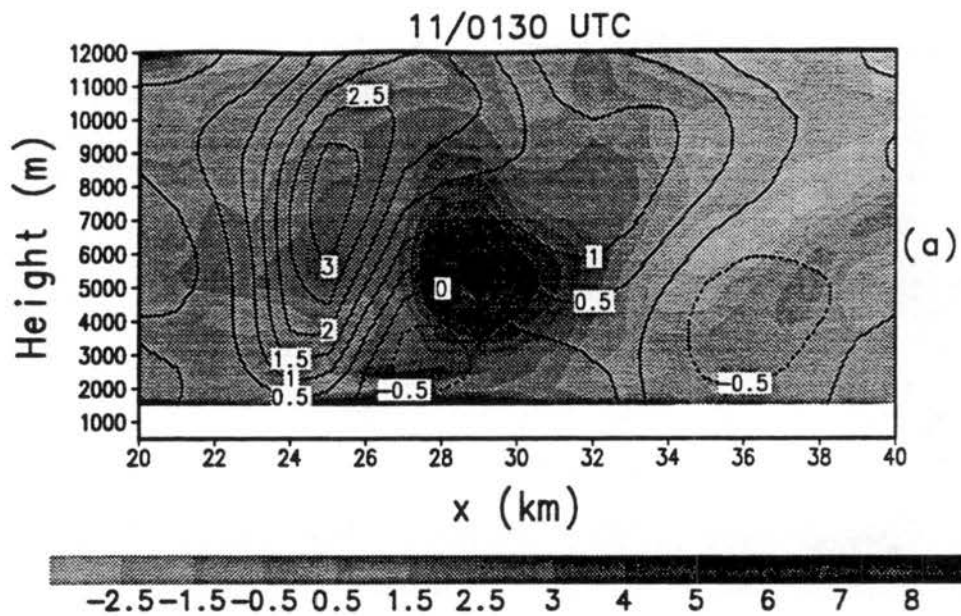


Figure 5.12: Vertical N-S sections at 11/0130 UTC through the “kink” in the convective line for (a) P (shaded – see color bar) and vertical velocities (contours), and (b) vertical velocities (shaded) and material change to potential temperature Q .

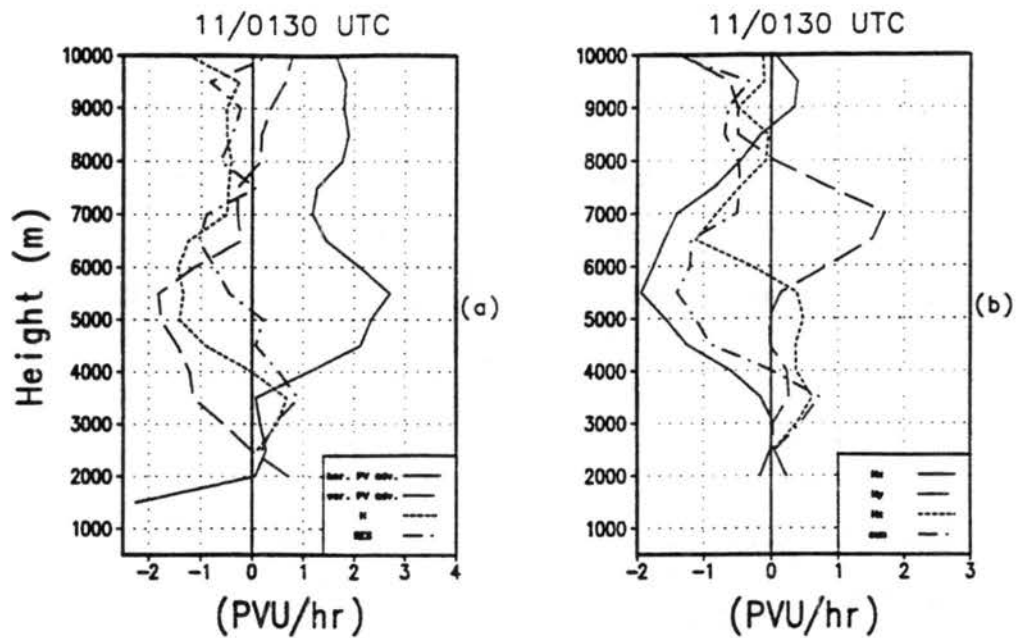


Figure 5.13: Vertical profiles through the negative \mathcal{P} anomaly north of the “kink” in the convective line, (a) \mathcal{P} equation terms, and (b) contributions to \mathcal{H} .

boundary between the updraft and downdraft. Figure (5.13a) shows the *actual* vertical profiles of the \mathcal{P} equation terms, while Fig. (5.13b) shows the corresponding contributions to \mathcal{H} . Horizontal advective effects are positive and relatively strong through most of the troposphere, reflecting NW flow advecting in positive \mathcal{P} air upstream of the negative anomaly. Vertical advective effects are negative below about 8 km due to negative vertical \mathcal{P} gradients and negative vertical velocities in the forming RTF branch. Diabatic effects are also negative above about 4 km, while RES changes sign but is negative and a minimum at 6.5 km, which appears to be the boundary between updrafts and downdrafts in this section of the storm.

Contributions to \mathcal{H} show a more complex picture than was seen during the initial stage of development. Below 5.5 km, \mathcal{H}_y is small but above this level shows a positive maximum at 7 km. This is explained with the help of Fig. (5.12b), a N–S section of vertical velocities and Q through the “kink” in the system. Below 5.5 km, $\partial Q/\partial y$ is small, while above this level it becomes negative. Although the ambient shear, $\partial u/\partial z$ is positive, in this region it

is negative, due to mid-level inflow and upper-level outflow. Unlike the initial time, \mathcal{H}_x is large (actually dominant) and negative at this time. This occurs because both $\partial v/\partial z$ and $\partial Q/\partial x$ are positive and \mathcal{H}_x can be approximated by the negative of their product. In vorticity terms, this anomaly is due to tilting of zonal vorticity while during the initial stages it was due to equal contributions from tilting of meridional vorticity and vorticity convergence (stretching). Thus by the growing stage, it may be difficult to build a simple conceptual model of the formation of the negative \mathcal{P} anomaly since it involves processes which depend on vertical wind shears which may be locally highly modified (relative to the ambient) by the storm itself.

During the growing stage of the 23–24 June case, at 24/0230 UTC, vertical advective effects are negative through a deep layer, as is \mathcal{H} at mid levels (Fig. 5.15b). The residual is very strong and positive and like the 10–11 June case, seems to act to deteriorate the negative \mathcal{P} . Contributions to \mathcal{H} show a profile similar to the earlier time (not shown). Hence, \mathcal{H}_y still dominates. The profiles through the average conditionally-sampled negative \mathcal{P} regions considered are evidently not as complex as the one negative region considered for the 10–11 June case. The conditionally-sampled averages may not be as representative of the individual regions as was the case for the conditionally-sampled positive anomalies.

By the mature stage (11/0330 UTC) the time series show a quite different situation (Fig. 5.14b). Diabatic effects are weaker and only negative between 4.5 and 7.5 km. Vertical advective effects are now negative through most of the troposphere, while horizontal advective effects are generally negative below 5.5 km and positive above. Once more, the residual is positive and dominant through most of the middle troposphere, again indicating it as the main agent responsible for deterioration of the negative anomaly. As the MCS matures, negative \mathcal{H}_z becomes more important, but is not dominant until the dissipating stages. After the growing stage, generation of \mathcal{P} by negative \mathcal{H} is never strong enough to counter positive effect by *RES*.

During the mature to dissipating stages of the 23–24 June MCS, we no longer have points which meet the sampling criteria ($\mathcal{P} < -0.5$ PVU) below 6 km. This is due to the deterioration of the negative anomaly primarily due to *RES*; which is still strong and

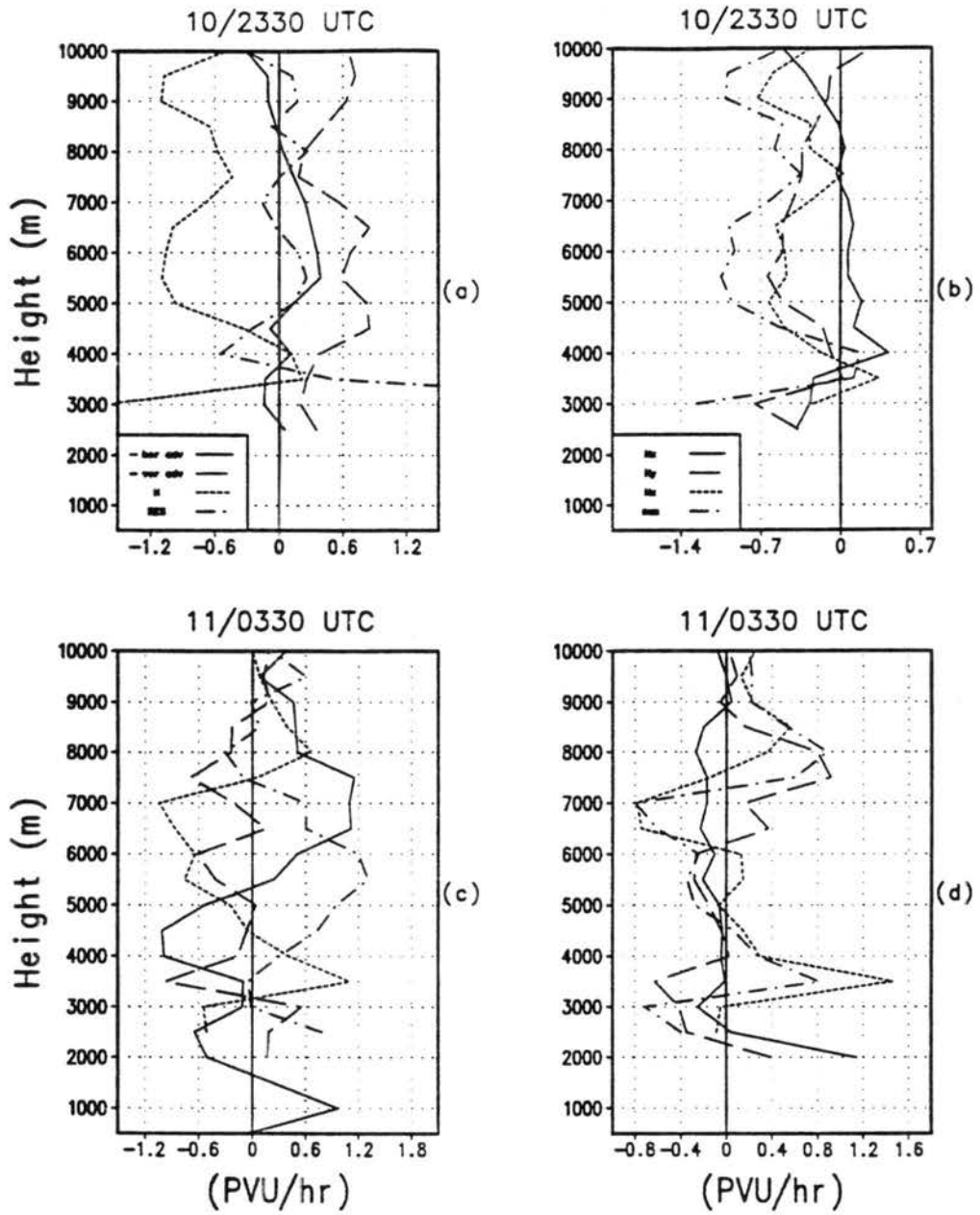


Figure 5.14: Vertical profile of the \mathcal{P} terms at (a) 10/2330 UTC, (c) 11/0330 UTC, and vertical profiles of contributions to \mathcal{H} at (b) 10/2330 UTC, (d) 11/0330 UTC.

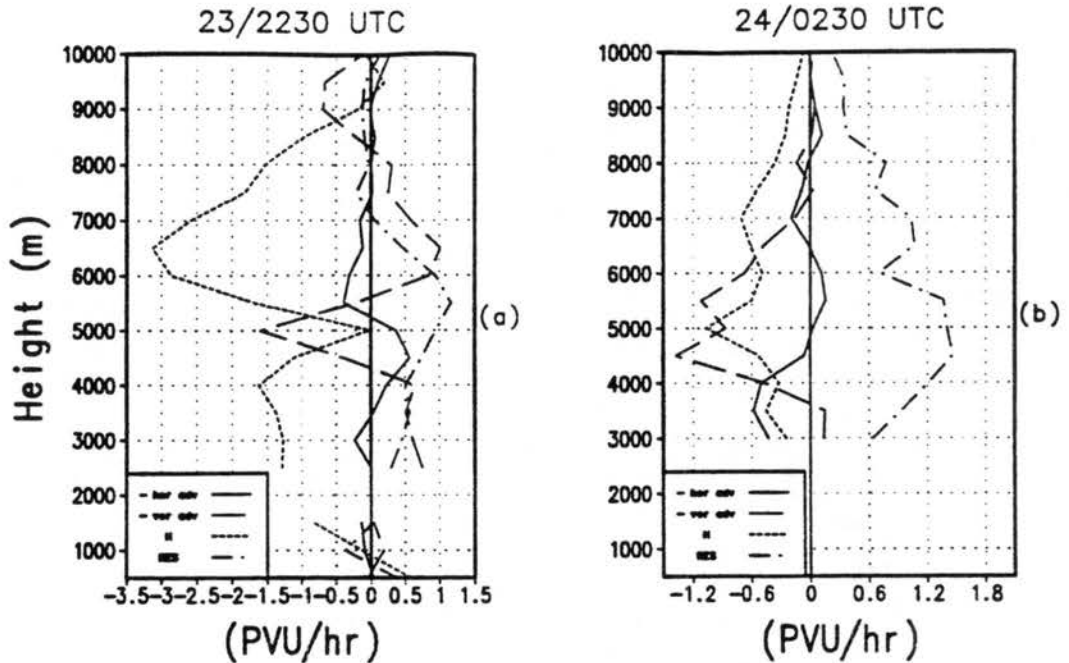


Figure 5.15: Vertical profile of the \mathcal{P} terms at (a) 23/2330 UTC, (b) 24/0230 UTC.

positive at or above 6 km at 24/0430 UTC. Very little negative \mathcal{P} forms after the mature stage, and what little does form does not meet the sampling criteria.

An example of *RES* related to the MCS is shown in Fig. (5.17), with vertical velocities and the N-S wind component. The RTF branch is beginning to develop at this time (largest vectors) and much of this is in weak descending flow (less than -0.2 ms^{-1}). The frictional effects in the convective line do not show much structure, but contained within the descending branch is a distinct maximum to 0.5 PVU hr^{-1} . This descending region is also where the negative \mathcal{P} anomaly at 5 km is located.

Thus, for both MCSs it appears that the mid-level negative anomaly forms initially due to negative diabatic effects (both horizontal and vertical), but shortly after the growing stage, this greatly weakens. Then, the residual is dominant and causes the anomaly to deteriorate by the mature stage.

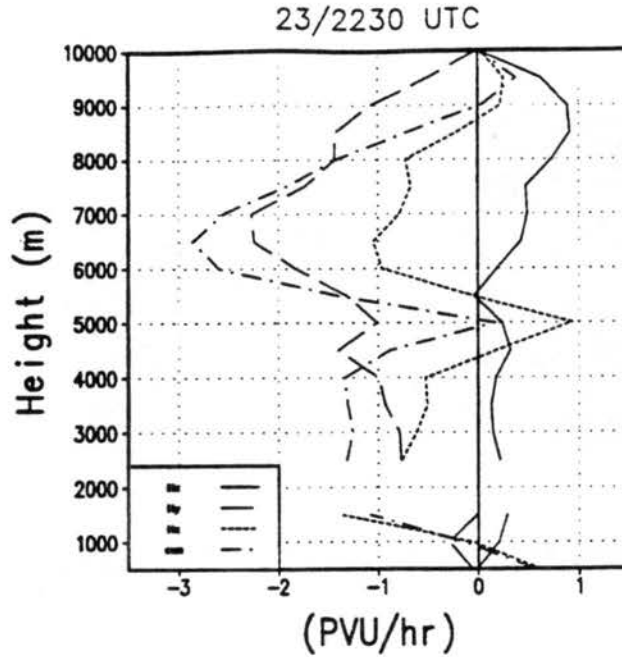


Figure 5.16: Vertical profiles of contributions to \mathcal{H} at 23/2330 UTC. Blank areas are those in which no points were sampled.

Storm-scale average at mid levels

On average, the positive \mathcal{P} anomaly dominates the MCS. Although the negative anomaly is at times as spatially extensive as the positive anomaly, especially in the initial stages, the latter is always stronger.

A time series of the 3-to-7 km layer and storm-scale average is shown in Fig.(5.18a) for the 10-11 June MCS. As was seen with the conditionally-sampled positive anomaly, \mathcal{H} is the dominant term, especially during the initial and growing stages. The broad peak in \mathcal{H} seen in the time series of the conditionally-sampled positive anomaly is not evident here. This is due to the conditionally-sampled negative anomaly, which is strong during the growing stage (cf. Figs. 5.4 and 5.11). Horizontal advective effects are negative throughout the MCS lifetime, while vertical advective effects change sign during the growing to mature stage; during the initial to growing stage, vertical advective effects do not balance \mathcal{H} . The residual remains positive and relatively weak throughout, thus on the storm-scale average, we do not see the deterioration of the negative anomaly due to this term.

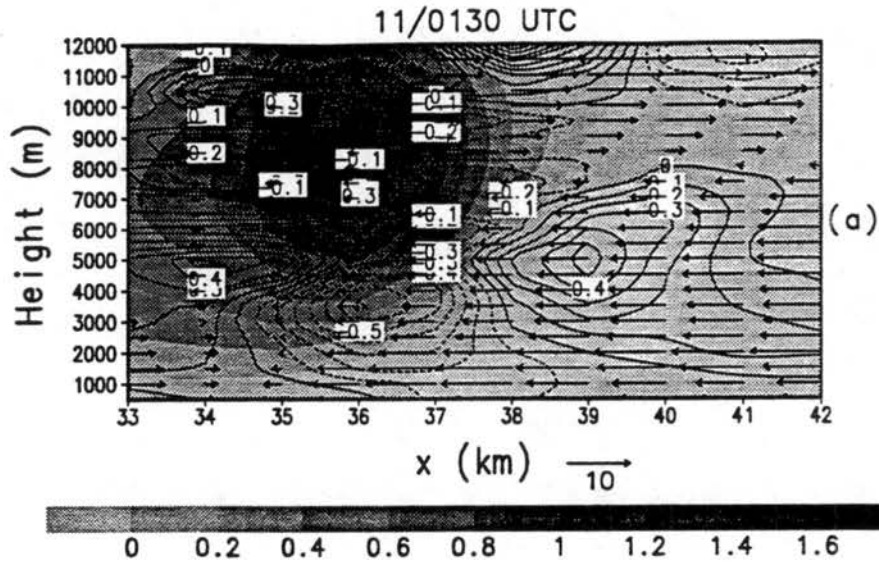


Figure 5.17: Vertical velocity (shaded – see color bar), the residual (RES) (contour), and v -component of the flow (vectors).

During the mature-to-dissipating stages (11/0200 UTC to 11/0500 UTC) all terms are weaker. Horizontal advective effects remain rather consistent at -0.1 PVU hr^{-1} , while RES remains very small. On the storm-scale then, it appears that the residual may not be due to shear associated with flow branches, since it should increase under this scenario. As mentioned, vertical advective effects change sign from negative to positive during this time. This could indicate a vertical displacement of the positive \mathcal{P} anomaly (assuming average positive vertical velocities). Since this is not seen, the more likely reason for the sign change is the deterioration of the negative anomaly, which would have the same effect.

For the 23–24 June MCS, the storm-scale average (Fig. 5.18b) shows that as in the 10–11 June case, \mathcal{H} is dominant, with peaks in the growing and matures stages. This term also tends to remain larger than in the previous case. Horizontal advective effects remain negative throughout the MCS lifecycle as before. In addition, vertical advective effects go from negative to positive, but later, towards the end of the mature stage. The residual accounts for the smallest contribution, but becomes positive between the growing

and mature stages. Recall *RES* was largest during the initial to growing stages during the 10–11 June MCS. From the storm-scale average perspective, it is even more difficult to speculate on the processes responsible for this term.

Summary – evolution at mid levels

We now summarize the evolution of \mathcal{P} at mid levels. The horizontal \mathcal{P} dipole that forms during the initial and growing stages of both MCSs occurs primarily because of non-advective fluxes due to diabatic effects. The positive anomaly forms mainly due to positive contributions from \mathcal{H}_z , while the negative anomaly forms due to almost equal negative contributions by \mathcal{H}_y and \mathcal{H}_z . As we will see in Section 5.2.4, \mathcal{H}_z and \mathcal{H}_y can be viewed from a vorticity perspective as stretching and tilting respectively. From studies of vorticity formation in individual thunderstorms, one might suppose that the formation of the two anomalies should be due to the same process, for instance, tilting of horizontal vorticity (Rotunno 1981). This is not the case because the vertical velocity distribution along the convective lines is more complex than a single thunderstorm updraft. Along the south end, strong vertical velocities lead to adjacent areas of positive and negative $\partial Q/\partial y$. Averaged over the positive \mathcal{P} anomaly, then, the contribution from \mathcal{H}_y is small and \mathcal{H}_z dominates. Along the north end of the both convective lines, vertical velocities and Q are weaker and drop off to the north, thus an average negative $\partial Q/\partial y$ (and hence relatively strong negative \mathcal{H}_y) forms in conjunction with the negative \mathcal{P} anomaly. A negative \mathcal{H}_z also contributes due to the positive vertical velocities.

The growing stage becomes more interesting. In general, the positive anomaly expands with the system, but shows signs of becoming dislocated from the maximum vertical velocities. Thus the system may be showing early signs of developing organized flow branches. Nonetheless, the positive \mathcal{P} anomaly at this time is due mainly to positive \mathcal{H} , the non-advective flux divergence associated with diabatic processes, and specifically due to contributions by \mathcal{H}_z . In terms of vorticity, the positive relative vorticity comes about due to vorticity convergence (stretching). The negative anomaly becomes much more complex. An average over conditionally-sampled negative \mathcal{P} still shows contributions by both \mathcal{H}_z and \mathcal{H}_y , but the magnitudes vary depending on the area sampled. A

vertical profile through just one of the negative anomalies shows that the contribution by \mathcal{P}_x dominates, while contributions by \mathcal{H}_y are secondary. This is not seen in any of the conditionally-sampled profiles. Thus the processes leading to the formation of the negative \mathcal{P} anomalies after the initial stage appear to be a highly complex interaction between gradients of diabatic heating and vertical shear (i.e., horizontal vorticity) of both ambient winds and flow excited by the MCS itself.

During the mature and dissipating stages, the positive \mathcal{P} anomaly is located behind the convective line, i.e., away from the strongest vertical velocities. This occurs somewhat in the 23–24 June case as well but it is much less apparent for that MCS. This displacement of the positive anomaly is likely due to transport by the FTR flow branch, but as mentioned previously, this transport is difficult to quantify. In this latter part of the MCS lifecycle, we still see positive \mathcal{H}_z although much weaker, and this dominates the positive anomaly. Negative \mathcal{H}_y is confined to an increasingly smaller area as the MCSs expand. This combined with the decreasing magnitude of negative \mathcal{H}_z causes less negative \mathcal{P} to form. At the same time, the residual becomes important, showing strong positive values which cause the deterioration of the negative \mathcal{P} anomaly. This seems to be associated with the descending RTF flow branch that develops as the MCSs mature. In terms of advective and non-advective fluxes of $\rho\mathcal{P}$, we find that the divergence of non-advective fluxes are mainly responsible for the distribution found at mid levels especially during the initial and growing stages. The divergence of advective fluxes play a role in the horizontal distribution as the heating weakens, especially during the mature to dissipating stages.

5.2.2 *Evolution at upper levels*

We now examine the \mathcal{P} evolution at upper levels. Theory and observations have shown that a negative \mathcal{P} anomaly usually forms aloft, positioned over the positive \mathcal{P} anomaly; both simulated MCSs here generally feature these negative anomalies. During the 10–11 June case, a small positive anomaly also forms aloft, possibly high- \mathcal{P} air advecting in from the inverted \mathcal{P} ridge northwest of the system.

Positive \mathcal{P} anomaly at upper levels during 10–11 June

From Chapter 4 we saw that a spatially small (compared to the negative anomaly) positive \mathcal{P} anomaly also forms aloft during the 10–11 June MCS. This feature was not seen during the 23–24 June MCS, most likely because the inverted \mathcal{P} ridge aloft was further displaced and did not transition across the MCS as in the former case.

Figure (5.19) shows a 9–to–11 km layer average of the conditionally–sampled time series of $\mathcal{P} > 1.2$ PVU. During the initial and growing stages, \mathcal{H} is large and negative. Vertical advective effects largely balance \mathcal{H} . Horizontal advective effects are positive until the mature to dissipating stages when this term becomes small. The residual peaks during the growing stage but then becomes relatively small as well. Since vertical advective effects do largely balance \mathcal{H} , it appears that the positive anomaly in this layer occurs because of horizontal advective effects, modified by *RES*.

Negative \mathcal{P} anomaly at upper levels

The negative anomaly aloft is conditionally–sampled using the criteria $\mathcal{P} < 0$. PVU, i.e., any negative values. Figure (5.20a) shows a time series of the 9–to–11 km layer average for the 10–11 June MCS. Apparent is the minimum in the diabatic effects during the growing stage. Recall from the previous chapter that during this period the main negative anomaly forms at 10 km. The diabatic effects are not offset by vertical advection. As the magnitude of \mathcal{H} decreases, horizontal advection goes from almost zero to negative values. This appears due to the fact that the strongest flow (positive values) is found in regions with positive horizontal \mathcal{P} gradients. The residual also becomes stronger by this time with positive values. The reason for this is unknown since by the time *RES* is positive, the negative \mathcal{P} anomaly is advecting away from the storm and would no longer be directly associated with strong divergent outflow. Thus it appears that the negative anomaly forms over the MCS primarily during the growing stage when deep mostly upright convection exists, and this subsequently advects away with the ambient flow while being somewhat modified by the residual.

During the 23–24 June MCS, the minimum in \mathcal{H} occurs much earlier, when a few deep convective cells exist but before the MCS is actually discernible (Fig. 5.20b). During this

early stage, the residual is negative and stronger than diabatic effects. This is possibly associated with strong divergent outflow. As in the 10–11 June case, RES weakens during the growing stage and becomes positive. One notable difference between the two systems is that although \mathcal{H} does weaken somewhat after the earliest stages of the 23–24 June case (as in the 10–11 June case), it does remain stronger and more consistent throughout the life of the MCS. As mentioned before, this is an indication of the more upright convection that persists through the life of the 23–24 June MCS.

Storm-scale average at upper levels

An average time series of \mathcal{P} equation terms taken over the MCS in a layer between 9 and 11 km is shown in Fig. (5.21a) for the 10–11 June case. A minimum in \mathcal{H} occurs during the initial to growing stages of the MCS. The diabatic effects remain negative in this layer throughout the MCS lifecycle. Vertical advective effects act to offset the diabatic heating; these are always positive and at times stronger than \mathcal{H} . Horizontal advective effects are positive and increase during the growing stage, reflecting the positive \mathcal{P} anomaly that forms aloft over the system. The residual remains small throughout in this layer. Recall that RES was also small for the mid-level storm-scale average, further indicating that this term may only be locally important.

The 23–24 June case shows that \mathcal{H} is negative but weaker during the initial stages over the storm-scale average (Fig. 5.21b). The diabatic effects remain relatively steady into the mature stage before decreasing in magnitude toward the dissipating stages. Vertical advective effects are positive as before, but remain weaker than \mathcal{H} . Horizontal advective effects and the residual remain small and positive, generally weakening somewhat over the MCS lifecycle.

Summary – evolution at upper levels

The evolution of \mathcal{P} at upper levels is much less complex than at mid levels. The main feature in \mathcal{P} at upper levels is a negative anomaly, with the exception of a positive anomaly which also develops for a time in the 10–11 June MCS. Time series of the \mathcal{P} equation terms

indicate that this feature is due to negative \mathcal{H} , i.e., negative non-advective flux due to diabatic effects.

The negative \mathcal{P} anomaly for the 23–24 June MCS is much more widespread (especially when considering \mathcal{P} which is less than or approximately zero) than in the 10–11 June MCS. This occurs because the 23–24 June system features deep, upright convection through most of its lifetime, hence stronger negative \mathcal{H} persists, whereas the 10–11 June system develops tilted updraft and downdraft flow branches. Deep upright convection causes stronger $-\partial Q/\partial z$ which we see as negative \mathcal{H} in the time series.

The residual is rather small on a storm-scale average, but tends to be stronger in regions with negative \mathcal{P} . Since this occurs over the deep convective updrafts, *RES* may be associated with strong, divergent outflow at these levels, but this remains speculative.

5.2.3 Comparison with Raymond (1992)

Introduction

Raymond (1992), hereafter R92, considers “*PV* thinking” at large Rossby number using a form of nonlinear balance (NLB) equations which he refers to as “semi-balanced”. Raymond derives a set of equations by retaining the total (i.e., balanced and unbalanced) winds in the predictive equation for *PV* and θ , but neglects the unbalanced winds in the definition of *PV*. His model is also hydrostatic and Boussinesq (i.e., ρ is replaced by ρ_0). Thus, using our notation from Chapter 2, we define

$$\mathcal{P}_{NLB} = \frac{1}{\rho_0} \left[\left(-\frac{\partial v_\psi}{\partial z} \right) \frac{\partial \theta}{\partial x} + \left(\frac{\partial u_\psi}{\partial z} \right) \frac{\partial \theta}{\partial y} + \left(\frac{\partial v_\psi}{\partial x} - \frac{\partial u_\psi}{\partial y} + f \right) \frac{\partial \theta}{\partial z} \right]. \quad (5.7)$$

Note that horizontal and vertical vorticity is defined in terms of the nondivergent winds, u_ψ, v_ψ ; the irrotational winds are neglected. We return to the lack of these winds in the next section.

Raymond considers the distribution of *PV* in an MCS due to the non-advective flux of \mathcal{P}_{NLB} . The semi-balance predictive equation, neglecting friction, is given by

$$\frac{d\mathcal{P}_{NLB}}{dt} = -\frac{1}{\rho_0} (-\nabla \cdot \mathcal{H}_{NLB} \zeta_{NLB}) \quad (5.8)$$

where

$$\mathcal{H}_{NLB} = \frac{1}{\rho_0} \left[\left(-\frac{\partial v_\psi}{\partial z} \right) \frac{\partial Q}{\partial x} + \left(\frac{\partial u_\psi}{\partial z} \right) \frac{\partial Q}{\partial y} + \left(\frac{\partial v_\psi}{\partial x} - \frac{\partial u_\psi}{\partial y} + f \right) \frac{\partial Q}{\partial z} \right]. \quad (5.9)$$

and ζ_{NLB} is calculated from irrotational winds only. This form can be compared to Eq. (2.10). Note from Eq. (5.8) that the non-advective flux is oriented parallel to, but in the opposite direction to the absolute vorticity vector, ζ_{NLB} .

Raymond next considers a situation in which ambient vertical vorticity is given by f and the horizontal vorticity is limited to the meridional component by positive westerly vertical shear only. Thus, we neglect the zonal vorticity part of \mathcal{H}_{NLB} and the ambient absolute vorticity vector points upwards and northwards. Next, consider a typical distribution of \mathcal{H}_{NLB} associated with an MCS, which has a maximum meridionally somewhere in the middle of the MCS and vertically, somewhere in the middle troposphere. Since \mathcal{P}_{NLB} varies due to the non-advective flux divergence (see Eqn.(5.8)), we end up with a positive anomaly in the southern regions of the MCS with a negative anomaly towards the northern end. The negative anomaly is also elevated somewhat in relation to the positive anomaly.

The degree to which the \mathcal{P}_{NLB} dipole is tilted vertically depends on the aspect ratio of the diabatic heating of the MCS. This ratio is defined by the vertical scale of the heating (h) over the horizontal scale (d). This ratio is compared to the ratio of f over the vertical shear vector, $S = du_0/dz$, where u_0 is the ambient zonal velocity. When $h/d \gg f/S$ transport of \mathcal{P}_{NLB} is effectively horizontal, while if $h/d \ll f/S$ transport of \mathcal{P}_{NLB} is effectively vertical. A conceptual model summarizing this idea is summarized in Fig.(5.22a), while results from an NLB simulation are shown in Fig.(5.22b).

Comparison between PRESTORM simulations and R92.

As we have noted, Fig. (5.22b) from R92 resembles the distribution found in our simulations (e.g., Fig. 4.2a). In addition, Fig. (5.22a) would indicate that if $h/d \approx f/S$, then the transport of \mathcal{P} should be a combination of horizontal and vertical transports. A N-S section through the \mathcal{P} dipole during the initial stages of both simulations show a slight vertical displacement of the anomalies (Fig. 4.4 and 4.12), with the negative

anomaly elevated over the positive anomaly as predicted by the theory of Raymond. Does this resemblance with results from our PE simulation indicate that the aspect ratio presented by R92 is generally valid?

Table 5.1: Horizontal dimension of heating d , vertical shear $S = \partial u / \partial z$, and for aspect ratio calculations. Vertical dimension of heating $h = 10$ km, and $f = 10^{-4} \text{s}^{-1}$.

time	d km	h/d	$S \text{ s}^{-1}$	f/S
10/2330 UTC	300	0.033	0.0024	0.042
11/0330 UTC	600	0.017	0.0032	0.032
23/2230 UTC	175	0.057	0.005	0.020
24/0430 UTC	500	0.020	0.002	0.045

Table 5.1 shows values for the calculation of aspect ratio for the initial and mature stages for both simulated MCSs. For all times, we assume $f = 10^{-4} \text{s}^{-1}$ and $h = 10$ km. During the initial stage of the 10–11 June case (10/2330 UTC), h/d is only slightly less than f/S , and thus vertical transport of \mathcal{P} should be slightly stronger than horizontal. By comparison, for the initial stage of the 23–24 June case, h/d is somewhat greater than f/S , thus horizontal transport should dominate vertical somewhat. Inspection of contributions to \mathcal{H} shows that for 10–11 June, \mathcal{H}_z does dominate in the positive anomaly (Fig. 5.6a), while for the 23–24 June case \mathcal{H}_z still dominates, but \mathcal{H}_y is somewhat stronger than during the previous case (Fig. 5.9a). For the negative anomaly in both cases \mathcal{H}_y is as strong, and sometimes even stronger than \mathcal{H}_z . Thus, there is some suggestion that the aspect ratio ideas hold, however, different processes are at work in each anomaly. This is a more complicated situation than envisioned by R92.

During the mature stage of both simulated MCSs, the systems have about doubled in horizontal extent and comparison of aspect ratios shows that $h/d < f/S$ and thus, vertical transport should dominate. As we saw in the previous section, by the mature stage, the negative anomaly is deteriorating and the positive anomaly is the main feature. Vertical non-advective flux (\mathcal{H}_z) is strongest in both cases, but the horizontal non-advective flux (\mathcal{H}_y) is actually stronger than at the initial stage for the 10–11 June MCS. Hence, once

again it appears that the aspect ratios hold, but ambiguity exists due to the complexity of the systems at this time compared to the simple heating distribution considered by R92.

Raymond also discusses transport of PV due to non-advective fluxes, e.g., meridional transport by

$$\left(\frac{\partial u}{\partial z} - \frac{\partial w}{\partial x} \right) Q.$$

But as we see from Fig. (5.22a), adapted from R92, it is the flux *divergence* that is important in the local redistribution of PV , e.g.,

$$\frac{\partial}{\partial y} \left[\left(\frac{\partial u}{\partial z} - \frac{\partial w}{\partial x} \right) Q \right].$$

We now consider flux divergences for our simulated MCSs. All sections presented have been averaged across the system, so these are height vs. “along-line” sections. During the initial stage, the sections are oriented N-S, but later orientations change so they are SW-NE for the 10-11 June case and E-W for the 23-24 June case.

Figure (5.23a,b) we show the horizontal and vertical non-advective flux divergences (due to diabatic effects only) during the initial stage of the 10-11 June MCS. These agree with the finding from the vertical profiles of conditionally-sampled averages from the previous section, as they of course should. The positive anomaly (south end) is dominated by positive \mathcal{H}_z , while the negative anomaly (north end) is comprised of almost equal contributions by \mathcal{H}_y and \mathcal{H}_z . Note the difference in contour intervals. So again direct comparison with R92 is difficult since neither horizontal nor vertical non-advective flux divergence dominate the entire system; overall \mathcal{H}_z does. We also note that a comparison between ratios is weak at this time since neither h/d nor f/S is *much* greater or less than the other.

By the mature stage of the 10-11 June MCS (Figs. 5.23c,d), \mathcal{H}_z is generally larger than \mathcal{H}_y . Note that the structure of the positive \mathcal{H}_z region appears to elevate towards the SW. This occurs because we are averaging along the line, and at this time the line is not straight (Fig. 3.4a). So the SW end of the section averages over more of the full system, capturing the convective line and stratiform region, whereas the NE end captures mostly the convective line. Values of \mathcal{H}_y are largest and (very) locally as large as \mathcal{H}_z

near the NE end of the line. This agrees with the vertical profiles of contributions to \mathcal{H} ; recall the horizontal non-advective flux gained relative strength at this time (Fig. 5.6b). The prediction by R92 that the vertical non-advective flux divergence should dominate horizontal non-advective flux divergence appears to hold for this MCS.

Examination of the 23–24 June system yields similar results. Again in agreement with the vertical profiles, during the initial stage, \mathcal{H}_y is somewhat stronger than \mathcal{H}_z compared to what was seen in the 10–11 June case. The latter dominates as before though. During the mature stage, \mathcal{H}_z becomes very dominant.

Summarizing, our findings show some agreement with R92, but the results are somewhat ambiguous due to the complexity of our simulated MCSs. This will likely be a problem comparing any PE simulation of a real system to more idealized PE simulations or NLB. Our system is never small enough to test the dominance by horizontal flux divergence. It would be interesting to investigate *PV* transport associated with a single deep convective cell (e.g., 10 km in the vertical and 10 km or less in the horizontal) using for instance the simulation of deep convection along sea-breeze fronts by Hertenstein and Cotton (1992). We note again that especially after the growing stage, the structure of the heating becomes more complicated than envisioned by Raymond. In addition, even during the initial stage, processes differ for the positive and negative anomalies. Finally, we note that our simulations agree with NLB in that it is the *ambient* vertical shear that is tilted in the negative anomaly that leads to our horizontal dipole structure. Also, it is the heating acting on ambient vorticity that is the main contributor to the positive anomaly. In this regard, NLB has captured the underlying dynamics.

5.2.4 *Comparison with Davis and Weisman (1994)*

Introduction

Davis and Weisman (1994), hereafter DW94, use the Klemp–Wilhelmson cloud model (Klemp and Wilhelmson 1978) employing horizontal grid spacing of 4 km to investigate the causes of Mesoscale Convective Vortices (MCVs) associated with an idealized squall line. They initialize their simulation using a wind profile with westerly shear in the lowest

2.5 km, the sounding of Skamarock et al. (1994), and six “warm thermals” in a line 200 km long. After 3 hours, this configuration results in a horizontal PV dipole at 2.1 km, with positive PV north and negative south. In the presence of background rotation (i.e., f), the dipole is asymmetric, with the northern positive PV anomaly the strongest. Note that this dipole is of the opposite sense shown by R92 at 5 km (see Fig. 5.22).

For their analysis, DW94 use a modified flux form of the PV equation,

$$\frac{\partial(\rho q)}{\partial t} \approx -\frac{\partial}{\partial x} \left[Q \left(\frac{\partial v}{\partial z} - \frac{\partial w}{\partial y} \right) + \rho u q \right] - \frac{\partial}{\partial y} \left[-Q \left(\frac{\partial u}{\partial z} - \frac{\partial w}{\partial x} \right) + \rho v q \right]. \quad (5.10)$$

In this form, the vertical advective and non-advective flux divergence,

$$-\frac{\partial}{\partial z} [-Q(\zeta + f) + \rho w q]$$

has been neglected. The following approximations are then made:

- Boussinesq
- $\theta = \bar{\theta}(z)$
- $w \approx Q(d\bar{\theta}/dz)^{-1}$
- $q = \frac{1}{\rho}(\zeta + f)\frac{d\bar{\theta}}{dz}$

With these, a vorticity equation can be derived from Eqn.(5.10) which takes the form

$$\frac{\partial \zeta}{\partial t} = -\frac{\partial}{\partial x} \left[w \frac{\partial v}{\partial z} + u(f + \zeta) \right] - \frac{\partial}{\partial y} \left[-w \frac{\partial u}{\partial z} + v(f + \zeta) \right]. \quad (5.11)$$

As the authors state, within the limits imposed by the above approximations, “ PV thinking” and “vorticity thinking” coalesce. Note that the twisting term in the vorticity equation, i.e.,

$$-\frac{\partial w}{\partial x} \frac{\partial v}{\partial z} + \frac{\partial w}{\partial y} \frac{\partial u}{\partial z}$$

is contained in the non-advective flux of Eqn. (5.10), i.e.,

$$-\frac{\partial Q}{\partial x} \frac{\partial v}{\partial z} + \frac{\partial Q}{\partial y} \frac{\partial u}{\partial z}.$$

Convergence of vorticity (stretching) is contained in the horizontal derivatives of the second term in each bracketed term of Eqs.(5.10) and (5.11).

As mentioned, the main result of the DW94 cloud model integration is a *PV* dipole at a height of 2.1 km with a positive anomaly north and a negative anomaly south. The authors explain this distribution from two perspectives. First, the *PV* perspective can be explained by inspection of Fig.(5.24). Shown are the total flux (J_y), the advective part of the flux (J_y -ADV), the non-advective part (J_y -NON), and the q time tendency. The fields have been zonally averaged (i.e., across the squall line) so that the sections shown are N-S, and we are viewing the squall line from the “front”, as it moves towards us. The time tendency shows the dipole development at lower levels, with a positive tendency north and a negative tendency south. From Fig.(5.24a), we see that below about 4.5 km, J_y has a maximum near the center of the domain. Since it is the flux divergence that changes the q distribution (see Eq.(5.10)), regions to the north of the maximum ($\partial J_y/\partial y > 0$) lead to a negative tendency, while regions south of the maximum ($\partial J_y/\partial y < 0$) lead to a positive tendency. Thus they argue that the q dipole at 2.1 km can be explained in terms of the total flux.

The vorticity perspective is explained by DW94 with the help of Fig. 5.25. As the squall line evolves, a cold pool develops. When the horizontal vorticity associated with the cold pool becomes greater than the horizontal vorticity associated with the ambient westerly shear, the system begins to tilt upshear (Rotunno et al. 1988). The FTR and RTF flow branches then develop, with negative meridional vorticity between the flow branches, and positive meridional vorticity below the RTF branch. The negative meridional vorticity is then tilted upwards by the mesoscale updraft in the FTR branch, while the positive meridional vorticity is tilted downwards by the descending RTF branch, leaving us with a vertical vorticity in the sense implied by Fig. 5.25. The authors further note that this mechanism could not occur in the NLB paradigm, since the horizontal vorticity associated with the flow branches is due to the unbalanced flow (i.e., $\partial u_x/\partial z$) and this vorticity is not tilted in the NLB system.

Some questions remain with the analysis and interpretation of DW94. First, is the neglect of the vertical divergence in Eq. 5.10 really valid? If this were so, it would largely invalidate the conceptual model presented in Figs. (2.2) and (2.3), in which the vertical

part of the diabatic heating is vital. Second, as DW94 state in their introduction, MCVs are often deep, extending from 2 to 8 km, and are generally a maximum in mid-levels, between 4 and 6 km. This concurs with the climatology of Bartels and Maddox (1991); MCVs visible by satellite would occur in mid level clouds. However, the flux and flux divergence change sign above about 4.5 km (see Fig. 5.24), thus we would expect a dipole in the opposite sense above this level. This is confirmed by inspection of Skamarock et al. (1994) (their Fig. 12). As DW94 point out, the two simulations yield almost identical results. Thus, the MCVs presented by DW94 are confined to the lower levels and at mid levels the dipole would be the same sense as R92. This leads to the third point. From the vorticity argument of DW94, deep MCVs should form since they propose horizontal vorticity tilted by the FTR branch augmented by horizontal vorticity (of the opposite sign) tilted by the RTF branch. As we just saw, this deep MCV does not appear to be simulated.

Comparison between PRESTORM simulations and DW94.

Our purpose in making comparisons between our simulations and those of DW94 is not to downplay their work. However, there do appear to be inconsistencies between the results of DW94, our simulations, and between a companion paper to DW94 (i.e., Skamarock et al. (1994), hereafter S94). We would also like to determine whether the horizontal flux divergence of $\rho\mathcal{P}$ is the dominant process in the formation of the horizontal \mathcal{P} dipole.

It is instructive to consider the aspect ratios proposed by R92 for the simulation of DW94. If we take $h = 10$ km and $d = 300$ km, then $h/d = 0.033$, while using $f = 10 \text{ s}^{-1}$, and $S = 4 \times 10^{-3} \text{ s}^{-1}$ yields $f/S = 0.25$. Thus these ratios are almost equal and we would expect both horizontal and vertical flux divergence to be important.

Consider the term neglected by DW94,

$$\frac{\partial}{\partial z} [(\zeta + f)Q - \rho wq]. \quad (5.12)$$

Using their approximations this term simplifies to

$$\frac{\partial}{\partial z} \left[(\zeta + f)w \frac{d\bar{\theta}}{dz} - \rho w \frac{1}{\rho} (\zeta + f) \frac{d\bar{\theta}}{dz} \right].$$

and the terms within brackets cancel identically.

Examination of our results show that the two terms in brackets are indeed approximately equal and of opposite sign. Consistent with DW94, this is not the case for the meridional advective and non-advective fluxes. However, it is the flux *divergence* that is important in changing $\rho\mathcal{P}$. Figure (5.26) shows a N-S section of meridional and vertical flux divergence for the 10–11 June MCS. The section is taken at 10/2330 UTC, during the initial stage when the horizontal \mathcal{P} dipole is prominent. The fields are somewhat complicated but notice that the two terms are of comparable magnitude. Thus it appears that the assumption made by DW94 that the vertical flux divergence does not appear to be negligible is not valid. Why would this be the case? One of the assumptions in eliminating the term in brackets involves using the large-scale form for PV , i.e., q defined above. But as we saw in Section 5.1, other contributions to \mathcal{P} can be important. Vertical flux divergence which includes the total \mathcal{P} also contains vertical derivatives of horizontal vorticity, which are not necessarily small in the MCS. In addition, DW94 justify the neglect of the Eqn. (5.12) by assuming that potential temperature surfaces are essentially horizontal, thus $\partial/\partial z$ is in the same direction as $\partial/\partial\theta$. Using the conservation theorem of Haynes and McIntyre (1987,1990), no PV can be transported across isentropic surfaces and hence none should be transported across Cartesian- z surfaces. However as pointed out by Peter Olsson (personal communication), DW94 do not balance their vertical shear with a meridional θ gradient. Thus, in the real atmosphere, θ surfaces would not coincide with Cartesian- z surfaces.

The interpretation of DW94 that the horizontal \mathcal{P} dipole can be explained in terms of meridional flux divergence does not hold for our two simulated MCSs. As we saw in Section 5.2.1, the vertical non-advective flux divergence (neglected by DW94) is most important in the formation of the positive \mathcal{P} anomaly. Both meridional and vertical non-advective flux divergence play a role in the formation of the negative \mathcal{P} anomaly.

Using the assumptions listed above DW94 draw an analogy between PV and vorticity viewpoints (cf. Eqn. 5.10 and 5.11). Note that vertical vorticity convergence is contained in Eqn. (5.12), i.e.,

$$(\zeta + f) \frac{\partial Q}{\partial z}.$$

Thus, we should see qualitative agreement between PV and vorticity perspectives from our results. Quantitative agreement would require assumption of a horizontal balance condition and use of an invertibility principle to extract winds from the PV anomaly. How does the vorticity perspective compare with our earlier analysis from a PV perspective?

Figure (5.27) shows vertical profiles of vorticity tilting and stretching averaged over the positive anomaly at 5 km for both MCSs. In low to mid levels, these show that positive stretching dominates, in agreement with the dominance of \mathcal{H}_z . Tilting is small in the low to mid levels of both cases but becomes negative in the upper levels. This is most likely due to negative $\partial Q/\partial y$ over a larger portion of the averaging area. Figure (5.28) shows the corresponding profiles through the negative anomaly. In both systems, negative tilting is strong through the mid levels. In the 23–24 June case, stretching is also negative but weaker above 3 km. In the 10–11 June case, stretching is negative below 5.5 km and positive above that. The positive stretching is due to $\partial Q/\partial z < 0$ above the mid levels. This combined with anticyclonic vorticity leads to positive stretching. Once again we see good qualitative agreement between vorticity term profiles and profiles of the contributions to \mathcal{H} examined earlier.

Davis and Weisman concentrate their analysis on the dipole that forms at 2.1 km. However, MCVs, their purported motivation for this study, usually occur between 2 and 8 km, as the authors themselves state. Following their interpretation combined with inspection of Fig. (5.24a) would indicate that we should see a \mathcal{P} dipole in the same sense as our simulations above 4.5 km. These levels are not considered in their work, DW94 however also state the following regarding the companion paper by S94 “our simulations reproduce all significant system–scale features seen in the higher–resolution runs by S94”. Thus we should be able to use S94 figures to help explain what is inferred from DW94. Figure (5.29) shows winds, vertical velocities, and potential temperature perturbations for after 4 hours of integration. Note that at 3 km, the flow field is the same sense as DW94. By 8 km, the sense of the flow is reversed, as predicted by Fig. (5.4a). The flow fields do not show the circulations as clearly as at lower levels since we are approaching levels where divergent outflow is becoming an influence. Unfortunately S94 do not present levels between 3 and 8 km.

Figure (5.30) also taken from S94, shows vorticity tilting and stretching. Note that no dominant pattern shows up in the vorticity tilting field, however, it appears that vorticity stretching is a maximized in the northern part of their system, which is where the positive \mathcal{P} anomaly forms. The authors also state that the most vigorous convective cells are also along the northern portion of the squall line. Thus it appears that further examination of DW94 results (seen indirectly via S94) actually seems to support our finding that vorticity stretching is more important in the formation of the positive \mathcal{P} anomaly.

Summarizing, the comparison between our results and those of DW94 do not agree, especially in terms of the processes responsible for the formation of the horizontal \mathcal{P} dipole. Davis and Weisman neglect the vertical flux divergence and stress the horizontal in their analysis. As we have seen, our analysis shows that the vertical flux divergence is not negligible and is largely responsible for the formation of the positive \mathcal{P} anomaly. Both horizontal and negative flux divergence play a role in the formation of the negative anomaly.

We are not suggesting that the dipole simulated by DW94 itself is incorrect. This brings up an interesting point, since our simulation also correctly simulated a \mathcal{P} dipole but of the opposite sense. It may be useless trying to generalize the formation and structure of PV distributions in "real" MCSs. The actual formation and structure seems to be a function of vertical wind shear (ambient or storm-induced), and the strength and structure of the vertical velocity field. Thus, a wide variety of vortical circulations can form depending on the details of the storm. However, the dominant feature is the mid-level positive PV anomaly and its associated positive relative vorticity.

Our findings do agree well with one main assertion of Davis and Weisman. Their results suggest that the vorticity field quickly forms, a fast-manifold process using their terminology, and the temperature field comes into balance with the wind fields. This is in contrast to a slow-manifold process where the wind field gradually comes into balance with a temperature perturbation due to the MCS heating. Our findings, e.g., the time series in Fig. (5.4) would support their conclusion.

5.2.5 Summary

This section dealt with the major processes responsible for the distribution of \mathcal{P} described in Chapter 4. We now briefly summarize the findings of this section.

The mid-level positive \mathcal{P} anomaly forms and is maintained by diabatic effects, especially by positive contributions by \mathcal{H}_z , the vertical vorticity part of the diabatic heating term. In terms of vorticity this is the convergence (or stretching) term. The negative anomaly at mid levels forms initially due to almost equal negative contributions by \mathcal{H}_y and \mathcal{H}_x . These terms contain tilting and stretching of vertical vorticity respectively. Since there is little if any negative relative vorticity initially, tilting must necessarily act first, but only for a short time, before stretching can become important. As the systems mature, the processes responsible for the mid-level anomalies become a very complex interaction of heating gradients and horizontal vorticity, the latter can be due to ambient vertical shear or shear formed within the MCS.

At upper levels, the situation is more straightforward. A negative \mathcal{P} anomaly forms due mainly to negative \mathcal{H}_z . The main negative anomaly simulated in the 10–11 June MCS forms during the initial and growing stages and then advects away. By comparison, the 23–24 June MCS exhibits more upright deep convection over most of its lifetime, hence negative \mathcal{H}_z remains stronger through the entire lifetime of this system and results in a more widespread negative anomaly than seen in the 10–11 June MCS.

The MCSs simulated here were never horizontally small enough to rigorously test the mostly horizontal \mathcal{P} transport predicted by Raymond (1992). Qualitatively, the horizontal \mathcal{P} dipole that Raymond predicts matches our simulations during the initial stages. However, we found that the processes responsible for the formation of our \mathcal{P} dipole is more complex than the scenario proposed by Raymond. As our simulated storms grow, the heating structure quickly becomes difficult to compare to the NLB model results.

A comparison was also made with the results of Davis and Weisman (1994) who concentrate on a lower-level (i.e., at 2.1 km) \mathcal{P} dipole which has an opposite sense to the PRE-STORM cases simulated here. A companion paper by Skamarock et al. (1994) shows that at 8 km, the sense of their dipole does match ours. Davis and Weisman (1994) explain

their 2.1 km \mathcal{P} distribution strictly in terms of horizontal advective and non-advective fluxes. They make an analogy between “*PV* thinking” and “vorticity thinking”; their associated vorticity distribution is due to tilting by their analysis. Davis and Weisman completely neglect vertical \mathcal{P} fluxes, which also means neglecting vorticity convergence associated with vertical heating gradients. We found this term to be dominant in the formation and maintenance of the positive \mathcal{P} anomaly. As we saw, the work by Skamarock et al. (1994) seems to support our findings.

5.3 Material change of \mathcal{P} due to the residual

As we saw in Section 5.2, the material change in \mathcal{P} due to *RES*, calculated as a residual in the predictive equation for \mathcal{P} , is not necessarily small. Surprisingly, this is even the case well away from the surface, where one might otherwise expect this term to be relatively large. In this section, we will take a closer look at the residual calculated as

$$RES = d\mathcal{P}/dt - \mathcal{H}$$

then investigate possible mechanisms responsible for this term. Results discussed here are for the 10–11 June MCS; similar results occurred for the 23–24 June MCS.

5.3.1 Residual (*RES*) in the predictive \mathcal{P} equation

During the early stages of the 10–11 June MCS, vertical profiles through the average positive or negative \mathcal{P} anomalies show that *RES* is sometimes a relatively large contribution to $\partial\mathcal{P}/\partial t$, on the order of 10–30%. As mentioned above, the maximum does not occur near the surface, as might be anticipated. On the storm-scale average profiles, *RES* acts with an opposite sign to the horizontal advection through much of the troposphere; this tendency is not seen in the average through positive or negative anomalies.

Later during the mature stage, *RES* increases in magnitude and is at some levels the strongest contribution to $\partial\mathcal{P}/\partial t$ (e.g., at 4 km through the negative anomaly). In general, the term is strongest in mid levels. The mid-level maximum is seen more clearly when viewed from conditionally-sampled profiles, which would indicate that *RES* follows the

tilted positive and negative \mathcal{P} anomalies. On a storm-scale average the tendency for the *RES* profile to have the opposite sign of horizontal advection is still seen.

As the MCS enters its dissipating stages, *RES* is relatively weak at most levels in the positive anomaly and storm-scale. However, in the negative anomaly, it is still fairly strong. As viewed from a storm-scale average, *RES* no longer appears to oppose the horizontal advection in sign.

5.3.2 Possible mechanisms for *RES*

What physical processes could account for the *RES* profiles discussed in the previous section? One possibility is that *RES* at mid levels is due to turbulence associated with shear in (or between) the FTR and RTF flow branches (e.g., Fig. 5.17). This seems feasible since *RES* at mid levels increases as the system matures.

Raymond (1992) discusses \mathcal{P} forcing due to “molecular and turbulent processes” and suggests a form

$$\mathbf{F} = -\rho_0^{-1} \nabla \left(-\rho_0^{-1} \nabla \cdot \mathbf{v}' \mathbf{v}' \right) \quad (5.13)$$

so that the material change of \mathcal{P} due to these effects becomes

$$\mathcal{F} = -\rho_0^{-1} \nabla \theta \cdot \nabla \times \left[-\rho_0^{-1} \nabla \cdot (\rho_0 \mathbf{v}' \mathbf{v}') \right]. \quad (5.14)$$

Expanding Eq.(5.14), we obtain 24 terms of the form of second partial derivatives of momentum fluxes times a potential temperature gradient.

Vertical profiles of all 24 terms were examined and the following four were found to dominate

$$\begin{aligned} & 2\rho_0^{-2} \frac{\partial^2 v' w'}{\partial z^2} \frac{\partial \theta}{\partial x} \\ & -2\rho_0^{-2} \frac{\partial^2 u' w'}{\partial z^2} \frac{\partial \theta}{\partial y} \\ & -2\rho_0^{-2} \frac{\partial^2 v' w'}{\partial x \partial z} \frac{\partial \theta}{\partial z} \\ & -2\rho_0^{-2} \frac{\partial^2 u' w'}{\partial y \partial z} \frac{\partial \theta}{\partial z} \end{aligned}$$

Here the primes denote a deviation from a spatial average. In true Reynold's averaging, these would be a deviation from a temporal average as well. These terms not only are

the strongest, but show a tendency to lower in elevation with time. This lends support to the notion that the residual may form as a result of turbulence associated with tilted flow branches.

Comparisons between RES and \mathcal{F} calculated using Eqn.(5.14) were discouraging. In general, vertical profiles show little agreement. Horizontal sections of both quantities show the overall system very well, but fields are noisy and the main positive or negative regions do not match. Vertical sections reveal similar results.

This lack of success points to the difficulty in isolating actually resolved turbulent processes from unresolved subgrid-scale processes. As pointed out by Raymond (1992), as well as others, \mathcal{P} defined from Reynold's averaged quantities, i.e.,

$$\overline{\mathcal{P}}_1 = \overline{1/\rho} \overline{\zeta_i} \partial \overline{\theta} / \partial x_i$$

is not the same as defining \mathcal{P} in terms of exact quantities and then Reynold's averaging. The latter yields

$$\begin{aligned} \overline{\mathcal{P}}_2 = & \overline{1/\rho} \overline{\zeta_i} \partial \overline{\theta} / \partial x_i + \\ & \overline{(1/\rho)\zeta_i' \partial \theta' / \partial x_i} + \\ & \overline{(1/\rho')\zeta_i \partial \theta' / \partial x_i} + \\ & \overline{(1/\rho')\zeta_i' \partial \theta / \partial x_i} + \\ & \overline{(1/\rho')\zeta_i' \partial \theta' / \partial x_i}. \end{aligned}$$

It is possible that on the 20 km grid used for analysis we should actually consider, or in some way parameterize, the subgrid-scale processes represented by $\overline{\mathcal{P}}_2$. Without finer grid spacing data, covering most of the MCS over the entire lifecycle, this task is difficult, and is a worthy topic for study on its own.

Terms: storm-scale average

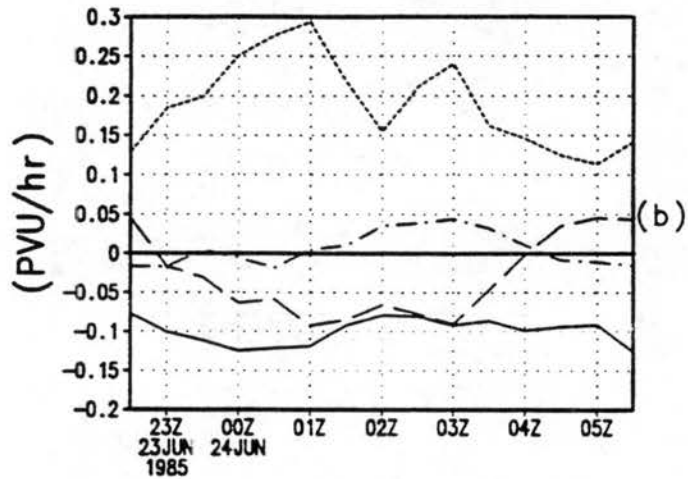
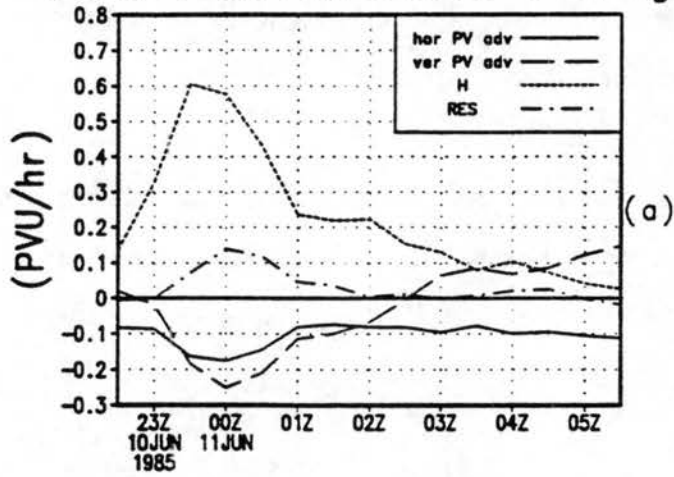


Figure 5.18: Storm-scale average of \mathcal{P} terms between 3 and 7 km for (a) 10-11 June, (b) 23-24 June.

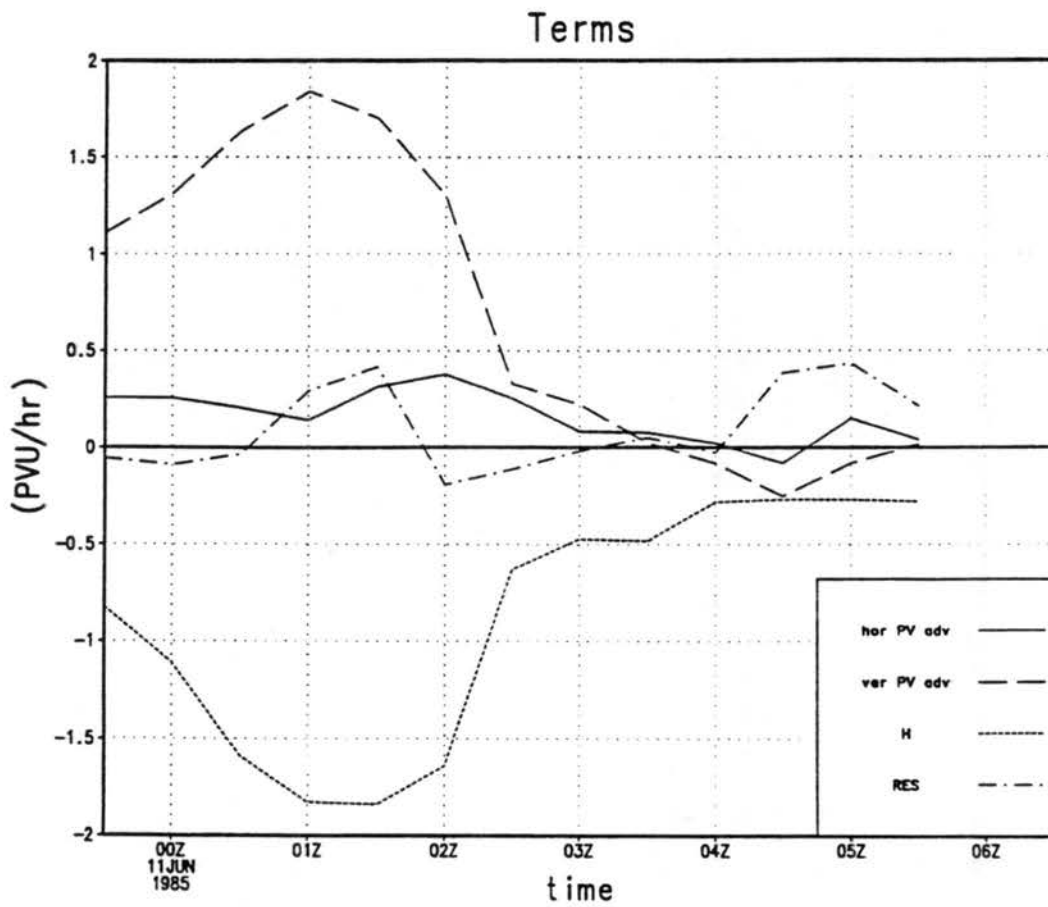


Figure 5.19: Time series of \mathcal{P} equation terms ($\mathcal{P} > 1.2$ PVU), between 9 and 11 km for the 10–11 June MCS.

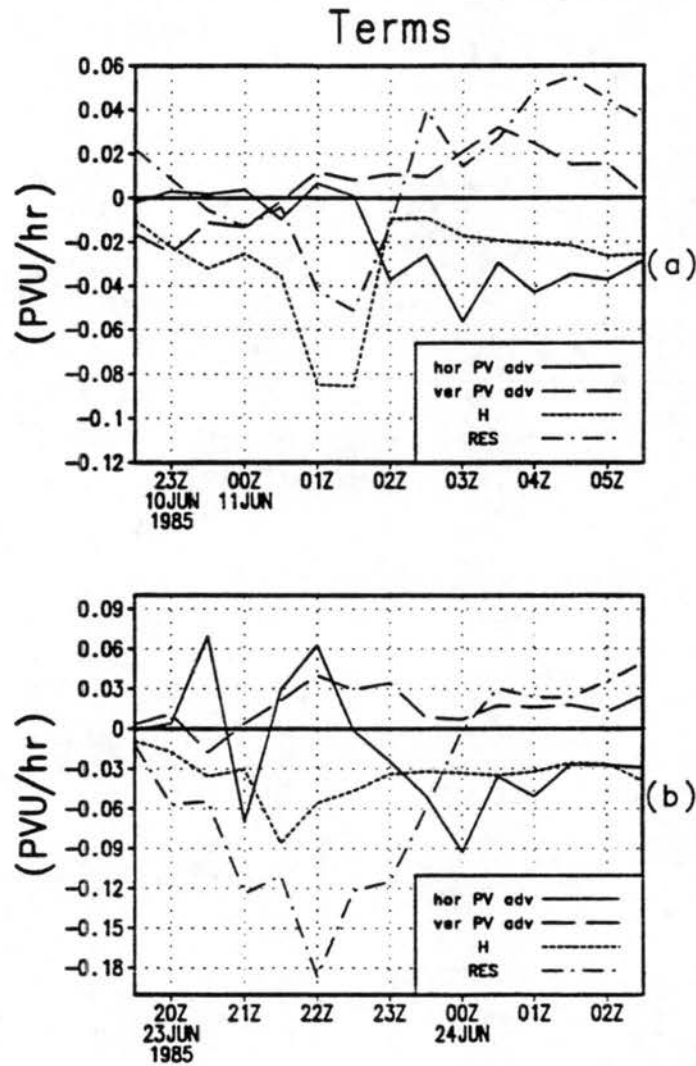


Figure 5.20: Time series of \mathcal{P} equation terms ($\mathcal{P} < 0$. PVU), (a) 10-11 June, (b) 23-24 June.

Terms: Storm-scale average

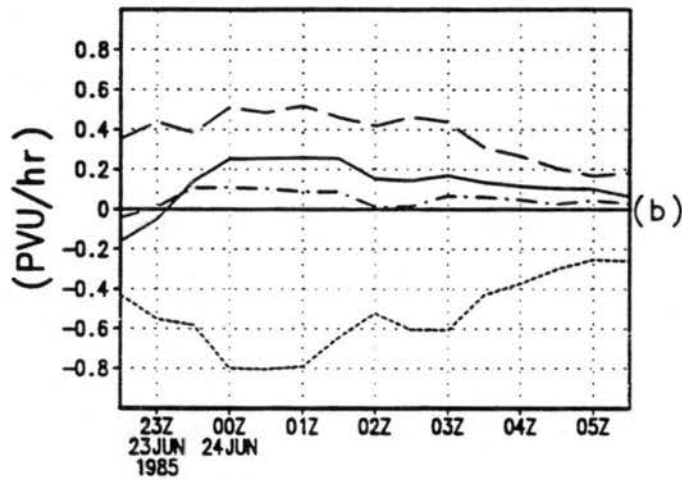
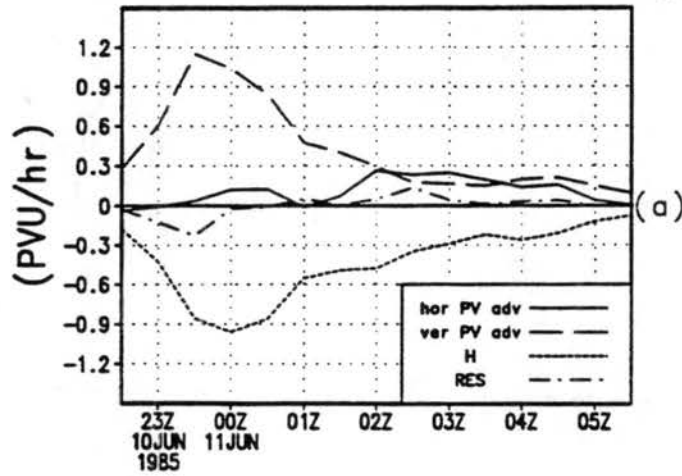


Figure 5.21: Time series of storm-scale average of \mathcal{P} equation terms between 9 and 11 km, (a) 10–11 June, (b) 23–24 June.

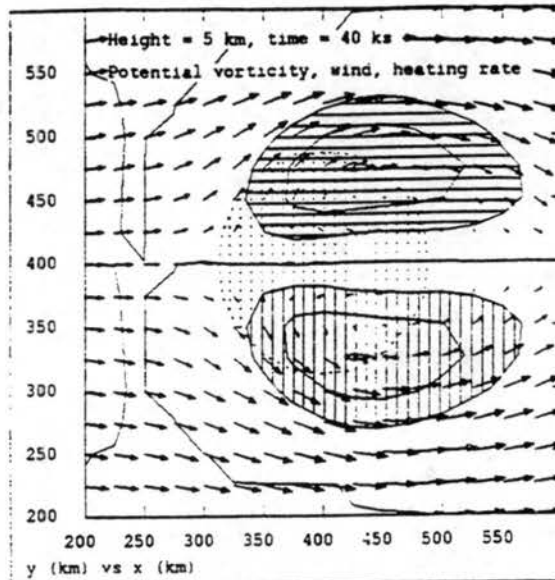
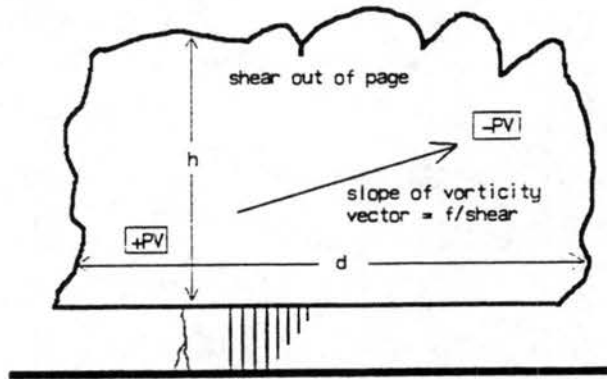


Figure 5.22: (a) Schematic of a convective storm looking west showing vertical and horizontal dimensions, h and d . Positive westerly shear is assumed, so that the shear vector is out of the page, and the absolute vorticity vector is shown (from Raymond 1992, his Fig. 10). (b) Horizontal section at 5km showing imposed heating (stippling), wind vectors, and PV (positive - vertical hatching, negative - horizontal hatching). Maximum PV is about 0.5 PVU (from Raymond 1992, his Fig. 11).

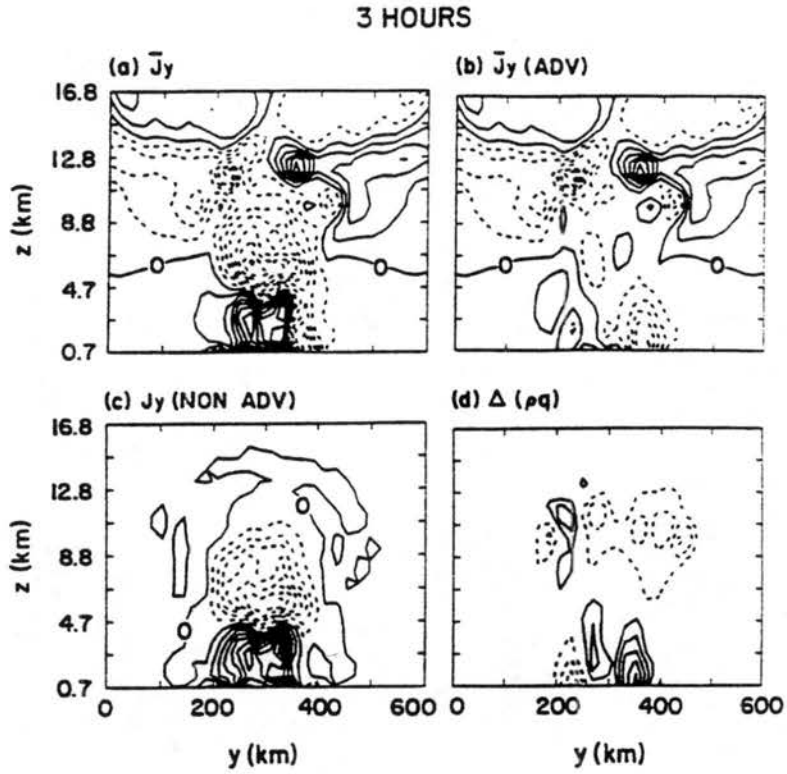


Figure 5.24: (a) Total flux, (b) advective flux, (c) nonadvective flux, (d) \mathcal{P}_{DW} tendency (from Davis and Weisman 1994, their Fig. 11). Contour interval for (a)–(c) is $6 \times 10^{-7} \text{ K s}^{-2}$.

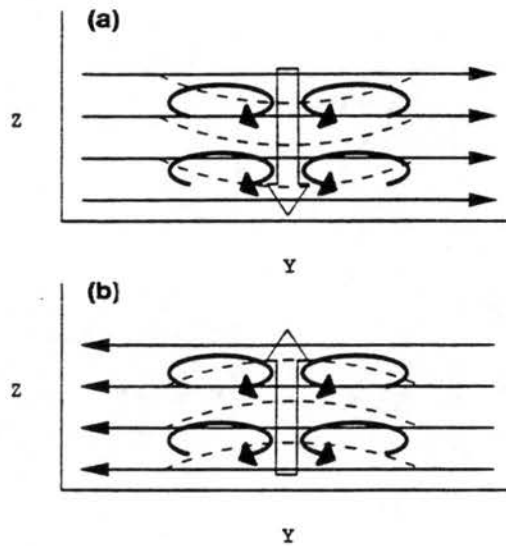


Figure 5.25: Schematic showing tilting of (a) westerly shear, and (b) easterly shear. View is towards the west (from Davis and Weisman 1994), their Fig. 13.

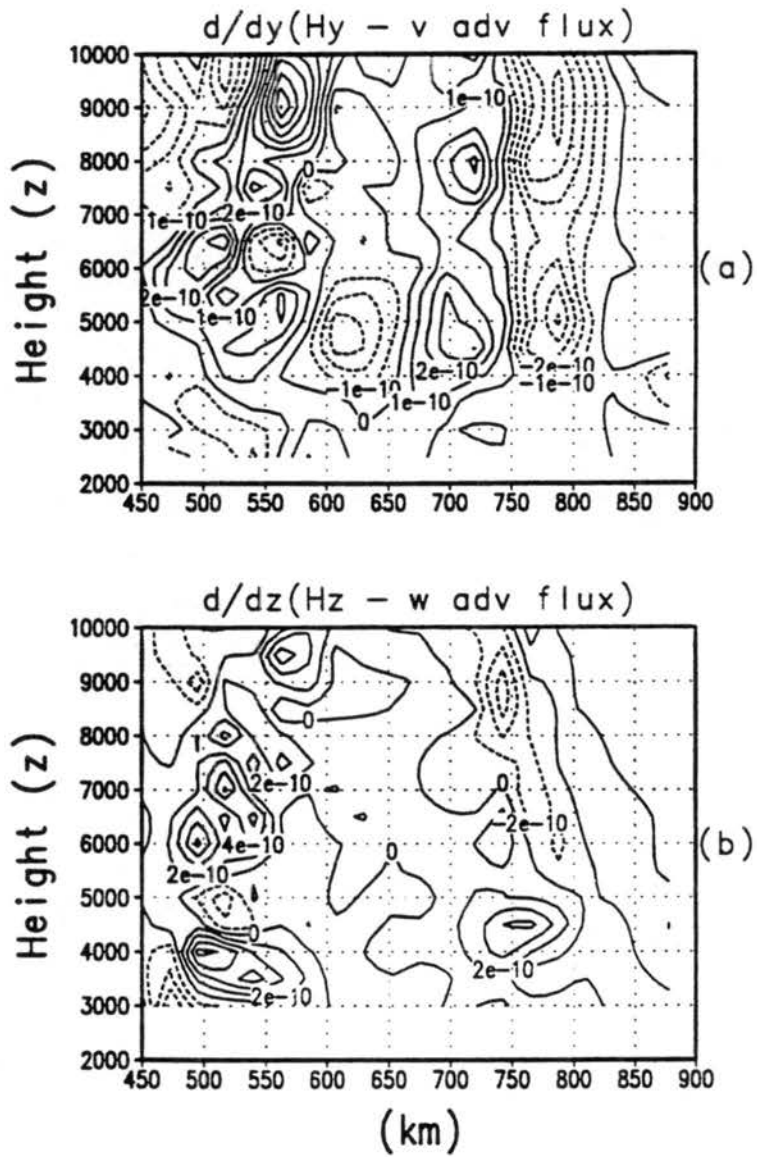


Figure 5.26: North-south section through the horizontal \mathcal{P} dipole at 10/2330 UTC, (a) meridional advective and non-advective flux divergence, (b) vertical advective and non-advective flux divergence.

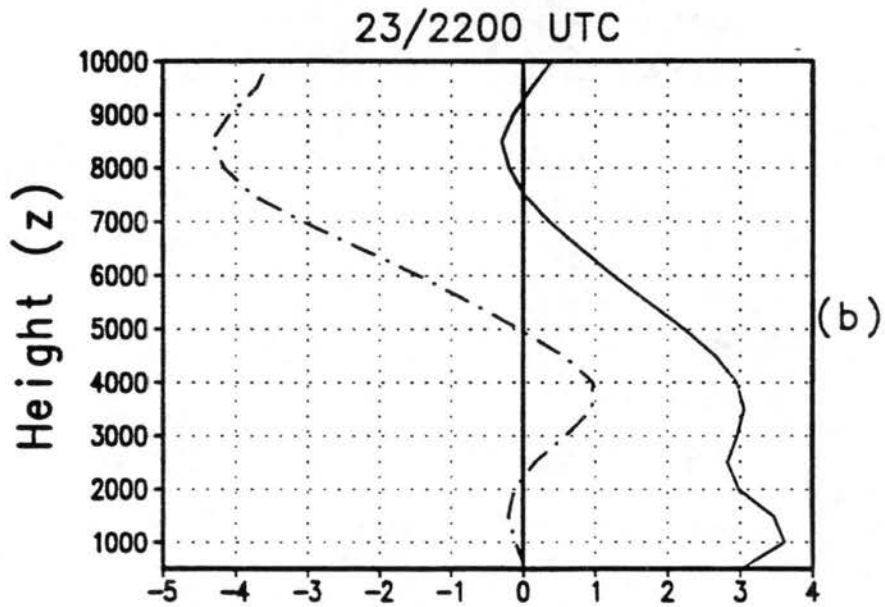
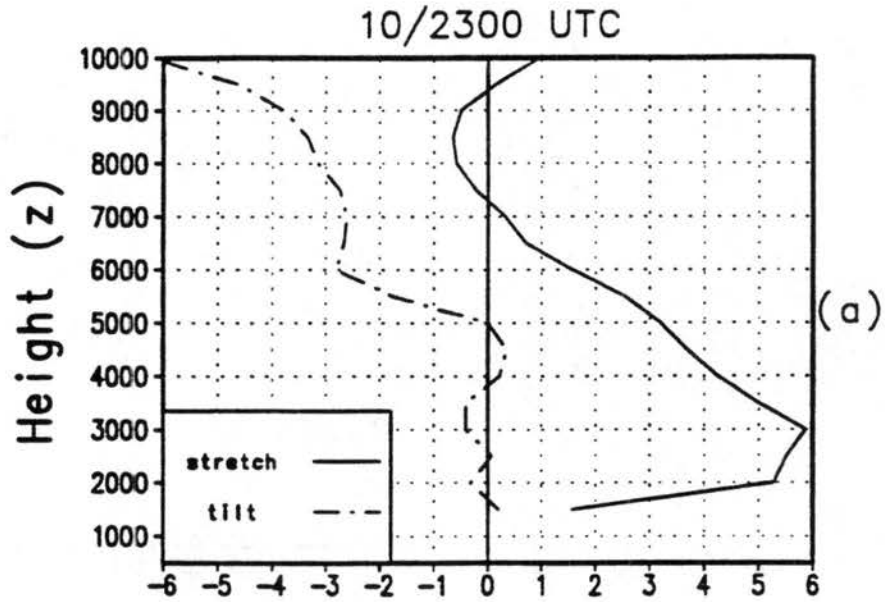


Figure 5.27: Vertical profiles of vorticity tilting and stretching (s^{-2}) averaged over the positive anomaly for, (a) 10/2300 UTC, and (b) 23/2200 UTC. Values along the abscissa have been multiplied by 10^8 .

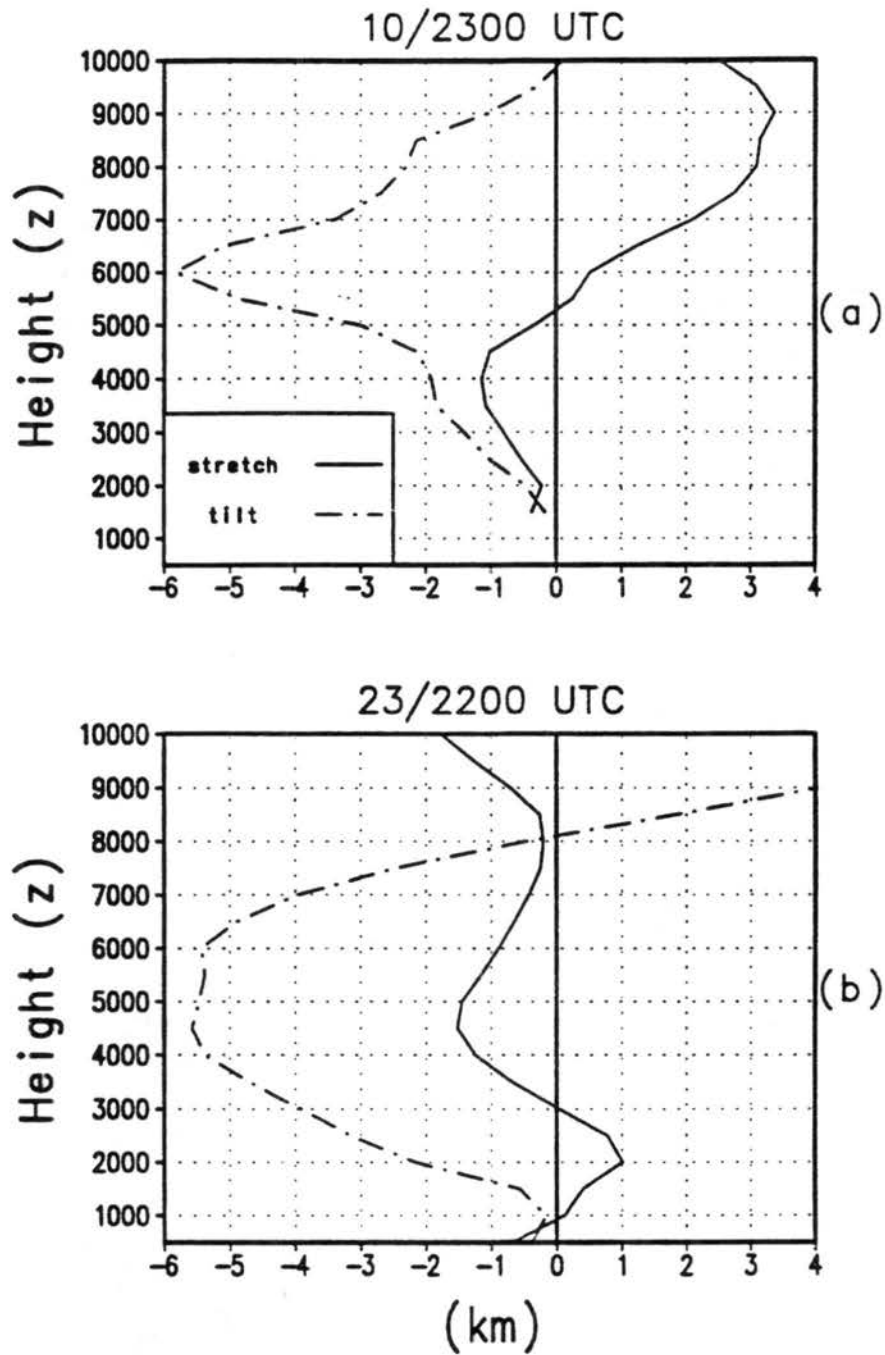


Figure 5.28: Vertical profiles of vorticity tilting and stretching (s^{-2}) averaged over the negative anomaly for, (a) 10/2300 UTC, and (b) 23/2200 UTC. Values along the abscissa have been multiplied by 10^3 .

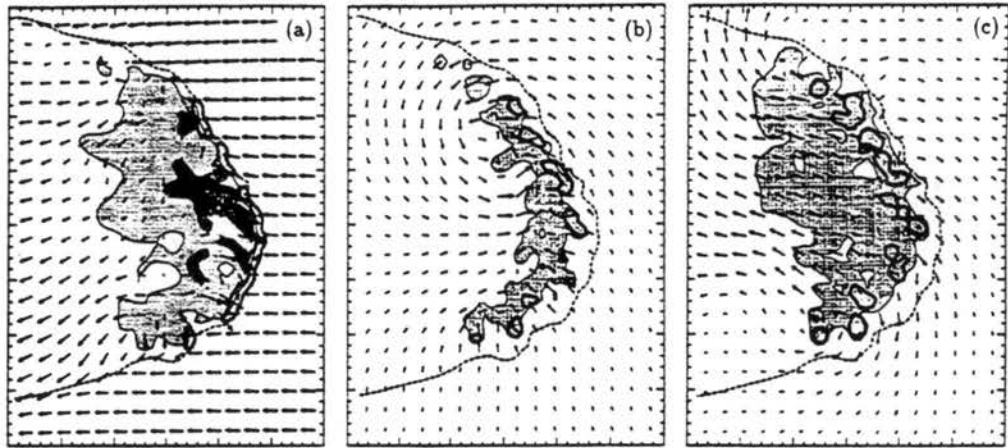


Figure 5.29: Horizontal section of flow vectors, vertical velocity (thick contours), and θ' (shading) at 6 hours, (a) near the surface, (b) 3 km, (c) 8 km. Plotting domain is 300 by 400 km (from Skamarock et al. 1994, their Fig. 13).

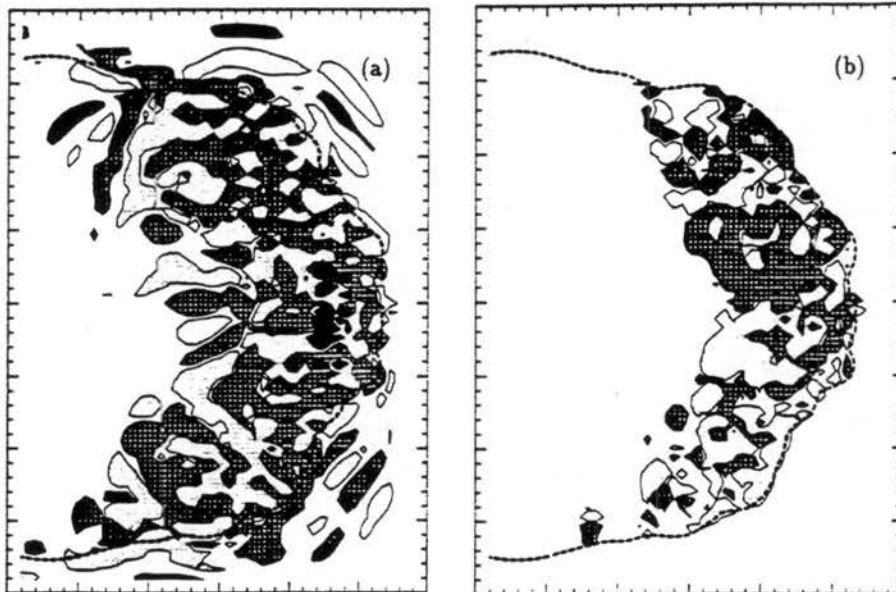


Figure 5.30: (a) horizontal vorticity tilting, (b) vorticity stretching, at 3 km and 6 hr of simulation. Darker shading indicates higher values (from Skamarock et al. 1994, their Fig. 9).

Chapter 6

SUMMARY AND CONCLUSIONS

6.1 Summary

This study was motivated by past studies of *PV* and associated vortical circulations associated with MCSs. These studies have included balance–model simulations, PE simulations of idealized scenarios, or observations using the synoptic–scale observing network. An investigation of the evolution of *PV* associated with actual MCSs has been thus far lacking. Two non–idealized simulations of mid–latitude MCSs were analyzed to examine the behavior of \mathcal{P} with these more realistic systems. These simulations used the nested–grid utility of RAMS, with grid spacings ranging from 80 to about 8 km, and the Level 2.5w convective adjustment scheme. Although the simulations did not verify perfectly in the “forecast” sense of observed MCS timing and position, this was found not to be critical for our analysis. Heating rates, however, which are important to the evolution of *PV*, compared favorably to available observations, thus the simulations were deemed suitable for our diagnostic analysis.

The evolution of Ertel’s potential vorticity, \mathcal{P} , was documented at mid and upper levels in Chapter 4. The evolution is not analyzed near the surface because of frictional dissipation of the flow, topography, and dry adiabatic layers, can lead to small values of \mathcal{P} even in the presence of strong vorticity, and thus the interpretation of \mathcal{P} is difficult. The evolution of \mathcal{P} is similar for both simulated MCSs. At mid levels, a horizontal \mathcal{P} dipole forms during the initial stage, with a positive anomaly along the south end of the convective line and a negative anomaly along the north end. As the systems grow, the dipoles evolve into larger regions of positive and negative anomalies, aligned parallel to the convective line. By the mature and dissipating stages, the mid–level negative

anomaly deteriorates and the system is dominated by a positive \mathcal{P} anomaly. At upper levels a negative \mathcal{P} forms during the initial and growing stages of both MCSs. During the later stages of the 10–11 June MCS, the main negative anomaly advects away with the ambient flow. By contrast, during the later stages of the 23–24 June MCS, early negative \mathcal{P} anomalies also advect away but in addition, new anomalies continue to form due to continued upright convection. Thus, the less-organized 23–24 June MCS appears to have a larger effect at upper levels. The upper-level analysis was performed on the larger Grid #1 in order to better evaluate the synoptic-scale influence.

Contributions to \mathcal{P} were investigated for both systems at various stages of development. The large-scale approximation, i.e., that \mathcal{P} can be approximated by the vertical vorticity contribution was found to be a marginal assumption for MCSs. In some regions of the MCS, the horizontal vorticity contributions were on the order of 20–30% of the total \mathcal{P} , especially during the mature stage when horizontal vorticity associated with flow branches was strongest. The horizontal vorticity itself (as opposed to horizontal potential temperature gradients) were mainly responsible for the strength of the contributions. Thus caution is needed when associating strong vertical vorticity with \mathcal{P} maxima in mesoscale systems.

Ertel's \mathcal{P} equation was examined next, including both diabatic and a residual. The flux form of the \mathcal{P} equation was also considered. In order to investigate the positive and negative \mathcal{P} anomaly at mid levels separately, a conditional sampling technique was used. At every level, each point meeting the sampling criteria was summed, then an average was taken at each level. Time series of the various \mathcal{P} equation terms could then be constructed at each level, as well as averages for specified layers. Vertical profiles of conditionally-sampled terms were also constructed at several times during the MCS lifecycle. In addition, vertical profiles were also constructed of the contributions to the non-advective flux divergence due to diabatic effects, \mathcal{H} , to determine whether vertical or horizontal contributions dominate and at which stages of MCS development. Whenever possible, links between "PV thinking" and "vorticity thinking" were noted.

Comparisons were then made with theories for PV evolution using nonlinear balance (Raymond 1992) and a PE simulation with idealized initial conditions (Davis and Weisman

1994). Here again, the link between a PV and vorticity viewpoint proved useful. In some instances this comparison proved difficult due to the more complex nature of the convective structure in the PRE-STORM simulations.

Finally, during the budget analysis described above, it was found that the non-advective flux divergence due to the processes, represented as a residual from the \mathcal{P} equation, was not always small, even well away from the surface. An effort was made to isolate the physical processes responsible for this term, using a form suggested by Raymond (1992). This led to speculation on the possible causes for this term, but no firm, quantifiable conclusion.

6.2 Conclusions

It is both easy and enticing to generalize about some phenomenon based on few samples. In this dissertation, we have examined results from only two simulated mid-latitude MCS. Based on this limited data set, the main conclusions of this dissertation are as follows:

- It appears that the mode of convection has a dramatic effect on the \mathcal{P} anomalies, especially at upper levels. The 10–11 June MCS started with upright convection but fairly quickly organized as a squall line with a tilted front-to-rear updraft followed by a tilted rear-inflow downdraft. The 23–24 June MCS also begins with deep upright convective cells, but although the cells eventually organize, they never form an organized, tilted updraft. Rather, somewhat randomly-organized deep convective cells continue to fire. A tilted rear-inflow does develop along portions of the MCS. The mid-level \mathcal{P} distribution is similar between the two systems. Overall, both systems display a positive \mathcal{P} anomaly. At upper levels, the 10–11 June MCS produces a strong negative anomaly when it is dominated by deep, upright convection. As the system matures, the tilted updrafts no longer produce much negative \mathcal{P} aloft, and the original negative anomaly quickly advects away. The 23–24 June MCS continually produces negative \mathcal{P} , due to its continuing deep, upright convection. Even though the early negative anomalies also advect away, they are continually replenished, and

this MCS produces a much larger negative anomaly aloft. Thus it appears that an MCS with more randomly organized upright convection has a much greater effect on the ambient upper-level environment than an MCS with organized tilted updrafts, such as a squall line.

- The structure and evolution of \mathcal{P} is highly three-dimensional. This is true both for MCSs with organized convection, as the 10–11 June case or more randomly-spaced convection. Even averages along the MCSs show greater detail temporally than would have been anticipated from two-dimensional model studies or two-dimensional sections across three-dimensional observational or model data sets. This complexity and variability makes one, simple conceptual model difficult. In addition, there is also the problem of scales. Mesoscale vortices or vortical circulations occur in a variety of convective storms, from supercell thunderstorms to large, organized MCSs. This influences both the potential lifetime of these circulations as well as processes responsible for the formation or dissipation of vortical flows. For instance, it may be that for a single thunderstorm, tilting of ambient vorticity may dominate, whereas for a larger, somewhat more organized system, vorticity advection and convergence may be more important. The structure and strength of vertical shear profiles and vertical velocity fields will determine the details of PV formation in a given MCS. However, aside from the details, the prevalent feature left in the wake of most MCSs is a mid-level positive PV anomaly.
- Although the “large-scale” approximation to \mathcal{P} , i.e., \mathcal{P}_z , is typically the dominant contribution, it is not always (spatially and temporally) the most important term. By “important”, we refer to the normal meteorological sense of greater than an order of magnitude. The horizontal vorticity contributions, i.e., \mathcal{P}_x and \mathcal{P}_y are also important, each sometimes accounting for 20 % of the total contribution and each is sometimes even the dominant term, especially in the vicinity of the mesoscale flow branches during the mature phase of the MCS. Also in the vicinity of the flow branches, horizontal vorticity is about two orders of magnitude greater than vertical

vorticity. This is balanced by the fact that vertical potential temperature gradients are often somewhat more than two orders of magnitude greater than horizontal potential temperature gradients. Thus, \mathcal{P}_z usually dominates. This does sound a note of caution in automatically interpreting high \mathcal{P} as regions of high vertical vorticity; this is not always the case.

- The residual in the predictive \mathcal{P} equation, defined as $RES = d\mathcal{P}/dt - \mathcal{H}$, is not always small. It has been assumed in most previous studies that frictional effects can be neglected. But our analysis show this may not be true. Surprisingly, this term is not a maximum near the surface, where frictional effects might be assumed to be most important. During the mature and dissipating stages, RES was found to be relatively large at mid levels. It was speculated that this could be due to turbulent momentum fluxes associated with strong shear near the flow branches. It appears that the main role of the residual is in the deterioration of the mid-level negative anomaly during the mature stage. One form for the residual was investigated to see whether it could account for the vertical structure or magnitude of RES . This was, unfortunately, not successful. This points to the difficulty in separating resolved processes from unresolved subgrid-scale processes.
- As we have seen, during the initial stages a horizontal \mathcal{P} dipole forms at mid levels. We found that the positive anomaly in both cases forms mainly due to positive \mathcal{H}_z , the vertical contribution to the non-advective flux divergence due to diabatic effects. From a vorticity standpoint, ambient absolute vorticity is transported upwards while simultaneously vorticity convergence (stretching) acts to rapidly increase relative vorticity. Horizontal contributions (\mathcal{H}_y) play only a minor role in the formation of the positive anomaly. The vorticity analogy for this term is tilting, thus for the positive \mathcal{P} anomaly in these simulations, tilting plays only a small role. This occurs because of strong updrafts associated with the positive \mathcal{P} anomaly; averaged over the anomaly positive and negative tilting effects cancel. Positive \mathcal{H}_z weakens but continues to be present over the lifetime of the MCS, maintaining this anomaly

and causing it to expand. During the mature to dissipating stages, the \mathcal{P} anomaly becomes vertically distorted by the tilted FTR flow branch, as in the 10–11 June MCS. Systems lacking a tilted FTR flow branch feature a more upright, symmetric positive anomaly, as in the 23–24 June MCS.

- The negative mid-level \mathcal{P} anomaly initially forms due to negative contributions by \mathcal{H} . This consists of contributions from both \mathcal{H}_y and \mathcal{H}_z , i.e., forms due to both vorticity tilting and stretching. In the absence of negative vorticity, tilting must occur first. In the 10–11 June pre-convective environment, weak ambient negative vorticity was present at mid levels. So tilting and stretching could occur simultaneously. However, in the 23–24 June pre-convective environment, no negative vorticity was detectable, thus tilting occurred first, followed by a combination of tilting and stretching. As the MCS grows and matures, the processes associated with the negative anomaly become more difficult to isolate. One surprising finding however, is that the negative anomaly appears to deteriorate due to the residual during the mature stage, as the RTF flow branch fully develops. By the dissipating stages of both MCSs, the negative anomaly has essentially completely deteriorated.
- From the above two conclusions, it appears that the positive \mathcal{P} and associated relative vorticity do not slowly form as a balanced response to thermal perturbations in the MCS. Rather, the vorticity forms quickly due to vertical transport and vorticity stretching. Thus the mass field likely comes into balance with the wind field as the system evolves.
- The comparison between our results and those of Raymond (1992) shows some agreement. Comparison of aspect ratios (height to width of diabatic heating compared against f to ambient vertical shear) generally show that the vertical PV transport dominates vertical transport. It should be remembered that neither ratio was *much* larger or smaller than the other. So according to Raymond's theory, both transports should be almost equally important. This was not the case in our simulations. Specifically, the positive and negative anomalies form due to different processes.

This is not covered by Raymond. Thus the resemblance between our results and the NLB results may be somewhat fortuitous.

- A comparison with the results of Davis and Weisman (1994) shows little agreement when considering the processes responsible for the formation of the horizontal \mathcal{P} dipole. First, it was found that the vertical divergence of advective and non-advective fluxes neglected by Davis and Weisman was not small. It appears, as a matter of fact, the process most important for the formation of the positive mid-level anomaly in our simulations is contained in the term neglected by Davis and Weisman. We conclude that their interpretation is not correct. As we have discussed, a companion paper by Skamarock et al. (1994) supports our findings. The conclusion by Davis and Weisman that vertical vorticity forms rapidly and the mass field subsequently balances the wind field is supported by our simulations. We disagree, however, with their interpretation of processes responsible for the vertical vorticity generation.

6.3 Conceptual model

We can also summarize the evolution of the mid-level positive \mathcal{P} anomaly with a conceptual model, which differs from earlier studies. During the initial stages, a short convective line forms and a \mathcal{P} dipole forms, with a negative anomaly north and a positive anomaly south. Qualitatively, this resembles the distribution predicted by Raymond (1992). The positive \mathcal{P} anomaly forms due to \mathcal{H}_z , the vertical non-advective flux divergence. In vorticity terms, this is vorticity stretching. The negative \mathcal{P} anomaly forms due to both \mathcal{H}_z and \mathcal{H}_y , vertical and horizontal non-advective flux divergence or in vorticity terms, stretching and tilting. As the system grows, same processes generally at work, and a banded positive-negative \mathcal{P} (and vorticity) is found. During the mature stage the positive \mathcal{P} is maintained mainly by weaker positive \mathcal{H}_z . The negative anomaly deteriorates due to *RES*. We believe turbulence generated between flow branches may be responsible for *RES* at this time. The MCS then dissipates. All processes are weak, and the positive anomaly is advected away, while the negative anomaly has completely deteriorated.

Although not captured by the simulations, hours or days after the MCS dissipates in a highly-sheared environment, the positive \mathcal{P} anomaly may become distorted or destroyed. In a low-vertical-shear environment, the anomaly may interact with the environment leading to new convection, MCSs, or TC genesis.

6.4 Future work

Based on the findings of this work, some recommended work for the future is as follows:

- Since MCVs occur on a variety of scales, associated with small and large convective systems, and in various locations within the convective systems, a thorough review of MCVs (including vortical circulations which are not “closed”) is needed. This would concentrate on common structures observed or simulated and would concentrate on categorization depending on the method of data acquisition (e.g., PE simulation vs. observations based on soundings, etc.). This review would also treat the scales of MCVs and treat processes leading to MCV formation depending on scale.
- It would be interesting to repeat the simulation of Davis and Weisman (1994) using RAMS. If reproducible, this would supply us with a data set to more directly test our conclusions against those of Davis and Weisman. In addition, this would allow us to expand their tests with different environments, e.g., one with a veering or backing wind profile.
- An interesting aspect of these simulations is the apparent transport of PV by the front-to-rear and rear-to-front mesoscale flow branches. It would be useful to devise a scheme whereby properties could be conditionally-sampled along flow branches, thus isolating processes occurring along them.
- One issue that remains unresolved is that of the processes responsible for the residual in Ertel’s \mathcal{P} equation. Our analysis found that this term is locally important to the \mathcal{P} budget but the interpretation of our results was only speculative.

- One area of interest not at all treated herein is the role of *PV* anomalies in the regeneration or even initiation of MCSs. This question has been treated theoretically using nonlinear balance simulations as well as with observations from the synoptic-scale network. As mentioned in Chapter 3, the 10–11 June case appeared to regenerate after the main system was well into the dissipating stage. Capturing this regeneration in a subsequent simulation would be very useful in understanding this phenomena.
- Another area of interest not covered herein is the possible role of the upper-level inverted \mathcal{P} which moves across the region during the lifecycle of the 10–11 June MCS. The fact that the MCS formed ahead of and aligned along this upper-level feature suggests that it may have played a role in the development and/or organization of the storm. Unfortunately, in this case, the nearness of the mountains makes analysis of any possible link much more difficult.
- As a lead-in to the final item, as computer power increases, high-resolution simulations (using 1 or 2 km grid spacings) of *entire* MCSs (i.e., spatially and over the entire lifecycle) without cumulus parameterization would be useful. Until observations exist on such fine scales over areas the size of an MCS, such simulations would provide the best data set.
- Finally, we make the ubiquitous plea for more cases on which to base conclusions. It would be useful if these case studies used *one* method of data acquisition. Comparing studies using radar, soundings, time compositing, NLB simulations, PE simulations idealized scenarios, PE simulations of real systems, or even PE simulations which use differing grid spacings, makes conclusions somewhat ambiguous. Ideally, we would have a set containing data on several, perhaps dozens, of systems using one tool, e.g., high-resolution PE simulations. This would undoubtedly require cooperation between several scientists from several research institutions and is admittedly a pipe dream given today's budget priorities.

References

- Alexander, G.D., and W.R. Cotton, 1994: Explicit simulation of a tropical mesoscale convective system. *Preprints: 10th Conference on Numerical Weather Prediction*, AMS, Portland, OR.
- Augustine, J.A., and K.W. Howard, 1988: Mesoscale convective complexes over the United States during 1985. *Mon. Wea. Rev.*, **116**, 685–701.
- Augustine, J.A., and K.W. Howard, 1991: Mesoscale convective complexes over the United States during 1986 and 1987. *Mon. Wea. Rev.*, **119**, 1575–1589.
- Augustine, J.A., and F. Caracena, 1994: Lower-tropospheric precursors to nocturnal MCS development over the central United States. *Wea. Forecasting*, **9**, 116–135.
- Bartels, D.L., and R.A. Maddox, 1991: Midlevel cyclonic vortices generated by mesoscale convective systems. *Mon. Wea. Rev.*, **119**, 104–118.
- Bennetts, D.A., and B.J. Hoskins, 1979: Conditional symmetric instability — a possible explanation for frontal rainbands. *Quart. J. Roy. Meteor. Soc.*, **105**, 945–962.
- Bennetts, D.A., and J.C. Sharp, 1982: The relevance of conditional symmetric instability to the prediction of mesoscale frontal rainbands. *Quart. J. Roy. Meteor. Soc.*, **108**, 595–602.
- Bernstein, B.C., and R.H. Johnson, 1994: A dual-Doppler radar study of an OK PRE-STORM heat burst event. *Mon. Wea. Rev.*, **122**, 259–273.

- Biggerstaff, M.I., and R.A. Houze, Jr., 1991a: Kinematic and precipitation structure of the 10–11 June 1985 squall line. *Mon. Wea. Rev.*, **119**, 3034–3065.
- Biggerstaff, M.I., and R.A. Houze, Jr., 1991b: Midlevel vorticity structure of the 10–11 June 1985 squall line. *Mon. Wea. Rev.*, **119**, 3066–3079.
- Biggerstaff, M.I., and R.A. Houze, Jr., 1993: Kinematics and microphysics of the transition zone of the 10–11 June 1985 squall line. *J. Atmos. Sci.*, **50**, 3091–3110.
- Bishop, C.H., and A.J. Thorpe, 1994: Potential vorticity and the electrostatics analogy: Quasi-geostrophic theory. *Quart. J. Roy. Meteor. Soc.*, **120**, 713–731.
- Blanchard, D.O., 1994: Jet-induced inertial instabilities and the growth of mesoscale convective systems. Ph.D. Dissertation, Atmos. Sci. Paper No. 571, Colorado State University, Ft. Collins, CO, 191 pp.
- Blanchard, D.O., and W.R. Cotton, 1994: Jet-induced inertial instabilities and mesoscale convective system growth. *Preprints: 6th Conference on Mesoscale Processes*, AMS, Portland, OR.
- Bleck, R., 1973: Numerical forecasting experiments based on the conservation of potential vorticity on isentropic surfaces. *J. Appl. Meteor.*, **12**, 737–752.
- Brandes, E.A., 1990: Evolution and structure of the 6–7 May 1985 mesoscale convective system and associated vortex. *Mon. Wea. Rev.*, **118**, 109–127.
- Bretherton, C.S., and C. Schär, 1993: Flux of potential vorticity substance: A simple derivation and a uniqueness property. *J. Atmos. Sci.*, **50**, 1834–1836.
- Browning, K.A., and R. Reynolds, 1994: Diagnostic study of a narrow cold-frontal rain-band and severe winds associated with a stratospheric intrusion. *Quart. J. Roy. Meteor. Soc.*, **120**, 235–257.

- Chen, C., and W.R. Cotton, 1983: A one-dimensional simulation of the stratocumulus-capped mixed layer. *Bound.-Layer Meteor.*, **25**, 289-321.
- Chen, C., and W.R. Cotton, 1987: The physics of the stratocumulus-capped mixed layer. *J. Atmos. Sci.*, **44**, 2951-2977.
- Chen, S.S., and W.M. Frank, 1993: A numerical study of the genesis of extratropical convective mesovortices. Part I: Evolution and dynamics. *J. Atmos. Sci.*, **50**, 2401-2426.
- Ciesielski, P.E., D.E. Stevens, R.H. Johnson, and K.R. Dean, 1989: Observational evidence for asymmetric inertial instability. *J. Atmos. Sci.*, **46**, 817-831.
- Clark, T.L., and R.D. Farley, 1984: Severe downslope windstorm calculations in two and three spatial dimensions using anelastic interactive grid nesting: A possible mechanism for gustiness. *J. Atmos. Sci.*, **41**, 329-350.
- Cifelli, R., 1995: Vertical motion structure in tropical mesoscale convective systems. Ph.D. Dissertation, Colorado State University, Ft. Collins, CO, 210pp.
- Colman, B.R., 1990: Thunderstorms above frontal surfaces in environments without positive CAPE. Part I: A climatology. *Mon. Wea. Rev.*, **118**, 1103-1121.
- Cooper, I.M., A.J. Thorpe, and C.H. Bishop, 1992: The role of diffusive effects on potential vorticity in fronts. *Quart. J. Roy. Meteor. Soc.*, **118**, 629-647.
- Cotton, W.R., and R.A. Anthes, 1989: *Storm and Cloud Dynamics*, Academic Press, New York, 880 pp.
- Cotton, W.R., M.-S. Lin, R.L. McAnelly, and C.J. Tremback, 1989: A composite model of mesoscale convective complexes. *Mon. Wea. Rev.*, **117**, 765-783.

- Cotton, W.R., G. Thompson, and P.W. Mielke, Jr., 1994: Real-time mesoscale prediction on workstations. *Bull. Amer. Meteor. Soc.*, **75**, 349–362.
- Cram, J.M., R.A. Pielke, and W.R. Cotton, 1992: Numerical simulation and analysis of a prefrontal squall line. Part I: Observations and basic simulation results. *J. Atmos. Sci.*, **49**, 189–208.
- Danielson, E.F., 1990: In defense of Ertel's potential vorticity and its general applicability as a meteorological tracer. *J. Atmos. Sci.*, **47**, 2013–2020.
- Danielson, E.F., R.S. Hipskind, S.E. Gaines, G.W. Sachse, G.L. Gregory, and G.F. Hill 1987: Three-dimensional analysis of potential vorticity associated with tropopause folds and observed variations of ozone and carbon monoxide. *J. Geophys. Res.*, **92**, 2103–2111.
- Davis, C.A., and M.L. Weisman, 1994: Balanced dynamics of mesoscale vortices produced in simulated convective systems. *J. Atmos. Sci.*, **51**, 2005–2030.
- Dunkerton, T.J., and D.P. Delisi, 1986: Evolution of potential vorticity in the winter stratosphere of January–February 1979. *J. Geophys. Res.*, **91**, 1199–1208.
- Eliassen, A., and E. Kleinschmidt, 1957: Dynamic Meteorology. *Handbuch der Physik*, Vol. 48, Berlin, Springer-Verlag, 1–154.
- Emanuel, K.A., 1979: Inertial instability and mesoscale convective systems. Part I: Linear theory of inertial instability in rotating viscous fluids. *J. Atmos. Sci.*, **36**, 2425–2449.
- Emanuel, K.A., 1983a: Conditional symmetric instability: A theory for rainbands within extratropical cyclones. *Mesoscale Meteorology: Theories, Observation and Models*, D.K. Lilly and T. Gal-Chen, Eds., D.Reidel Publishing Co., 231–245.

- Emanuel, K.A., 1983b: On assessing local conditional symmetric instability from atmospheric soundings. *Mon. Wea. Rev.*, **111**, 2016–2033.
- Emanuel, K.A., N. Renno, L.R. Schade, M. Bister, M. Morgan, D.J. Raymond, and R. Rotunno, 1993: Tropical cyclogenesis over the eastern North Pacific: Some results of TEXMEX. *Preprints: 20th Conference on Hurricanes and Tropical Meteorology*, AMS, Miami, FL.
- Ertel, H., 1942: Ein neuer hydrodynamischer Wirbelsatz. *Met. Z.*, **59**, 271–281.
- Fortune, M.A., W.R. Cotton, and R.A. McAnelly, 1992: Frontal-wave-like evolution in some mesoscale convective complexes. *Mon. Wea. Rev.*, **120**, 1279–1300.
- Fritsch, J.M. and R.A. Maddox, 1981: Convectively driven mesoscale weather systems aloft. Part I: Observations. *J. Appl. Meteor.*, **20**, 9–19.
- Fritsch, J.M. and J.M. Brown, 1982: On the generation of convectively driven mesohighs aloft. *Mon. Wea. Rev.*, **110**, 1554–1563.
- Fritsch, J.M., R.J. Kain, and C.R. Chelius, 1986: The contribution of mesoscale convective weather systems to the warm-season precipitation in the U.S. *J. Clim. Appl. Meteorol.*, **25**, 1333–1345.
- Fritsch, J.M., J.D. Murphy, and J.S. Kain, 1994: Warm core vortex amplification over land. *J. Atmos. Sci.*, **51**, 1780–1807.
- Gallus, W.A., Jr., and R.H. Johnson, 1991: Heat and moisture budgets of an intense midlatitude squall line. *J. Atmos. Sci.*, **48**, 122–146.
- Gallus, W.A., Jr., and R.H. Johnson, 1992: The momentum budget of an intense midlatitude squall line. *J. Atmos. Sci.*, **49**, 422–450.

- Gao, K., D.-L. Zhang, M.W. Moncrieff, and H.-R. Cho, 1990: Mesoscale momentum budget in a midlatitude squall line: A numerical case study. *Mon. Wea. Rev.*, **118**, 1011–1028.
- Guinn, T.A., and W.H. Schubert, 1994: Reply to comments on “Hurricane spiral bands”. *J. Atmos. Sci.*, **51**, 3545–3546.
- Haynes, P.H., and M.E. McIntyre, 1987: On the evolution of vorticity and potential vorticity in the presence of diabatic heating and frictional or other forces. *J. Atmos. Sci.*, **44**, 828–841.
- Haynes, P.H., and M.E. McIntyre, 1990: On the conservation and impermeability theorems for potential vorticity. *J. Atmos. Sci.*, **47**, 2021–2031.
- Hertenstein, R.F.A. and W.H. Schubert, 1991: Potential vorticity anomalies associated with squall lines. *Mon. Wea. Rev.*, **119**, 1663–1672.
- Hertenstein, R.F., W.R. Cotton, and M.J. Weissbluth, 1992: Quasi-three-dimensional simulations of deep convection. *Preprints: 5th Conference on Mesoscale Processes*, AMS, Atlanta, GA.
- Hertenstein, R.F., P.Q. Olsson, and W.R. Cotton, 1994: Evolution of potential vorticity associated with two mesoscale convective systems. *Preprints: 6th Conference on Mesoscale Processes*, AMS, Portland, OR.
- Hoskins, B.J., 1974: The role of potential vorticity in symmetric stability and instability. *Quart. J. Roy. Meteor. Soc.*, **100**, 480–482.
- Hoskins, B.J., 1990: Theory of extratropical cyclones. *Extratropical Cyclones: The Eric Palmen Memorial Volume*, C. Newton and E. Holopainen Eds., Amer. Meteor. Soc., 63–80.

- Hoskins, B.J., and P. Berrisford, 1988: A potential vorticity perspective of the storm of 15–16 October 1987. *Weather*, **43**, 122–129.
- Hoskins, B.J., M.E. McIntyre, and A.W. Robertson, 1985: On the use and significance of isentropic potential vorticity maps. *Quart. J. Roy. Meteor. Soc.*, **111**, 877–946.
- Houze, R.A., Jr., B.F. Smull, and P. Dodge, 1990: Mesoscale organization of springtime rainstorms in Oklahoma. *Mon. Wea. Rev.*, **118**, 613–654.
- Jiang, H., and D.J. Raymond, 1995: Simulation of a mature mesoscale convective system using a nonlinear balance model. *J. Atmos. Sci.*, **52**, 161–175.
- Johnson, R.H., and P.J. Hamilton, 1988: The relationship of surface pressure features to the precipitation and airflow structure of an intense midlatitude squall line, *Mon. Wea. Rev.*, **116**, 1444–1472.
- Johnson, R.H., and D.L. Bartels, 1992: Circulations associated with a mature-to-decaying midlatitude mesoscale convective system. Part II: Upper-level features. *Mon. Wea. Rev.*, **120**, 1301–1320.
- Johnson, R.H., S. Chen, and J.J. Toth, 1989: Circulations associated with a mature-to-decaying midlatitude mesoscale convective system. Part I: Surface features—heat bursts and mesoscale development. *Mon. Wea. Rev.*, **117**, 941–959.
- Johnson, R.H., W.A. Gallus, Jr., and M.D. Vescio, 1990: Near-tropopause vertical motion within the trailing stratiform region of a midlatitude squall line. *J. Atmos. Sci.*, **47**, 2200–2210.
- Johnson, R.H., B.D. Miner, and P.E. Ciesielski, 1995: Circulations between mesoscale convective systems along a cold front. *Mon. Wea. Rev.*, **123**, 585–599.
- Kasahara, A., 1974: Various vertical coordinate systems used for numerical weather prediction. *Mon. Wea. Rev.*, **102**, 509–522.

- Keyser, D., and R. Rotunno, 1990: On the formation of potential–vorticity anomalies in upper–level jet–front systems. *Mon. Wea. Rev.*, **118**, 1914–1921.
- Kleinschmidt, E., 1950a: Ueber Aufbau und Entstehung von Zyklonen (1. Teil). *Meteor. Runds.*, **3**, 1–6.
- Kleinschmidt, E., 1950b: Ueber Aufbau und Entstehung von Zyklonen (2. Teil). *Meteor. Runds.*, **3**, 54–61.
- Kleinschmidt, E., 1951: Ueber Aufbau und Entstehung von Zyklonen (3. Teil). *Meteor. Runds.*, **4**, 89–96.
- Klemp, J.B., and R.B. Wilhelmson, 1978: The simulation of three–dimensional convective storm dynamics. *J. Atmos. Sci.*, **35**, 1070–1096.
- Knupp, K.R., and W.R. Cotton, 1987: Internal structure of a small mesoscale convective system. *Mon. Wea. Rev.*, **115**, 629–645.
- Laing, A.G., and J.M. Fritsch, 1993a: Mesoscale convective complexes in Africa. *Mon. Wea. Rev.*, **121**, 2254–2263.
- Laing, A.G., and J.M. Fritsch, 1993b: Mesoscale convective complexes over the Indian Monsoon region. *J. Climate*, **6**, 911–919.
- Lait, L.R., 1994: An alternate form for potential vorticity. *J. Atmos. Sci.*, **51**, 1754–1759.
- Loehrer, S.M., and R.H. Johnson, 1995: Surface pressure and precipitation life cycle characteristics of PRE–STORM mesoscale convective systems. *Mon. Wea. Rev.*, **123**, 600–621.
- Maddox, R.A., 1980: Mesoscale Convective Complexes. *Bull. Amer. Meteor. Soc.*, **61**, 1374–1387.

- Maddox, R.A., and C.A. Doswell, III, 1982: An examination of jet stream configurations, 500 mb vorticity advection and low-level thermal advection patterns during extended periods of intense convection. *Mon. Wea. Rev.*, **110**, 184–197.
- Maddox, R.A., D.J. Perkey, and J.M. Fritsch, 1981: Evolution of upper tropospheric features during the development of a mesoscale convective complex. *J. Atmos. Sci.*, **38**, 1664–1674.
- McAnelly, R.L., and W.R. Cotton, 1989: The precipitation lifecycle of mesoscale convective complexes over the central United States. *Mon. Wea. Rev.*, **117**, 784–808.
- McAnelly, R.L., and W.R. Cotton, 1992: Early growth of mesoscale convective complexes: A meso- β -scale cycle of convective precipitation? *Mon. Wea. Rev.*, **120**, 1851–1877.
- Mellor, G. L. and Yamada, T., 1974: A hierarchy of turbulence closure models for planetary boundary layers. *J. Atmos. Sci.*, **31**, 1791–1806.
- Menard, R.D., and J.M. Fritsch, 1989: A mesoscale convective complex-generated inertially stable warm core vortex. *Mon. Wea. Rev.*, **117**, 1237–1261.
- Miller, D., and J.M. Fritsch, 1991: Mesoscale convective complexes in the western Pacific region. *Mon. Wea. Rev.*, **119**, 2978–2992.
- Montgomery, M.T., and B.F. Farrell, 1992: Polar low dynamics. *J. Atmos. Sci.*, **49**, 2484–2505.
- , and —, 1993: Tropical cyclone formation. *J. Atmos. Sci.*, **50**, 285–309.
- Nachamkin, J.E., R.A. McAnelly, and W.R. Cotton, 1992: An observational analysis of a developing mesoscale convective complex. *Mon. Wea. Rev.*, **122**, 1168–1188.

- Olsson, P.Q., 1994: On the evolution of balanced flows in a mesoscale convective complex. Ph.D. Dissertation, Atmos. Sci. Paper No. 570, Colorado State University, Ft. Collins, CO, 177 pp.
- Pedlosky, J., 1979: *Geophysical Fluid Dynamics*, Springer-Verlag, New York, 624 pp.
- Pielke, R.A., W.R. Cotton, R.L. Walko, C.J. Tremback, W.A. Lyons, L.D. Grasso, M.E. Nicholls, M.D. Moran, D.A. Wesley, T.J. Lee, and J.H. Copeland, 1992: A comprehensive meteorological modeling system - RAMS. *Meteorol. Atmos. Phys.*, **49**, 69-91.
- Pryse, P.V., 1993: Group invariant solutions of the Ernst equation. *Class. Quantum. Grav.*, **10**, 163-175.
- Raymond, D.J., 1992: Nonlinear balance and potential vorticity thinking at large Rossby number. *Quart. J. Roy. Meteor. Soc.*, **118**, 987-1015.
- Raymond, D.J., and H. Jiang, 1990: A theory for long-lived mesoscale convective systems. *J. Atmos. Sci.*, **47**, 3067-3077.
- Read, W.L., and R.A. Maddox, 1983: Apparent modification of synoptic-scale features by widespread convection. *Mon. Wea. Rev.*, **111**, 2123-2128.
- Rodgers, D.M., K.W. Howard, and E.C. Johnston, 1983: Mesoscale convective complexes over the United States during 1982. *Mon. Wea. Rev.*, **111**, 2363-2369.
- Rodgers, D.M., M.J. Magnano, and J.H. Arns, 1985: Mesoscale convective complexes over the United States during 1983. *Mon. Wea. Rev.*, **113**, 888-901.
- Rossby, C.G., 1940: Planetary flow patterns in the atmosphere. *Quart. J. Roy. Meteor. Soc.*, **66**, Suppl., 68-87.

- Rotunno, R., 1981: On the evolution of thunderstorm rotation. *Mon. Wea. Rev.*, **109**, 577–586.
- Rotunno, R., J.B. Klemp, and M.L. Weisman, 1988: A theory for strong, long-lived squall lines. *J. Atmos. Sci.*, **45**, 463–485.
- Rutledge, S.A., 1991: Middle latitude and tropical mesoscale convective systems. *Rev. Geophys.*, Supplement, 88–97.
- Rutledge, S.A., R.A. Houze, Jr., M.I. Biggerstaff, and T. Matejka, 1988: The Oklahoma-Kansas mesoscale convective system of 10–11 June 1985: Precipitation structure and single-Doppler radar analysis. *Mon. Wea. Rev.*, **116**, 1409–1430.
- Schubert, W.H., S.R. Fulton, and R.F.A. Hertenstein, 1989: Balanced atmospheric response to squall lines. *J. Atmos. Sci.*, **46**, 2478–2483.
- Seman, C.J., 1994: A numerical study of nonlinear, nonhydrostatic conditional symmetric instability in a convectively unstable atmosphere. *J. Atmos. Sci.*, **51**, 1352–1371.
- Shapiro, M.A., 1976: The role of turbulent heat flux in the generation of potential vorticity in the vicinity of upper-level jet stream systems. *Mon. Wea. Rev.*, **104**, 892–906.
- Skamarock, W.C., M.L. Weisman, and J.B. Klemp 1994: Three-dimensional evolution of simulated, long-lived squall lines. *J. Atmos. Sci.*, **51**, 2563–2584.
- Smull, B.F., and J.A. Augustine, 1993: Multiscale analysis of a mature mesoscale convective complex. *Mon. Wea. Rev.*, **121**, 103–132.
- Snook, J.S., 1992: Current techniques for real-time evaluation of conditional symmetric instability. *Wea. Forecasting*, **7**, 430–439.

- Staley, D.O., 1960: Evaluation of potential vorticity changes near the tropopause and the related vertical motions, vertical advection of vorticity, and transfer of radioactive debris from stratosphere to troposphere. *J. Met.*, **17**, 591-620.
- Stensrud, D.J., and R.A. Maddox, 1988: Opposing mesoscale circulations: A case study. *Wea. Forecasting*, **3**, 189-204.
- Tremback, C.J., 1990: Numerical simulation of a mesoscale convective complex: model development and numerical results. Ph.D. dissertation, Atmos. Sci. Paper No. 465, Colorado State University, Ft. Collins, CO, 247 pp.
- Tremback, C.J., and R. Kessler, 1985: A surface temperature and moisture parameterization for use in mesoscale numerical models. *Preprints, 7th AMS Conference on Numerical Weather Prediction*, June 17-20, Montreal, Quebec, Canada, 355-358.
- Trier, S.B., and D.B. Parsons, 1993: Evolution of environmental conditions preceding the development of a nocturnal mesoscale convective complex. *Mon. Wea. Rev.*, **121**, 1078-1098.
- Tripoli, G.J., 1986: A numerical investigation of an orogenic mesoscale convective system. Ph.D. dissertation, Atmos. Sci. Paper No. 401, Colorado State University, Ft. Collins, CO, 290 pp.
- Tripoli, G.J., and W.R. Cotton, 1982: The Colorado State University three-dimensional cloud/mesoscale model - 1982. Part I: General theoretical framework and sensitivity experiments. *J. de Rech. Atmos.*, **16**, 185-219.
- Uccellini, L.W. and D.R. Johnson, 1979: The coupling of upper and lower tropospheric jet streaks and implications for the development of severe convective storms. *Mon. Wea. Rev.*, **107**, 682-703.
- Velasco, I. and J.M. Fritsch, 1987: Mesoscale convective complexes in the Americas. *J. Geophys. Res.*, **92**, 9591-9613.

- Verlinde, J. and W.R. Cotton, 1990: A mesoscale vortex couplet observed in the trailing anvil of a multicellular convective complex. *Mon. Wea. Rev.*, **118**, 993-1010.
- Weissbluth, M.J. and W.R. Cotton, 1993: The representation of convection in mesoscale models. Part I: Scheme fabrication and calibration. *J. Atmos. Sci.*, **50**, 3852-3872.
- Zhang, D.-L., 1992: The formation of a cooling-induced mesovortex in the trailing stratiform region of a midlatitude squall line. *Mon. Wea. Rev.*, **120**, 2763-2785.
- Zhang, D.-L. and J.M. Fritsch, 1988: A numerical investigation of a convectively generated, inertially stable, extratropical warm-core mesovortex over land. Part I: Structure and evolution. *Mon. Wea. Rev.*, **116**, 2660-2687.
- Zhang, D.-L., and K. Gao, 1989: Numerical simulation of an intense squall line during 10-11 June 1985 PRE-STORM. Part II: Rear inflow, surface pressure perturbations and stratiform precipitation. *Mon. Wea. Rev.*, **117**, 2067-2094.
- Zhang, D.-L. and H.-R. Cho, 1992: The development of moist potential vorticity in the stratiform region of a simulated squall line. *Mon. Wea. Rev.*, **120**, 1322-1341.
- Zhang, D.-L., K. Gao, and D.B. Parsons, 1989: Numerical simulation of an intense squall line during 10-11 June 1985 PRE-STORM. Part I: Model verification. *Mon. Wea. Rev.*, **117**, 960-994.
- Zipser, E.J., 1982: Use of conceptual models of the life-cycle of mesoscale convective systems to improve very-short-range forecasts. Nowcasting, Academic Press, K.A. Browning Ed., 191-204.